THEORY AND MEASUREMENT OF THE FRET SIGNATURES OF MEMBRANE PROTEINS

by
Christopher R. King

A dissertation submitted to Johns Hopkins University in conformity with the requirements for the degree of Doctor of Philosophy

Baltimore, Maryland

October, 2016

Abstract

FRET is an indispensable tool for the study of membrane proteins, however the theory to describe the measured FRET of membrane proteins is not complete, and a robust method to measure FRET from small regions of fluorescence of labeled membrane proteins in live cells does not exist. In this work, I extend the theory of FRET for two-dimensional distributions of membrane proteins to account for FRET that occurs in the absence of specific protein-protein interactions, and occurs solely due to confinement in two dimensions. I then develop a fluorescence imaging methodology that allows for the measurement of membrane protein surface densities and FRET efficiencies in small, ~3 micron-sized patches of membrane in live cells, in a mathematically approximation-free manner. I demonstrate the utility of this improved FRET theory and new methodology by measuring the thermodynamic properties of one specific cell membrane receptor that is critical for angiogenesis, VEGFR2, in the absence and presence of its activating ligand, VEGF.

Thesis Committee:
Dr. Kalina Hristova (advisor, reader)
Dr. Margaret Johnson (reader)
Dr. Jie Xiao
Dr. Elijah Roberts
Dr. Herschel Wade
Dr. Sarah Woodson

Preface

This work would not have been possible without the great support and advice of my advisor, Dr. Kalina Hristova. She is patient, caring, fair, and intelligent, and I am forever grateful that she has allowed me the honor of getting to know her and for the privilege of doing science in her lab. She is the best PI one could hope to have. I am deeply indebted to my collaborators for contributions to several theoretical aspects of this work, Dr. Michael Stoneman and Dr. Valerica Raicu from the Department of Physics at the University of Wisconsin-Milwaukee. I am also thankful for mentorship and guidance from Dr. Martin Ulmschneider of the Department of Materials Science and Engineering. I must acknowledge the hard work and dedication of Samuel Workman, an undergraduate from the Department of Biophysics at JHU. Sam performed a majority of the image analysis for the experiments in the absence of VEGF using the software that I developed. He has analyzed several thousand cell images under my guidance. Additionally, I must also acknowledge the hard work of Daniel Wirth, a visiting graduate student from Mainz, Germany. Under my direction, he performed the subcloning to create the D5:D7-TM VEGFR2 construct, and imaged about one third of the cells for that dataset. His quick learning and perseverance have enabled us to continue to perform many experiments on other membrane proteins throughout the writing of this thesis. Lastly, I am especially thankful and forever indebted for the friendship and support of Kevin Sanders, Ranice Crosby, Pat Byrne, Robert Trachman, and Shaun Greene.

Contents

List of Figures

Chapter 1. Introduction

Chapter 2. Theory of FRET for Membrane Proteins

Chapter 3. Simulations Reveal the (non)Uniqueness of the FRET of Interacting Membrane Proteins

Chapter 4. In Vivo Measurement of Membrane Protein Surface Densities and FRET Efficiencies with Fully Quantified Spectral Imaging

Chapter 5. Application of FRET Theory and FSI: VEGFR2 Mutagenesis and EC Domain Truncations Reveal Sequence-Specific Interactions in the Absence of VEGF

Chapter 6. Advanced Application of FRET Theory and FSI: Measurement of VEGF Binding Affinity

List of Tables

List of Figures

List of Figures

List of Figures

List of Figures

List of Figures

Chapter 1. Introduction

1-1. VEGF and VEGFR2

Belonging to the second largest family of signal transducing proteins, Receptor Tyrosine Kinases (RTKs) epitomize functional regulation through lateral interaction in the plasma membrane [1-5]. RTK dimerization is necessary for RTK function, as contacts between the intracellular kinase domains lead to kinase cross-phosphorylation and initiation of downstream signaling cascades that control cell growth, differentiation and motility during development and in the adult, and in many pathologies such as cancers and growth disorders[1,6]. While RTK dimerization has been long assumed to occur in response to ligand binding, recent work has suggested that RTKs have a propensity to interact and even in the absence of bound ligand, thus challenging the canonical view of RTK ligand-induced dimerization and activation [7,8]. It is thus possible that the intrinsic thermodynamic properties of the RTK present a 'pre-formed' dimer that is primed for a structural shift upon ligand binding. Yet, the mode of activation of many RTKs has thus far remained controversial, and is still a topic of intense investigations and debate.

Vascular Endothelial Growth Factor Receptor-2 (VEGFR2) is a 151 kDa member of the RTK family. After heavy glycosylation, the final form of VEGFR2 is has a molecular weight of nearly 250 kDa[9]. VEGFR2 is the main regulator for angiogenesis, the formation of new blood vessels from existing vasculature, and vasculogenesis, the de novo formation of new blood vessels in tissues [10-14]. VEGFR2 has a typical RTK structure consisting of an Extracellular (EC) domain, a single-pass alpha-helical Transmembrane (TM) domain, and an intracellular Kinase domain. VEGFR2's EC domain is one of the largest of the RTK family, consisting of seven Ig-like domains, known as subunits D1-D7. Subunit D1 is a the N-terminal side of the protein, with subunits D2-D3 consisting of the binding domain for VEGFR2's activating ligand. Subunits D4 and D7 have been identified as domains participating in "homotypic contacts," which are essential for stabilizing the active form of the ligand-bound VEGFR2 dimer[15-18]. It is currently an open question as to whether these homotypic contacts can occur in the absence of ligand, and roles of each subunit in the context of the live cell membrane remain unknown.

VEGFR2 is a signal transducing protein which is primarily found in the membranes of endothelial cells in the vascular system, though a number of difference cell types in various tissues also express VEGFR2 in their membranes[19-22]. VEGFR2 is activated upon paracrine or autocrine stimulation by Vascular Endothelial Growth Factor (VEGF), which is predominantly released by cells under hypoxic conditions, though a number of different conditions and events can elicit VEGF secretion by cells[23,24]. Enhanced and suppressed VEGF signaling occurs in a number of pathogenic conditions, making VEGF and VEGFR2 active targets for both anti- and pro-angiogenic research and drug development.

VEGF is found in the body as a disulfide linked homodimer [25]. There are several isoforms of VEGF, and the focus of this work will be with the 'labile' form of VEGFA, VEGF121. VEGF121 is a 28 kDa soluble disulfide-linked homodimer of two 121 amino acid chains, which lacks the binding site required for retention in extracellular matrix. This binding site enables interactions between VEGF and a number of binding partners besides VEGFR2 such as heparan-sulfate proteoglycans or Neuropilin 1[14,26,27]. VEGF121 binds specifically to VEGFR2's EC domain, and it is not retained in the extracellular matrix of the cells, like other forms of VEGF[11,13,14,24,28]. This property of VEGF121 makes it a great candidate for the study of VEGF interactions with VEGFR2 EC domains, as non-specific ligand-cell interactions are minimized.

It was recently shown in the Hristova Lab that full-length VEGFR2 constructs dimerize in the absence of VEGF, with low levels of basal kinase domain cross-phosphorylation [29]. It was also shown that a structural shift occurs upon VEGF binding to VEGFR2 under saturating conditions of VEGF, and this structural shift is responsible for transmitting the ligand-bound state to the intracellular side of the cell, allowing for full cross-phosphorylation and signal transduction [29].

Current knowledge of the VEGF affinity for VEGFR2 is limited in that it is not known whether or not the affinity of VEGF is enhanced for dimeric VEGFR2 on the cell surface, or if the affinity is simply twice that of the affinity of VEGF for monomeric VEGFR2 due to the symmetric binding sites in the dimer. This lack of understanding is due to the lack of methodology to study receptor-ligand interactions at the molecular level, and in the context of the live-cell membrane. Previous studies have utilized estimations of the surface area of the cell, around 1,000 square-microns, and the number of receptors per cell for measurements of the affinity of VEGF for VEGFR2. Other research groups have utilized ITC binding experiments to measure the affinity of soluble, isolated VEGFR2 EC domains in an artificially constructed monomeric or dimeric form [15]. However, these models do not account for the monomeric and dimeric fractions of VEGFR2, as driven by the local effective concentration of receptors on the cell surface through the law of mass action.

Several mechanisms for VEGF activation of VEGFR2 can be postulated. One possible mechanism for VEGF activation of VEGFR2 is that the VEGF can bind to monomeric VEGFR2, with then undergoes dimerization with a structural shift that is transmitted to the Kinase domains through the TM domain, and allows for full cross-phosphorylation and activation of the receptor. A second possibility is that VEGF binds to a pre-formed dimer of VEGFR2, which exists naturally in a monomer-dimer equilibrium in the membrane of the cell, and then after VEGF binds, a structural shift occurs that is then transmitted to the Kinase domains, which are then properly oriented for full cross-phosphorylation and signal transduction. Under heavily saturating conditions of VEGF, one could even imagine a situation where the monomeric forms of VEGFR2 all have a bound VEGF molecule, which would then inhibit dimerization of VEGFR2 through a steric clash of a bound VEGF molecule on each monomeric receptor. Despite the fact that VEGF and VEGFR2 are one of the most intensely studied signaling components, the sequence-specific EC domain interactions of VEGFR2 are still not fully understood, and mode of activation of VEGFR2 by VEGF binding remains unclear. **Figure 1-1** below shows the current understanding of VEGFR2/VEGF interactions at the beginning of my work, summarized as a cartoon.

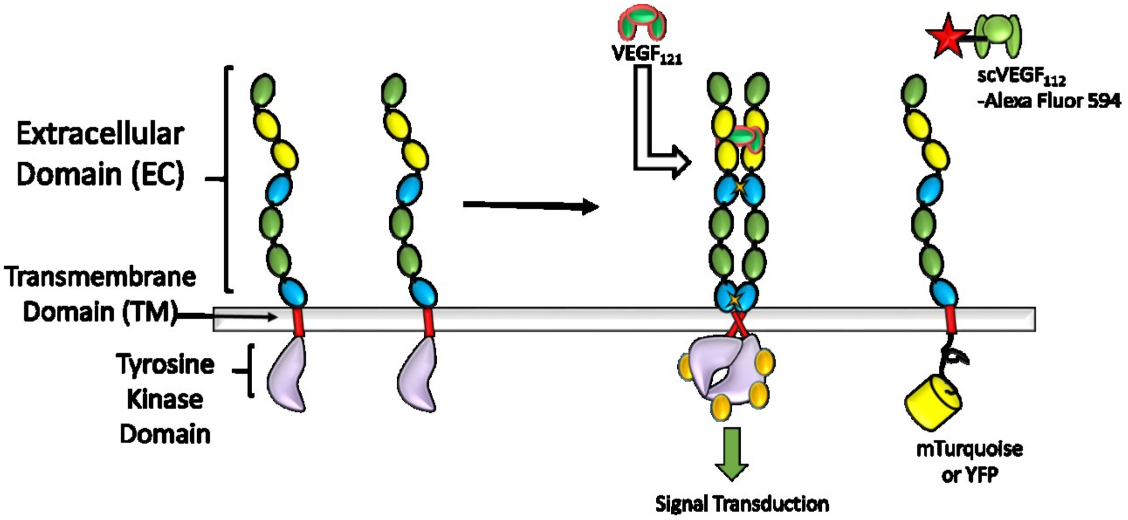

Figure 1-1. The model for VEGFR2-VEGF interactions at the start of my work. Left: VEGFR2 is a membrane protein belonging to the RTK family of receptors, and it is essential for angiogenesis. From N-terminus to C-terminus, it consists of an Extracellular (EC) domain with seven Ig-like subunits D1-D7, a single-pass alpha helical Transmembrane) domain, and an intracellular tyrosine kinase domain, as shown on the left. Upon stimulation of VEGFR2 with VEGF, which binds to the D2 and D3 (yellow) domains of VEGFR2 dimers. Homotypic D4-D4 and D7-D7 contacts (blue subdomains, with stars indicating contacts) stabilize the ligand-bound dimer, which then undergoes cross-phosphorylation of the kinase domains and subsequent signal transduction. Far right: In this work, I utilize VEGF labeled with Alexa Fluor 594(AF594-VEGF), and a truncated form of VEGFR2 having only the EC and TM domains, VEGFR2 ECTM. I utilize VEGFR2 ECTM in which the kinase domain is replaced with a fluorescent protein, YFP, to study the interactions of VEGFR2 ECTM domains with themselves in the absence of VEGF, and the binding affinity of VEGF for monomeric and dimeric forms of VEGFR2 EC domains in the context of the live cell membrane.

1-2. Förster's Theory of Resonance Energy Transfer

When the electrons of an optically-active molecule such as a fluorescent protein absorb energy, they are energized to higher energy levels. The probability that a fluorophore will emit a photon given an excitation event is known as the quantum yield, Q, of that fluorophore. When another optically active molecule is near a fluorophore existing in an excited electronic state, the excited molecule can transfer its energy to the nearby molecule in a radiation-less transfer of energy. This second molecule can then fluoresce, and emit a photon. In this manner, the quantum yield of the donor is reduced by the quenched donor fluorescence in the presence of acceptor chromophores. Similarly, the acceptor's fluorescence is enhanced, or sensitized, and the quantum yield of the acceptor is enhanced in the presence of donors[30-33]. This radiation-less transfer of energy between donor and acceptor chromophores is a quantum mechanical phenomenon that was first described mathematically through a consideration of classical electrodynamics and an excited-state dipole-dipole coupling by Theodore Förster, in 1946[34]. Appropriately, this form of resonant energy transfer is known as Förster's Resonance Energy Transfer, or FRET [32,35].

Förster calculated a R^{-6} distance dependence on the rate of FRET between a donor and an acceptor as given in Förster's Equation:

$$k_{RET} = \frac{1}{\tau_D}\left(\frac{R_0}{R}\right)^6 \tag{1-1}$$

In **Equation (1-1),** τ_D is the fluorescence lifetime of the donor in the absence of FRET. R is the distance from the donor to the acceptor chromophore and R_0 is a numerical quantity known as the Förster radius, which is typically ~5 nm. This strong distance dependence is the reason FRET is now often referred to as a "molecular ruler," as it is capable of probing distances on the range of 10-100 nm.

The efficiency of resonant energy transfer between a single donor and acceptor molecule is known as the intrinsic FRET Efficiency of the donor-acceptor pair and is defined as:

$$\tilde{E} = \frac{k_{RET}}{k_D + k_{RET}} \tag{1-2}$$

Equation (1-2), the intrinsic FRET efficiency is the ratio of the rate of donor de-excitation to the sum of all intrinsic donor de-excitation pathways, including FRET. These intrinsic de-excitation rate pathways include the fundamental radiative emission rate, the rate of internal conversion leading to de-excitation without emission of a photon, rates of intersystem crossing, collisional quenching, the rate of photo-destruction, etc.

Substitution of **Equation (1-1)** into **Equation (1-2)** gives the FRET efficiency of a single donor-acceptor pair separated by a distance, R :

$$\tilde{E} = \frac{1}{1 + \left({}^{R}/_{R_0}\right)^6} \tag{1-3}$$

.

Förster's radius is the distance at which the rate of donor radiation in the absence of FRET is equal the rate of resonant energy transfer and is a physical property of the donor-acceptor FRET pair ($\tilde{E} = 0.5$ at this distance):

$$R_0 = \left[{}^{9\ln(10)\,\kappa^2 Q_D \cdot J(\lambda)}\!\Big/_{128\pi^5 N_A n^4}\right]^{1/6} \tag{1-4}$$

R_0 is a function of the index of refraction, n, the quantum yield of the donor in the absence of FRET, Q_D, a dipole-dipole orientation factor known as kappa-squared, κ^2, and an overlap integral, $J(\lambda)$. N_A is Avagadro's number. In **Equation (1-4)**, R_0 and λ are in units of centimeters.

The overlap integral, $J(\bar{v})$, is an integral over all emission wavelengths, over the product of the acceptor's molar extinction coefficient, $\varepsilon_A(\lambda)$, in units of cm^{-1} mol^{-1}, with the normalized fluorescence emission spectrum of the donor, $f_D(\lambda)$, and the wavelength to the fourth power:

$$J(\lambda) = \int_0^\infty \varepsilon_A(\lambda)\, f_D(\lambda) \lambda^4 d\lambda \tag{1-5}$$

The dipole-dipole orientation factor known as kappa-squared, κ^2, is a function of the spatial orientation of the donor and acceptor chromophores, and is given here as a dot product:

$$\kappa^2 = \left\{\left[2cos(\theta_D)\hat{\boldsymbol{r}} + sin(\theta_D)\hat{\boldsymbol{\theta}}_{\boldsymbol{D}}\right] \cdot \hat{\boldsymbol{\mu}}_{\boldsymbol{A}}\right\}^2 \tag{1-6}$$

Here, $\hat{\boldsymbol{\mu}}_{\boldsymbol{A}}$ is the unit dipole moment of the acceptor. $\hat{\boldsymbol{r}}$ is the unit vector that points from the donor chromophore to the acceptor chromophore, and $\hat{\boldsymbol{\theta}}_{\boldsymbol{D}}$ is the unit normal vector to $\hat{\boldsymbol{r}}$, and is parallel to the plane defined by $\hat{\boldsymbol{r}}$ and and $\vec{\boldsymbol{\mu}}_{\boldsymbol{D}}$, the donor dipole moment. If one assumes that the acceptor samples all possible configurations during the FRET lifetime, ~ 10^{-9} seconds, the defining characteristic of the dynamic isotropic regime for FRET, then $\kappa^2 = 2/3$.

In this work, I utilize the fluorescent proteins mTurquoise and YFP connected to membrane proteins through a flexible GGS_5 linker to measure FRET, and to ultimately determine membrane protein thermodynamic properties through these FRET measurements. mTurquoise and YFP are fluorescent proteins that were both derived from GFP, the original green fluorescent protein isolated from the jellyfish *Aequorea victoria*[36,36-39]. Comprised of 238 amino acids, these fluorescent proteins are large 27 kDa moieties with a eleven-stranded beta-barrel structure. The chromophore of the fluorescent proteins exists within a kinked alpha helix found in the center of the fluorescent protein's beta barrel. The quantum yield of mTurqoise, the donor, is $Q_D = 0.84$, with YFP as the FRET acceptor, having a quantum yield, $Q_A = 0.61$. I have measured the Förster radius of the mTurquoise-YFP FRET pair to be 5.5 nm.

The nanosecond FRET lifetime is far too short for any appreciable motion of the fluorescent proteins to occur, and thus the FRET experiments in this work occur in the static isotropic regime, instead of the dynamic isotropic regime described above. The use of the GGS_5 flexible linkers ensures that the distribution of excited fluorescent proteins in the voxel is random. In the static isotropic regime, all possible donor-acceptor orientations are found in the excited ensemble, but their motion is static during the FRET lifetime [40]. This means that in general, in my experiments, the orientation factor κ^2 is not equal to 2/3 [40]. However, it has been shown that even a 100% error in the value of orientation factor only leads to a 12% error in the value of the calculated Förster radius, R_0. In general, the error in the orientation factor and the associated error in R_0 are smaller than the error of cell-membrane total apparent FRET efficiency measurements performed in these experiments [40]. Regardless, I will avoid talking about the distance between the donor and the acceptor for a given intrinsic FRET value, but if I do give a distance, I will utilize the assumption of $\kappa^2 = 2/3$. Thus, if the intrinsic FRET of a donor-acceptor pair increases when some condition is changed, the donor-acceptor distance must necessarily decrease, and vice versa for a decrease in the intrinsic FRET efficiency where the donor-acceptor distance must increase, regardless of the value of the orientation factor.

It should be stressed that the value of the Förster radius will only explicitly come into use during the interpretation of the measured intrinsic FRET efficiency, if a donor-acceptor distance is calculated from an intrinsic FRET value. The theory described above only accounts for the FRET between a single donor and an acceptor and in Chapter 2, I will extend the theory of FRET to entire ensembles of excited donor and acceptors existing in two-dimensions. As shown in Chapter 4, the actual measurements of the FRET efficiencies do not utilize the calculable value for R_0, and only uses only the well-known donor and acceptor quantum yields in the absence of FRET.

1-3. Objectives

Out of the many interactions that occur between biological macromolecules, the interactions between membrane proteins are the least understood due to lack of adequate quantitative experimental methodologies [41-46]. Yet, these interactions regulate vital cellular processes such as signal transduction, nutrient uptake, and motility. Since roughly one third of the open reading frames in the human genome encode for membrane proteins, this means that we are very far from truly understanding cells and membrane proteins at a meaningful level. One experimental tool that has provided a wealth of knowledge on membrane proteins is fluorescence microscopy, and in particular, measurements of the FRET, Förster resonant energy transfer [47-54]. In these experiments, membrane proteins linked to fluorescent proteins are used to probe the stoichiometry and association strengths. However, since fluorescent protein (FP)-labeled membrane proteins are confined to the locally two-dimensional lipid bilayer, the stochastic FRET, or FRET due to close proximity of an acceptor to an excited donor, but without any direct protein-protein interaction, becomes a substantial component of the measured signal. Furthermore, it was not even known if FRET measurements of the kind being currently performed actually meant anything, as the limits of oligomer discernment with two-color FRET is not known.

The primary, though admittedly not the initial, objective for my thesis research was to fully understand the effects of stochastic FRET and the limitations of FRET measurements in general. At the beginning of my time with the Hristova Lab, the effects and magnitude of the stochastic FRET were not understood, though it was known that stochastic FRET could occur. The models for the theoretical FRET were written down without accounting for stochastic FRET. Through collaboration with Dr. Raicu in the mathematical extension of the FRET theory to account for inter-oligomeric FRET as well as intra-oligomeric FRET, I have developed a mathematical framework that allows one to properly account for stochastic FRET in the data analysis of a quantitative FRET experiment, where the total concentration of labeled membrane proteins is known, in addition to the total apparent FRET efficiency. I performed simulations of static quenching FRET experiments in cell membranes, and I show that the association constant and the oligomerization state can be extracted from the total apparent FRET efficiency. I also have surprisingly (or not, depending on whom is asked) found that the FRET signatures of oligomerizing membrane proteins are not unique. In other words, static quenching FRET experiments can be used to distinguish monomeric, and dimeric membrane proteins, but cannot discern the order of higher order oligomerization because the total apparent FRET efficiency of higher order oligomerization is not unique. This is a controversial finding, as many researchers are currently claiming measurements of tetramers or higher-order oligomers.

In addition to the theoretical issues surrounding analysis of FRET measurements in membranes, there are quantitative issues surrounding the measurement of FRET itself, in solution and in cell membranes. Thus, the second objective of my thesis work was to develop a robust method for FRET measurement in live cells. Prior to this work, quantitative FRET experiments were performed using models with adjustable parameters to account for filter and excitation source bleed through effects. The intrinsic excitation of the donor or acceptor molecules during different scans was/is often approximated to be zero, even though this approximation is usually not completely true.

Using a spectral imaging system with two-photon excitation in the IR wavelengths, in collaboration with Dr. Stoneman and Dr. Raicu in the derivation of the equations, I have developed a quantitative fluorescence imaging methodology, termed Fully Quantified Spectral Imaging (FSI), with unique capabilities to probe the stoichiometry and stability of protein complexes in biological membranes, *in vivo*[55]. FSI utilizes a fully-solved system of equations and yields two-dimensional membrane concentrations and FRET efficiencies in native plasma membranes, without the use of filters or correction factors, or constraints on the excitation wavelengths utilized. In combination with the FRET theory I developed, FSI can be used to characterize the association of membrane proteins: to differentiate between monomers, dimers, or oligomers, to produce binding (association) curves, and to measure the free energies of association in the membrane.

The last objective of my thesis work was to understand the thermodynamic properties of VEGFR2 in the absence and presence of VEGF. Thus, I utilized FSI and the newly developed theory for stochastic FRET to directly measure unknown physical-chemical properties of VEGFR2 in the absence and presence of its activating ligand, VEGF, in the cell membrane of living cells. By studying truncations of the VEGFR2 EC domain, I have identified the functional role of the homotypic interactions seen in the ligand-bound dimer, in the absence of ligand. This information on unliganded VEGFR2 interactions is new and unique, as there is no phosphorylation signal to monitor in the absence of VEGF and this type of direct measurement has not been performed in cells. Finally, I pushed the limits of the technology and methodology and utilize a full thermodynamic cycle and fluorescently-labeled VEGF to measure the association constant of VEGF for monomeric and dimeric forms of VEGFR2 on the surface of live cells. This information can be used to predict the active fraction (ligand-bound dimeric fraction) of VEGFR2 at any surface density and free-VEGF concentration.

The theory and methodology developed here should be applied to study many membrane proteins, such as the rest of the RTKs, GPCRs, co-receptors, adhesion molecules, etc., and will ultimately aid in the development of diverse molecular therapies through proper understanding of protein behavior in the cell membrane that is based on thermodynamic principles and truly quantitative methodology.

Chapter 2. Theory of FRET for Membrane Proteins

2-1. Introduction

Many of the label-free techniques that are commonly used to study soluble protein interactions cannot be extended to membrane proteins in their native environment. Instead, fluorescence methods, particularly approaches that rely on Förster resonant energy transfer (FRET), are often used [48,50,51,56,57]. A major advantage of the FRET-based assessment of molecular interactions in the membrane is that experiments can be performed in cells or in a cell-derived system, without the need for membrane protein extraction and purification[58-62].

FRET involves the non-radiative transfer of energy from an optically excited donor to an appropriate acceptor molecule [34]. In FRET experiments, the membrane proteins of interest are tagged with genetically encoded donor and acceptor fluorescent proteins such as CFP, GFP, YFP, and mCherry [36,37,63]. The steady-state FRET efficiency in this case can be easily measured in a standard fluorescence microscope. This measured FRET is termed the "total apparent FRET efficiency."

However, quantitative assessment of the strength of interactions between the tagged membrane proteins remains a challenge, partially because of the unknown "proximity FRET" or "stochastic FRET" contribution to the total apparent FRET efficiency. Stochastic FRET occurs when a donor and an acceptor approach each other by chance within distances of about two Förster radii, and does not reflect specific interactions between the tagged membrane proteins [64]. The magnitude of this effect is significant because the fluorophores are confined to diffuse in two dimensions. As we will see, without a correction for stochastic FRET, the results of a FRET-based measurement of membrane protein interactions will be incorrect and misleading. Thus, it is critical that the effect is understood and reliably predicted even in cases when it is not directly measurable. I have spent considerable time and effort on this problem, ultimately culminating in a full theoretical description for the combined effects of the unwanted stochastic FRET and the desired FRET due to sequence-specific protein-protein interactions, known as the "oligomeric FRET."

I will discuss the theoretical models for the FRET due to protein-protein interactions, the oligomeric FRET. I will begin with the case of non-interaction, or monomeric membrane proteins. In this case, all FRET is due to stochastic FRET. Then, I will introduce the Kinetic Theory of Oligomeric FRET for dimerizing and higher-order oligomerization of membrane proteins, and demonstrate the method for incorporation of a thermodynamic model into the Kinetic Theory of Oligomeric FRET. I will then derive the general Kinetic Theory of FRET. The Kinetic Theory of FRET describes the total apparent FRET efficiency as would be measured in an experiment and accounts for stochastic FRET and the FRET due to specific protein-protein interactions, the "oligomeric FRET."

2-2. A Numeric Description of the FRET of Monomeric Membrane Proteins

When confined to two dimensions, even at relatively low concentrations, donors and acceptors can randomly approach each other such that the energy of an excited donor can be transferred to an acceptor with significant probability. This type of random stochastic FRET will occur even in the absence of sequence specific interactions. Unlike the FRET of specific protein-protein interactions, there is no analytical solution that describes the stochastic FRET as a function of fluorophore surface density (concentration). Thus, a numeric model of the stochastic FRET is necessary.

Wolber and Hudson developed a model for FRET in two dimensions that accounts for random encounters of monomeric donors and acceptors, while assuming that the size of the donor and acceptor fluorophores is negligible, and the chromophores can come infinitely close to each other [64]. This theoretical model has been shown to explain FRET data in lipid bilayers when the donor and the acceptor are small organic molecules. However, the model is not applicable to large beta-barrel fluorescent proteins used in cellular studies because of their rather large finite size (~ 3-4 nm), which limits the distance of closest approach between donors and acceptors chromophores. A model that is useful in this case was developed by Snyder and Freire, who used computer simulations to predict proximity FRET for monomeric fluorophores with finite size that are confined to a plane in two dimensions [65].

As shown by Wolber and Hudson [64], in a static quenching FRET experiment, the relative quantum yield for a donor surrounded by a random configuration, β, of N acceptor molecules is:

$$q_r^{(\beta)} = \left[1 + \sum_{i=1}^{N_\beta} \left({}^{R_0}/_{R_i}\right)^6\right]^{-1} \tag{2-1}$$

In **Equation (2-1)** above, R_i is the distance from the i'th acceptor molecule to the donor and R_0 is the Förster Radius, a property of the donor-acceptor FRET pair. The Förster radius is the donor-acceptor distance, R_0, at which resonant energy transfer efficiency, E, is decreased to 50% [34].

$$E = \frac{1}{1 + {}^{R^6}/_{R_0^6}} \tag{2-2}$$

The ensemble average of **Equation (2-1)** over all configurations of acceptor molecules equals the ratio of the donor quantum yield in the presence (Q_{DA}) and absence (Q_D) of the acceptor molecule [64]:

$$ {}^{Q_{DA}}/_{Q_D} = \lim_{M\to\infty}\left[\frac{1}{M}\sum_{\beta=1}^{M} q_r^{(\beta)}\right] \tag{2-3}$$

The stochastic FRET depends only on the acceptor concentration (because more donors do not contribute to additional FRET), and thus it can be predicted based on quantum yield calculations for a single donor surrounded by a random configuration of acceptors. However, certain cases are more complex (see below), and configurations of multiple donors may need to be considered. As shown by Snyder and Freire [65], if multiple excited donors, N_D, are available to transfer their energies to a random configuration of acceptors, the ratio of quantum yields shown in equation (2-3) becomes:

$$Q_{DA}/Q_D = \lim_{M\to\infty}\left[\frac{1}{M}\sum_{\beta=1}^{M}\frac{1}{N_D}\sum_{j=1}^{N_D}(1+\sum_{i=1}^{N_\beta}R_0/R_i)^{-1}\right] \tag{2-4}$$

The stochastic FRET transfer efficiency, E_{prox}, for a given acceptor concentration is then given by:

$$E_{prox} = 1 - Q_{DA}/Q_D \tag{2-5}$$

Wolber and Hudson developed analytic equations to calculate proximity FRET as a function of acceptor concentration[64]. These equations, however, are valid for point fluorophores only, and break down when the excluded volumes of donors and acceptor molecules becomes relevant, as in the case of fluorescent proteins with diameters of ~ 3 nm and Förster radius of ~ 5.4 nm. Snyder and Freire used computer simulations and the equations above to determine proximity FRET [65] that is valid for monomers of finite size. As discussed below, here I have improved upon their numerical result by simulating over a wider range of exclusion radii, and a finer grid of acceptor concentrations.

In my simulations, I specifically model the case of integral membrane proteins that are labeled with fluorescent proteins at their C-termini, on the intracellular side of the membrane. I assume that the attachment of the fluorescent proteins is through an intrinsically disordered linker, and thus the fluorophores adopt random orientations. I assume that $\kappa^2 = 2/3$ and that R_0 is constant between all donor-acceptor pairs in this work. The fluorescent proteins are confined to the two-dimensional region in the immediate vicinity of the membrane when attached to a membrane protein as described. Thus, I can forego simulations of the complicated membrane environment and focus solely on the generation of random 2-D configurations of fluorophores with limited distances of closest approach, L. The simulation is performed in 2-D, and the fluorophores are modeled as circles of a fixed exclusion radius, r, with the chromophore at the center of the circle. In the case where donor and acceptor molecules are fluorescent proteins fused to identical species of membrane-bound protein, this distance of closest approach, L, is twice the exclusion radius, $2r$, of a three-dimensional volume sampled freely by the fluorescent protein.

To simulate the stochastic FRET for monomeric membrane proteins, a lone donor molecule is placed within the center of a two-dimensional, square simulation region (Figure 2-1). For each simulated acceptor concentration, the number of acceptor molecules is calculated and acceptors are placed one by one into the simulation region until the desired surface density is reached. For each acceptor molecule to be placed, a random position is chosen within the simulation region and evaluated against the condition of no overlap. If no overlap occurs between the newly placed acceptor and any other previously placed molecule, including the central donor molecule, the position is chosen as acceptable. If not, then a new random position is chosen and the position is evaluated again against the condition of no overlap. This is repeated until all of the acceptor molecules are successfully placed without overlap within the simulation region. **Equation (2-1)** is then used to calculate the quantum yield of the central donor in the presence of the random configuration of acceptors. After this is done for a large ensemble of such configurations, **Equations (2-3) ((2-4) for simulations of n > 1)** is used to calculate the simulated stochastic FRET as a function of acceptor concentration.

The stochastic FRET contribution due to random approach of monomeric fluorophores was simulated on a 150 x 150 nm^2 2-D plane (see **Figure 2-1**). Acceptor concentrations ranging from 0 to 0.01 acceptors/nm^2 were used in the simulations, and the simulations were run for exclusion radii ranging from 0 to 4 nm, in 0.02 nm steps. These simulations were performed for N = 40,000 different configurations at each acceptor concentration. The Forster radius for the YFP-mCherry FRET pair of 5.4 nm was utilized in the generation of the curves of relative quantum yield. In Figure 2-1, I show a sample configuration of monomeric donors and acceptors, when the distance of closest approach is 2.8 nm, corresponding to an effective exclusion radius of 1.4 nm.

The case of stochastic FRET in the case of non-interacting fluorophores with finite volume has been considered previously by Snyder and Freire, with the only difference being the method of molecular placement [66]. They used an elegant Monte Carlo approach to generate the various acceptor configurations, from which curves of Q_{DA}/Q_D were generated for different values of L/R_0 [65].

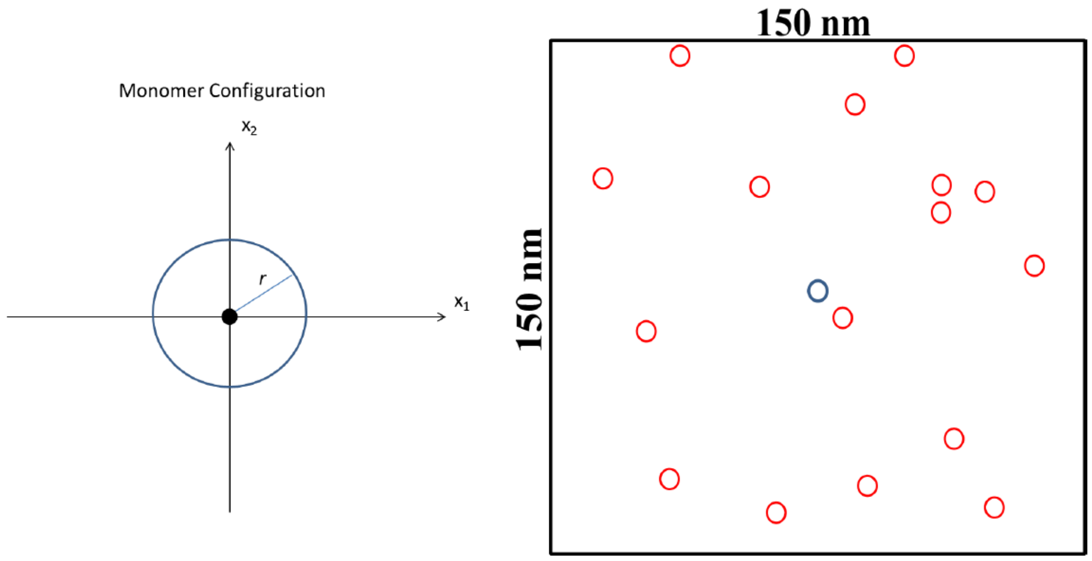

Figure 2-1. A random configuration of acceptors (red) surrounding a donor (blue), for acceptor concentration of 0.00071 fluorophores/nm^2. 40000 such configurations are created, and their FRET efficiency is averaged to create a prediction for "proximity FRET" at this concentration. The fluorophore radius is 1.4 nm; figure not to scale

Each curve was fitted to an exponential function of acceptor concentration per R_0^2, [c], and the dependence of the best-fit parameter was modeled with a third-order polynomial function of L/R_0:

$$Q_{DA}/Q_D = \exp(A(L, R_0) * C) \tag{2-6}$$

Where

$$A(L, R_0) = \sum_{i=0}^{3} a_i \left(\frac{L}{R_0}\right)^i \tag{2-7}$$

And

$$C = [c] * R_0^2 \tag{2-8}$$

With the a_i determined by fitting A as a function of L/R_0, this form of the relative quantum yield can be used in any nonlinear least squares fitting algorithm to determine the best-fit value of L for a dataset, when R_0 is known.

Thirty years have passed since the publication of these results, during which time computer power has increased immensely. As such, I performed monomer-only simulations over a much finer mesh of acceptor concentrations and exclusion radii than performed previously. I have found, in agreement with previous work, that the relative quantum yields, as a function of acceptor concentration, were modeled well as an exponential function of the form shown in **Equation (2-6)**. Employing a finer mesh of simulated exclusion radii allowed me to confirm that $A(L, R_0)$ was indeed a smooth function of the exclusion radius. The finer mesh of acceptor concentrations used in the simulations, which determines the value of A in a least-squares sense, showed that a fifth-order polynomial more accurately models the dependence of $A(L, R_0)$ as a function of the fluorophore exclusion radius.

Thus, the refined prediction for the relative quantum yield is given here:

$$A(L, R_0) = \sum_{i=0}^{5} a_i \left(\frac{L}{R_0}\right)^i \tag{2-9}$$

And

$a_0 = -3.638$ $a_1 = 0.354$ $a_2 = -0.214$

$a_3 = 7.007$ $a_4 = -5.642$ $a_5 = 0.919$

Table 2-1. The coefficients for use in **Equation (2-9)**, an improved model of Veatch and Stryer, to model the FRET of non-interacting, monomeric membrane proteins.

2-3. A Theoretical Description of The Intra-Oligomeric FRET of Dimerization and Higher-Order Oligomerization

The function of membrane proteins is often modulated by their lateral association in the membrane. Thus, the association state of a membrane protein (monomer, dimer, oligomer, etc.) is of primary interest, and static-quenching FRET is often the method of choice in the study of the association state. Two models are currently in use for modeling the oligomeric FRET, or FRET arising from specific protein-protein interactions, of static quenching FRET experimental data. The primary model is the Kinetic Theory of Oligomeric FRET, derived in 2007, which is applicable to fully quantitative FRET experiments where the total surface densities of donor and acceptor labeled membrane proteins are known or measured, but the oligomeric state is unknown. The second is the Veatch and Stryer model, derived in 1977, which unfortunately is still often utilized in semi-quantitative FRET experiments to determine the oligomeric state of membrane proteins[67]. In these experiments, the donor to acceptor ratio is known, but the total surface density of donor and acceptor labeled fluorophores is unknown. In this chapter and this work, I will focus primarily on the Kinetic Theory of Oligomeric FRET and in a later chapter, I show that the model of Veatch and Stryer is not useful. As given, neither model accounts for the effect of stochastic FRET and must be utilized with very low total concentrations of membrane proteins to minimize the contamination of the total apparent FRET efficiency by stochastic FRET. Thus, these models describe the intra-oligomeric FRET that will occur in a static quenching FRET experiment.

2-3.1 Receptor Dimerization and Oligomerization: the Kinetic Theory of Intra-Oligomeric FRET

The Kinetic Theory of Intra-Oligomeric FRET provides a theoretical description of the FRET arising from the protein-protein interactions that will be measured for an excited ensemble of oligomeric membrane proteins [68,69]. A complete description of the system requires knowledge of the donor-acceptor distances and orientation factors within an oligomer. These distances are known in these simulations, but in a real-world experimental situation, these distances are unknown. For this reason, in this work I utilize the working assumption that nothing is known about the true oligomerization state of the protein before analysis, even though later we will use simulations to predict the FRET by constructing virtual oligomers of definite size. A simplified expression for the Kinetic Theory of Oligomeric FRET can be derived, however, if we assume equal donor to acceptor distance for all D-A pairs. In this case, the oligomeric FRET efficiency is given**:**

$$E_{oligo}^{Dq} = \frac{\mu_{oligo}}{[D]} \sum_{k=1}^{n-1} \frac{k(n-k)\tilde{E}}{1+(n-k-1)\tilde{E}} \binom{n}{k} P_D^k P_A^{n-k} \qquad (2\text{-}10)$$

In **Equation (2-10)**, *n* represents the oligomer order. μ_{oligo} represents the concentration of oligomers in the ensemble. It is through μ_{oligo} that the Kinetic Theory of Oligomeric FRET can be utilized to study the thermodynamic properties of membrane proteins by application of the law of mass action, described next. The sum is performed over the k acceptors in the oligomer. The sum begins at one because there is no intra-oligomeric FRET if there are no acceptor molecules in the complex, and ends at n-1 because there must be at least one FRET donor present (if there are no donors or acceptors in the oligomer, any measured FRET is due to stochastic FRET). $\tilde{E}$ is the intrinsic FRET efficiency of a donor-acceptor pair in the oligomer, given by **Equation (2-2)**. $\binom{n}{k}$ is the binomial coefficient, ${}^{n!}/_{k!\,(n-k)!}$, and represents the number of ways of choosing k acceptors from an oligomer of size n, as shown below in **Figure 2-2**. P_D and P_A are the fractions of donors and acceptors in the oligomer. For large numbers of molecules, these are equal to the fraction of donor and acceptors, respectively: x_D and x_A. $x_A = \frac{[A]}{[D]+[A]}$, with $[D]$ and $[A]$ representing the total donor and acceptor concentrations, and $x_D + x_A = 1$.

Equation (2-10) gives the theoretical intra-oligomeric donor-quenched energy transfer efficiency for dimers and higher-order oligomers, E_{oligo}, assuming an equal donor to acceptor distance for all D-A pairs in the oligomer. For the case of n = 2, a dimer, and n =3 with a trimer arranged as an equilateral triangle, this is always correct as there is only one donor to acceptor distance in the oligomer. For tetramers and above, this is an approximation which minimizes the number of adjustable parameters in the theoretical model for FRET (28).

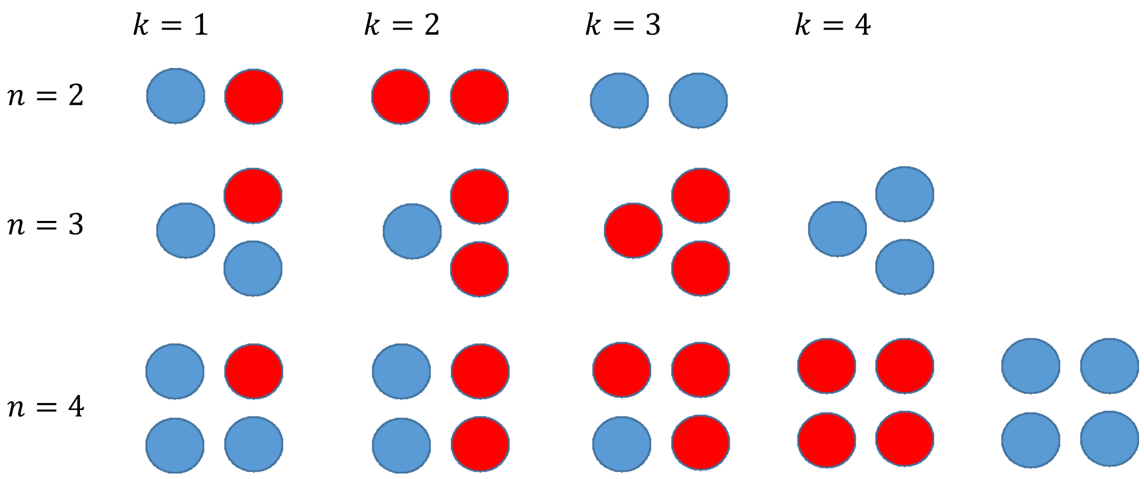

Figure 2-2. Donors and acceptors (blue and red, respectively) arranged as dimers, trimers, and tetramers. For each value of k (number of acceptors in the oligomer) there are $^{n!}/_{k!\,(n-k)!}$ ways to distribute the k acceptors in an oligomer of size n. For each n, the last two shown distributions shown on the far right result in zero oligomeric FRET.

2-3.2 Receptor Dimerization and Oligomerization: The model of Veatch and Streyer

In some experimental situations, the concentrations of donors and acceptors may not be known, but the ratio of donor to acceptor molecules is known or measured. In this case, the model of Veatch and Stryer is often utilized in the analysis of apparent FRET efficiencies to determine the oligomeric state of the membrane proteins of interest, as shown below:

$$E_{app} \approx E_{max}(1 - x_D^{n-1}) = E_{max}\left(1 - (1 + \left(\frac{[A]}{[D]}\right)^{-1})^{n-1}\right) \qquad (2\text{-}11)$$

In E**quation (2-11)**, E_{max} is an adjustable parameter corresponding to $\tilde{E}$ for dimers (equation 2-2), but for higher order oligomers, E_{max} is interpreted simply as an adjustable parameter to aid in the fitting and has no physical meaning. x_D is the molar fraction of donors, which can be written as a function of the acceptor to donor ratio, [A]/[D], and n is the oligomer order, as defined for **Equation (2-10)**. Compared to the Kinetic Theory of Oligomeric FRET, this model assumes a single donor to acceptor distance in the oligomer, and it also assumes a single FRET species in the mixture which contains a single donor, corresponding to the $k = 1$ term in the summation of **Equation (2-10).**

The assumptions of the model of Veatch and Stryer are correct for constitutively dimeric species, however for non-constitutive dimers and higher order oligomerization, this model simplifies the geometry of the oligomer, and it does not take into account the combinatorial manner in which a number of donors and acceptors can be found within an oligomer. In a later chapter, I will show that this model is incapable of properly determining the order of oligomerization of membrane proteins.

2-4. Building a Thermodynamic Model with the Kinetic Theory of Oligomeric FRET

Here I describe the procedure for incorporating a thermodynamic equilibrium into the Kinetic Theory of Oligomeric FRET. The basic idea is to write the concentration of oligomers, μ_{oligo} of **Equation (2-10)**, in terms of the total membrane protein (fluorophore) concentration and an association constant. First we begin with the description of monomeric membrane proteins, and then we explicitly derive the analytic relation for membrane proteins in a monomer-dimer equilibrium. Finally, we show the general procedure of constructing the thermodynamic model using trimers, $n = 3$, as an example.

2-4.1. A special case: Monomeric Receptors

As a special case of non-interactions, the Kinetic Theory of FRET does not predict the total apparent FRET efficiency, in this case occurring solely due to stochastic FRET. The apparent FRET efficiency of monomeric membrane proteins tagged with fluorophores of non-negligible exclusion radius, i.e. 2D distributions of fluorescent proteins, is described by the numeric results of Wolber and Hudson, and verified experimentally with fluorescent protein tagged ECTM domains of several RTKs. The prediction for the relative quantum yield of a monomeric donor in the presence of random configurations of acceptors as a function of acceptor concentration, R0, and distance of closest approach L, is given by the following exponential function:

$$ {}^{Q_{DA}}/_{Q_D} = \exp(A(L, R_0) \cdot C) \tag{2-12} $$

with $A(L,R_0) = \sum_{i=0}^{5} a_i \left(\frac{L}{R_0}\right)^i$, $C = [A] \cdot R_0^2$, the acceptor concentration per R_0-squared, and the a_i given previously in **Table 2-1**. In the simulations of FRET described in a later chapter, the exclusion radius utilized is 1.4 nm, giving L/R0 = 0.51.

2-4.2 Dimerizing and Oligomerizing Receptors

Next, the thermodynamic model for membrane protein interactions based on the Kinetic Theory of Intra-Oligomeric FRET, **Equation (2-10)**, and the law of mass action is described here. We start by letting n = 2 in Equation 20 above and multiplying by [T]/[T]:

$$E_{dimer}^{Dq} = \frac{\mu_{oligo}}{[D]_T}\tilde{E} \cdot 2 \cdot f_D x_A = 2\frac{\mu_{oligo}}{[T]}\frac{[T]}{[D]_T} x_D x_A \tilde{E} \qquad (2\text{-}13)$$

$$E_{dimer}^{Dq} = f_d \, x_A \tilde{E} \qquad (2\text{-}14)$$

The fraction of dimers, f_d, can be written as a function of an equilibrium association constant, K_A, and total receptor concentration, [T], i.e. $f_D(K_A,[T])$. To do so, we write down the equation for the fraction of dimers:

$$f_d = \frac{2[d]}{[T]} = \frac{2[d]}{[m]+2[d]} \qquad (2\text{-}15)$$

Here, $[m]$ is the concentration of monomeric receptors and $[d]$ is the concentration of dimeric receptors. For the two-state monomer-dimer equilibrium, we define the equilibrium association constant, K_A:

$$m + m \rightleftharpoons d$$

$$K_A = \frac{[d]}{[m]^2} \tag{2-16}$$

First, we solve for the fraction of monomers:

$$f_m = \frac{1}{1 + 2K_A[m]} \tag{2-17}$$

Since $[T] = [m] + 2[d] = [m] + 2K_A[m]^2$, we use this quadratic equation to solve for [m] as a function of the coefficients of the polynomial, K_A and [T]. There are two real roots to this equation, one positive and one negative. We use the positive root as the physical solution.

$$[m] = \frac{\sqrt{1 + 8K_A[T]} - 1}{4K_A} \tag{2-18}$$

$$f_m = \frac{1}{1+2K_A[m]} = \frac{\sqrt{1+8K_A[T]}-1}{4K_A[T]} \tag{2-19}$$

By using the relationship $f_d + f_m = 1$, we solve for the fraction of dimers, f_D, as a function of K_A and $[T]$:

$$f_d(K_A,[T]) = 1 - f_m = 1 - \frac{\sqrt{1+8K_A[T]}-1}{4K_A[T]} \tag{2-20}$$

The thermodynamic model of oligomeric FRET for a mixed population of monomers and dimers can be then completed with the dimeric fraction $f_D(K_A,[T])$ according to **Equation (2-14):**

$$E_{dimer}^{Dq} = f_D(K_A,[T])x_A\tilde{E}$$

The analytic solutions for the roots become more intractable as n becomes 3 or higher, and there is no analytic solution for the roots of a polynomial greater than order five. Instead of writing down the solution for the fraction of oligomers as a function of total receptor concentration, I instead utilize a MATLAB root finding function to calculate the roots of the binding polynomial. I take the largest real root as the physical solution to the n'th order polynomial which yields $[m_i]$ as a function of K_A and $[T_i]$.

The general procedure for $n = 3$ (trimers) is now described, and the same procedure is applied to all dimeric, trimeric, tetrameric, pentameric, and hexameric model construction of E_{oligo}. Direct use of **Equation (2-20)** in **Equation (2-14)** is not recommended, in general. For the case of a monomer-trimer equilibrium, the theoretical apparent FRET efficiency is described by letting $n = 3$ in **Equation (2-10)**:

$$E^{Dq}_{trimer} = \frac{\mu_{trimer}}{[D]_T}\left(\frac{6\tilde{E}}{1+\tilde{E}}P_D\, P_A^2 + 6 * \tilde{E}P_D^2P_A\right) \tag{2-21}$$

Letting $E = \left(\frac{6k\tilde{E}}{1+\tilde{E}}P_D\, P_A^2 + 6 * \tilde{E}P_D^2P_A\right)$ and multiplying the right side by [T]/[T] we have:

$$E^{Dq}_{trimer} = \frac{\mu_{trimer}}{[D]_T}\frac{[T]}{[T]}E = \frac{f_{trimer}}{3x_D}E \tag{2-22}$$

Now that we have a theoretical representation for the FRET efficiency, we focus on the fraction of trimers.

$$f_{trimer} = \frac{3[tri]}{T} = \frac{3[tri]}{[m] + 3[tri]} \tag{2-23}$$

Here, $[tri]$ is the concentration of trimeric receptors. The goal is to express the fraction of trimers in terms of the equilibrium association constant and the total receptor concentration. For the two-state monomer-trimer equilibrium model, we write:

$$m + m + m \rightleftharpoons tri$$

$$K_A = \frac{[tri]}{[m]^3} \tag{2-24}$$

Writing the total concentration of macromolecules in terms of K_A and $[m]$ and rearranging the third order polynomial in [m] gives:

$$3K_A[m]^3 + [m] - [T] = 0 \tag{2-25}$$

Next, I use a root-finding algorithm to find the largest positive, real root, [m](K_A,[T]), and write the fraction of trimers as:

$$f_{trimer} = \frac{3[tri]}{[T]} = \frac{3K_A[m]^3}{[T]} \tag{2-26}$$

The thermodynamic model of oligomeric FRET for a mixed population of monomers and trimers can then be calculated with the trimeric fraction $f_{trimer}(K_A, [T])$:

$$E^{Dq}_{trimer} = \frac{f_{trimer}(K_A, [T])}{3x_D} E \tag{2-27}$$

In cases when the oligomeric fraction, determined in the fit, exceeds 95% over the very broad range of concentrations used in the simulations or measured during experiments (typically 1e-5 rec/nm^2-8e-3 rec/nm^2), I term the best-fit oligomer to be “a constitutive oligomer.”

2-5. A Complete Theoretical Description of the Total Apparent FRET Efficiency With the Kinetic Theory

The total donor-quenched apparent FRET efficiency, E_{app}, is defined as the ratio of the rate of resonant energy transfer, k_{RET}, to the over-all rate of all donor de-excitation pathways, including FRET, as shown:

$$E_{app} \equiv \frac{k_{RET}}{k_D + k_{RET}} \tag{2-28}$$

where k_D denotes the sum of all-de-excitation rates excluding FRET. When the fluorophores are confined to two dimensions, FRET can occur stochastically through tagged membrane proteins that are not undergoing dimerization, or oligomerization, in addition to the FRET of protein-protein interactions. This idea is described in **Equation (2-29)** below, by breaking apart k_{RET} into the sum of two components: k_{RET}^{Oligo}, the rate of donor de-excitation due to FRET of protein-protein interactions and k_{RET}^{prox}, the rate of donor de-excitation due to FRET of proximity to neighboring acceptors in other oligomers or monomers.

$$E_{app} = \frac{k_{RET}^{prox} + k_{RET}^{Oligo}}{k_D + k_{RET}^{prox} + k_{RET}^{Oligo}} \tag{2-29}$$

As mentioned previously, this stochastic FRET contribution is a non-negligible component of the total apparent FRET efficiency, and is a function of the concentration, interaction propensity, and oligomerization state of the fluorescent protein-tagged membrane proteins. Until this work, there had been no theoretical model for the total apparent FRET efficiency that accounts for all FRET contributions in a bulk, donor-quenched static quenching FRET experiment.

In an ideal world, we could set up an experimental situation in which $k_{RET}^{prox} = 0$ and a measurement of E_{app} would yield E_{oligo}:

$$E_{oligo} \equiv \frac{k_{RET}^{oligo}}{k_D + k_{RET}^{oligo}} \tag{2-30}$$

Conversely, one could also imagine a situation where only the stochastic FRET was measured, E_{prox}:

$$E_{prox} \equiv \frac{k_{RET}^{prox}}{k_D + k_{RET}^{prox}} \tag{2-31}$$

Unfortunately, one cannot experimentally decouple the two contributions from the total measured apparent FRET efficiency. However, by solving for k_{RET}^{oligo} in **Equation (2-31)** and for k_D in **Equation (2-31)**, and substituting into **Equation (2-29)**, one can write down the explicit dependence of E_{app} on E_{oligo} and E_{prox}, as shown:

$$E_{app} = \frac{E_{prox} + E_{oligo} - 2\,E_{prox}E_{oligo}}{1 - E_{oligo}E_{prox}} \tag{2-32}$$

Examination of **Equation (2-32)** shows that if one knows an appropriate stochastic FRET contribution, it can be used along with the measured apparent FRET efficiency to determine the actual FRET due to protein-protein interactions in the membrane. Alternatively, **Equation (2-32)** can be solved for the total stochastic FRET efficiency contribution, as a function of the total apparent FRET efficiency and the oligomeric FRET efficiency as shown:

$$E_{prox} = \frac{E_{app} - E_{oligo}}{1 - 2E_{oligo} + E_{app}E_{oligo}} \tag{2-33}$$

Examination of **Equations (2-32) or (2-33)** shows that as $E_{oligo} \rightarrow 0, E_{app} \rightarrow E_{prox}$ as expected for monomeric proteins. Similarly, as $E_{prox} \rightarrow 0, E_{app} \rightarrow E_{oligo}$, showing that if the stochastic FRET contribution can be minimized by experimental design, the measured apparent FRET is due to protein-protein interactions.

Sometimes, the two contributions are summed up in the literature, i.e, the total apparent FRET efficiency is assumed to be equal to the sum of the oligomeric FRET of protein-protein interactions, and the stochastic FRET contribution. **Equation (2-32)** shows that this is not correct in the general case. However, if one of the contributions is very small, a Taylor expansion yields:

$$E_{app} \approx E_{oligo} + E_{prox} \tag{2-34}$$

In the next chapter, I will briefly investigate the validity of this approximation, but in general now that the full Kinetic Theory of FRET has been developed and a computer is required for analysis, there is no need to utilize this simplification in the analysis of FRET data from static quenching FRET measurements of membrane proteins.

Chapter 3. Simulations Reveal the (non)Uniqueness of the FRET of Interacting Membrane Proteins

3-1. Introduction

In this section, I describe the theory that I have developed for simulations of static-quenching FRET experiments. With this, one can use simulations to predict the total apparent FRET efficiency that would be measured for any experimental situation desired involving 2-D distributions of fluorophores. I have performed simulations of FRET between membrane proteins labeled with fluorescent proteins by creating discrete two-dimensional distributions of non-overlapping circles, intended to represent the non-negligible volume of the fluorescent protein beta barrel structure. This limits the distance of closest approach, similarly to that between the chromophores located at the center of the beta barrel in a fluorescent protein. I then use this methodology to simulate the measured FRET for a variety of situations of high interest to membrane protein researchers: monomeric, dimeric, trimeric, tetrameric, monomer-dimer equilibrium, and monomer-tetramer equilibrium. Analysis of this data with the two primary models, the Kinetic Theory of FRET[68], and the Veatch and Stryer model[67] described in Chapter 2, reveal the limitations of both models with respect to determination of association constants, donor-acceptor distance, and oligomer-order. These simulations also reveal physical limitations of static quenching, two-color FRET experiments to provide different FRET signatures for higher order oligomerization, n > 2.

3-2. *Theory of FRET for 2-D Static Distributions of Fluorescent Proteins*

As described by Wolber and Hudson[64], for a 2-D a static quenching FRET experiment containing multiple excited donors, the ratio of the quantum yield of the donor in the presence of acceptors (and FRET), ${}^{Q_{DA}}/_{Q_D}$, can be estimated through computer simulations by generating many different configurations, β, of donors and acceptors in a 2-dimensional plane. This is exactly the physical situation encountered experimentally when a large region, several square microns, is excited for microsecond or millisecond intervals in a microscope-based FRET experiment. Many donors are excited and the excitation interval lasts for thousands of FRET lifetimes. Thus, the measured FRET is a measurement taking place on a large ensemble of many proteins. The relative total instantaneous quantum yield of a single configuration of fluorophores, $q_{r,j,tot}^{(\beta)}$, is calculated and averaged over the donors, N_D, per configuration, and over all of the M configurations, as shown below. After averaging over the M configurations, we have a numerical estimate of the total apparent relative quantum yield, ${}^{Q_{DA}}/_{Q_D}$:

$$q_{r,j,tot}^{(\beta)} = \left[1 + \sum_{i=1}^{N_\beta} \left({}^{R_0}/_{R_{i,j}}\right)^6\right]^{-1} \tag{3-1}$$

$$ {}^{Q_{DA}}/_{Q_D} = \lim_{M\to\infty} \left[\frac{1}{M}\sum_{\beta=1}^{M}\frac{1}{N_D}\sum_{j=1}^{N_D} q_{r,j,tot}^{(\beta)}\right] \tag{3-2}$$

The total apparent FRET efficiency is then defined as:

$$E_{app} \equiv 1 - {}^{Q_{DA}}\!/_{Q_D} \tag{3-3}$$

In **Equation (3-1)**, the sum is over N acceptors in the $\beta' th$ configuration. R_0 is the Förster radius (5.5 nM for the mTurquoise-YFP FRET pair), and $R_{i,j}$ is the distance from the i'th acceptor to the j'th donor. The relative total instantaneous quantum yield of the quenched donor, $q_{r,j,tot}^{(\beta)}$, is a sum over all acceptors, including acceptors that are participating in oligomeric FRET (intra) and acceptors that experience FRET due to proximity, stochastic FRET (inter).

In order to determine the FRET due to oligomerization (E_{Oligo} as estimated with **Equation (2-10)** without a stochastic FRET contribution, I define the relative oligomeric instantaneous quantum yield $q_{r,j,oligo}^{(\beta)}$ as a sum over only the I = m, n, o, … acceptor distances, the intra-oligomeric acceptors to the j'th donor in the β'th configuration, as shown below in **Equation (3-4)**:

$$q_{r,j,oligo}^{(\beta)} \equiv \left[1 + \sum_{i=m,n,o,\ldots}^{N_\beta} \left({}^{R_0}\!/_{R_{ij}}\right)^6\right]^{-1} \tag{3-4}$$

In **Equation (3-4)**, if a donor is monomeric or if an oligomer is comprised solely of donors, then $q_{r,j,oligo}^{(\beta)} = 1$. In the case of a donor dimerized with an acceptor, it is equal to 1 - $\tilde{E}$, the FRET efficiency of the donor-acceptor pair in the dimer.

Averaging $q_{r,oligo}^{(\beta)}$ over many donors and many configurations leads to the definition of the oligomeric donor-quenched FRET efficiency:

$$Q_{DA,Oligo}\Big/Q_D = \lim_{M\to\infty}\left[\frac{1}{M}\sum_{\beta=1}^{M}\frac{1}{N_D}\sum_{j=1}^{N_D} q_{r,j,oligo}^{(\beta)}\right] \tag{3-5}$$

$$E_{Oligo} \equiv 1 - Q_{DA,Oligo}\Big/Q_D \tag{3-6}$$

Similarly to the relative oligomeric instantaneous quantum yield, the relative stochastic instantaneous quantum yield of the $j'th$ donor is defined as the sum over all acceptors that do not belong to same oligomer as the $j'th$ donor:

$$q_{r,j,prox}^{(\beta)} \equiv \left[1 + \sum_{i=1;i\neq m,n,o,\ldots}^{N_\beta}\left(R_0\big/R_{ij}\right)^6\right]^{-1} \tag{3-7}$$

If the j’th donor is monomeric, then $q_{r,j,prox}^{(\beta)} = q_{r,j,tot}^{(\beta)}$.

Next, in the spirit of **Equation (2-32)**, we return to **Equation (3-1)** and we see that the relative total instantaneous quantum yield can be written in terms of the relative oligomeric and stochastic instantaneous quantum yields, as shown:

$$\begin{aligned} q_{r,j,tot}^{(\beta)} &= \frac{1}{{}^{1}\!/_{q_{r,prox}^{(\beta)}} + {}^{1}\!/_{q_{r,oligo}^{(\beta)}} - 1} \\ &= \frac{q_{r,j,prox}^{(\beta)} * q_{r,j,oligo}^{(\beta)}}{q_{r,j,oligo}^{(\beta)} + q_{r,j,prox}^{(\beta)} - q_{r,j,prox}^{(\beta)} * q_{r,j,oligo}^{(\beta)}} \end{aligned} \tag{3-8}$$

Substitution of **Equation (3-8)** into **Equation (3-2)** shows the complicated configurational dependence of the total apparent FRET efficiency on the relative stochastic and oligomeric instantaneous quantum yields:

$$\begin{aligned} E_{app} &= 1 - {}^{Q_{DA}}\!/_{Q_D} \\ &= 1 - \lim_{M\to\infty}\left[\frac{1}{M}\sum_{\beta=1}^{M}\frac{1}{N_D}\sum_{j=1}^{N_D}\frac{q_{r,j,prox}^{(\beta)} * q_{r,j,oligo}^{(\beta)}}{q_{r,j,oligo}^{(\beta)} + q_{r,j,prox}^{(\beta)} - q_{r,j,prox}^{(\beta)} * q_{r,j,oligo}^{(\beta)}}\right] \end{aligned} \tag{3-9}$$

Now I define the total stochastic FRET efficiency as:

$$E_{prox} \equiv 1 - {}^{Q_{DA,prox}}\!/_{Q_D} \tag{3-10}$$

Using **Equation (3-10)**, the oligomeric FRET efficiency (**Equation (3-6)**) and the definition of the apparent FRET efficiency (**Equation (3-3)**), I can write the total apparent FRET efficiency in terms of the ratios of the oligomeric and stochastic quantum yields by using **Equation (2-32)**:

$$E_{app} = 1 - {}^{Q_{DA}}\!/_{Q_D} = \frac{E_{prox} + E_{oligo} - 2\,E_{prox}E_{oligo}}{1 - E_{oligo}E_{prox}}$$

$$= \frac{\left({}^{Q_{DA,prox}}\!/_{Q_D}\right) + \left({}^{Q_{DA,Oligo}}\!/_{Q_D}\right) - 2\left({}^{Q_{DA,prox}}\!/_{Q_D}\right)\left({}^{Q_{DA,Oligo}}\!/_{Q_D}\right)}{\left({}^{Q_{DA,prox}}\!/_{Q_D}\right) + \left({}^{Q_{DA,Oligo}}\!/_{Q_D}\right) - \left({}^{Q_{DA,prox}}\!/_{Q_D}\right)\left({}^{Q_{DA,Oligo}}\!/_{Q_D}\right)}$$

Therefore:

$${}^{Q_{DA}}\!/_{Q_D} = \frac{\left({}^{Q_{DA,prox}}\!/_{Q_D}\right) * \left({}^{Q_{DA,Oligo}}\!/_{Q_D}\right)}{\left({}^{Q_{DA,Oligo}}\!/_{Q_D}\right) + \left({}^{Q_{DA,prox}}\!/_{Q_D}\right) - \left({}^{Q_{DA,prox}}\!/_{Q_D}\right) * \left({}^{Q_{DA,Oligo}}\!/_{Q_D}\right)} \tag{3-11}$$

Interestingly, **Equation (3-11)**, has the same form as the relative total instantaneous quantum yield, $q_{r,j,tot}^{(\beta)}$ in **Equation (3-8)**, despite the summations. Thus, even though the oligomeric and the stochastic FRET are not separable in an actual experiment where the total apparent FRET efficiency is measured, with computer simulations we can determine each component and understand effects of oligomeric and stochastic FRET on the total apparent FRET efficiency.

3-3. Computational Methods

The fluorescent proteins are modeled as circles in two dimensions with a 1.4nm "exclusion radius" as described previously in **Chapter 2** for the initial simulations of monomeric proteins, which is intended to represent the fluorescent proteins existing in a plane which is parallel to the bilayer.

To model the FRET arising from two dimensional distributions of donor and acceptor fluorescent proteins with non-negligible finite size, I create non-overlapping ensembles of circles representing donors or acceptors organized as monomers or oligomers of order n, with random orientations (random ϕ in **Figure 3-1**). Then I calculate the total and oligomeric relative quantum yields per configuration, as described in **Equation (3-2), and Equation (3-5)**. $M = 1{,}000$ trials are performed for each acceptor fraction, generating new configurations at each trial and determining the total donor quenching and oligomeric quenching and FRET efficiencies as shown in **Equations (3-3, and Equation (3-6)**. The total stochastic quenching contribution is algebraically calculated from E_{app} and E_{oligo} as shown in **Equation (2-33)**.

Oligomers are constructed as n-sided regular polygons with circles at the vertices, and with a line connecting the circle centers of the oligomer. The side length, or center-to-center distance for the circles representing fluorescent proteins is chosen based on a distance determined from Förster's Equation for a given FRET efficiency. With a dimer and a trimer, this distance is exactly $\tilde{E}$, the FRET efficiency of a single donor-acceptor pair.

For example, a monomer is represented as a simple circle, a dimer as two circles connected by a line, a trimer as an equilateral triangle, tetramers as squares, and pentamers as pentagons with circles at the corners. **Figure 3-1** shows the geometries of the oligomers utilized in the simulations.

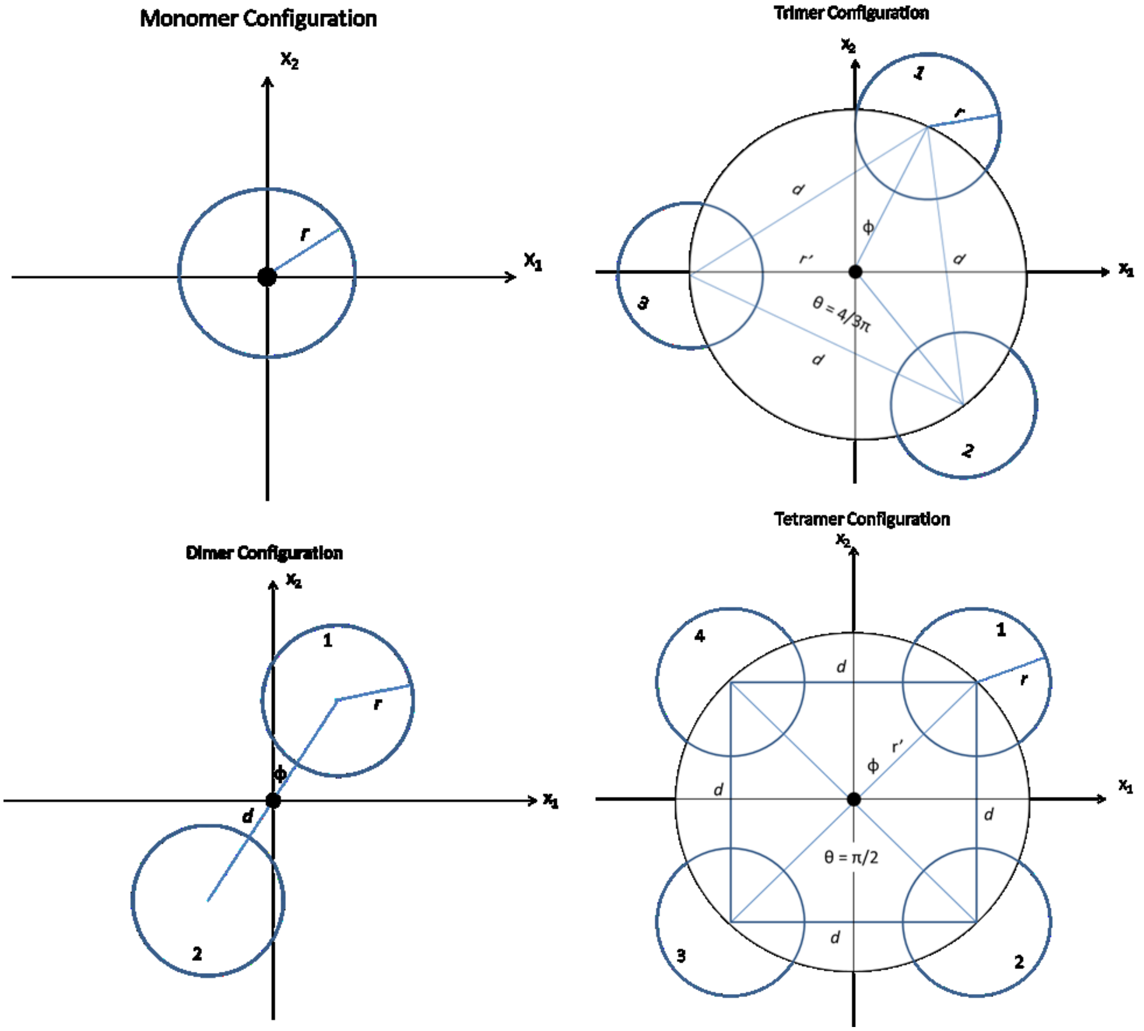

Figure 3-1. The geometries of the monomeric, dimeric, trimeric, and tetrameric organizations of fluorescent proteins utilized in the simulations. Fluorescent proteins are modeled as circles, with d related to $\tilde{E}$, the intrinsic FRET efficiency of a donor-acceptor pair, as given in **Equation (2-2):**

$$\tilde{E} = \frac{1}{1 + {d^6}/{R_0^6}}$$

Non-overlapping ensembles of circles representing fluorescent proteins are generated by first choosing a random position and orientation for all oligomers (including monomers). The computer iterates through the list of oligomers, examining it for overlap with any other oligomers. If overlap occurs, then a new random position is chosen for the oligomer of interest until a suitable position is found. We continue in this manner until all monomers and oligomers are placed in a non-overlapping manner.

For all the simulations described here, I utilize a pool of 4,000 fluorophores, which are randomly placed in a square region that is sized according to the desired fluorophore concentration. I utilized $M = 1{,}000$ trials per D:A ratio, per simulated total concentration value. After placement, the circles are then randomly assigned to be donor or acceptor molecules. In order to avoid edge effects, only donors that are positioned five Förster radii, $5R_0$, away from the edges of the region are utilized in the calculations of oligomeric, total, and stochastic FRET, as described above. A Förster radius of 5.5nm, corresponding to that of the mTurquoise-YFP FRET pair with an assumed $\kappa^2 = 2/3$ was used for the simulations in this work. Simulated surface densities in this chapter range from a minimum of 1e-5 fluorophores/nm^2 (10 per square micron) to a maximum of 8e-3 fluorophores/nm^2 (8,000 per square micron), with acceptor fractions ranging from 0.1 to 0.9 in 0.1 steps.

3-4. Analysis of E_{app}: Stochastic FRET Considerations

The Kinetic Theory of Oligomeric FRET[47,48,56,68,70] only accounts for intra-oligomeric FRET, and does not take into account stochastic FRET, or FRET that occurs due to random approach of donors and acceptors in the membrane within distances of ~100 Å. I have shown in other work, however, that stochastic FRET can represent a significant contribution to the measured FRET efficiency for dimerizing membrane proteins. I have also previously shown that the stochastic FRET contribution decreases when the oligomer order increases, and this phenomenon will be seen in the simulated FRET predictions of this chapter. It is thus possible that stochastic FRET becomes negligible for large oligomers. To investigate if this is the case, and to determine a possible oligomer size cut-off, I compare the fitting results with and without a proximity FRET contribution where we have utilized a numeric estimation of the stochastic FRET, as shown in Tables 1 and 2.

For all $n > 1$, when we have a monomer-oligomer equilibrium or constitutive oligomers, the stochastic FRET contribution, as given by **Equation (2-32)** or **Equation (2-33)**, can comprise a major component of the total apparent FRET efficiency, E_{app} (see Table 3-1). Since there is no analytic form for the stochastic FRET occurring between fluorophores with non-negligible size as a function acceptor concentration, I simulated proximity FRET for all $n = 2{:}6$ over a gridded multidimensional space of the two adjustable parameters: $\tilde{E}$, and K_A, for acceptor concentrations ranging from zero to 0.008 acceptors/nm^2 (see **Computational Methods**), with a 1.4nm exclusion radius. $\tilde{E}$ values range from 0.05 to 0.90, with association constants, K_A, varying from monomer-only ($K_A \longrightarrow 0$) through constitutive oligomerization ($K_A \longrightarrow \infty$) in steps of 0.5 kcal/mol. This "library" of thousands of stochastic FRET estimations is used to perform a gridded search for the best-fit model to the dataset by building a theoretical model for the apparent FRET efficiency that includes the appropriate stochastic FRET contribution, as in **Equation (2-32)**.

The stochastic FRET is a function of all of the parameters of interest in a FRET measurement of membrane proteins, $\tilde{E}$and K_A, and accordingly, the choice of a stochastic FRET model fixes the choice of the parameters in the terms of the fraction of oligomers and the intrinsic FRET.

It is computationally expensive to estimate the stochastic FRET for every possible combination of the intrinsic FRET and dimeric association constant, and furthermore, small changes to these parameters have little effect on the magnitude of the stochastic FRET contribution. As such, after the above analysis I then "polish" the best-fit intrinsic FRET and dimeric association constant values found during the gridded search by fixing the best-fit proximity model to that found above in the gridded search, and utilizing a MATLAB non-linear least squares fitting algorithm to find the best fit values of the intrinsic FRET, $\tilde{E}$, and the equilibrium association constant, K_A (See **Equation (2-32) and Equation (2-27)**).

The best-fit mean-squared errors (MSEs) for all oligomer orders, $n = 1{:}\,6$, are compared and the overall lowest MSE value is chosen as the best-fit model to represent a given dataset. I have performed two separate analyses utilizing the Kinetic Theory of FRET. First, for all n, I fit the total apparent FRET efficiency, as shown in **Figures 1C, 3B, 5B, 7B, 9C, 12C, and Supplementary Figures 1A, 3A, 4A, 6A, 7A,** directly with the Kinetic Theory of FRET (as in **Equation (2-10)**) and ignore the stochastic FRET contributions. These results are summarized as a plot of the best-fit MSE as a function of oligomer order, n, as **black** circles. Additionally, for $n = 2{:}6$, I utilized a stochastic FRET contribution (described above) in **Equation (2-32)**, and examine the minimized MSE and best-fit parameters of the model. The analysis results including the stochastic FRET contribution are summarized in the MSE vs. oligomer order plots with a **blue** circle. The MSE is calculated according to:

$$MSE\left(K,\tilde{E}\right) = \frac{1}{N} \sum_{i=1}^{\substack{N\ data \\ points}} \left(E_{app,theory,i} - E_{app,i}\right)^2 \qquad (3\text{-}12)$$

Finally, in order to perform a statistical analysis on the *quality* of fits, I simulated again the total apparent FRET efficiency for monomer only, monomer-dimer equilibrium, constitutive dimers, constitutive trimers, monomer-tetramer equilibrium, and the constitutive tetramer cases as described above, as shown in **Supplementary Figures 5 and 8**. I generated 2,700 data points, with randomly chosen total surface densities of fluorophores, and donor to acceptor ratios over the same ranges as given previously. Next, Gaussian-distributed random error was generated for each data point, with $\mu = 0$ and $\sigma = 0.08$, giving absolute error values typically within 0-24%. This random error was added to the simulated total apparent FRET efficiency to create a simulated dataset with noise similar to that found in actual experiments. For all $n = 1\ through\ 6$, I minimize the reduced chi-square value for every n, as shown below, and choose the model with the overall minimum chi-square value as the best-fit model, given the data and its associated error.

$$\chi^2_{red}(K,\tilde{E}) = \frac{1}{N-2-1} \sum_{i=1}^{N\ data\ points} \left(\frac{E_{app,theory,i} - E_{app,i}}{\sigma_i}\right)^2 \tag{3-13}$$

I then subjected the reduced chi-square values for every n's best-fit value to the chi-square test for a $1 - \alpha = 0.95$ confidence limit. All models with a reduced chi-square value less than 1.04 are deemed acceptable within the 95% confidence limit. This information is plotted in the MSE vs. Order figures (use the right axis for χ^2_{red} values), as **green** X's for analysis with a stochastic FRET contribution, and as **black** X's for analysis without a stochastic FRET contribution, along with a magenta line repenting the 95% cutoff limit. All models with a reduced chi-square value above the line (> 1.04) are rejected as statistically different from the measured data, while all models below the cutoff are accepted. See **Supplementary Figures 5 and 8** for the best-fit results to for the simulated data sets with noise.

3-5. Monomeric Membrane Proteins

Figure 3-2 shows the predictions of the monomer-only simulation of E_{app}. To start, I created configurations of monomeric receptors (**Figure 3-2A**) and simulated E_{app} using **Equation (3-1)** and **Equation (3-2)**. In this case of no protein-protein interactions, E_{app} is equal to E_{prox}, according to **Equation (2-32).** The predicted E_{app} are plotted in **Figure 3-2B** as a function of the total concentration, for different the values of x_A. There is a strong dependence on the acceptor fraction, with the highest FRET efficiencies corresponding to the highest acceptor fractions. **Figure 3-2C** shows the dependence of E_{app} on the acceptor fraction, for different total concentrations, where the dashed lines connect data points with equal total fluorophore concentrations.

As seen in **Figure 3-2**, high stochastic FRET can be recorded even for monomeric receptors, especially at high acceptor concentrations. In cases when the association state is unknown, researchers may blindly apply the two oligomerization models, the Veatch and Stryer model, and the thermodynamic model based on the kinetic theory of FRET, to interpret the monomeric FRET data. The results of such analysis of my monomeric FRET predictions with the two models is shown in **Figure 3-3**. In **Figure 3-3A**, the apparent FRET efficiencies are plotted as a function of the acceptor to donor ratio of surface densities. This is a typical way to represent the data when using the model of Veatch and Stryer. There is a strong dependence on the total concentration of fluorophores, with increasing curvature of the apparent FRET efficiency as the surface density increases. Thus, I applied the model of Veatch and Stryer[67] to three different simulated curves of total apparent FRET efficiency vs. acceptor fraction for three different total concentrations of receptors: a very low surface density at $[T]$ = 1e-5 rec/nm^2, a moderate surface density at $[T]$ = 4e-3 rec/nm^2, and a relatively high surface density at $[T]$ = 8e-3 rec/nm^2.

With the Veatch and Stryer[67] model, I optimize for E_{max} and n (**Equation 2-11**), and the best-fit parameters are shown in **Table 3-1**. The three fits are shown as red lines in **Figure 3-3A**. At all surface densities, the model indicates the presence of dimers. Of note, at the low surface density fitting, the adjustable parameter E_{max} is equal to zero, due to a lack of any FRET. In any case, the model of Veatch and Stryer does not predict correctly that the proteins are monomeric because the effect of the stochastic FRET, the only contribution to FRET in the monomer case, is not taken into account. Thus, the use of this model will lead to the incorrect conclusion that the measured FRET occurs due to the presence of dimers. If one takes time to review the literature, it will be found that many groups are arguing with other groups over the oligomerization status of their membrane protein, and here I have shown that they are simply wasting their time trying to use this model, as it won't even tell them if their monomeric proteins are in fact, monomeric. But, I digress, and now we return to the quantitative limitations of bulk FRET measurements in membranes.

Figure 3-3B shows the results of the analysis of the simulation predictions with the thermodynamic model based on the Kinetic Theory of FRET. In this case, the mean squared errors and the reduced chi-square values are plotted as a function of oligomer size . In the special case of the monomer-only model, I utilize the model of King *et al.* and optimize for the best fit-distance of closest approach, L, which is twice the exclusion radius for the circular models of fluorescent proteins in this work (here, 1.4nm) (**Equation 2-6**). For n = 2-6, I utilize an oligomer model (**Equation 2-10 in Equation 2-32**) while also taking stochastic FRET into account (MSE shown with a blue open circle) and without taking stochastic FRET into account (MSE shown with a black open circle, **direct fitting of Equation 2-10**). We optimize for $\tilde{E}$ and K_A, and I show the overall best-fit values in **Table 3-1**, after the tetramer simulation section.

Next, the simulated total apparent FRET efficiency data with added Gaussian-distributed random error was fitted and the reduced chi-square value was minimized by optimizing for $\tilde{E}$ and K_A (L for $n = 1$) for all $n = 1 - 6$. The best-fit reduced chi-square values are plotted as a function of oligomer order in **Figure 3-3B,** as black X's for analysis without a stochastic FRET contribution, as above, and green X's for analysis that includes a stochastic FRET contribution, with the optimal $\tilde{E}$ and K_A given in **Table 3-1**.

We see in **Figure 3-3B** that minimizing the MSE of the total apparent FRET efficiency provides a minimum in the MSE when n=1 for analysis that does not consider stochastic FRET. The MSE for $n = 2 - 6$, when the stochastic FRET is taken into account, is also low and is indistinguishable from that for case of n = 1 (**Figure 3-3B,** blue circles). However, the best-fit parameters for the oligomeric fitting indicate a practical lack of interactions with $\Delta G° > 0$. Further, we see that all of the models for the dataset with added random error pass the reduced chi-square test at 95% confidence, indicating that all models represent the data equally well. However, as with the MSE minimization, the best-fit parameters for all $n = 2 - 6$ indicate a practical lack of protein-protein interactions. We see that without use of a stochastic FRET contribution, the reduced chi-square analysis indicates that the $n = 3$, a trimer model, is the best-fit to the data. Thus, only the use of the stochastic FRET approximation and the thermodynamic model based on the Kinetic

Theory of FRET leads to the correct conclusion that the proteins are monomeric and do not have measurable interactions.

If we do not account for stochastic FRET and only look for interactions (i.e. if we, in **Figure 3-3B**, disregard the analysis for $n = 1$ and we disregard the blue points and green X's) it will appear that the MSE, and reduced chi-square is minimized at $n = 3$. Thus, we will reach the incorrect conclusion that we have trimers when in fact we have monomers. Failure to account for stochastic FRET will therefore lead to erroneous data interpretation with the Kinetic Theory of FRET.

While it is easy to make a mistake by not accounting for stochastic FRET (as demonstrated above), it is also easy to correctly account for it, and to arrive at a correct conclusion. When plotted as a function of the acceptor concentration (**Figure 3-3C**), we see that the total apparent FRET efficiency collapses into a curve that is independent of the total concentration, and depends only on the acceptor surface densities, in accordance with the accepted theory for monomeric proteins. As discussed above, we can use the approach of King et al (**Equation 2-6 and Equation 2-9**) to fit a monomer-only model, when optimizing for the distance of closest approach between fluorophores. The fit is excellent, and yields $r_{exclusion} = 1.4 \pm 0.1\ nm$. This is exactly the simulated exclusion radius, and a value that is generally consistent with the size of a fluorescent protein.

The above analysis shows that knowledge of stochastic FRET is critically important for the correct interpretation of FRET measurements of monomeric proteins. Concentrations of donors and acceptors need to be measured, along with the FRET efficiencies. Then, the measured FRET should be plotted as a function of acceptor concentration, and the data fitted with **Equation (2-9)**. Even relatively weak sequence-specific interactions will yield values of $r_{exclusion}$ which are either very small or negative. If however, $r_{exclusion}$ is a reasonable measure of the size of the exclusion radius of the protein, then it is highly likely that the FRET measured in the experiment is due to stochastic FRET occurring between monomeric proteins. At the very least, the case of non-interaction cannot be statistically excluded.

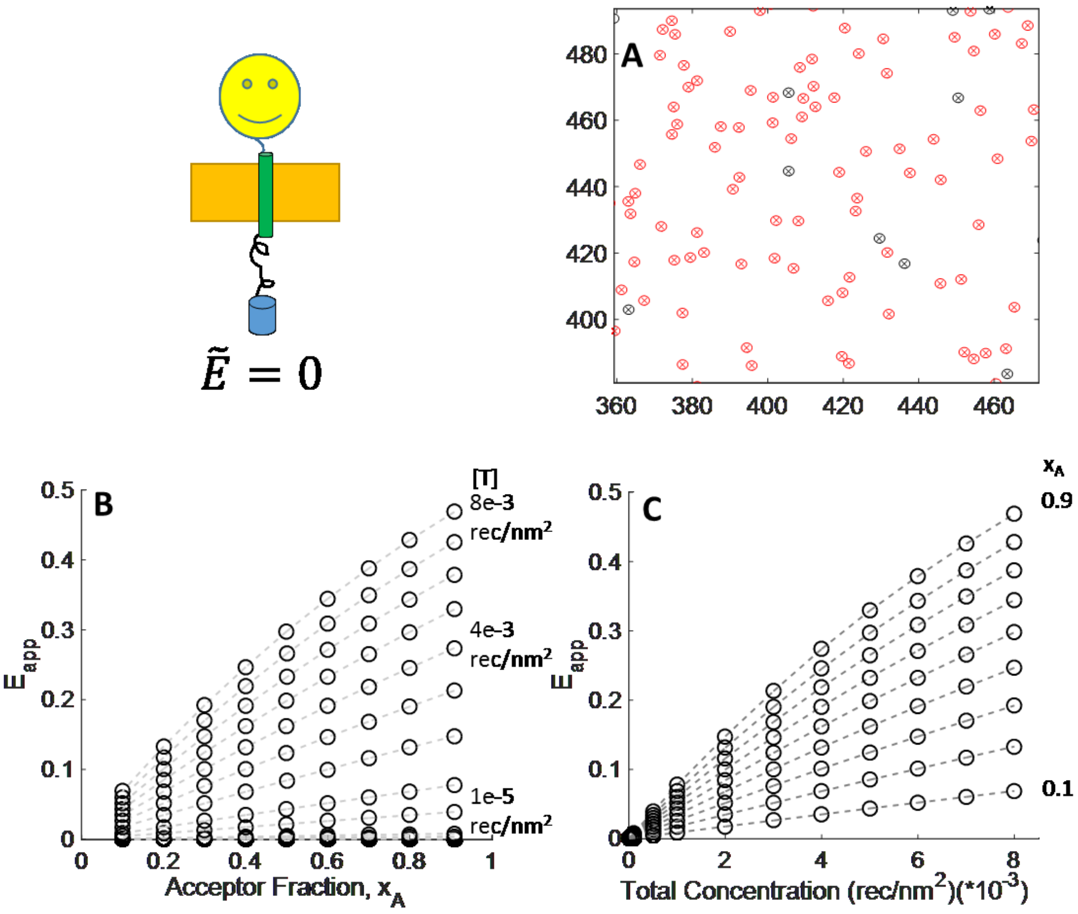

Figure 3-2. The predictions of the monomer-only simulation. **A.** A sample configuration of monomers from the simulation. Figure is drawn to scale, axes units are in nm. **B.** E_{app} plotted as a function of acceptor fraction. The dashed lines connect data points with constant $[T]$, as indicated by the numbers on the right side. **C**. E_{app} is plotted as a function of the total concentration, $[T]$. The dashed lines connect data points with constant acceptor fraction, x_A, as indicated on the right.

Figure 3-3. Analysis results for the monomer-only simulations. **A.** The total apparent FRET efficiency for the monomer-only simulations as a function of the A:D ratio (black circles). The dashed lines connect data points at constant [T], as indicated on the right. In addition, the best fit model of Veatch and Stryer for analysis of $\mathrm{E_{app}}$ at [T] = 0.008 rec/nm2 (top), [T] = 0.004 rec/nm2 (middle), and [T] = 0.00001 rec/nm2 (bottom) are shown in red. **B**. The best-fit MSE (left axis) versus oligomer order for the analysis of $\mathrm{E_{app}}$ with the thermodynamic model based Kinetic Theory of FRET, without a stochastic FRET contribution (black circles). The blue circles mark the best-fit MSE for fitting $\mathrm{E_{app}}$ with a stochastic FRET contribution as in **Equation (2-32)**. In both cases, the best-fit MSE is $n = 2$. Right axis: The best-fit reduced chi-square versus oligomer order for the analysis of $\mathrm{E_{app}}$ in the presence of random noise with the thermodynamic model based Kinetic Theory of FRET, without a stochastic FRET contribution (black X's). The green X's mark the best-fit reduced chi-square value for fitting $\mathrm{E_{app}}$ in the presence of random noise with while including a stochastic FRET contribution, as in **Equation (2-32)**. The magenta line is the 95% confidence cutoff for the reduced chi-square test- all X's above this line are rejected and all X's below this line are accepted as equally likely models, given the data and its associated error. Analysis without a stochastic FRET contribution does produce acceptable models $n = 1$ and $n = 3$. Analysis with the stochastic FRET consideration shows that all models provide an acceptable fit to the data, but the best-fit ΔG° indicates a lack of interactions. **C.** The apparent FRET efficiency is plotted as a function of the acceptor surface density (black circles), and the best-fit monomer-only model (blue line), for an exclusion radius of 1.4nm (see **Equation (3-9) and Table 3-1**).

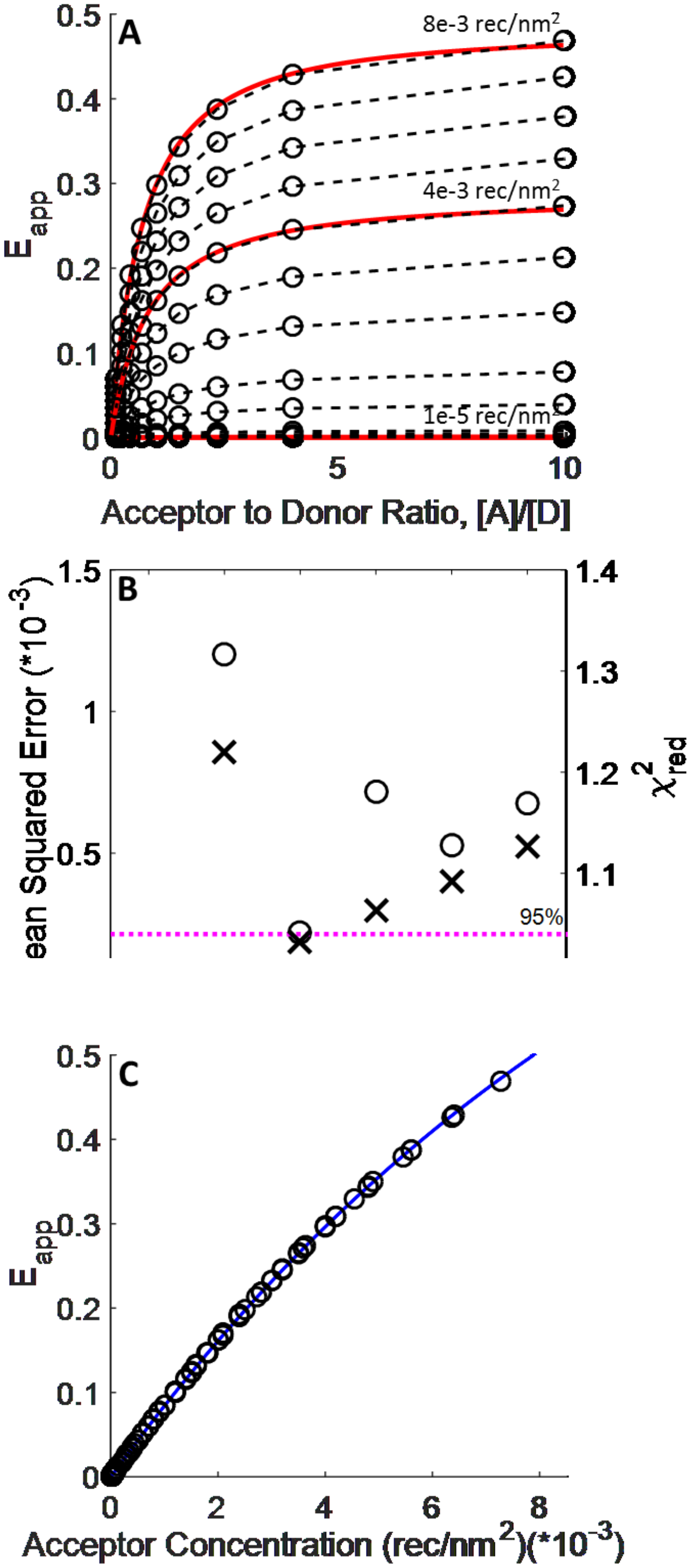
A
8e-3 rec/nm²
4e-3 rec/nm²
1e-5 rec/nm²
E_app
0
0.1
0.2
0.3
0.4
0.5
0
5
10
Acceptor to Donor Ratio, [A]/[D]
B
ean Squared Error (*10^-3)
1.5
1
0.5
1.4
1.3
1.2
1.1
χ²_red
95%
C
E_app
0
0.1
0.2
0.3
0.4
0.5
0
2
4
6
8
Acceptor Concentration (rec/nm²)(*10^-3)

3-6. Dimeric Membrane Proteins

Figure 3-4 shows the E_{app} prediction for dimers, when $\tilde{E} = 0.70$. The total concentrations of fluorophores were varied from 1e-5 fluorophores/nm^2, to a maximum surface density of 8e-3 fluorophores/nm^2, while the acceptor fraction, x_A, was varied from 0.1 to 0.9. **Figure 3-4A** shows one example of a dimer configuration. **Figure 3-4B** shows the predictions of E_{app} (using equations 8 and 9) and E_{Oligo} (using equations 10 and 11), as a function of the total concentration, for acceptor fractions (x_A increasing from 0.1 to 0.9). We see that oligomeric FRET, E_{Oligo}, is a constant (for a given x_A) across the entire concentration range. On the other hand, E_{app} increases as a function of the total concentration, due to stochastic FRET. **In Figure 3-4C**, we compare the simulated E_{app} to the stochastic FRET contribution, E_{prox}, calculated with equation (5). Eprox increases monotonically from zero as a function of total concentration to a maximum of ~40% for x_A = 0.9, a very significant contribution that cannot be neglected. **Figure 3-6** shows the E_{app} prediction for dimers, when $\tilde{E} = 0.30$. We see that for this low value of the intrinsic FRET efficiency, the stochastic FRET contribution is a much greater component of the total apparent FRET efficiency, and at the highest total concentrations and acceptor fractions, stochastic FRET comprises a large component of the total apparent FRET efficiency.

For a dimer, E_{Oligo} (E_{Dimer}) is linear when viewed as a function of the acceptor fraction, x_A (**Equation 2-14**). Often, this linear relationship is used to discern a dimer from a higher order oligomer. My simulation predicts this linear behavior, as shown in **Figure 3-4D.** Here, E_{Oligo} is plotted as a function of acceptor fraction with a blue line. This line is plotted for $[T]$ = 1e-5 rec/nm^2, where the stochastic FRET contribution is close to zero and for $[T]$ = 8e-3 rec/nm^2 with maximal stochastic FRET. The two blue lines overlap exactly, as stochastic FRET has no effect on the magnitude of the dimer FRET.

E_{app} as a function of acceptor fraction is also plotted in **Figure 3-4D** for low $[T]$ = 1e-5 rec/nm^2 and high $[T]$ = 8e-3 rec/nm^2. We see that the curve for low total surface density overlaps exactly the curve of E_{Oligo} vs x_A. Thus, at low surface densities stochastic FRET is minimized and $E_{Oligo} = E_{app}$. E_{app} is also linear with the acceptor fraction (overlap of blue and black lines). When $[T]$ = 8e-3 rec/nm^2, however, the stochastic FRET contribution to the total apparent FRET efficiency is significant, and in this case E_{app} is not a linear function of x_A (top black curve in **Figure 3-4D**). This effect is also seen in the case of $\tilde{E} = 0.30$, shown in **Figure 3-6D**. Thus, the stochastic FRET contribution introduces curvature in the E_{app} versus x_A plot at moderate to high surface densities for dimers, and we see that this curvature is not an indication of higher order oligomer formation, as is often assumed.

Figure 3-5 and **Figure 3-7** show the applications of the models of Veatch and Stryer, and the thermodynamic model based on the Kinetic Theory of FRET, to the simulated dimer predictions for $\tilde{E} = 0.70$ and $\tilde{E} = 0.30$, respectively. In **Figure 3-5A** and **Figure 3-7A**, we fitted the constitutive dimer predictions with the model of Veatch and Stryer (**Equation 2-11**) and optimized for E_{max} and n. We did this for two different total concentrations, $[T]$ = 8e-3 rec/nm^2 (high total concentration) and $[T]$ = 1e-5 rec/nm^2 (low total concentration). The best-fit Veatch and Stryer (**Equation 2-11**) fitting results are plotted as red curves in **Figure 3-5A and Figure 3-7A** and the best fit parameters are given in **Table 3-1** for $\tilde{E} = 0.70$ and **Table 3-2** for $\tilde{E} = 0.30$. When the total concentration is low and the stochastic FRET contribution is negligible, the fitting procedure yields the correct oligomerization order, n=2, and the correct $E_{max} = \tilde{E}$, in both cases of $\tilde{E} = 0.7$ and $\tilde{E} = 0.3$.

Fitting E_{app} at high total concentration, however, yields $n = 2.5$ for $\tilde{E} = 0.7$, and $n = 2.5$ for $\tilde{E} = 0.3$. Thus, the model of Veatch and Streyer, does not predict correctly the oligomer size for dimers. Furthermore, the prediction depends on the total concentration, and gives the false impression that the oligomer size increases when the total concentration increases. This seeming dependence of n on total concentration is an artifact occurring because the total concentrations and the stochastic FRET contributions are not taken into account in the model of Veatch and Stryer[67].

Figure 3-5B and Figure 3-7B show the best-fit mean squared error and the best-fit reduced chi-square as a function of oligomer order, for analysis with and without a stochastic FRET contribution. When the data is analyzed without a stochastic FRET contribution, we see that for both the MSE and the reduced chi-square minimizations, the best-fits occur for $n = 2$. However, none of the models without a stochastic FRET contribution are able to pass the reduced chi-square test, indicating poor fits to the data. When the proper stochastic FRET contribution is included analysis, the minimum MSE and reduced chi-square value for $n = 2$ fitting of E_{app} becomes very pronounced, (blue circles, green X's in **Figure 3-5B**) and the simulated parameters are properly extracted through the analysis (**Table 3-1**). We also see that the dimer model is the only model that passes the reduced chi-square test at a 95% confidence level. Thus, the total apparent FRET efficiency of a dimer is statistically different from the FRET efficiencies of other oligomerization orders for, $\tilde{E} = 0.7$. In the case of a low value of intrinsic FRET, $\tilde{E} = 0.3$, we see in **Figure 3-7B** that acceptable best-fit reduced chi-squared values were obtained for n=2-5. Thus, for low values of intrinsic FRET, it will be difficult or impossible to determine the oligomerization state of the protein under study.

In conclusion, we see that use of the model of Veatch and Stryer can lead to misleading results for the case of dimers. We also see that the donor and acceptor concentrations in the FRET experiments need to be known, such that the Kinetic Theory formalism can be applied with a stochastic FRET contribution as with **Equation (2-32).** We see that the stochastic FRET contribution must be accounted for when analyzing the data of a constitutively dimeric system. When the stochastic FRET is taken into account, however, we are able to correctly identify the presence of constitutive dimers and to recover the correct $\tilde{E}$ from the simulated dimeric E_{app} data.

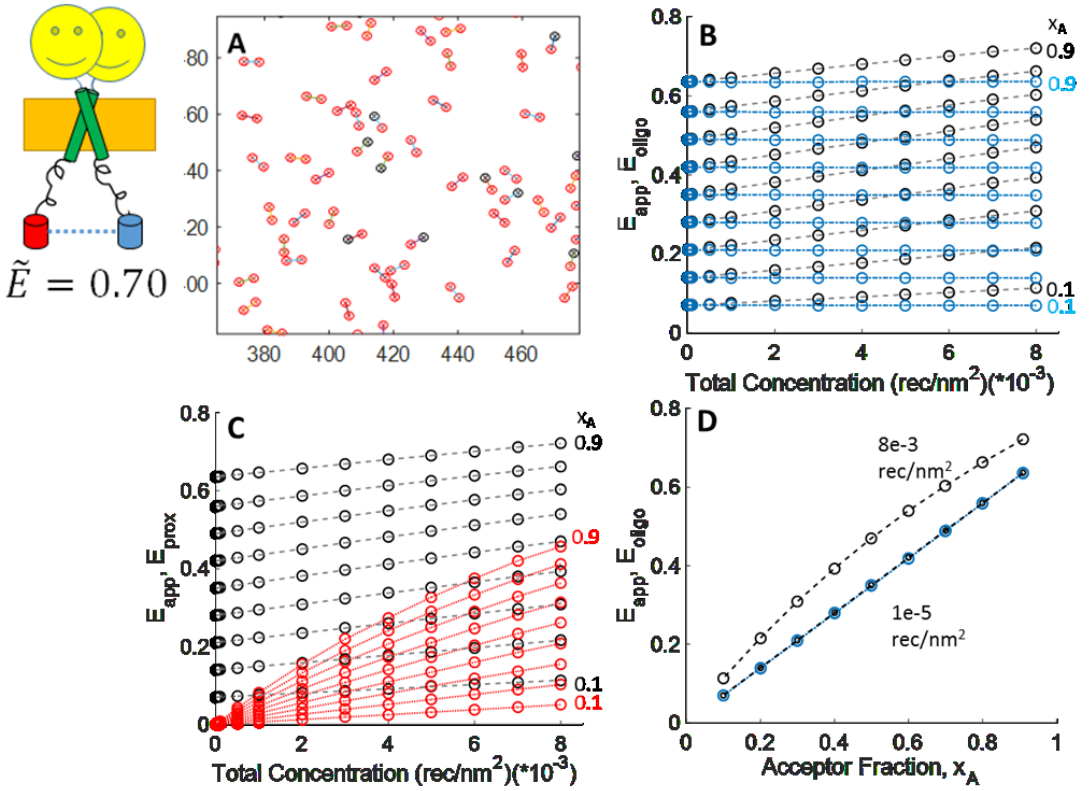

Figure 3-4. Predictions of the dimer-only simulation, $\tilde{E} = 0.70$. **A.** A sample configuration of dimers, as utilized in the simulation, with $[T]$ = 8e-3 fluorophores/nm^1. Figure is drawn to scale, units of axes are in nm. Donors: blue circles, Acceptors: red circles. **B.** E_{app} (black circles) and E_{Oligo} (blue circles) are plotted as a function of acceptor fraction, x_A for $[T]$ = 0.008 rec/nm^2 (upper curve), and $[T]$ = 0.00001 rec/nm^2 (lower curve). Dashed lines connect data points at constant $[T]$. The E_{Oligo} curves overlap for all $[T]$. **C.** E_{app} (black circles) and E_{prox} (red circles) as a function of total fluorophore surface density. In both panels, dashed lines connect data points at constant acceptor fraction, x_A, as indicated by the numbers on the right. **D.** E_{app} and E_{Oligo} as a function of total concentration, $[T]$. Dashed lines connect data points at constant total concentration, $[T]$, as indicated.

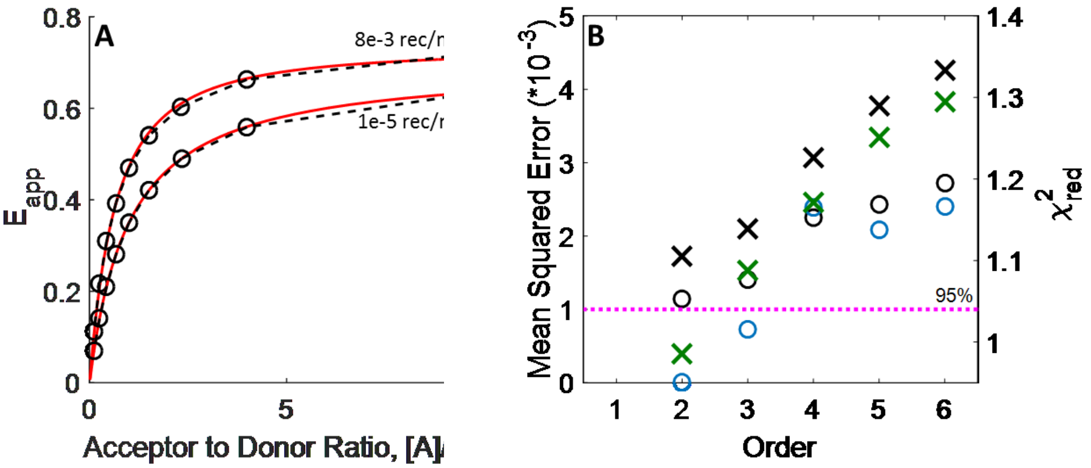

Figure 3-5. Analysis results of the dimer-only simulations, $\widetilde{E} = 0.70$. **A**. E_{app} (black circles) versus A:D ratio, and the best-fit Veatch and Streyer model (red lines), for [T] = 1e-5 rec/nm^2 and [T] = 8e-3 rec/nm^2 (lower, upper curves respectively). **B**. The best-fit MSE (left axis) versus oligomer order for the analysis of E_{app} with the thermodynamic model based Kinetic Theory of FRET, without a stochastic FRET contribution (black circles). The blue circles mark the best-fit MSE for fitting E_{app} with a stochastic FRET contribution as in **Equation (2-32)**. In both cases, the best-fit MSE is n = 2. Right axis: The best-fit reduced chi-square versus oligomer order for the analysis of E_{app} in the presence of random noise with the thermodynamic model based Kinetic Theory of FRET, without a stochastic FRET contribution (black X's). The green X's mark the best-fit reduced chi-square value for fitting E_{app} in the presence of random noise with while including a stochastic FRET contribution, as in **Equation (2-32)**. The magenta line is the 95% confidence cutoff for the reduced chi-square test- all X's above this line are rejected and all X's below this line are accepted as equally likely models, given the data and its associated error. Analysis without a stochastic FRET contribution does not produce acceptable models for any order. Analysis with the stochastic FRET consideration shows that the n = 2 model is the only model that passes the reduced chi-square test.

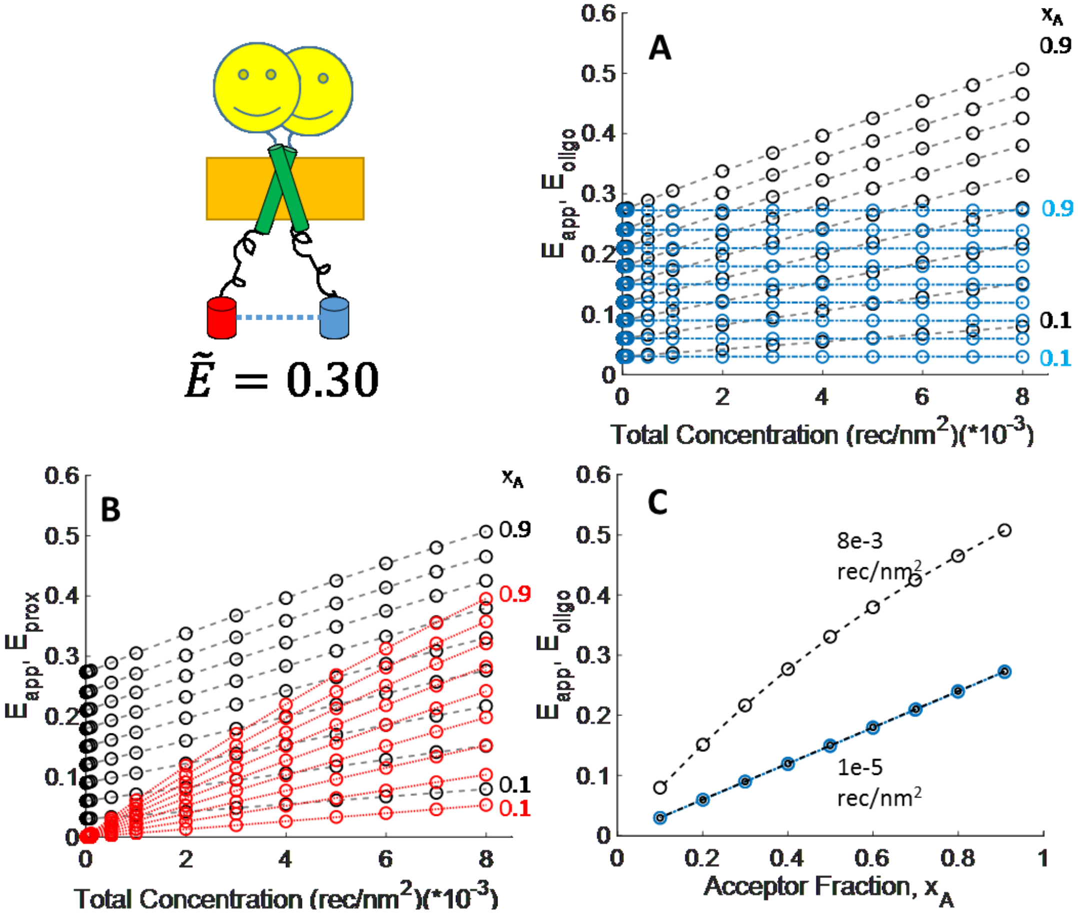

Figure 3-6. The predictions of the constitutive dimer simulations, for $\tilde{E} = 0.30$. **A.** E_{app} (black circles) and E_{Oligo} (blue circles) versus total concentration. The dashed lines connect data points of constant acceptor fraction, as indicated on the right. **B.** E_{app} (black circles) and E_{prox} (red circles) versus total concentration. **C.** E_{app} (black circles) and E_{Oligo} (blue circles) versus acceptor fraction, x_A, for $[T]$ = 1e-5 rec/nm^2 (lower curve) and $[T]$ = 8e-3 rec/nm^2 (upper curve). E_{Oligo} overlaps with itself at both concentrations for all acceptor fractions. At low surface density, $[T]$ = 1e-5 rec/nm^2, $E_{app} = E_{Oligo}$.

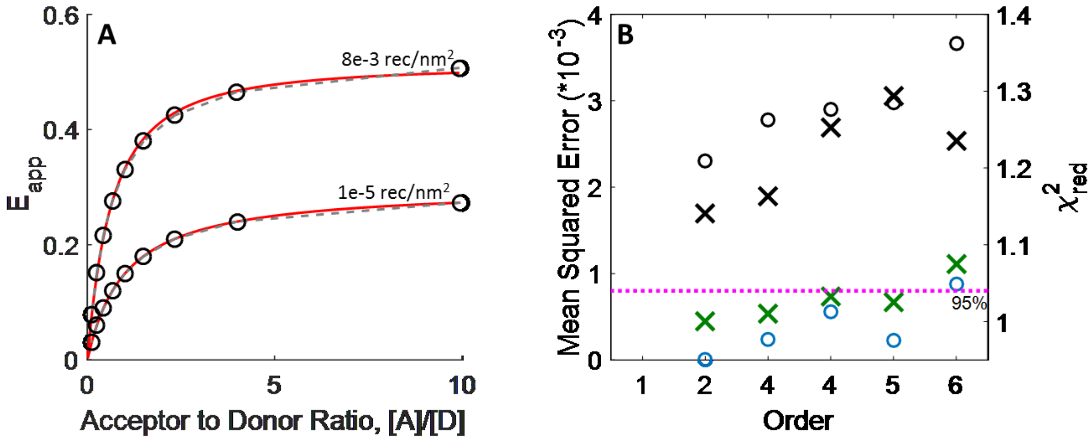

Figure 3-7. Analysis results of the dimer-only simulations, for $\tilde{E} = 0.30$. **A**. E_{app} (black circles) versus A:D ratio, and the best-fit Veatch and Streyer model (red lines), for $[T]$ = 1e-5 rec/nm^2 and $[T]$ = 8e-3 rec/nm^2 (lower, upper curves respectively). **B**. The best-fit MSE (left axis) versus oligomer order for the analysis of E_{app} (black circles) with the thermodynamic model based Kinetic Theory of FRET, without a stochastic FRET contribution. The blue circles mark the best-fit MSE for fitting E_{app} with a stochastic FRET contribution as in **Equation (2-32)**. In both cases, the best-fit MSE is n = 2. Right axis: The best-fit reduced chi-square versus oligomer order for the analysis of E_{app} (black X's) with the thermodynamic model based Kinetic Theory of FRET, without a stochastic FRET contribution. The green X's mark the best-fit reduced chi-square value for fitting E_{app} with while including a stochastic FRET contribution, as in **Equation (2-32)**. The magenta line is the 95% confidence cutoff for the reduced chi-square test- all X's above this line are rejected and all X's below this line are accepted as equally likely models, given the data and its associated error. Analysis without a stochastic FRET contribution does not produce acceptable models for any order. Analysis with the stochastic FRET consideration shows a minimum at n=2, but n = 2-5, corresponding to dimer through pentamer models, all provide an acceptable fit to the data.

3-7. *Trimeric Membrane Proteins*

Figure 3-8 shows the FRET predictions for the constitutive trimer simulations, where trimers are arranged circles placed at the vertices of an equilateral triangle with a center to center distance on a side corresponding $\tilde{E} = 0.70$. **Figure 3-8A** shows a sample configuration of trimeric fluorophores utilized in the simulations. The total concentrations of fluorophores were varied from 1e-5 fluorophores/nm^2 to a maximum surface density of 8e-3 fluorophores/nm^2, while the acceptor fraction, x_A, was varied from 0.1 to 0.9. E_{app} and E_{Oligo} are plotted as a function of total fluorophore concentration in **Figure 3-8B** as black and blue circles. We find that the total apparent FRET efficiency is much closer in value to the oligomeric FRET efficiency for constitutive trimers than with constitutive dimers across the range of simulated concentrations. As in the case of the constitutive dimers, the total oligomeric FRET of the trimer-only case is constant as a function of total fluorophore concentration for a given acceptor fraction. **Figure 3-8C** shows the total apparent FRET efficiency along with the stochastic FRET contribution as a function of total concentration.

Compared to the constitutive dimer simulations, the total stochastic FRET is reduced by nearly 10% at the highest surface densities, yet still increases with increasing total surface density of fluorophores. The combination of the increasing stochastic FRET contribution along with the constant oligomeric FRET contribution to the total apparent FRET efficiency means that E_{app} also increases as a function of total fluorophore concentration. With a low value of the intrinsic FRET efficiency, $\tilde{E} = 0.30$, as shown in **Figure 3-10A and 3-10B**, the effect of the stochastic FRET on the total apparent FRET efficiency is more pronounced. At the highest concentrations the stochastic FRET contribution is only ~10% less than the oligomeric FRET contribution in the total apparent FRET efficiency.

Figure 3-9 and **Figure 3-10** shows the results of the analyses of the trimer-only simulations with the models of Veatch and Stryer, and the thermodynamic model based on the Kinetic Theory of FRET for $\tilde{E} = 0.70$ and $\tilde{E} = 0.30$, respectively. In **Figure 3-9A**, I plot the total apparent FRET efficiency as a function of acceptor to donor ratio, as previously with dimers, for two total concentrations: low surface density, $[T]$ = 1e-5 rec/nm^2, and high surface density, $[T]$ = 8e-3 rec/nm^2. We see that the reduced stochastic FRET contribution in the trimer-only case leads to a reduced total concentration dependence on the curvature of E_{app} vs A/D, when compared to the dimer-only simulations. Optimizing for E_{max} and n in the model of Veatch and Stryer, **Equation 2-11**, we find that for low and high surface densities, the results for $\tilde{E} = 0.70$ are nearly identical: n indicates trimer formation with values of 2.7 and 3.0, but E_{max} does not reflect the true intrinsic FRET of a D:A pair in the trimer with values of 0.80 and 0.81, respectively. The best-fit Veatch and Stryer models are shown in **Figure 3-9A** as red lines, and show good agreement with the fitted data. Of note is the fact that at a low value of the intrinsic FRET, $\tilde{E} = 0.30$, the model of Veatch and Stryer indicates dimer formation, with $n = 2$ for low surface density. Meanwhile, at high surface density, the model indicates trimer formation. This behavior could be incorrectly interpreted as a concentration-dependent oligomer order.

Figure 3-9B shows the best-fit mean squared error (MSE, left axis, circles) and the reduced chi-squared value (left axis, X's) as a function of oligomer order and the best-fit parameters, $\Delta G°$ and $\tilde{E}$, for the trimer fitting are given in **Table 3-1** and **Table 3-2**. We see that the stochastic FRET correction has little effect on the overall best-fit MSE for $n > 2$ (compare blue and black open circles). The overall minimum MSE is found for the trimeric model, and the best-fit $n = 3$ parameters for fitting E_{app} are very close to the actual simulated parameters. These results indicate that the effect of the stochastic FRET contribution for a constitutive trimer with high intrinsic FRET is essentially negligible, with regards to determination of the intrinsic FRET efficiency and the oligomeric state through analysis. We also see that for the constitutive trimer reduced chi-square analysis with a stochastic FRET contribution, both the trimer and tetramer models are viewed as acceptable models, given the data. This is due to two factors: the approximation of the single-donor-to-acceptor distance in the oligomer, which is true for equilateral trimers, but becomes worse and worse for $n > 3$, and the fact that the total apparent FRET efficiency for higher order oligomer formation, n > 2, is not unique. For example, even though the data is not shown, I can adjust the intrinsic FRET and association constant parameters of a pentamer simulation such that the total apparent FRET efficiency matches the trimeric total apparent FRET efficiency to within 1%.

For the case of a low value of the intrinsic FRET efficiency, $\tilde{E} = 0.30$, we see that all $n > 1$ provide acceptable reduced chi-squared values when a stochastic FRET contribution is modeled in the analysis (**Figure 3-10D).** Without a stochastic FRET contribution, none of the models produce acceptable best-fit reduced chi-square values at 95% confidence. Thus, we find trimer formation will be indiscernible from other oligomerization models in bulk two-color, static quenching FRET experiment. Further, for a low value of intrinsic FRET, we find that a stochastic FRET contribution is necessary in the model for proper extraction of the oligomeric fraction (see **Table 3-2**).

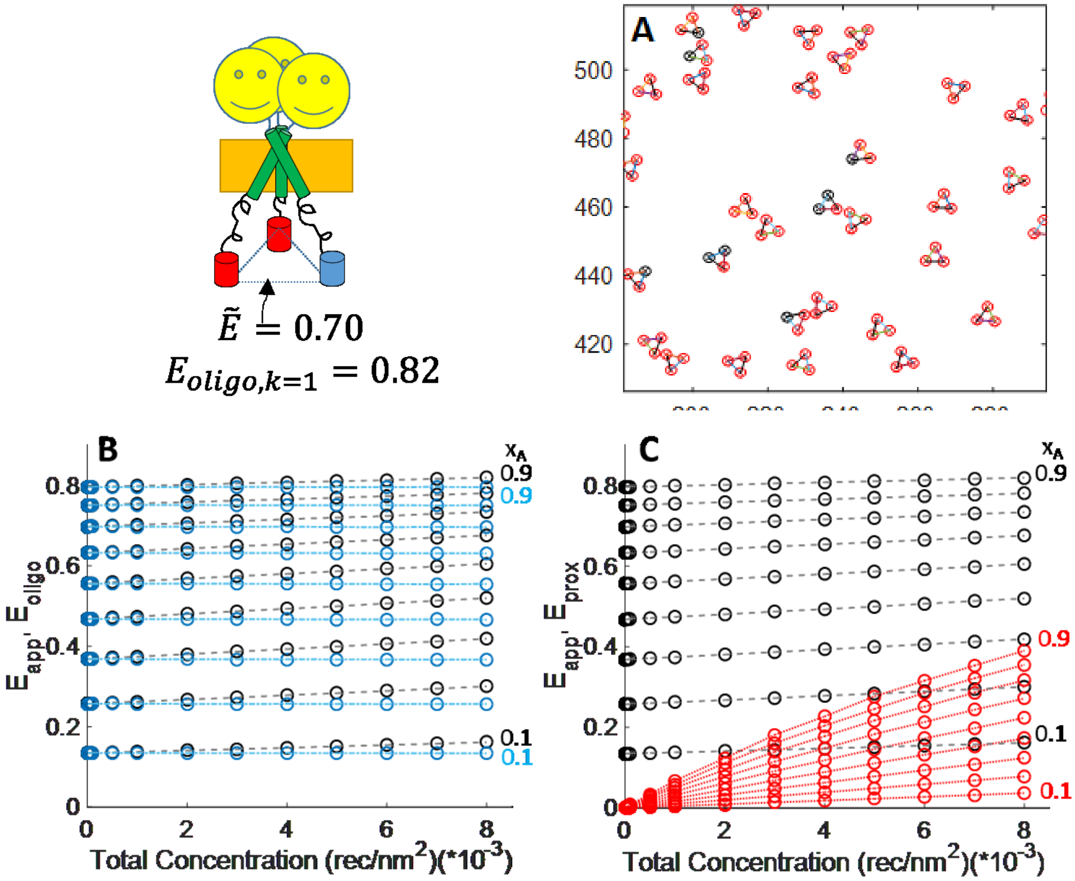

Figure 3-8. The predictions of the trimer-only simulation, $\tilde{E} = 0.70$. **A.** A sample configuration of randomly labeled trimers, as utilized in the simulations. Figure is drawn to scale, with donors represented by blue circles and acceptors as red circles. **B.** E_{app} and E_{Oligo} versus total concentration, $[T]$ (black and blue circles, respectively). **C.** E_{app} and E_{prox} are plotted as a function of total concentration, $[T]$ (black circles and red circles, respectively). In both panels, the dashed lines connect data points of constant acceptor fraction, x_A, as indicated by the numbers on the right.

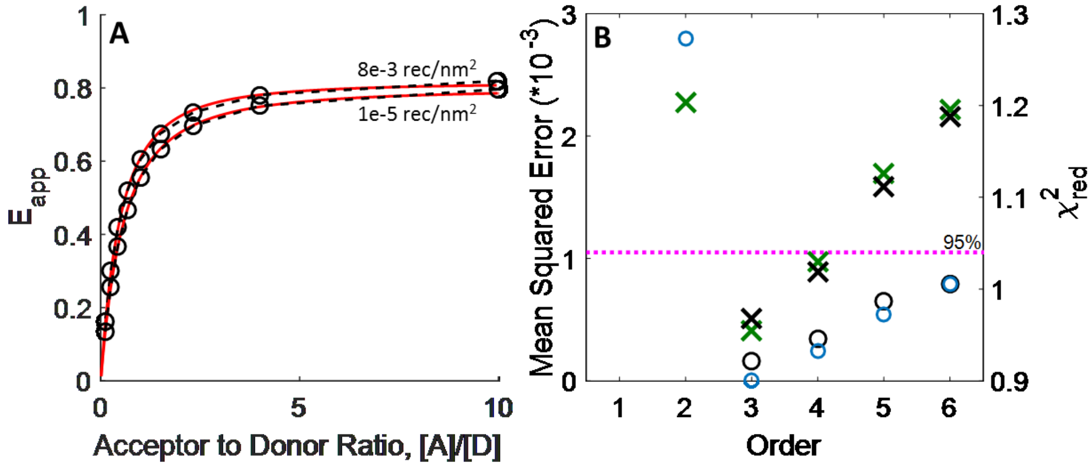

Figure 3-9. Analysis results for the constitutive-trimer simulation, $\tilde{E} = 0.70$. **A.** The best-fit Veatch and Stryer model plotted (red lines) on top of the measured E_{app} vs. A:D ratio for $[T]$ = 1e-5 fluorophores/nm^2 (lower curve, black circles) and for $[T]$ = 8e-3 fluorophores/nm^2 (upper curve, black circles) . **B.** The best-fit MSE(left axis, circles) and reduced chi-square value (right axis, X's) versus oligomer order for the analysis of E_{app} with the thermodynamic model based on the Kinetic Theory of FRET with a stochastic FRET contribution (blue circles, green X's), and without a stochastic FRET contribution (black circles, black X's). In both cases, the minimum MSE occurs at $n = 3$. The line in magenta denotes the 95% confidence limit for the reduced chi-square test. All X's above this line are rejected and all X's below this line are accepted as equally likely models, given the data and its associated error. In the presence of random noise, $n = 3$ and $n = 4$ models without a stochastic FRET contribution both pass the reduced chi-square test, and similarly, $n = 3$ and $n = 4$ provide acceptable fits to the data when a stochastic FRET contribution is included. Thus, the oligomer order is not discernable for this dataset.

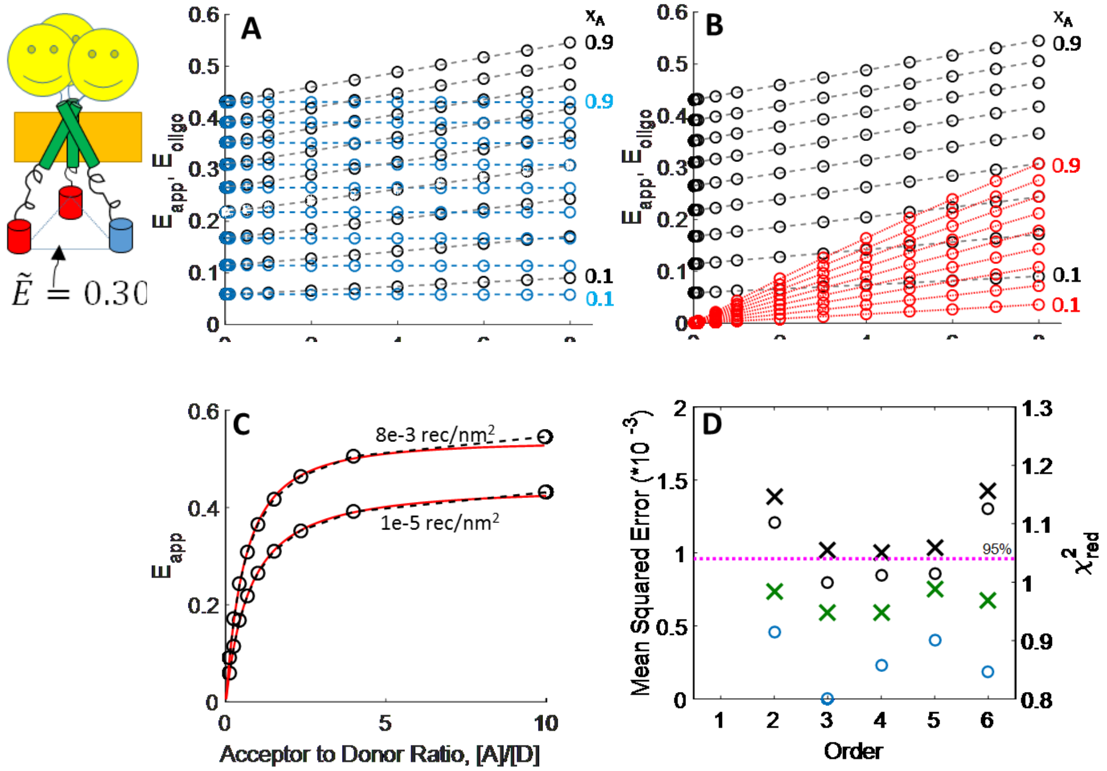

Figure 3-10. The predictions of the constitutive-trimer simulations and the results of the analyses, for $\tilde{E} = 0.30$. **A.** E_{app} (black circles) and E_{Oligo} (blue circles) versus total concentration. The dashed lines connect data points of constant acceptor fraction, as indicated on the right. **B.** E_{app} (black circles) and E_{prox} (red circles) versus total concentration **C.** E_{app} (black circles) versus A:D ratio, and the best-fit Veatch and Streyer model (red lines) , for $[T]$ = 1e-5 rec/nm^2 and $[T]$ = 8e-3 rec/nm^2 (lower, upper curves respectively). **D.** The best-fit MSE(left axis, circles) and reduced chi-square value (right axis, X's) versus oligomer order for the analysis of E_{app} with the thermodynamic model based on the Kinetic Theory of FRET with a stochastic FRET contribution (blue circles, green X's), and without a stochastic FRET contribution (black circles, black X's). The line in magenta denotes the 95% confidence limit for the reduced chi-square test. In the presence of random noise, all models without a stochastic FRET contribution fail the reduced chi square test, and all $n > 1$ provide acceptable fits to the data when a stochastic FRET contribution is included. Thus, the oligomer order is not discernable for this dataset.

3-8. Tetrameric Membrane Proteins

Figure 3-11 and Figure 3-13 shows the results of the simulations for constitutively tetrameric distributions of fluorophores for $\tilde{E} = 0.70$ and $\tilde{E} = 0.30$. **Figure 3-11A** shows a sample configuration of tetrameric fluorophores, represented by circles arranged in a square configuration. The total concentrations of fluorophores utilized ranged from $[T] =$ 1e-5 fluorophores/nm^2 to a maximum surface density of 8e-3 fluorophores/nm^2, with the acceptor fraction ranging from 0.1-0.9. **Figure 3-11B** shows E_{app} and E_{Oligo} plotted as a function of total concentration as black and blue circles, respectively. We see that compared to the constitutive dimer and trimer simulations, the difference between E_{app} and E_{Oligo} is further reduced. We also see that as before, the oligomeric FRET is constant for all concentrations, while the total apparent FRET efficiency slowly increases due to stochastic FRET. In **Figure 3-11C**, we plot E_{app} and E_{prox} as a function of total fluorophore surface density.

A comparison of the stochastic FRET contribution for tetramers with that of trimers and dimers shows a drastically reduced stochastic FRET contribution in the constitutive tetramer simulations, for both $\tilde{E} = 0.70$ and $\tilde{E} = 0.30$ simulations. Additionally, we see that the total apparent FRET efficiencies for the constitutive trimer simulations and constitutive tetramer simulations are nearly equal (compare **Figures 3-8B, C** and **Figures 3-11, C**). Furthermore, due to the reduced stochastic FRET contribution, the oligomeric FRET and the total apparent FRET efficiency are nearly equal across all concentration ranges for $\tilde{E} = 0.70$. **Figure 3-13A, B** shows that for low intrinsic FRET, $\tilde{E} = 0.30$, stochastic FRET becomes a significant component of the total apparent FRET efficiency, contributing to the steeper increase of the total apparent FRET efficiency with increasing surface density of fluorophores.

Figure 3-12 and **Figure 3-13C, D** show the analysis results of the constitutive tetramer simulations with the models of Veatch and Stryer, and the thermodynamic model based on the Kinetic Theory of FRET for $\tilde{E} = 0.70$ and $\tilde{E} = 0.30$, respectively. The results of these analyses are summarized in **Table 3-1**, below (see **Table 3-2** for $\tilde{E} = 0.30$). In **Figure 3-12A**, I plot the total apparent FRET efficiency as a function of acceptor to donor ratio, as previously with dimers and trimers for two total concentrations: low surface density, $[T]$ = 1e-5 rec/nm^2, and high surface density, $[T]$ = 8e-3 rec/nm^2. We see that the reduced stochastic FRET contribution in the tetramer-only case leads to a reduced total concentration dependence on the curvature of E_{app} vs A/D, when compared to the dimer- and trimer-only simulations. Optimizing for E_{max} and n in the model of Veatch and Stryer, **Equation 2-11**, we find that for low and high surface densities, the results for $\tilde{E} = 0.70$ are nearly identical: n indicates trimer formation with values of 2.9 and 3.1, but E_{max} does not reflect the true intrinsic FRET of a D:A pair in the tetramer with a value of 0.81. The best-fit Veatch and Stryer models are shown in **Figure 3-12A** as red lines. Of note is the fact that at a low value of the intrinsic FRET, $\tilde{E} = 0.30$, the model of Veatch and Stryer indicates dimer formation with n = 2.4 for low surface density, and gives an indication of trimer formation with n = 2.6 at high surface density. As with trimers, for tetramers, this behavior could be incorrectly interpreted as a concentration-dependent oligomer order.

Analysis of the total apparent FRET efficiency data with the thermodynamic model based on Kinetic Theory of FRET (**Equation (3-10)**) reveals an apparent minimum at n = 4 in the MSE versus oligomer-order plot (**Figure 3-12B**) when the stochastic FRET is ignored. However, with the stochastic FRET contribution included in the MSE and reduced chi-square analysis, we find that the FRET of tetramer formation is indistinguishable from the total apparent FRET efficiency of trimer formation. Both models for $n = 3$ and $n = 4$ pass the reduced chi-square test at 95% confidence, as shown by the green X's in **Figure 3-12B**. We see that for a low value of intrinsic FRET, $\tilde{E} = 0.30$, the MSEs for n > 2 are all nearly equal and the best-fit reduced chi-square values for all produce acceptable fits, for analysis with a stochastic FRET contribution (**Figure 3-13D**). This is a consequence of both the single D:A distance approximation in the Kinetic Theory of FRET in **Equation (3-10)** and the low $\tilde{E}$ value, and further enhanced due to the non-uniqueness of the total apparent FRET efficiency for higher-order oligomer formation, compare to constitutive trimer results, and also discussed later. Thus, as with trimers, I have found find that tetramer formation will be indistinguishable from that of trimer formation in a two-color static quenching FRET experiment. Since I have shown the essential and important distinguishable features in a bulk, static-quenching membrane protein FRET experiment, I will not continue this to higher oligomer orders, and as such I do not analyze or present simulations of pentameric and higher-order constitutive oligomers.

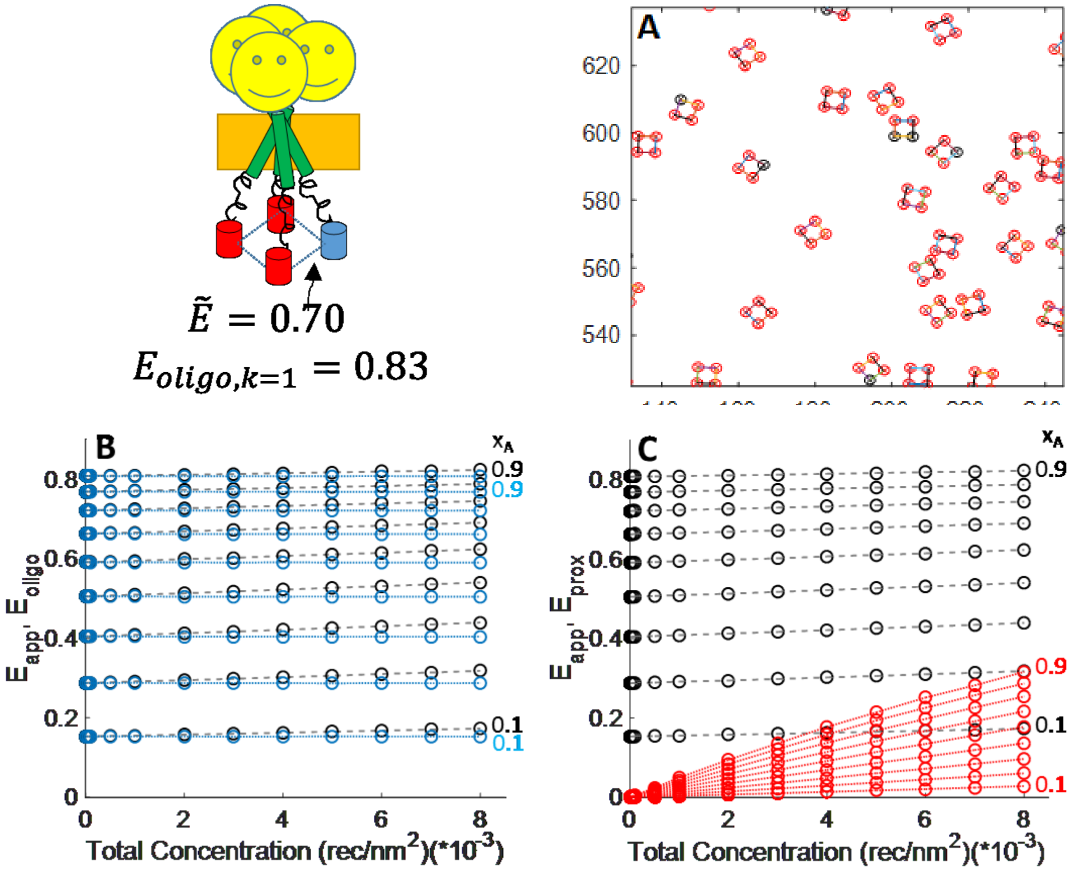

Figure 3-11. Predictions of the constitutive tetramer simulation, $\tilde{E} = 0.70$. **A.** A sample configuration of tetramers, as used in the simulation with a total surface density, $[T] =$ 8e-3 fluorophores/nm^2. Figure drawn to scale, axes units in nm. **B.** E_{app} and E_{Oligo} versus $[T]$ (black and blue circles, respectively). **C.** E_{app} (black circles) and E_{prox} (red circles) as a function of total fluorophore concentration. In both panels, dashed lines connect data points of constant acceptor fraction, x_A, as indicated by the numbers to the right.

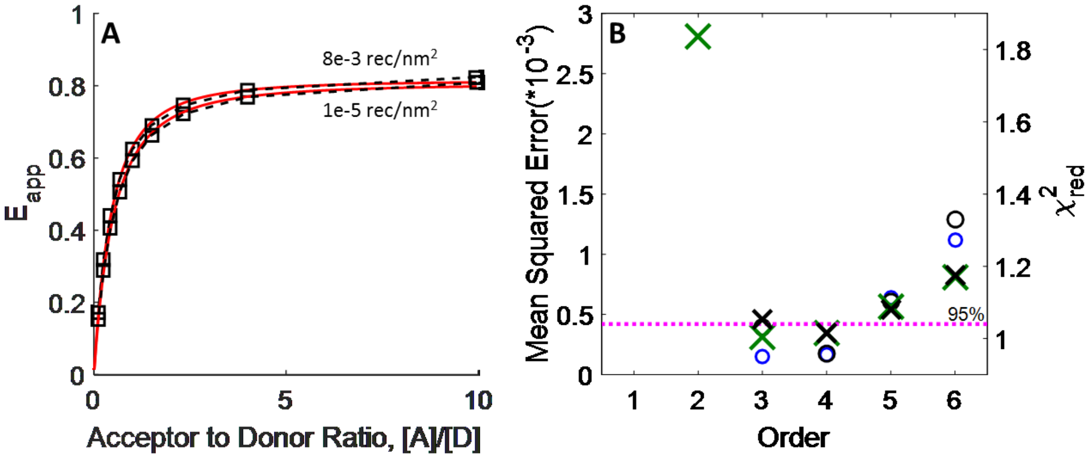

Figure 3-12. Analysis results for the constitutive-tetramer simulations, $\widetilde{\mathrm{E}} = 0.70$. **A.** E_{app} plotted as a function of A:D ratio, for [T] = 1e-5 rec/nm^2 (lower line) and for [T] = 8e-3 rec/nm^2 (top line) (black circles) along with the best-fit Veatch and Stryer model (red lines). **B.** The best-fit MSE(left axis, circles) and reduced chi-square value (right axis, X's) versus oligomer order for the analysis of E_{app} with the thermodynamic model based on the Kinetic Theory of FRET with a stochastic FRET contribution (blue circles, green X's), and without a stochastic FRET contribution (black circles, black X's). Without a stochastic FRET contribtution, the minimum MSE occurs at $n = 4$, but occurs at $n = 3$ when a stochastic FRET model is utilized (see **Equation (2-32)**). The line in magenta denotes the 95% confidence limit for the reduced chi-square test (X's, right axis). In the presence of random noise, most models without a stochastic FRET contribution fail the reduced chi-square test, except for the $n = 4$ model. Both $n = 3$ and $n = 4$ both provide acceptable fits to the data when a stochastic FRET contribution is included. Thus, the oligomer order is not discernable for this dataset, but the presence of dimers is excluded.

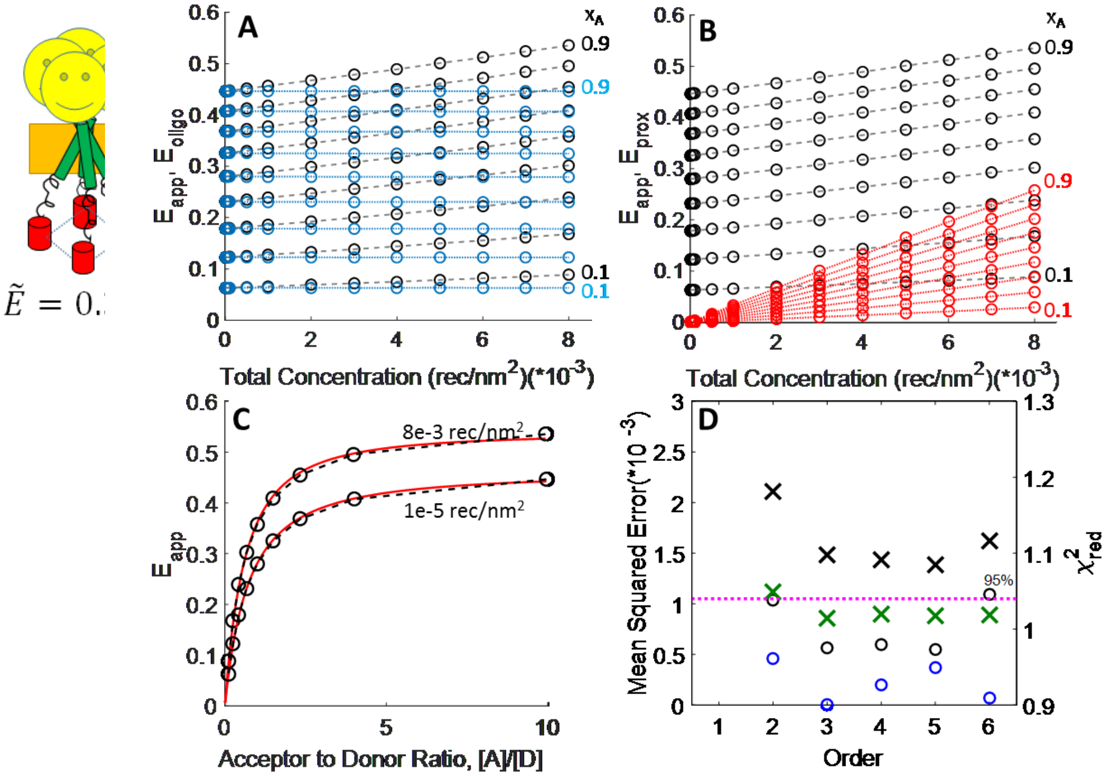

Figure 3-13. The predictions of the constitutive-tetramer simulation and the results of the analyses, for $\tilde{E} = 0.30$. **A.** E_{app} (black circles) and E_{Oligo} (blue circles) versus total concentration. The dashed lines connect data points of constant acceptor fraction, as indicated on the right. **B.** E_{app} (black circles) and E_{prox} (red circles) versus total concentration. **C.** E_{app} (black circles) versus A:D ratio, and the best-fit Veatch and Streyer model, for $[T]$ = 1e-5 rec/nm^2, and $[T]$ = 8e-3 rec/nm^2 (lower, upper curves, respectively). **D.** The best-fit MSE(left axis, circles) and reduced chi-square value (right axis, X's) versus oligomer order for the analysis of E_{app} with the thermodynamic model based on the Kinetic Theory of FRET with a stochastic FRET contribution (blue circles, green X's), and without a stochastic FRET contribution (black circles, black X's). The line in magenta denotes the 95% confidence limit for the reduced chi-square test (X's, right axis). In the presence of random noise, all models without a stochastic FRET contribution fail the reduced chi-square test, and all n>2 provide acceptable fits to the data when a stochastic FRET contribution is included. Thus, the oligomer order is not discernable for this dataset, but the presence of dimers is excluded.

Figure 3-14. Dimer, trimer, and tetramer simulated data (black dots) and best-fit model (green dots) of the simulated oligomer order for N = 2700 datapoints at random total concentrations, with acceptor fraction ranging from 0.1 – 0.9 in 0.1 steps. Gaussian distributed random noise, $\mu = 0, \sigma = 0.08$, was added to each data point prior to analysis with the reduced chi-squared test. **A.** Simulated data and best-fit dimer model for $\tilde{E} = 0.70$ **B.** Simulated data and best-fit dimer model for $\tilde{E} = 0.30$. **C.** Simulated data and best-fit trimer model for $\tilde{E} = 0.70$. **D.** Simulated data and best-fit trimer model for $\tilde{E} = 0.30$. **E.** Simulated data and best-fit tetramer model for $\tilde{E} = 0.70$. **F.** Simulated data and best-fit tetramer model for $\tilde{E} = 0.30$. Later, it will be useful to compare these simulated FRET experiments to the FRET that I have measured in the membranes of live cells.

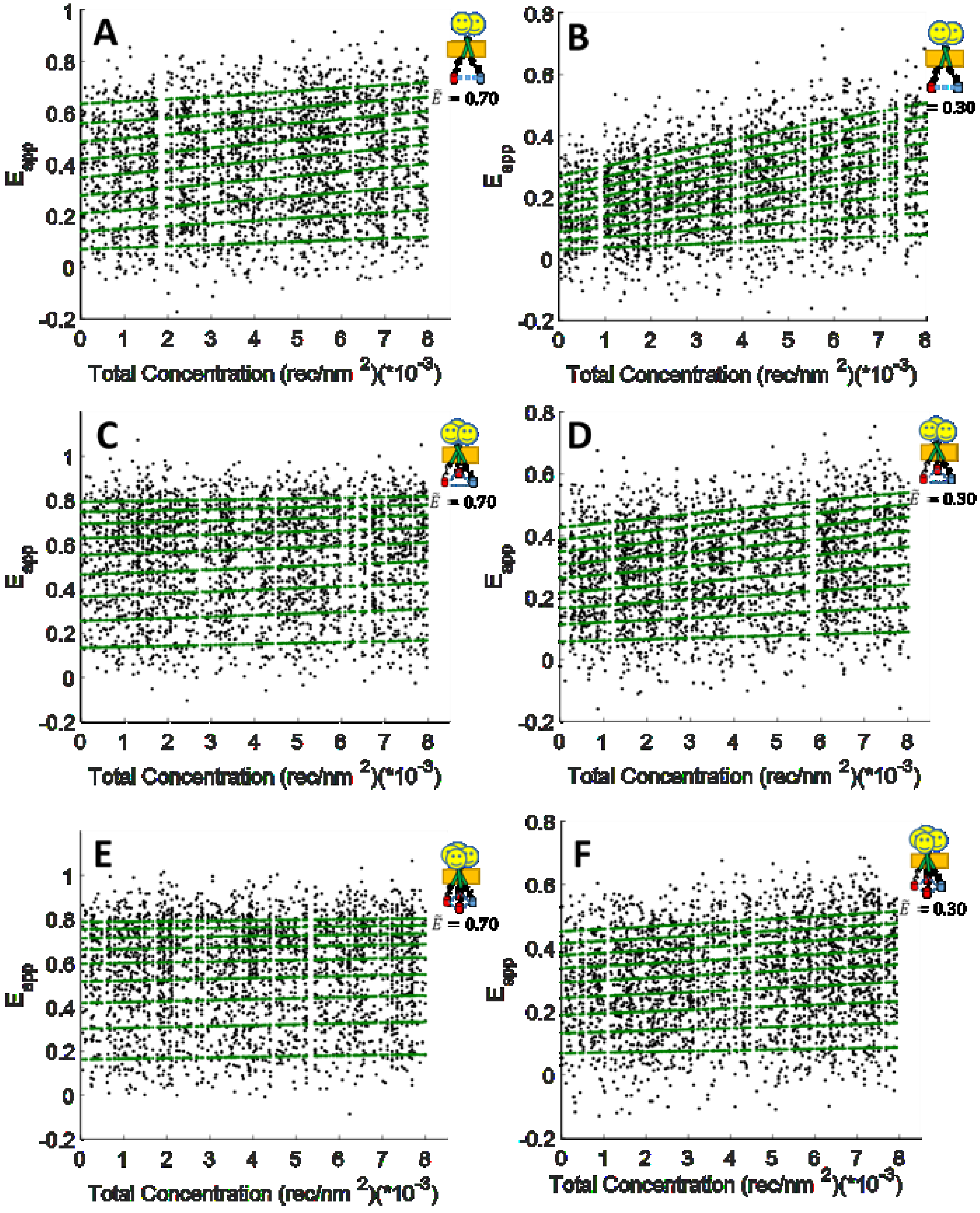
A
B
C
D
E
F
E_{app}
Total Concentration (rec/nm ^{2})(*10^{-3})
$\bar{E}$ = 0.70
$\bar{E}$ = 0.30
$\bar{E}$ = 0.70
$\bar{E}$ = 0.30
$\bar{E}$ = 0.70
$\bar{E}$ = 0.30
0
1
2
3
4
5
6
7
8
-0.2
0
0.2
0.4
0.6
0.8
1

Table 3-1. Combined results for analysis of the constitutive oligomer simulations for dimers (Order = 2), trimers (Order = 3), and tetramers (Order = 4) with the models of Veatch and Stryer and the thermodynamic model based on the Kinetic Theory of FRET, for $\tilde{E} = 0.70$. The analysis with the model of Veatch and Stryer was performed at two different total concentrations: $[T]$=1e-5 rec/nm^2 and $[T]$=8e-3 rec/nm^2, and the best-fit parameters n and E_{max} are provided in the columns. The thermodynamic model based on the Kinetic theory of FRET was used for fitting of simulated FRET data without error for a minimization of the Mean Squared Error(MSE). The **black** text indicates fitting without utilization of a stochastic FRET model and the **blue** text indicates the best-fit results for analysis that includes a stochastic FRET model (see **Equation (2-32)**). Additionally, the reduced chi-square minimization was performed for analysis with the thermodynamic model based on the Kinetic Theory of FRET (N=2,700 data points with added Gaussian-distributed random noise). The rows with **black** text indicate analysis results without utilizing a stochastic FRET model, as with the MSE minimization column, and the **green** text indicates the best-fit reduced chi-squared results for fitting with a stochastic FRET model.

Order	Simulation Values	Veatch & Stryer			Kinetic Theory of FRET	
		[T] = 1e-5 rec/nm^2	[T] = 4e-3 rec/nm^2	[T] = 8e-3 rec/nm^2	MSE Minimization	χ^2_{red} Minimization (+random noise)
1	monomer-only $r_{excl} = 1.4$nm	$n = 1.9$	n = 2.2	$n = 2.4$	monomer-only $r_{excl} = 1.4$nm	Monomer-only: no interactions
		$E_{max} = 0.00$	$E_{max} = 0.28$	$E_{max} = 0.48$	monomer-only $r_{excl} = 1.4$nm	All n; no interactions
		[T] = 1e-5 rec/nm^2	[T] = 8e-3 rec/nm^2			
2	*Constitutive Dimer*	$n = 2.0$	$n = 2.5$		> 70% *Dimeric Fraction* *Constitutive Dimer*	> 70% *Dimeric Fraction* *Constitutive Dimer*
	$\tilde{E}_{simulated} = 0.70$	$E_{max} = 0.70$	$E_{max} = 0.73$		$\tilde{E}_{best\ fit,n=2} = 0.80$ $\tilde{E}_{best\ fit,n=2} = 0.70$	$\tilde{E}_{best\ fit,n=2} = 0.81 \pm 0.01$ $\tilde{E}_{best\ fit,n=2} = 0.70 \pm 0.01$
3	*Constitutive Trimer*	$n = 2.7$	$n = 3.0$		*Constitutive Oligomer* *Constitutive Oligomer*	*>90% Oligomeric Fraction* *Constitutive Oligomer*
	$\tilde{E}_{simulated} = 0.70$	$E_{max} = 0.80$	$E_{max} = 0.81$		$\tilde{E}_{best\ fit,n=3} = 0.73$ $\tilde{E}_{best\ fit,n=3} = 0.70$	$\tilde{E}_{best\ fit,n=3} = 0.74 \pm 0.01$ $\tilde{E}_{best\ fit,n=3} = 0.70 \pm 0.01$
4	*Constitutive Tetramer*	$n = 2.93$	$n = 3.14$		*Constitutive Oligomer* *Constitutive Oligomer*	*Constitutive Oligomer* *Constitutive Oligomer*
	$\tilde{E}_{simulated} = 0.70$	$E_{max} = 0.81$	$E_{max} = 0.81$		$\tilde{E}_{best\ fit,n=4} = 0.61$ $\tilde{E}_{best\ fit,n=4} = 0.60$	$\tilde{E}_{best\ fitn=4} = 0.61 \pm 0.01$ $\tilde{E}_{best\ fit,n=4} = 0.60 \pm 0.01$

Table 3-2. Combined results for analysis of the constitutive oligomer simulations for dimers (Order = 2), trimers (Order = 3), and tetramers (Order = 4) with the models of Veatch and Stryer and the thermodynamic model based on the Kinetic Theory of FRET, for $\tilde{E} = 0.30$. The analysis with the model of Veatch and Stryer was performed at two different total concentrations: $[T]$=1e-5 rec/nm^2 and $[T]$=8e-3 rec/nm^2, and the best-fit parameters n and E_{max} are provided in the columns. The thermodynamic model based on the Kinetic theory of FRET was used for fitting of simulated FRET data without error for a minimization of the Mean Squared Error(MSE). The **black** text indicates fitting without utilization of a stochastic FRET model and the **blue** text indicates the best-fit results for analysis that includes a stochastic FRET model (see **Equation (2-32)**). Additionally, the reduced chi-square minimization was performed for analysis with the thermodynamic model based on the Kinetic Theory of FRET (N=2,700 data points with added Gaussian-distributed random noise). The rows with **black** text indicate analysis results without utilizing a stochastic FRET model, as with the MSE minimization column, and the **green** text indicates the best-fit reduced chi-squared results for fitting with a stochastic FRET model.

Order	Simulation Values	Veatch & Stryer		Kinetic Theory of FRET	
		[T] = 1e-5 rec/nm^2	[T] = 8e-3 rec/nm^2	MSE Minimization	χ^2_{red} Minimization (+random noise)
2	$\tilde{E}_{simulated} = 0.30$	$n = 2.0$	$n = 2.5$	$>$ 40% *Dimeric Fraction*	$>$ 10% *Dimeric Fractio*
				Constitutive Dimer	*Constitutive Dimer*
	Constitutive Dimer	$E_{max} = 0.30$	$E_{max} = 0.51$	$\tilde{E}_{best\ fit,n=2} = 0.49$	$\tilde{E}_{best\ fit,n=2} = 0.70 \pm 0.01$
				$\tilde{E}_{best\ fit,n=2} = 0.30$	$\tilde{E}_{best\ fit,n=2} = 0.30 \pm 0.01$
3	$\tilde{E}_{simulated} = 0.30$	$n = 2.3$	$n = 2.7$	$>$ 80% *Oligomeric fraction*	$>$ 60% *Oligomeric fraction*
				Constitutive Oligomer	*Constitutive Oligomer*
	Constitutive Trimer	$E_{max} = 0.44$	$E_{max} = 0.54$	$\tilde{E}_{best\ fit,n=3} = 0.38$	$\tilde{E}_{best\ fit,n=3} = 0.36 \pm 0.01$
				$\tilde{E}_{best\ fit,n=3} = 0.30$	$\tilde{E}_{best\ fit,n=3} = 0.30 \pm 0.01$
4	$\tilde{E}_{simulated} = 0.30$	$n = 2.4$	$n = 2.6$	$>$ 90% *Oligomeric fraction*	*Constitutive Oligomer*
				Constitutive Oligomer	*Constitutive Oligomer*
	Constitutive Tetramer	$E_{max} = 0.46$	$E_{max} = 0.53$	$\tilde{E}_{best\ fit,n=4} = 0.26$	$\tilde{E}_{best\ fit,n=4} = 0.26 \pm 0.01$
				$\tilde{E}_{best\ fit,n=4} = 0.24$	$\tilde{E}_{best\ fit,n=4} = 0.24 \pm 0.01$

3-9. Membrane Proteins in Monomer-Dimer Equilibrium

Figure 3-15 and **Figure 3-17** show the results of the monomer-dimer equilibrium simulations, for $\Delta G° = -4.0\ kcal/mol$ and donor-to-acceptor distances corresponding to $\tilde{E} = 0.70$ and $\tilde{E} = 0.30$. In these simulations and Gibbs free energy of dimerization, the dimeric fraction ranges from ~ 0% at the lowest simulated fluorophore density of 1e-5 fluorophores/nm^2, to a maximum of ~80% dimeric fraction at the highest surface densities of 8e-3 fluorphores/nm^2, as shown in **Figure 3-15A**. **Figure 3-15B** shows a sample configuration of monomers and dimers as used in the simulations. **Figure 3-15C** shows the total apparent FRET efficiency and the dimeric FRET efficiency as a function total fluorophore concentration. We see that the oligomeric FRET contribution increases proportionally to the dimeric fraction, and that the total apparent FRET efficiency is substantially higher than the oligomeric FRET for most of the total concentration range.

Figure 3-15D shows E_{app} and the stochastic FRET, E_{prox}, plotted as a function of total concentration. We see that the stochastic FRET contribution comprises a major component of the total apparent FRET efficiency with a maximum of nearly 50% at T = 8e-3 rec/nm^2 and x_A = 0.9. Comparison of the stochastic FRET efficiency and the oligomeric FRET contributions in these two panels shows that they approximately of equal magnitude at the highest total fluorophore surface densities. For the monomer-dimer simulation with $\tilde{E} = 0.30$, the stochastic FRET contribution is even greater than the oligomeric FRET contribution to the total apparent FRET efficiency, as we see in **Figure 3-17A, 3-17B**. In **Figure 3-16A**, the total apparent FRET efficiency and the oligomeric FRET plotted as a function of the acceptor fraction, x_A, for $[T]$ = 1e-5 fluorophores/nm^2 (lower curve), $[T]$ = 4e-3 fluorophores/nm^2 (middle curve) and $[T]$ = 8e-3 fluorophores/nm^2 (upper curve). E_{app} is plotted as black circles, connected by black dashed lines, and E_{Oligo} is plotted as blue circles connected by blue dashed lines. We see that the total concentration, which affects the thermodynamically-driven dimeric fraction, has a distinct effect on the curvature and maximal FRET of the apparent FRET efficiency versus x_A curves. For E_{Oligo}, we see in **Figure 10A** that the lines are straight, but the slope of the lines increases with increasing dimeric fraction.

Figure 3-16B,C depicts the results of the analysis of the monomer-dimer simulated data with the model of Veatch and Stryer (**Equation 2.11**) and the thermodynamic model based on the Kinetic Theory of FRET. **Figure 3-16B** shows the results of the Veatch and Stryer analysis, plotted as red lines. In the Veatch and Stryer analysis, we fit E_{app} vs. acceptor to donor ratio for three values of the total concentration: low, moderate, and high total receptor concentrations as a function of D:A ratio (red lines) for $\tilde{E} = 0.70$ (see **Figure 3-17C** for $\tilde{E} = 0.30$ results). When fitting with the Veatch and Stryer model at the lowest total simulated fluorophore surface density, the best-fit oligomer order is a dimer, $n = 2$, but $E_{max} = 0.01$ occurs because little FRET was measured. For moderate total concentration fitting, we find the best-fit oligomer order is n = 2.3, which properly indicates dimer formation with minimal effect by stochastic FRET on the fit results. However, for fitting the low surface density data $E_{max} = 0.56$, which is not the proper value for $\tilde{E}$. When fitting the highest total fluorophore surface densities, 8e-3 fluorophores/nm^2, the $E_{max} = 0.66$, which is close to the simulated value, $\tilde{E} = 0.70$. The stochastic FRET contribution at this fluorophore surface density is of the same magnitude as the oligomeric FRET contribution to the total measured apparent FRET efficiency, and the additional curvature gives a best-fit n = 2.5, which would incorrectly be interpreted as a trimer. These results are summarized below in **Table 3-3** and in **Table 3-4** for the $\tilde{E} = 0.30$ simulations. For this low value of intrinsic FRET, we see a very similar behavior in the Veatch and Stryer analysis at low, medium and high surface densities. Again, initially dimerization is indicated at low concentration, but at high concentration, the model indicates trimer formation. In both cases of low and high intrinsic FRET, we see that the best-fit parameters give no information about the presence of a concentration-dependent monomer-dimer equilibrium. Furthermore, the seeming dependence of *n* on the total concentration (due to the stochastic FRET contribution *and* the concentration-dependent association) could be interpreted as a concentration dependent change in oligomeric state, with order increasing with total concentration, as we have seen previously.

Figure 3-16C shows the results of the mean-squared error and the reduced chi-square analyses of the $\tilde{E} = 0.70$ monomer-dimer equilibrium simulations with the thermodynamic model based on Kinetic Theory of FRET (**Equation (3-10)**). The results for the low intrinsic FRET, $\tilde{E} = 0.30$, are summarized in **Figure 3-17D**. For the $\tilde{E} = 0.70$ simulations, we see that fitting the E_{app} versus total concentration data without a stochastic FRET contribution leads to a minimum mean-squared error at n = 3, with n = 2 and n = 3 providing similar best-fit MSE values. The best-fit of a trimer, when directly fitting the total apparent FRET efficiency is incorrect, and similar to the results of the Veatch and Stryer model for fitting at high $[T]$, where the stochastic FRET contribution is maximal. If one neglects to fit for higher-order oligomer formation and only looks for dimers, then the best-fit donor-to-acceptor FRET efficiency in the dimer pair, $\tilde{\mathrm{E}} = 0.96$, a non-physical value (see **Table 3-3**). With the appropriate stochastic FRET correction, the minimum MSE for fitting the apparent FRET efficiency becomes very pronounced at n = 2 (see

Figure 3-16C and Table 3-3, and Figure 3-17D and Table 3-4). We also see that the n = 2 model with a stochastic FRET contribution is the only model that passes the reduced chi-squared test at 95% confidence. Thus, the best-fit model is a dimeric state, with proper extraction of ΔG° and $\widetilde{\mathrm{E}}$ from the analysis occurring only when stochastic FRET is properly taken into consideration. The best-fit monomer-dimer equilibrium model parameters for fitting the total apparent FRET efficiency with and without consideration for the stochastic FRET are shown along with the actual, simulated parameters in **Table3-3 and Table 3-4**. For a low value of intrinsic FRET, $\tilde{E} = 0.30$, the reduced chi-square test shows that acceptable fits were found for all n>1. Thus, for a monomer-dimer equilibrium with a low value of the intrinsic FRET < 0.5, a monomer-dimer model will be difficult to distinguish from other monomer-oligomer states.

Finally, I investigated the applicability of a linear approximation to E_{app} as a sum of stochastic and dimeric FRET, **Equation (2-34),** to properly model the simulation predictions for the total apparent FRET efficiency. I utilized the stochastic FRET contribution, as defined in **Equation (2-33)**, in a linear sum with the oligomeric FRET for the monomer-dimer simulations described here with $\tilde{E} = 0.30$ and $\tilde{E} = 0.70$. **Figure 3-18** shows E_{app} and the linear approximation as a function of total concentration. The area shaded in green in **Figure 3-18** shows the acceptable (<10% error in E_{app}) region for the linear approximation. We see that at low concentrations and low acceptor fractions, the linear approximation, **Equation (2-34))** models the total apparent FRET relatively well, while for high acceptor fractions and moderate surface densities, the linear approximations overestimate the total apparent FRET efficiency. The linear approximation has a wider range of applicability for low intrinsic FRET values, as can be seen by comparing the x_A

coverage of the shaded regions in **Figure 3-18**. As mentioned in the previous chapter, now that I have developed the full description of the total apparent FRET efficiency as defined in **Equation 2-32**, and we know that with a library of stochastic FRET estimations we can extract the true physical parameters for dimerization, there is no need further need for this approximation.

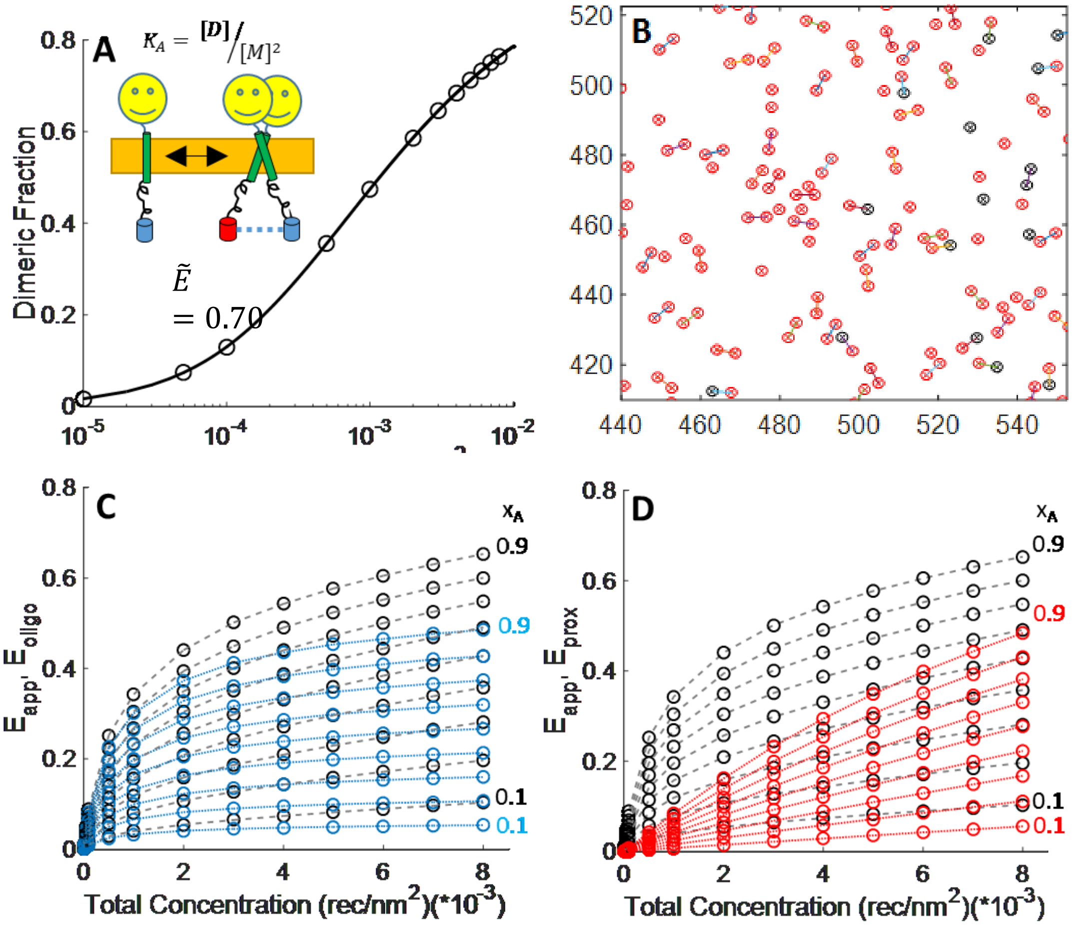

Figure 3-15. Predictions of the monomer-dimer simulation, $\tilde{E} = 0.70$. **A.** The dimeric fraction utilized in the monomer-dimer simulation ranges from ~0 % to ~80%. **B.** A sample configuration with a mixture of monomers and dimers at $[T]$ = 8e-3 fluorophores/nm^2 is shown. Dimers are represented by circles with a connecting line. Donors: blue, acceptors: red. Figure is drawn to scale, axes units are in nm. **C.** E_{app} (black circles) and E_{prox} (red circles) are plotted as a function of the total fluorophore concentration. **D.** E_{app} and E_{Oligo} (black and blue circles, respectively) vs $[T]$. The dashed lines connect data points at constant acceptor fraction, x_A, as indicated by the numbers on the right.

Figure 3-16. Analysis results of the monomer-dimer simulations, $\widetilde{\mathrm{E}} = 0.70$. **A.** $\mathrm{E_{app}}$ and $\mathrm{E_{Oligo}}$ vs. acceptor fraction for [T] = 0.008 rec/nm^2 (top), [T] = 0.004 rec/nm^2(middle), and [T] = 0.00001 rec/nm^2 (black circles, blue circles respectively). Dashed lines connect data points at constant [T], as indicated. **B.** $\mathrm{E_{app}}$ versus A:D ratio for [T] = 0.00001 rec/nm^2 (low), [T] = 0.004 rec/nm^2(middle), and [T] = 0.008 rec/nm^2 (high) as black circles. Dashed lines connect data points of constant [T, as indicated]. The best-fit Veatch and Stryer model is shown in red. **C.** The best-fit MSE (left axis) versus oligomer order for the analysis of $\mathrm{E_{app}}$ with the thermodynamic model based Kinetic Theory of FRET, without a stochastic FRET contribution (black circles). The blue circles mark the best-fit MSE for fitting $\mathrm{E_{app}}$ with a stochastic FRET contribution as in **Equation (2-32)**. Without a stochastic FRET model, the best-fit MSE is $n = 3$. With a stochastic FRET model, the best-fit MSE occurs at n=2. Right axis: The best-fit reduced chi-square versus oligomer order for the analysis of $\mathrm{E_{app}}$ in the presence of random noise with the thermodynamic model based Kinetic Theory of FRET, without a stochastic FRET contribution (black X's). The green X's mark the best-fit reduced chi-square value for fitting $\mathrm{E_{app}}$ in the presence of random noise with while including a stochastic FRET contribution, as in **Equation (2-32)**. The magenta line is the 95% confidence cutoff for the reduced chi-square test- all X's above this line are rejected and all X's below this line are accepted as equally likely models, given the data and its associated error. Analysis without a stochastic FRET contribution does not produce acceptable models for any order. Analysis with the stochastic FRET consideration shows that the $n = 2$ model is the only model that passes the reduced chi-square test.

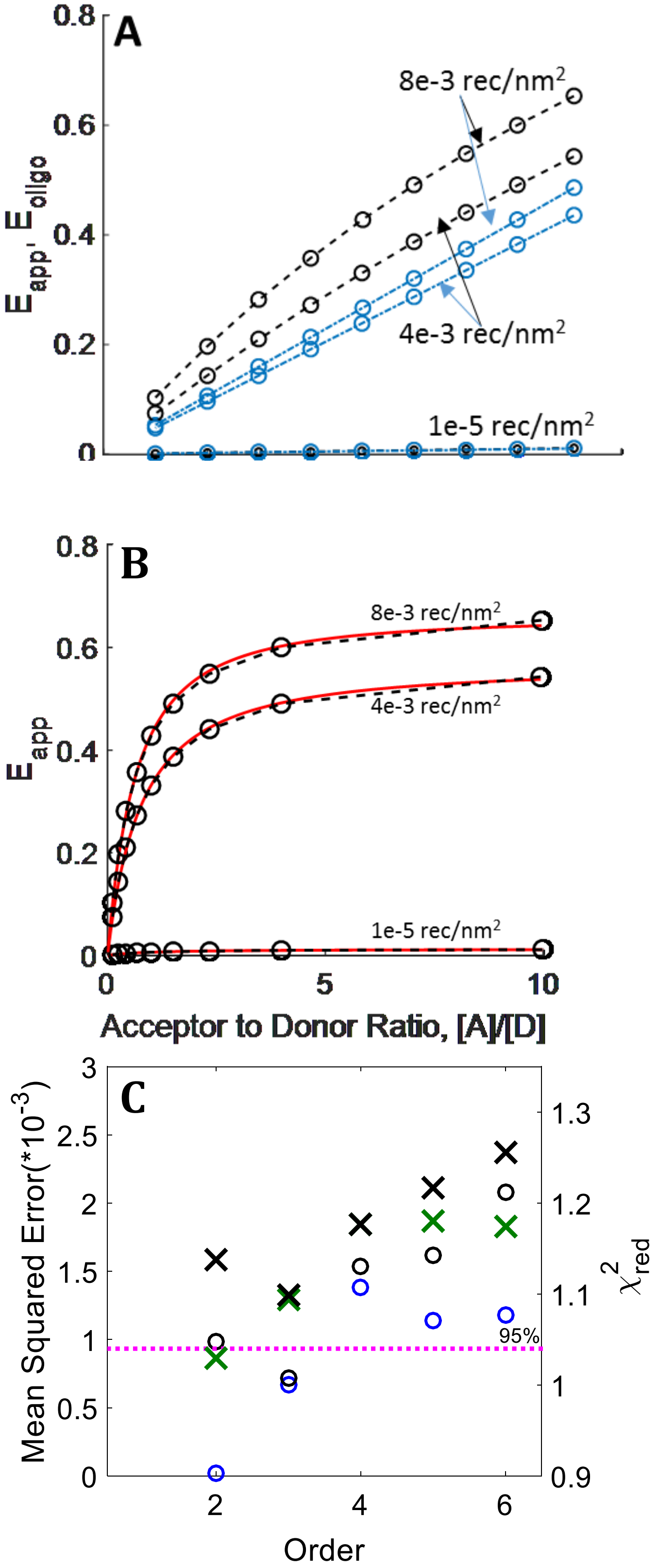
A
0.8
0.6
0.4
0.2
0
E_{app}, E_{oligo}
8e-3 rec/nm^2
4e-3 rec/nm^2
1e-5 rec/nm^2
B
0.8
0.6
0.4
0.2
0
E_{app}
8e-3 rec/nm^2
4e-3 rec/nm^2
1e-5 rec/nm^2
0
5
10
Acceptor to Donor Ratio, [A]/[D]
C
3
2.5
2
1.5
1
0.5
0
Mean Squared Error(*10^{-3})
1.3
1.2
1.1
1
0.9
χ^2_{red}
95%
2
4
6
Order

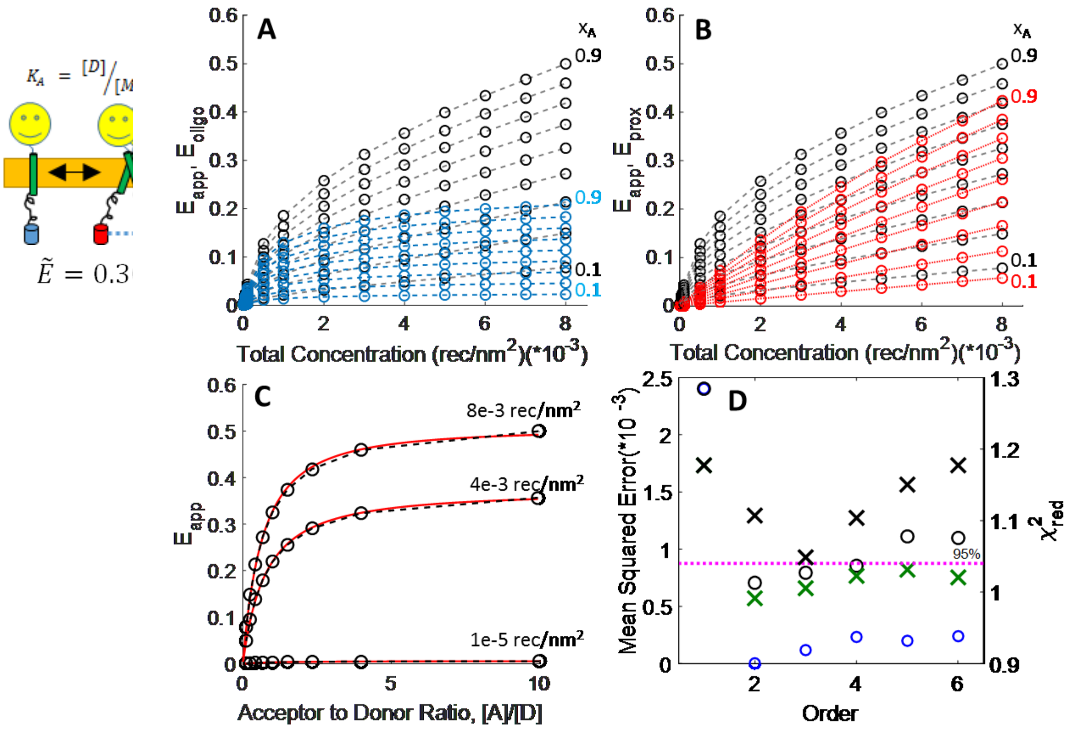

Figure 3-17. The predictions of the monomer-dimer simulations and the results of the analyses, for $\tilde{E} = 0.30$, $\Delta G^\circ = -4\ kcal/mol$ **A.** E_{app} (black circles) and E_{Oligo} (blue circles) versus total concentration. The dashed lines connect data points of constant acceptor fraction, as indicated on the right. **B.** E_{app} (black circles) and E_{prox} (red circles) versus total concentration. **C.** E_{app} (black circles) versus A:D ratio, and the best-fit Veatch and Streyer model, for $[T]$ = 1e-5 rec/nm^2, and $[T]$ = 8e-3 rec/nm^2 (lower, upper curves, respectively). **D.** The best-fit MSE(left axis, circles) and reduced chi-square value (right axis, X's) versus oligomer order for the analysis of E_{app} with the thermodynamic model based on the Kinetic Theory of FRET with a stochastic FRET contribution (blue circles, green X's), and without a stochastic FRET contribution (black circles, black X's). Without a stochastic FRET consideration, the best-fit MSE indicates trmers, but when a stochastic FRET model is included in the analysis, the best-fit MSE indicates n = 2. The magenta line denotes the 95% confidence limit for the reduced chi-square test (X's, right axis). In the presence of random noise, all models without a stochastic FRET contribution fail the reduced chi-square test, and all n>1 provide acceptable fits to the data when a stochastic FRET contribution is included. The overall reduced chi-square minimum is $n = 2$ for the green X's, however the oligomer order is not discernable for this dataset.

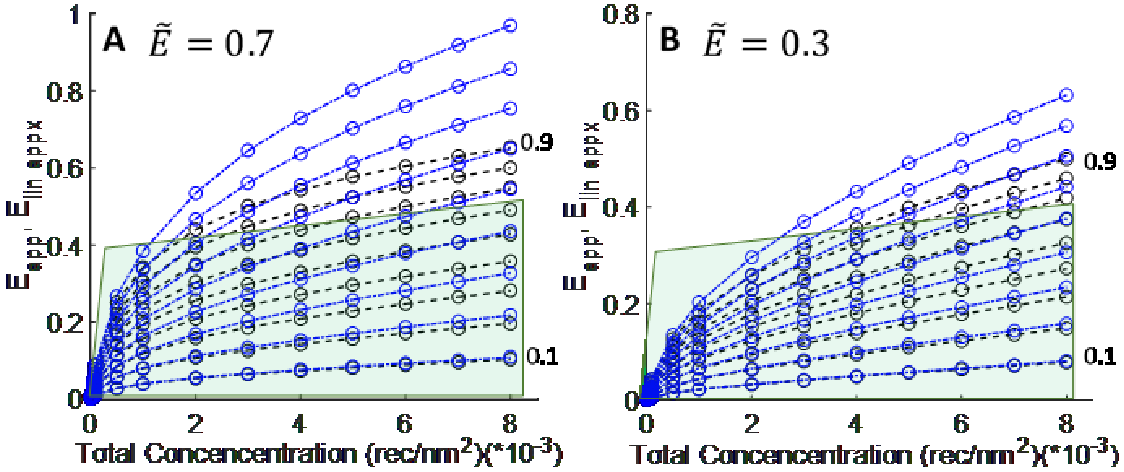

Figure 3-18. The predictions of the monomer-dimer simulations as a function of total concentration for $\tilde{E} = 0.70$ (panel A) and $\tilde{E} = 0.30.$ (panel B), plotted as black circles. The linear approximation, $E_{app} = E_{prox} + E_{oligo}$,, as a function of total concentration is plotted as blue circles. The dashed lines connect data points of constant acceptor fraction, x_A, as indicated on the right. The green shaded areas represent the regions of applicability of the linear approximation, **Equation (2-34)**.

3-10. Membrane Proteins in a Monomer-Tetramer Equilibrium

Figure 3-18 and **Figure 3-20** show the results for the case of a non-constitutive tetramerization of membrane proteins. We utilized the geometry square tetramers, where the fluorophores on a side of the square are separated by a distance corresponding to $\tilde{E} = 0.70$, or 4.7 nm, and $\tilde{E} = 0.30$ for a side-length of 6.3 nm. Similarly to the monomer-dimer simulations, the monomer-tetramer equilibrium constant was set corresponding to a $\Delta G° = -12.0\ kcal/mol$, such that the fraction of tetramers ranges from ~0% at the lowest simulated surface density, $[T]$ = 1e-5 fluorophores/nm^2, to a maximum of near ~80% at the surface density of 8e-3 fluorophores/nm^2, the highest simulated concentration, as shown in **Figure 3-18A**. A sample configuration from the simulations at the maximum simulated fluorophore concentration is shown in **Figure 3-18B.**

The predictions of the monomer-tetramer simulation for $\tilde{E} = 0.70$ are shown in **Figures 3-18C, D** and **Figure 3-20A, B** for $\tilde{E} = 0.30$. In **Figure 3-18C**, we see that the total apparent FRET efficiency (black circles) ranges from zero at the lowest simulated concentration (with zero tetrameric fraction) to a maximum at the highest simulated fluorophore surface densities (~80% tetrameric fraction). The oligomeric FRET, plotted in blue circles, also increases with the total concentration, as the increase drives tetramer formation and a higher tetrameric fraction. In **Figure 3-18D**, we see E_{app} plotted as a function of total concentration (black circles) alongside the stochastic FRET contribution, Eprox (red circles). Comparing the stochastic FRET in **Figure 3-18D** to that of the constitutive tetramer simulation predictions, shown in **Figure 3-11C**, we see that the presence of monomers greatly increases the stochastic FRET contribution (red circles) to the total apparent FRET efficiency (black circles), similarly to the monomer-dimer simulations.

In **Figure 3-19A**, I've plotted the total apparent FRET efficiency data as a function of acceptor for three total concentrations of fluorophores: low at 1e-5 fluorophores/nm^2, moderate at 4e-3 fluorophores/nm^2, and high at 8e-3 fluorophores/nm^2 (see **Equation 2-11**). Examination of **Figure 3-19A** shows the effect of concentration-dependent oligomerization on the curvature of the apparent FRET efficiency vs acceptor ratio is drastic: at low concentration, the total apparent FRET efficiency is ~0 for all A:D ratios, while at high concentration, the high surface densities of tetrameric fluorophores leads to a higher curvature.

Figure 3-19B, C summarizes the results of analysis of the monomer-tetramer simulation data with the model of Veatch and Stryer, and the thermodynamic model based on the Kinetic Theory of FRET. The best-fit models for the Veatch and Stryer analysis are shown in **Figure 3-19B** and **Figure 3-20C**, with the results summarized in **Table 3-3 and Table 3-4** for $\tilde{E} = 0.70$ and $\tilde{E} = 0.30$, respectively. We see that at low concentrations, the lack of FRET means there is no useable signal, $E_{max} = 0.0$, and at high concentrations we fail to identify a proper oligomer order of four, and instead measure trimer formation with n = 3.1. Additionally, as with the monomer-dimer simulation analysis, the Veatch and Stryer model gives no indication about the presence of monomers.

Figure 3-19C shows the best-fit MSEs for the thermodynamic model (**Equation (3-10)**) as a function of oligomer order, with and without a stochastic FRET contribution (left axis, black and blue circles, respectively). Also shown in **Figure 3-19C** is the result of the reduced chi-squared analysis with and without a stochastic FRET contribution (green, black X's respectively) as a function of oligomer order (right axis). We see that the best-fit MSE values are all essentially equal for n > 2, indicating that the different oligomeric models fit the data almost equally well, with or without a stochastic FRET contribution in the model. We also see that the n = 3 and n = 4 models give essential equal reduced chi-square values, both under the 95% cutoff. Despite the fact that the oligomer order is not well-determined with a monomer-oligomer thermodynamic association, we find that the oligomeric fraction is still obtainable, with essentially the proper concentration-dependent oligomeric fraction determined whether fitting E_{app} with or without a stochastic FRET contribution, for any n > 2. The best-fit parameters for the n = 4 analysis are shown in **Table 3-3** and **Table 3-4**, for $\tilde{E} = 0.70$ and $\tilde{E} = 0.30$, respectively. We see that the best-fit Gibbs free energy is equal, within error, to the simulated value $\Delta G° = -12.0\ kcal/mol$. Additionally, the best-fit intrinsic FRET, $\tilde{E} = 0.59$, is lower than modeled, but is an expected consequence of the single D-A distance in the simplified Kinetic Theory of FRET. This occurs with a square geometry due to the increased distance across the center of the square.

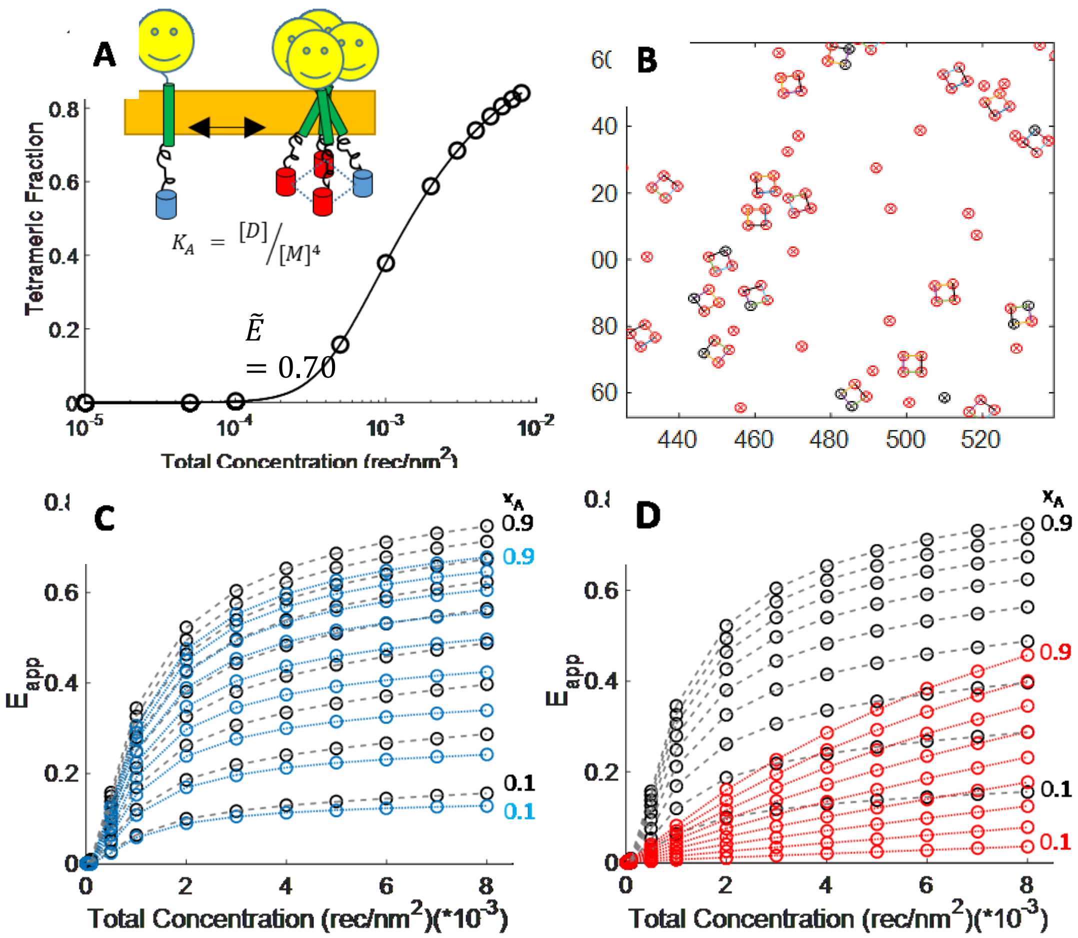

Figure 3-18. The results of the monomer-tetramer simulations, for $\tilde{E} = 0.70$. **A.** The tetrameric fraction as a function of total receptor surface density. **B.** A sample configuration from the simulations at [T] = 0.008 rec/nm^2. Donors: blue cirles, Acceptors: red cirles. **C.** E_{app} and E_{Oligo} versus total concentration (black and blue circles, respectively). **D.** E_{app} and E_{prox} versus total concentration (black and red circles, respectively). The dashed lines connect datapoints of constant x_A, as indicated on the right.

Figure 3-19. Analysis results of the monomer-tetramer simulations, for $\widetilde{\mathrm{E}} = 0.70$. **A.** $\mathrm{E_{app}}$ (black circles) and $\mathrm{E_{Oligo}}$ (blue circles)versus acceptor fraction, $\mathrm{x_A}$, for [T] = 0.008 rec/nm^2(top), [T] = 0.004 rec/nm^2 (middle), and [T] = 0.00001 rec/nm^2 (lower). Dashed lines connect data points with constant [T] as indicated. **B.** $\mathrm{E_{app}}$ versus A:D ratio plotted as black circles for [T] = 0.008 rec/nm^2(top), [T] = 0.004 rec/nm^2 (middle), and [T] = 0.00001 rec/nm^2 (lower). Dashed lines connect data points with constant [T]. The red lines represent the best-fit Veatch and Stryer models. **C.** The best-fit MSE (left axis) versus oligomer order for the analysis of $\mathrm{E_{app}}$ with the thermodynamic model based Kinetic Theory of FRET, without a stochastic FRET contribution (black circles). The blue circles mark the best-fit MSE for fitting $\mathrm{E_{app}}$ with a stochastic FRET contribution as in **Equation (2-32)**. Without a stochastic FRET model, the best-fit MSE is $n = 3$. With a stochastic FRET model, the best-fit MSE occurs at $n = 4$. Right axis: The best-fit reduced chi-square versus oligomer order for the analysis of $\mathrm{E_{app}}$ in the presence of random noise with the thermodynamic model based Kinetic Theory of FRET, without a stochastic FRET contribution (black X's). The green X's mark the best-fit reduced chi-square value for fitting $\mathrm{E_{app}}$ in the presence of random noise with while including a stochastic FRET contribution, as in **Equation (2.32)**. The magenta line is the 95% confidence cutoff for the reduced chi-square test- all X's above this line are rejected and all X's below this line are accepted as equally likely models, given the data and its associated error. Analysis without a stochastic FRET contribution does not produce acceptable models for any order. Analysis with the stochastic FRET consideration shows that the $n = 3$ and $n = 4$ models both pass the reduced chi-square test. Thus, the oligomer order is not discernable for this data set.

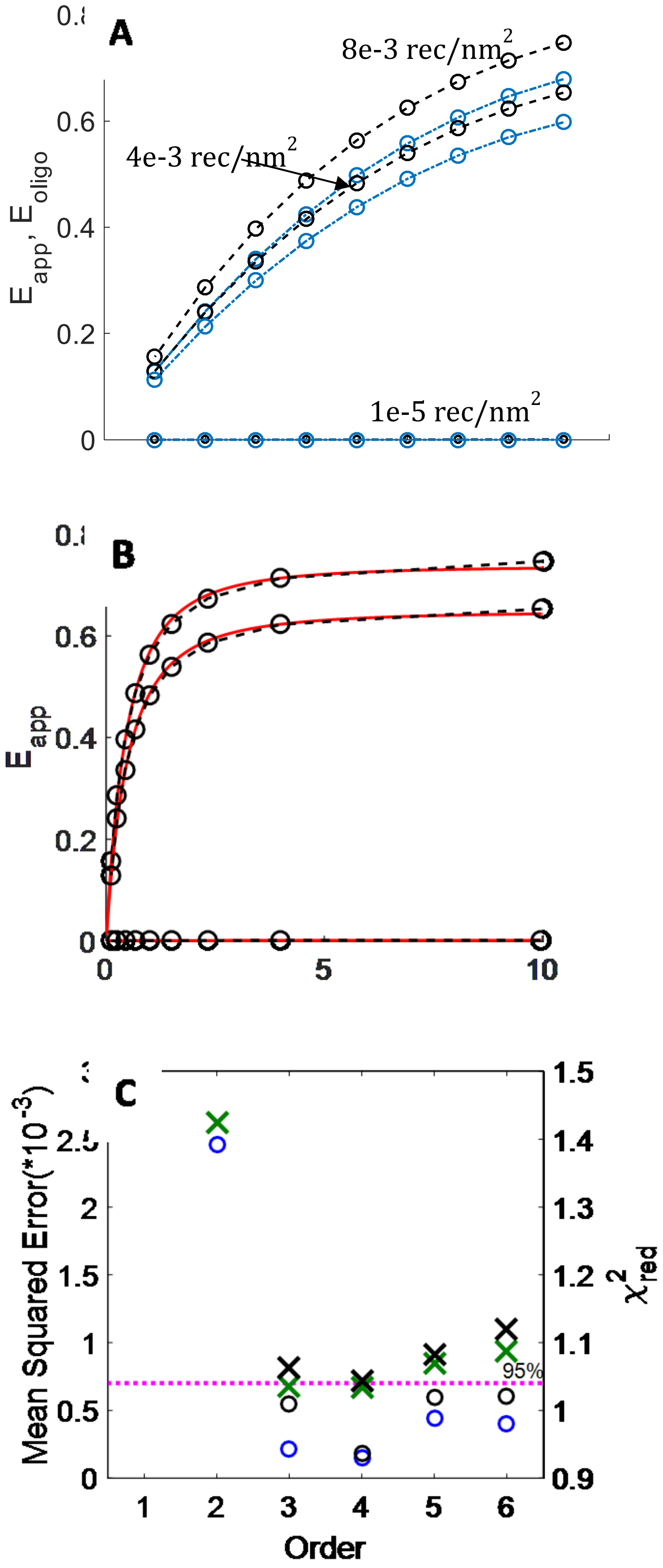A
8e-3 rec/nm^2
4e-3 rec/nm^2
1e-5 rec/nm^2
E_{app}, E_{oligo}
0.6
0.4
0.2
0
B
E_{app}
0.6
0.4
0.2
0
0
5
10
C
Mean Squared Error(*10^{-3})
2.5
2
1.5
1
0.5
0
1.5
1.4
1.3
1.2
1.1
1
0.9
χ^2_{red}
95%
1
2
3
4
5
6
Order

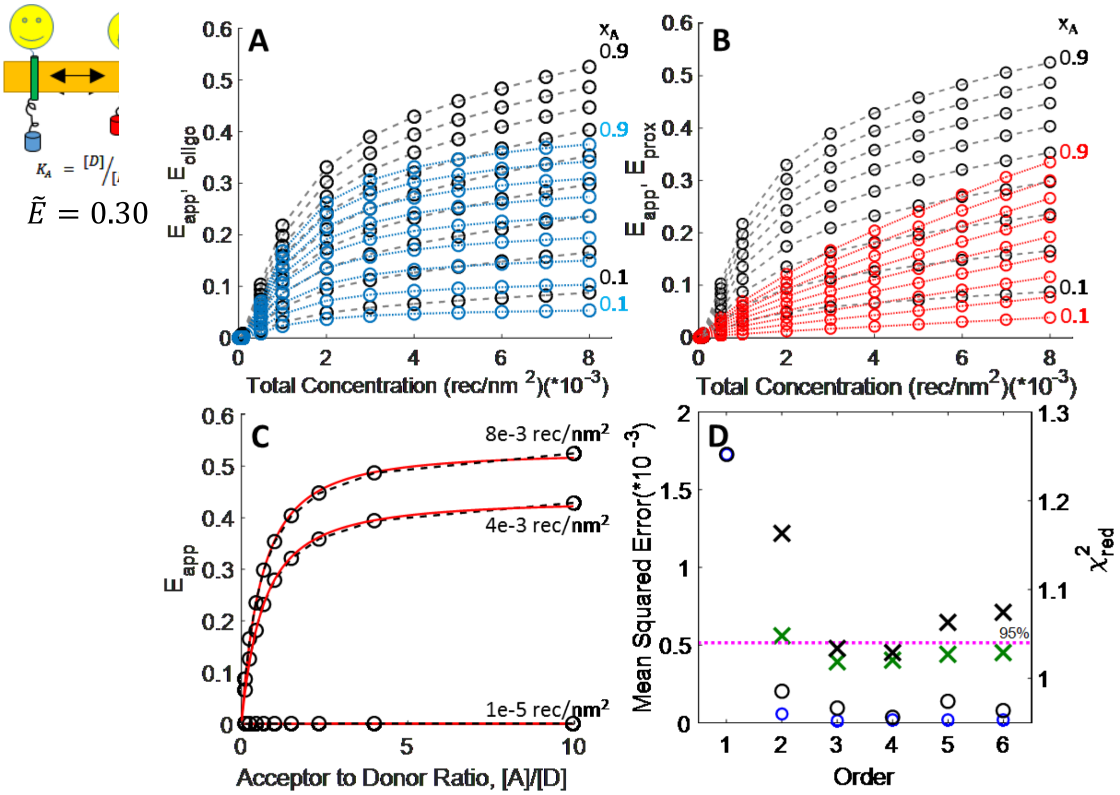

Figure 3-20. The predictions of the monomer-tetramer simulations and the results of the analyses, for $\tilde{E} = 0.30$, $\Delta G° = -12\ kcal/mol$ **A.** E_{app} (black circles) and E_{Oligo} (blue circles) versus total concentration. The dashed lines connect data points of constant acceptor fraction, as indicated on the right. **B.** E_{app} (black circles) and E_{prox} (red circles) versus total concentration. **C.** E_{app} (black circles) versus A:D ratio, and the best-fit Veatch and Streyer model, for $[T]$ = 1e-5 rec/nm^2, and $[T]$ = 8e-3 rec/nm^2 (lower, upper curves, respectively). **D.** The best-fit MSE(left axis, circles) and reduced chi-square value (right axis, X's) versus oligomer order for the analysis of E_{app} with the thermodynamic model based on the Kinetic Theory of FRET with a stochastic FRET contribution (blue circles, green X's), and without a stochastic FRET contribution (black circles, black X's). The magenta line denotes the 95% confidence limit for the reduced chi-square test (X's, right axis). In the presence of random noise, n=3 and n=4 models without a stochastic FRET contribution both pass the reduced chi-square test, and all n>2 provide acceptable fits to the data when a stochastic FRET contribution is included. Thus, the oligomer order is not discernable for this monomer-tetramer equilibrium dataset.

Order	Simulation Values	Veatch & Stryer			Kinetic Theory of FRET	
		[T] = 1e-5 rec/nm^2	[T] = 4e-3 rec/nm^2	[T] = 8e-3 rec/nm^2	MSE Minimization	χ^2_{red} Minimization (+random noise)
1-2	$\Delta G^\circ_{simulated} = -4.0\ kcal/mol$	$n = 2.0$	$n = 2.3$	$n = 2.5$	$\Delta G^\circ_{best\ fit,n=2} = -3.9\ kcal/mol$	$\Delta G^\circ_{best\ fit,n=2} = -3.9 \pm 0.1\ kcal/mol$
					$\Delta G^\circ_{best\ fit,n=2} = -4.0\ kcal/mol$	$\Delta G^\circ_{best\ fit,n=2} = -4.0 \pm 0.1\ kcal/mol$
	$\tilde{E}_{simulated} = 0.70$	$E_{max} = 0.01$	$E_{max} = 0.56$	$E_{max} = 0.66$	$\tilde{E}_{best\ fit,n=2} = 0.96$	$\tilde{E}_{best\ fit,n=2} = 0.95 \pm 0.01$
					$\tilde{E}_{best\ fit,n=2} = 0.70$	$\tilde{E}_{best\ fit,n=2} = 0.70 \pm 0.01$
1-4	$\Delta G^\circ_{simulated} = -12.0\ kcal/mol$	$n = 2.0$	$n = 3.0$	$n = 3.1$	$\Delta G^\circ_{best\ fit,n=4} = -12.0\ kcal/mol$	$\Delta G^\circ_{best\ fit,n=4} = -12.0 \pm 0.1\ kcal/mol$
					$\Delta G^\circ_{best\ fit,n=4} = -12.0\ kcal/mol$	$\Delta G^\circ_{best\ fit,n=4} = -12.1 \pm 0.1\ kcal/mol$
	$\tilde{E}_{simulated} = 0.70$	$E_{max} = 0.00$	$E_{max} = 0.64$	$E_{max} = 0.74$	$\tilde{E}_{best\ fit,n=4} = 0.69$	$\tilde{E}_{best\ fit,n=4} = 0.68 \pm 0.01$
					$\tilde{E}_{best\ fit,n=4} = 0.59$	$\tilde{E}_{best\ fit,n=4} = 0.59 \pm 0.01$

Table 3-3. Combined results for analysis of simulations for monomers-dimer (Order = 1-2) and monomer-tetramer (Order = 1-4) equilibria with the models of Veatch and Stryer and the thermodynamic model based on the Kinetic Theory of FRET, for $\tilde{E} = 0.70$. The analysis with the model of Veatch and Stryer was performed at two different total concentrations: $[T]$=1e-5 rec/nm^2 and $[T]$=8e-3 rec/nm^2, and the best-fit parameters n and E_{max} are provided in the columns. The thermodynamic model based on the Kinetic theory of FRET was used for fitting of simulated FRET data without error for a minimization of the Mean Squared Error(MSE). The **black** text indicates fitting without utilization of a stochastic FRET model and the **blue** text indicates the best-fit results for analysis that includes a stochastic FRET model (see **Equation (2-32)**). Additionally, the reduced chi-square minimization was performed for analysis with the thermodynamic model based on the Kinetic Theory of FRET (N=2,700 data points with added Gaussian-distributed random noise). The rows with **black** text indicate analysis results without utilizing a stochastic FRET model, as with the MSE minimization column, and the **green** text indicates the best-fit reduced chi-squared results for fitting with a stochastic FRET model.

Order	Simulation Values	Veatch & Stryer			Kinetic Theory of FRET	
		[T] = 1e-5 rec/nm^2	[T] = 4e-3 rec/nm^2	[T] = 8e-3 rec/nm^2	MSE Minimization	χ^2_{red} Minimization (+random noise)
1-2	$\Delta G^\circ_{simulated} = -4.00\ kcal/mol$	$n = 2.0$	$n = 2.3$	$n = 2.5$	$\Delta G^\circ_{best\ fit,n=2} = -3.4\ kcal/mol$	$\Delta G^\circ_{best\ fit,n=2} = -3.4 \pm 0.2\ kcal/mol$
					$\Delta G^\circ_{best\ fit} = -4.0\ kcal/mol$	$\Delta G^\circ_{best\ fit,n=2} = -4.0 \pm 0.1\ kcal/mol$
	$\tilde{E}_{simulated} = 0.30$	$E_{max} = 0.01$	$E_{max} = 0.37$	$E_{max} = 0.51$	$\tilde{E}_{best\ fit,n=2} = 0.81$	$\tilde{E}_{best\ fit,n=2} = 0.79 \pm 0.01$
					$\tilde{E}_{best\ fit} = 0.30$	$\tilde{E}_{best\ fit,n=2} = 0.29 \pm 0.01$
1-4	$\Delta G^\circ_{simulated} = -12.0\ kcal/mol$	$n = 2.0$	$n = 2.5$	$n = 2.6$	$\Delta G^\circ_{best\ fit,n=4} = -11.9\ kcal/mol$	$\Delta G^\circ_{best\ fit,n=4} = -11.9 \pm 0.1\ kcal/mol$
					$\Delta G^\circ_{best\ fit,n=4} = -12.1\ kcal/mol$	$\Delta G^\circ_{best\ fit,n=4} = -12.0 \pm 0.2\ kcal/mol$
	$\tilde{E}_{simulated} = 0.30$	$E_{max} = 0.00$	$E_{max} = 0.43$	$E_{max} = 0.52$	$\tilde{E}_{best\ fit,n=4} = 0.35$	$\tilde{E}_{best\ fit,n=4} = 0.35 \pm 0.02$
					$\tilde{E}_{best\ fit,n=4} = 0.20$	$\tilde{E}_{best\ fit,n=4} = 0.21 \pm 0.01$

Table 3-4. Combined results for analysis of simulations for monomers-dimer (Order = 1-2) and monomer-tetramer (Order = 1-4) equilibria with the models of Veatch and Stryer and the thermodynamic model based on the Kinetic Theory of FRET, for $\tilde{E} = 0.30$. The analysis with the model of Veatch and Stryer was performed at two different total concentrations: $[T]$=1e-5 rec/nm^2 and $[T]$=8e-3 rec/nm^2, and the best-fit parameters n and E_{max} are provided in the columns. The thermodynamic model based on the Kinetic theory of FRET was used for fitting of simulated FRET data without error for a minimization of the Mean Squared Error(MSE). The **black** text indicates fitting without utilization of a stochastic FRET model and the **blue** text indicates the best-fit results for analysis that includes a stochastic FRET model (see **Equation (2-32)**). Additionally, the reduced chi-square minimization was performed for analysis with the thermodynamic model based on the Kinetic Theory of FRET (N=2,700 data points with added Gaussian-distributed random noise). The rows with **black** text indicate analysis results without utilizing a stochastic FRET model, as with the MSE minimization column, and the **green** text indicates the best-fit reduced chi-squared results for fitting with a stochastic FRET model.

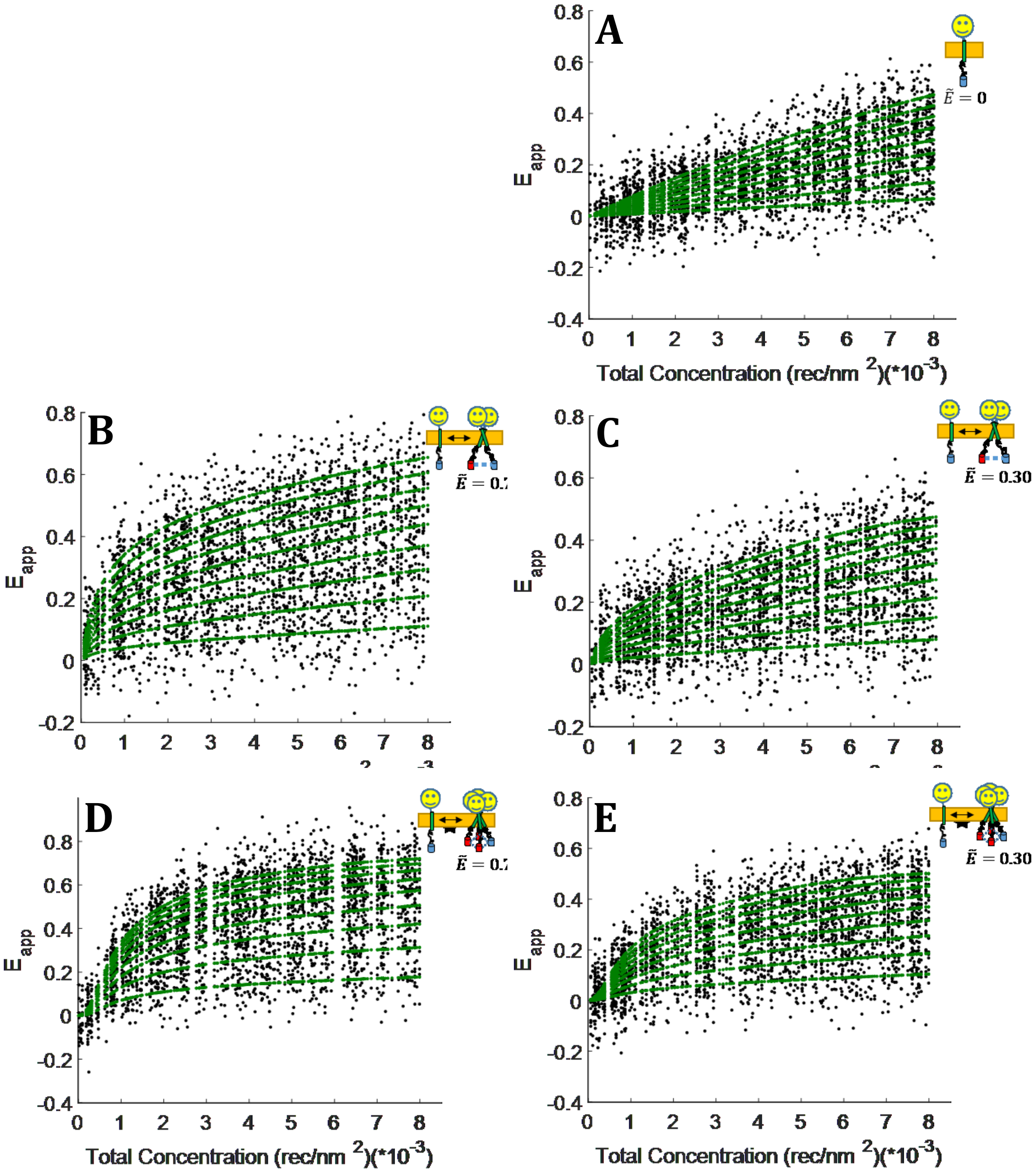

Figure 3-21. Monomer-only, monomer-dimer, and monomer-tetramer simulated data (black dots) and best-fit model (green dots) of the simulated oligomer order for N = 2700 datapoints at randomly chosen total concentrations, with acceptor fraction ranging from 0.1 – 0.9 in 0.1 steps. Gaussian distributed random noise, $\mu = 0, \sigma = 0.08$, was added to each data point prior to analysis with the reduced chi-squared test. **A.** Simulated data and best-fit monomeric model. **B.** Simulated data and best-fit monomer-dimer model for $\tilde{E} = 0.70$. **C.** Simulated data and best-fit monomer-dimer model for $\tilde{E} = 0.30$. **D.** Simulated data and best-fit monomer-tetramer model for $\tilde{E} = 0.70$. **E.** Simulated data and best-fit monomer-tetramer model for $\tilde{E} = 0.30$.

3-11. The Non-Unique FRET of Higher-Order Oligomers

Figure 3-22 compares the total apparent FRET efficiency, as a function of total concentration, for the cases of constitutive trimers ($\tilde{E} = 0.74$), tetramers ($\tilde{E} = 0.70$), and pentamers ($\tilde{E} = 0.74$). We see that the total apparent FRET efficiency for all of these oligomers is nearly the same, with a maximum deviation of less than 3%. Thus, the total apparent FRET efficiency for higher-order oligomerization is not unique for $n > 2$, and no amount of data points can ever determine the oligomer order for $n > 2$ in a two-color static quenching FRET experiment. For $\tilde{E} < 0.5$, even dimerization does not provide a unique FRET signature. Thus, the indeterminacy of the analysis for trimers and tetramers, and for all orders with low intrinsic FRET, observed earlier is not only due to the assumption of a single donor-acceptor distance in the simplified Kinetic Theory of Oligomeric FRET, but also due to the non-uniqueness of the total apparent FRET efficiency.

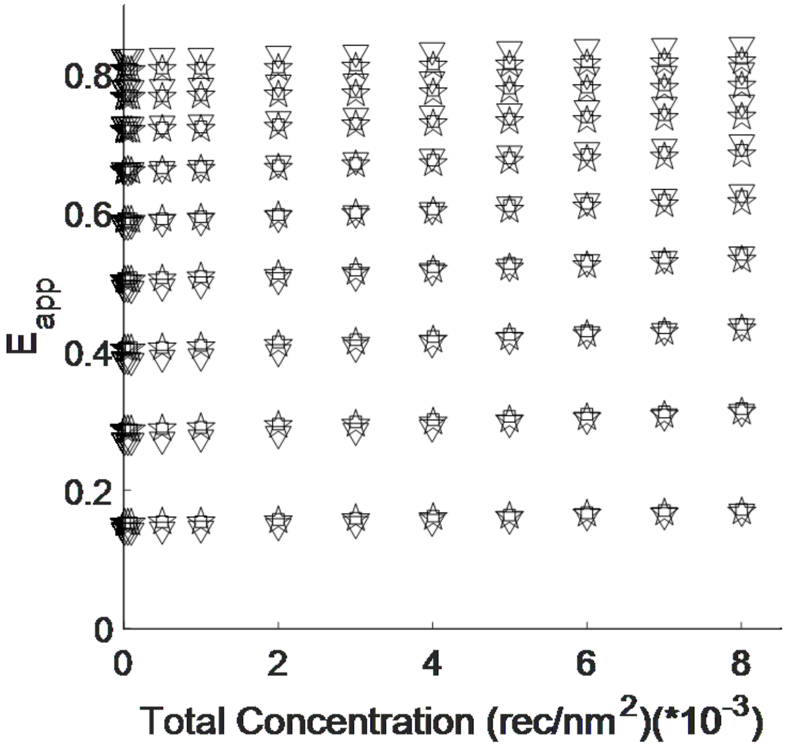

Figure 3-22. The total apparent FRET efficiency for higher-order oligomerization is not unique. Here I simulated constitutive trimers, tetramers, and pentamers and compare the results. The total apparent FRET efficiency as a function of total concentration for trimers, $\tilde{E} = 0.74$, plotted as triangles, constitutive tetramers and constitutive pentamers, $\tilde{E} = 0.70$, plotted as squares and stars, respectively.

3-12. Conclusions

In this chapter, I simulated the total apparent FRET efficiency for ensembles of non-overlapping fluorophores organized as monomers, dimers, trimers, tetramers, a total concentration-based monomer-dimer equilibrium, and a total concentration-based monomer-tetramer equilibrium over a range of physically realizable membrane protein surface densities. I then subjected the total apparent FRET efficiency, as would be measured in a donor-quenched static FRET efficiency measurement, to analysis with the two primary models available for use by researchers to analyze FRET data.

My goal for this work is to understand the consequences of ignoring the stochastic FRET in each case of higher-order oligomer formation ($n > 1$) with respect to analysis results, and the limitations of each model to correctly describe the intrinsic FRET efficiency, oligomeric fraction, and the oligomer order. I performed simulations of FRET in the ideal situation which lacks experimental error and complications from assumptions about kappa-squared in the Förster radius. I also attempted to minimize the complications of oligomer geometry by choosing regular polygons, the most ideal geometry for both the Kinetic Theory of Oligomeric FRET and the model of Veatch and Stryer. When the oligomeric geometries deviate from the ideal polygon, the assumption of the single D:A distance in the oligomer found in both the Veatch and Streyer model and the model of the Kinetic Thoery of FRET becomes less and less realistic.

The model of Veatch and Stryer is often utilized by researchers performing semi-quantitative FRET experiments on membrane proteins, in which the total surface density of labeled membrane proteins is unknown, but the donor to acceptor ratio is known either through experimental design or measurement. I find that, in general, if one does not know the oligomer order before the experiment, the model of Veatch and Stryer will give the researcher confusing and usually incorrect oligomer results. Of particular surprise was the fact that for monomers, the model indicated dimer formation. In the case of a constitutive dimer, the model of Veatch and Stryer will provide a correct result if the concentration is kept at a minimum to minimize the stochastic FRET contribution, but fitting of the total apparent FRET efficiency at high fluorophore surface densities leads to an indication of trimer formation by the model, due to the non-negligible stochastic FRET contribution. If the acceptor concentrations are not known, then it is not possible to make an appropriate stochastic FRET correction to the apparent FRET efficiency, or to even know if one is even in a regime of surface densities and acceptor fractions in which the stochastic FRET contribution is minimal. Thus, I find that this model has severe limitations for the analysis of static quenching FRET experiments to determine dimerization or higher order oligomerization and should never be used for data interpretation. Thus, even though the model of Veatch and Stryer is simple, it is not capable of properly modeling FRET.

Only recently (in 2007), the Kinetic Theory of Oligomeric FRET was derived which accounts for the thermodynamically driven oligomer concentration and the oligomeric architecture, along with a combinatorial mixing contribution. However, one needs to know the geometry of the oligomer in order to use the full Kinetic Theory of Oligomeric FRET. This information is not known for most membrane proteins under study. Fortunately, a simplified theory, with the assumption of equal donor-to-acceptor distances in the oligomer (an assumption that is true for dimers and the trimers utilized in this work) is available.

I have found that in general, and despite the assumption of a single D:A distance in the oligomer, the simplified Kinetic Theory of Oligomeric FRET can provide the researcher with the proper oligomer order, association energetics, and intrinsic FRET efficiency when used with a stochastic FRET estimation in the Full Kinetic Theory of FRET. The monomer-only simulation results highlight the importance of checking all possible models for their fits to the data. We see that for dimer formation, the magnitude of the stochastic FRET contribution means that it cannot be ignored in the analysis. Thus, with the case of a monomer-dimer equilibrium or a constitutive dimer, a model for the total stochastic FRET efficiency is necessary to determine the proper association constant and intrinsic FRET efficiency value (D:A distance in the dimer). Unfortunately, this model is only available through the use of computer simulation, but fortunately, it is rather easy to estimate with a computer (**see Computational Methods**). All scientists today should be proficient enough with a computer to recreate these results. With higher-order oligomer formation, $n > 3$, analysis of the total apparent FRET efficiency and with and without a stochastic FRET contribution yielded essentially the same results, indicating that the stochastic FRET contribution is negligible with respect to analysis for these situations. Interestingly, even though the oligomer order was not discernable for higher-order oligomer formation, the best-fit oligomeric fraction determined for each oligomer order > 2 closely matched the simulated tetrameric fraction in the case of the monomer-tetramer equilibrium predictions analysis.

This work shows that the total concentration information must be known in order to properly determine the oligomer order and fraction in quantitative FRET with the Kinetic Theory of FRET. I have also shown that the total apparent FRET efficiencies of higher-order oligomer formation is not unique as a function of total concentration. Thus, bulk two-color FRET static quenching experiments provide the most useful information with regards to the detailed study of monomer, monomer-dimer, and constitutively dimeric membrane proteins, and are intrinsically limited in their ability to distinguish the order of higher order oligomerization. Yet, we note that even though the oligomer order is not distinguishable in this case, the ability to distinguish non-constitutive oligomer formation from that of the presence of a constitutive oligomeric state remains and can provide a great deal of insight into the behavior the oligomerizing system under study. The above limitations must be carefully considered by researchers in the design of FRET experiments with fluorescent-protein labeled membrane proteins, especially when higher order oligomerization is the subject of study.

All of this improvement in theory and analysis was made possible by a simple realization: people have spent forever thinking about the oligomeric FRET by ignoring stochastic FRET. My idea was simply to ignore oligomeric FRET and concentrate on stochastic FRET. It is interesting that understanding the FRET of non-interaction is what would lead to the understanding of the total FRET, including that of interactions.

Chapter 4: Theory of Fully Quantified Spectral Imaging

4-1. Introduction

The function of membrane proteins is often regulated through protein-protein interactions in cellular membranes [6,13,71-73]. While methods to study interactions between soluble proteins are well established, methodologies to quantify membrane protein interactions have been slow to emerge[42-44,74-79]. Great challenges remain, particularly for complex membrane proteins, which cannot be overexpressed in large quantities, and cannot be purified and properly reconstituted in model systems.

Here I introduce a method that I have developed, **F**ully Quantified **S**pectral **I**maging (FSI), which yields both three-dimensional concentrations of fluorophores in a voxel, two-dimensional membrane concentrations and FRET efficiencies, and ultimately reports on the stoichiometry and stability of protein complexes in live cells. I derive the equations and describe the implementation of the FSI method, created for use with spectral imaging systems in which an emission spectrum is measured for every pixel in an image. I describe the results of a set control experiments performed with soluble fluorescent proteins which demonstrate successful application of the method. In later chapters, I will demonstrate the implementation and usefulness of the FSI method by using it to study the properties of VEGF_{121} and VEGFR2 in live cells.

The FSI methodology requires the use of a spectral imaging system, in which a full emission spectrum is captured for every pixel within an image, acquired under magnification with any standard microscope. In the Hristova Lab, we have the OptiMis True Line spectral imaging system and a Zeiss inverted wide-field microscope, with a 63x water immersion objective. This instrument is capable of measuring the full emission spectrum of fluorescent molecules for every pixel in a 300 x 440 pixel image in seconds. The measurement of the full visible emission spectrum by OptiMis enables a full mathematical treatment of emission spectra for the determination of FRET efficiencies. Furthermore, we utilize two-photon excitation in the infrared wavelengths, outside of the detectable range of OptiMis. The use of two-photon IR excitation and the spectral imaging allows us to measure FRET without the use of any band-pass filters, as are traditionally utilized in fluorescence microscopy to separate fluorescence from different flavors of fluorophores.

The basic operating principle of OptiMis is actually very simple[80,81]. The exciting laser beam, initially circularly shaped encounters a cylindrical lens (a curved mirror) that shapes the beam into a line. This line is scanned over the sample by computer control. The line of excitation elicits a line of fluorescence is captured by the objective lens and sent toward the CCD via a mirror. The emission fluorescence from the sample passes through a transmission grating before hitting the CCD, thus enabling the simultaneous measurement of the emission spectra for every pixel in the line. The concept is illustrated below in **Figure 4-1.** The spectral properties of the fluorescent proteins mTurquoise and YFP, widely used in the work, are shown in **Figure 4-2**

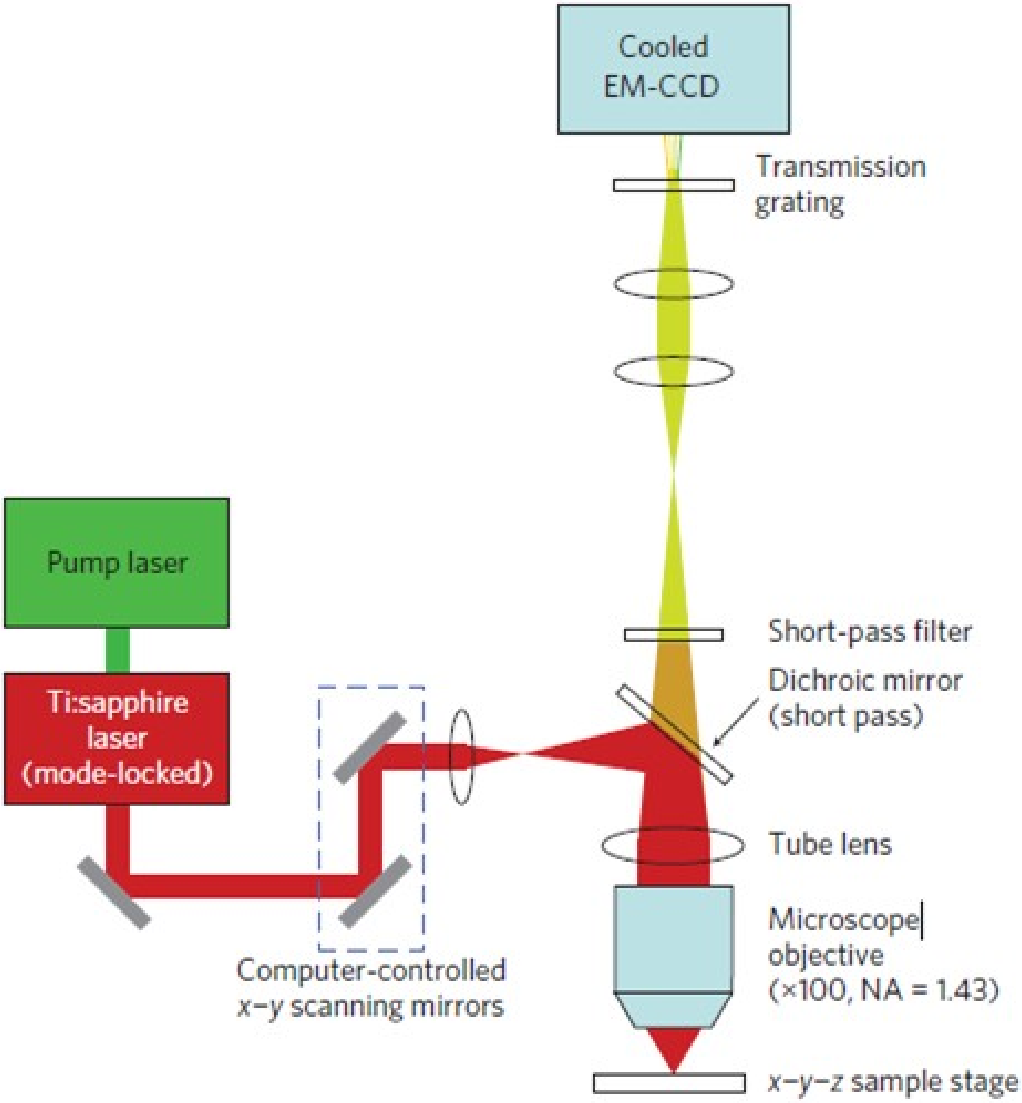

Figure 4-1. A basic schematic diagram of the major components of the OptiMis spectral imaging system. A green laser serves as a pump to elicit pulsed-femtosecond IR lasing. A Gaussian beam is expanded and then shaped into a line at the first mirror, and the y-scanning mirror is used to scan the line over the sample. The line of fluorescence emitted from the sample passes through a dichroic mirror and through a transmission grating, enabling the CCD to measure fluorescence emission spectra from the entire line of fluorescence simultaneously. Image used with permission [80]

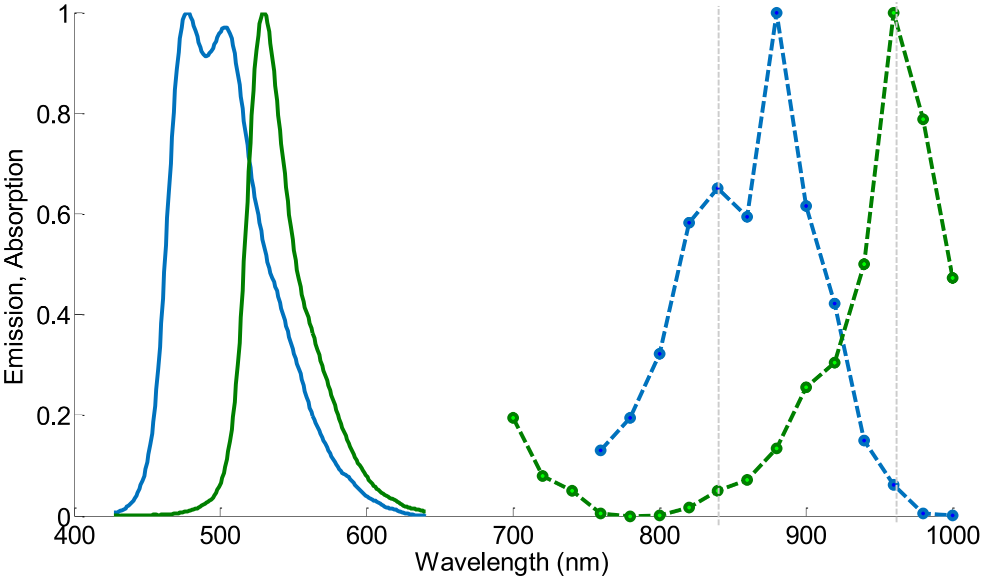

Figure 4-2. mTurquoise (blue) and YFP (green) spectral properties, with emission shown as solid lines and two-photon absorption shown as dashed lines. The two vertical lines (grey) at 840 nm and 960 nm represent the excitation wavelengths λ_1 and λ_2 utilized in the FRET and Acceptor scans, respectively. The FSI equations can account for intrinsic YFP excitation occurring at 840 nm without the use of approximations or filters. Similarly, the FSI equations account for intrinsic excitation of the donor and FRET that occurs when performing the Acceptor scan at 960 nm.

The analysis of the emission spectra from the pixels of a co-transfected cell expressing both the donor and the acceptor fluorophores, excited in a "FRET scan" at λ_1, and in an "Acceptor Scan" at λ_2, provides all of the information needed to calculate the concentrations of donor and acceptor fluorophores and the apparent FRET efficiency, E_{app}. The fluorescence emission spectrum from a pixel of the cotransfected cell at both excitation wavelengths is assumed to be a linear sum of three contributions: the fluorescence of the donor in the presence of the acceptor, $F^{DA}(\lambda)$, the fluorescence of the acceptor in the presence of the donor, $F^{AD}(\lambda)$, and a background contribution:

$$F(\lambda)_{\lambda_1,\lambda_2}^{pixel} = F^{DA}(\lambda) + F^{AD}(\lambda) + background(\lambda) \tag{4-1}$$

I modeled the pixel-level background contribution in every pixel as a line, as shown below (see **Figure (4-3)**.

$$F(\lambda)_{\lambda 1,\lambda 2}^{pixel} = k_{\lambda 1,\lambda 2}^{DA} \cdot F^{D}(\lambda) + k_{\lambda 1,\lambda 2}^{AD} \cdot F^{A}(\lambda) + a\lambda + b \tag{4-2}$$

In **Equation (4-2)**, $F^D(\lambda)$ is the normalized emission spectrum of the donor and $F^A(\lambda)$ is the normalized emission spectrum of the acceptor fluorophore. **Figure 4-4** shows an image of a transiently transfected HEK293T cell, expressing VEGFR2-ECTM-GGS$_5$-mTurquoise and YFP linked membrane proteins. The total fluorescence from a pixel of the cell is a combination of donor and acceptor fluorescence.

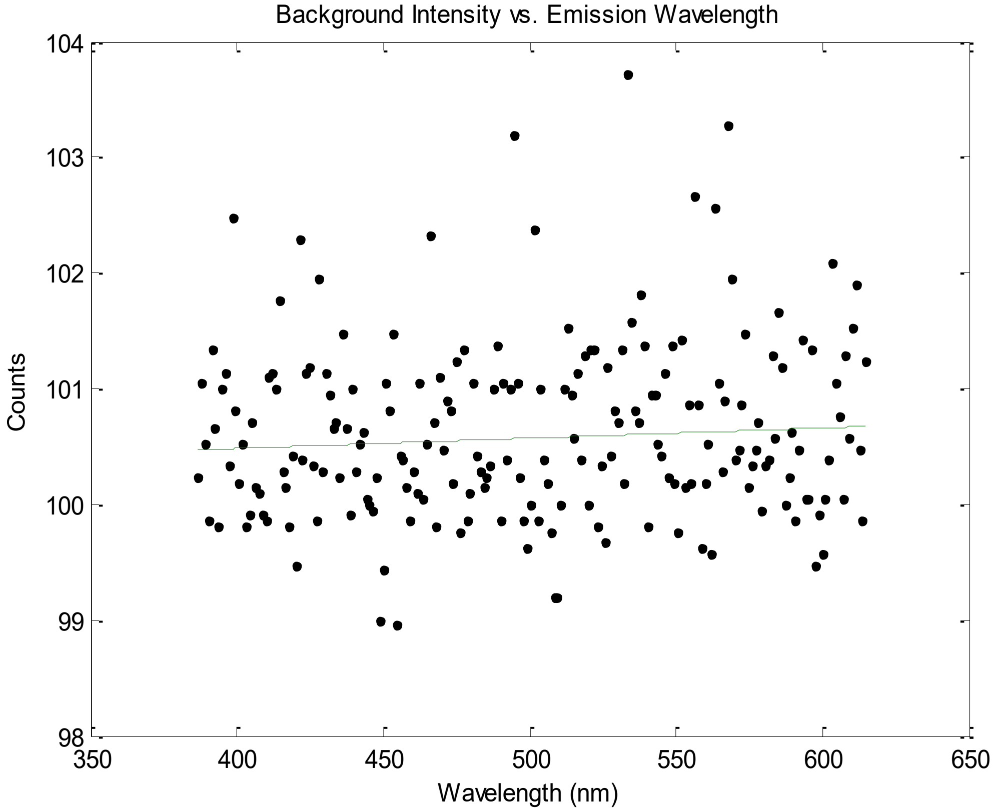

Figure 4-3. A pixel from an OptiMis spectral image of buffer-only with no fluorescence, showing that a line, $ax + b$, is a relatively good model for the background contribution. Traditionally, a single number is subtracted from all wavelength values for all pixels, but from an analytical perspective it is preferable to model the background contribution for each pixel individually.

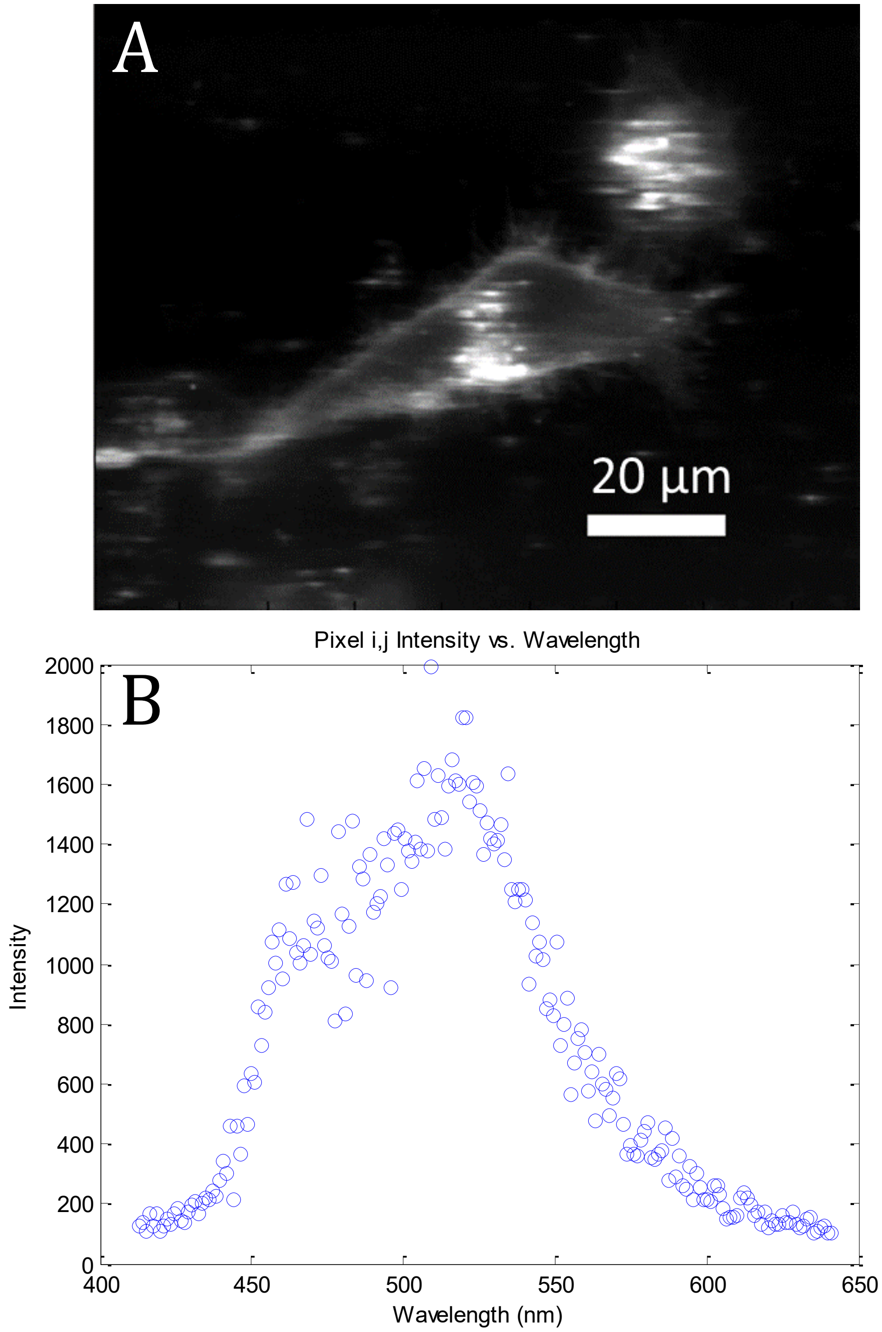

Figure 4-4. A transiently transfected HEK293T cell expressing VEGFR2-ECTM-GGS$_5$-mTurquoise/YFP. **A.** An “image” of the cell in a traditional sense is obtained from OptiMis by integrating the emission spectrum of every pixel over the measured wavelengths. **B.** An emission spectrum from a pixel in the membrane is composed of some combination of mTurquoise and YFP fluorescence.

Linear least squares optimization then yields the "best fit" coefficients (i.e, $k_{\lambda 1,\lambda 2}^{DA}$, $k_{\lambda 1,\lambda 2}^{AD}$, and *background* (a and b in **Equation (4-2)**) that minimizes the chi-square value for the fit [82]. The pixel-level integrated intensities of the donor in the presence of the acceptor and of the acceptor in the presence of the donor are then readily calculated [56]:

$$F_{\lambda 1,\lambda 2}^{DA} = k_{\lambda 1,\lambda 2}^{DA} \cdot w^{D} \qquad (4\text{-}3)$$

$$F_{\lambda 1,\lambda 2}^{AD} = k_{\lambda 1,\lambda 2}^{AD} \cdot w^{A} \qquad (4\text{-}4)$$

Here, w^{D} and w^{A} are the integrated normalized spectra of the donor and acceptor:

$$w^{D,A} = \int F^{D,A}(\lambda) d\lambda \qquad (4\text{-}5)$$

The unmixed fluorescence from a pixel's FRET and Acceptor scans is shown in **Figure 4-5.**

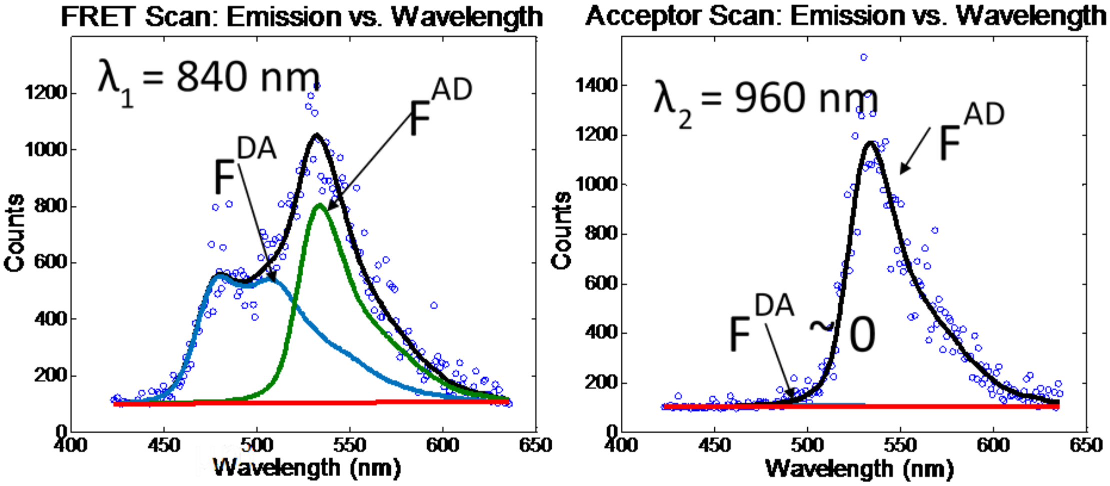

Figure 4-5. The fluorescence emission spectra from a pixel in an image of a HEK293T cell expressing VEGFR2 ECTM-GGS$_5$-mTurquoise/YFP. **Left**: The donor, mTurquoise, is primarily excited during the FRET scan with excitation at 840 nm, but due to protein-protein interactions in the membrane and FRET, there is a large YFP fluorescence signal. **Right**: During the Acceptor scan at 960 nm, the acceptor is primarily excited and there is minimal donor fluorescence, but this approximation is not necessary with the FSI method.

4-2. *Fluorescent Protein Solution Standards*

The FSI method relies on calibration curves obtained by imaging solution standards of the donor and acceptor fluorophores of known concentration. Given that the total fluorescence from a volume of solution containing excited fluorescent molecules is proportional to the number of fluorescent molecules present in the solution, we can write [83]:

$$F_{FP} \propto N_{FP}$$

$$F_{FP,B} = k_{FP} N_{FP,B} = k_{FP}[FP]_B dV \qquad (4\text{-}6)$$

Here, $F_{FP,B}$, stands for the total integrated fluorescence emission of the fluorophore (in our case, a fluorescent protein) in a Bulk solution. k_{FP} is a proportionality constant that accounts for the dependence of fluorescence on quantum yield, excitation rate and wavelength, and other physical parameters. **Equation (4-6)** yields an explicit dependence of the fluorescence from a bulk solution of fluorophores on the concentration of the fluorescent protein and the excitation volume.

The same relationship of **Equation (4-6)** can be written when the fluorophore is attached to a protein of interest, by fusing the gene encoding the fluorescent protein to the gene of interest, with B replaced by S, representing the Sample of interest.

$$F_{FP,S} = k_{FP} N_{FP,S} = k_{FP}[FP]_S dV \qquad (4\text{-}7)$$

Equating the proportionality constant, k_{FP}, of **Equations (4-6)** and **(4-7)**:

$$\frac{F_{FP,B}}{[FP]_B dV} = \frac{F_{FP,S}}{[FP]_S dV} \tag{4-8}$$

Rearranging **Equation (4-8)** and solving for the concentration of the fluorescent protein in the sample:

$$[FP]_S = \frac{F_{FP,S} \cdot [FP]_B}{F_B} \tag{4-9}$$

Thus, the concentration of the fluorophore in the sample can be calculated from the known concentration and fluorescence intensity of the fluorophore in the bulk solution, and the experimentally determined fluorescence intensity of the fluorescent protein in the sample.

By rearranging **Equation (4-9)** and adding the subscripts 1 and 2 to represent two different known concentrations of the fluorescent protein solution standards, we arrive at:

$$[FP]_S \cdot F_{B,1} = F_S\, [FP]_{B,1} \cdot [FP]_{B,1} \tag{4-10}$$

$$[FP]_S \cdot F_{B,2} = F_S [FP]_{B,2} \cdot [FP]_{B,2} \tag{4-11}$$

Subtracting and rearranging these equations:

$$\frac{F_S}{[FP]_S} = \frac{\Delta F_B}{\Delta[FP]_B} \tag{4-12}$$

In the limit of $\Delta \rightarrow 0$, the ratio of the change in bulk fluorescence to the change in bulk solution standard concentration is replaced by ***i***, the slope of a line fit to a solution standard fluorescence intensity versus concentration calibration curve:

$$\frac{F_{S,\lambda}}{[FP]_{S,\lambda}} = i_\lambda \tag{4-13}$$

Equation (4-13) allows the calculation of the concentration of the fluorophore in the sample from its fluorescence intensity upon excitation at a specific wavelength. Imaging the same sample at the two different excitation wavelengths, λ_1 and λ_2, and equating the concentrations in **Equation (4-13)**, yields the following relations:

$$\frac{F^D{}_{\lambda 1}}{i_{D,\,\lambda 1}} = \frac{F^D{}_{\lambda 2}}{i_{D,\,\lambda 2}} \tag{4-14}$$

$$\frac{F^A{}_{\lambda 1}}{i_{A,\,\lambda 1}} = \frac{F^A{}_{\lambda 2}}{i_{A,\,\lambda 2}} \tag{4-15}$$

These relations allow the conversion of donor or acceptor fluorescence at one wavelength to the fluorescence at the other excitation wavelength through the ratios of the slopes of the fluorescence calibration curves.

As stated earlier, the two excitation wavelengths are chosen based on the fluorescence and emission properties of the fluorescent proteins utilized: λ_1 is chosen to primarily excite the donor; and λ_2 is chosen to maximally excite the acceptor. Several concentrations of soluble fluorescent proteins are imaged at both excitation wavelengths, and a line is fit to the integrated intensity versus concentration data for every pixel of the sample image (see **Figure 4-6B**). The four slopes, $i_{D,\lambda 1}$, $i_{D,\lambda 2}$, $i_{A,\lambda 1}$, and $i_{D,\lambda 2}$, are calculated for every pixel, for both the donor and acceptor fluorescent protein solution standards, at the two excitation wavelengths, λ_1 and λ_2.

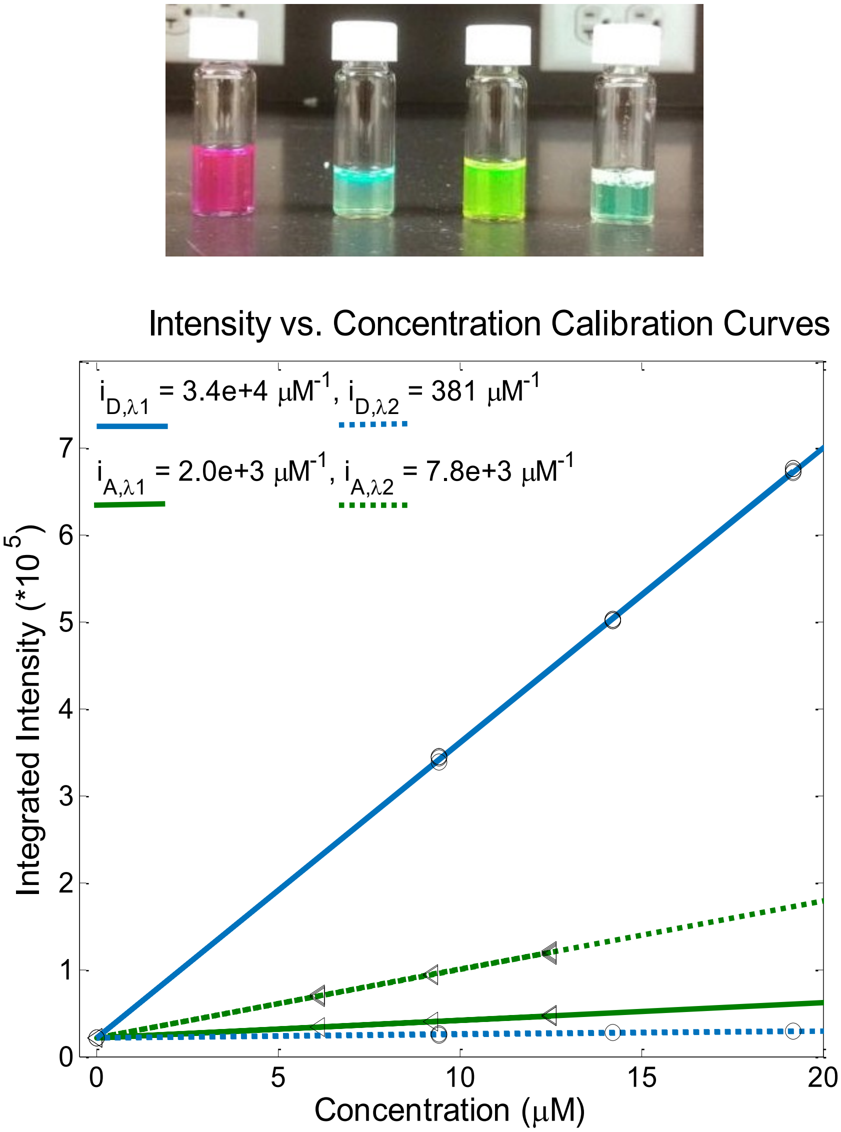

Figure 4-6. Top. Fluorescent proteins are expressed in *E. coli*, purified, and stored in PBS buffer at near milimolar concentration. Dilutions to make 100%, 75%, and 50% solution standards are prepared and imaged. **Bottom.** Images of soluble donor and acceptor solution standards are acquired for three known solution concentrations, along with images of buffer-only (PBS) controls at two excitation wavelengths, λ_1 = 840 nm and λ_2 = 960 nm. After integration of the fluorescence over the emission wavelengths, a line is fit to every pixel's integrated intensity vs. concentration solution standard data, yielding the slopes $i_{D,\lambda1}$, $i_{D,\lambda2}$, $i_{A,\lambda1}$, and $i_{D,\lambda2}$. The solid and dashed lines are the best fit lines to the measured integrated intensity versus concentration data with excitation at λ_1 and at λ_2, respectively. The best-fit lines for the donor and the acceptor are shown in blue and green, respectively.

4-3. *Theory of Fully Quantified Spectral Imaging*

In the FSI method, two scans of a sample are performed: a "FRET scan" at excitation wavelength λ_1, in which the donor is primarily excited and an "Acceptor scan" at excitation wavelength λ_2, in which the acceptor is maximally excited. By using these two scans and calibration curves of fluorescence versus known concentration of donor and acceptor "solution standards," one can solve for the full donor fluorescence and the acceptor fluorescence in the absence of FRET, as discussed below.

The fluorescence of the donor in the presence of the acceptor, $F_{\lambda n}^{DA}$, and the fluorescence of the acceptor in the presence of the donor, $F_{\lambda n}^{AD}$, at both excitation wavelengths, λ_1 and λ_2, can be written as a sum of two terms:

$$F_{\lambda n}^{DA} = F_{\lambda n}^{D} - F_{RET,\lambda n}^{D} \tag{4-16}$$

$$F_{\lambda n}^{AD} = F_{\lambda n}^{A} + F_{RET,\lambda n}^{A} \tag{4-17}$$

In **Equations (4-16) and (4-17)**, $F_{\lambda n}^{D}$ and $F_{\lambda n}^{A}$ (n=1, 2) are the donor and acceptor fluorescence emission spectra after direct excitation at λ_1 and λ_2, in the absence of FRET. $F_{RET,\lambda n}^{D}$ and $F_{RET,\lambda n}^{A}$ are the loss and gain of fluorescence by the donor and the acceptor fluorophores due to FRET, respectively. **Figure 4-5** shows the components $F_{\lambda n}^{DA}$ and $F_{\lambda n}^{AD}$ for excitation of the sample at λ_1 and λ_2.

As derived in [56], a relationship exists between $F_{RET,\lambda n}^{D}$ and $F_{RET,\lambda n}^{A}$. If one considers the number of FRET events from a donor to an acceptor molecule during the excitation period, N_{RET}, then a fraction of those events, Q_D, would be detected as photons from the donor molecule, $F_{RET,\lambda n}^{D}$:

$$N^{RET} \cdot Q_D = F_{RET,\lambda n}^{D} \tag{4-18}$$

Similarly, once transferred to the acceptor molecule, a fraction of those excitation events, Q_A, will be detected as photons emitted from the acceptor:

$$N^{RET} \cdot Q_A = F_{RET,\lambda n}^{A} \tag{4-19}$$

Q_D and Q_A in **Equations (4-18)** and **(4-19)** are the quantum yields of the donor and acceptor fluorophores, respectively. By solving for N^{RET} and equating **Equations (4-18)** and **(4-19)**, (conservation of RET events) we arrive at a general and indispensable relationship between $F_{RET,\lambda n}^{D}$ and $F_{RET,\lambda n}^{A}$:

$$\frac{F_{RET,\lambda n}^{D}}{Q_D} = \frac{F_{RET,\lambda n}^{A}}{Q_A} \tag{4-20}$$

The "apparent FRET efficiency" of energy transfer, E_{app}, is a measure of the interaction between the donor and the acceptor. It can be written in terms of "donor quenching" or the loss of fluorescence by the donor due to resonant energy transfer to an acceptor:

$$E_{app}^{Dq} = \frac{F_{RET,\lambda 1}^{D}}{F_{\lambda 1}^{D}} \tag{4-21}$$

By solving for $F_{RET,\lambda 1}^{D}$ in **Equation (4-16)** and substituting into **Equation (4-21)**, we arrive at the commonly seen relation for the donor-quenched FRET efficiency:

$$E_{app}^{Dq} = 1 - \frac{F_{\lambda 1}^{DA}}{F_{\lambda 1}^{D}} \tag{4-22}$$

Thus, we need an expression for the fluorescence of the donor in the absence of FRET, $F_{\lambda 1}^{D}$, in order to calculate the donor-quenched apparent FRET efficiency.

4-3.1 Calculation of $\boldsymbol{F^{D}_{\lambda 1}}$, the unquenched donor fluorescence in the absence of FRET

Rearranging **Equation (4-16)** for $F^{D}_{\lambda 1}$ gives **Equation (4-23)**:

$$F^{D}_{\lambda 1} = F^{DA}_{\lambda 1} + F^{D}_{RET,\lambda 1} \tag{4-23}$$

Using **Equation (4-20)**, we express $F^{D}_{RET,\lambda 1}$ in terms of the ratio of quantum yields of the donor and acceptor, and $F^{A}_{RET,\lambda 1}$, as shown:

$$F^{D}{}_{\lambda 1} = F^{DA}{}_{\lambda 1} + \frac{Q^{D}}{Q^{A}} F^{A}{}_{RET,\lambda 1} \tag{4-24}$$

By solving **Equation (4-17)** for $F^{A}{}_{RET,\lambda 1}$, and inserting into **Equation (4-24)**, we arrive at the following relation:

$$F^{D}{}_{\lambda 1} = F^{DA}{}_{\lambda 1} + \frac{Q^{D}}{Q^{A}} (F^{AD}{}_{\lambda 1} - F^{A}{}_{\lambda 1}) \tag{4-25}$$

The first term, $F^{DA}_{\lambda 1}$, is determined by linear least squares "unmixing" of the pixel-level emission spectrum. In the literature, the assumption is often made that $F^{A}{}_{\lambda 1} \approx 0$ and E^{Dq}_{app} is the estimated based on this assumption. Here I show, however, that $F^{A}{}_{\lambda 1}$ can be determined exactly using **Equation (4-15)** derived in the section, **Fluorescent Protein Solution Standards.**

The exact expression for $F^{D}{}_{\lambda 1}$ is**:**

$$F^{D}{}_{\lambda 1} = F^{DA}{}_{\lambda 1} + \frac{Q^{D}}{Q^{A}}\left(F^{AD}{}_{\lambda 1} - \frac{i_{A,\lambda 1}}{i_{A,\lambda 2}} F^{A}{}_{\lambda 2}\right) \qquad (4\text{-}26)$$

where $i_{A,\lambda 1}$ and $i_{A,\lambda 2}$ are concentration calibration constants, namely the slopes of the acceptor fluorescence versus concentration calibration curves. $F^{A}{}_{\lambda 2}$ is determined using information acquired in an "Acceptor scan" of the sample as described next. Thus, $F^{D}{}_{\lambda 1}$ can be calculated exactly using **Equation (4-26)**.

4-3.2. Calculation of $F^A_{\lambda 2}$, the fluorescence of the acceptor in the absence of FRET

By rearranging **Equation 4-7** to solve for $F^A_{\lambda 2}$ and utilizing the fundamental relationship **(4-20)**, we arrive at **Equation (4-27)** below:

$$F^A{}_{\lambda 2} = F^{AD}{}_{\lambda 2} - \frac{Q_A}{Q_D} F^D{}_{RET,\lambda 2} \tag{4-27}$$

Then write $F^D{}_{RET,\lambda 2}$ in terms of the ratios of the donor standard slopes at λ_1 and λ_2 (see **Equations (4-14), and (4-15)** in the section, ***Fluorescent Protein Solution Standards***):

$$F^A{}_{\lambda 2} = F^{AD}{}_{\lambda 2} - \frac{Q_A}{Q_D}\frac{i_{D,\lambda 2}}{i_{D,\lambda 1}} F^D{}_{RET,\lambda 1} \tag{4-28}$$

By using the fundamental relationship **(4-20)**, we solve for $F^D{}_{RET,\lambda 1}$ in terms of $F^A{}_{RET,\lambda 1}$ and the ratio of the donor and acceptor quantum yields. Insertion into **Equation (4-28)** above allows for the quantum yields to cancel:

$$F^A{}_{\lambda 2} = F^{AD}{}_{\lambda 2} - \frac{i_{D,\lambda 2}}{i_{D,\lambda 1}} F^A{}_{RET,\lambda 1} \tag{4-29}$$

Solving for $F^{A}{}_{RET,\lambda 1}$ in E**quation 4-7** and inserting into **Equation (4-29)** brings us to **Equation (4-30)**:

$$F^{A}{}_{\lambda 2} = F^{AD}{}_{\lambda 2} - \frac{i_{D,\lambda 2}}{i_{D,\lambda 1}}(F^{AD}{}_{\lambda 1} - F^{A}{}_{\lambda 1}) \tag{4-30}$$

Finally, convert from $F^{A}{}_{\lambda 1}$ to $F^{A}{}_{\lambda 2}$ using the ratios of the calibration slopes as derived in section ***Soluble Fluorescent Protein Solution Standards****:*

$$F^{A}{}_{\lambda 2} = (F^{AD}{}_{\lambda 2} - \frac{i_{D,\lambda 2}}{i_{D,\lambda 1}}F^{AD}{}_{\lambda 1}) \cdot (1 - \frac{i_{A,\lambda 1}}{i_{A,\lambda 2}}\frac{i_{D,\lambda 2}}{i_{D,\lambda 1}})^{-1} \tag{4-31}$$

$F^{A}{}_{\lambda 2}$ in **Equation (4-31)** is written exactly in terms of quantities that can be measured experimentally.

Equation (4-31), along with **Equation (4-26)**, provides an approximation-free calculation of ${F^{D}}_{\lambda 1}$, and allows for the calculation of E_{app}^{Dq} according to **Equation (4-22)**. In addition, **Equation (4-31)** allows the direct calculation of the pixel-level donor and acceptor concentrations (an effective pixel-level concentration for non-freely diffusing fluorophores), based on their fluorescence and the calibration slopes i of the intensity versus concentration, at the fluorophores' primary excitation wavelengths, as shown:

$$[D] = \frac{{F^{D}}_{\lambda 1}}{i_{D,\,\lambda 1}} \tag{4-32}$$

$$[A] = \frac{{F^{A}}_{\lambda 2}}{i_{A,\,\lambda 2}} \tag{4-33}$$

The relevant equations are collected below:

$$E_{app} = {F^{D}}_{RET,\,\lambda 1} / {F^{D}}_{\lambda 1} = 1 - {F^{DA}}_{\lambda 1} / {F^{D}}_{\lambda 1}$$

$$[D] = \frac{{F^{D}}_{\lambda 1}}{i_{D,\,\lambda 1}} = \frac{1}{i_{D,\,\lambda 1}}\left({F^{DA}}_{\lambda 1} + \frac{Q^{D}}{Q^{A}}\left({F^{AD}}_{\lambda 1} - \frac{i_{A,\lambda 1}}{i_{A,\lambda 2}}{F^{A}}_{\lambda 2}\right)\right)$$

$$[A] = \frac{{F^{A}}_{\lambda 2}}{i_{A,\,\lambda 2}} = \frac{1}{i_{A,\,\lambda 2}}\left({F^{AD}}_{\lambda 2} - \frac{i_{D,\lambda 2}}{i_{D,\lambda 1}}{F^{AD}}_{\lambda 1}\right) \cdot \left(1 - \frac{i_{A,\lambda 1}}{i_{A,\lambda 2}}\frac{i_{D,\lambda 2}}{i_{D,\lambda 1}}\right)^{-1}$$

4-3.3. Verification of the FSI Methodology

To validate the capabilities of the FSI method to accurately yield pixel-level concentrations and FRET efficiencies, I performed experiments with mixtures of purified mTurqoise and YFP soluble fluorescent proteins. I imaged six different samples, and acquired four FRET and acceptor images for each sample. In three of these samples, the concentration was held constant (~10 μM) while the donor (mTurqoise) to acceptor (YFP) ratio was varied. The other three samples contained a fixed donor to acceptor ratio (1:3) while the total FP concentration was varied from 2 to 14 μM. Concentrations of mTurquoise and YFP in the samples were first measured via UV-Vis spectroscopy using the Nanodrop 2000C. Next, the mixtures were imaged in a FRET scan with excitation at 840 nm and an Acceptor scan with excitation at 960nm in the two-photon microscope. Spectral unmixing and the FSI equations were then used to obtain the FRET efficiencies (**Figure 4-7A**) and the concentrations of mTurqoise and YFP in the sample mixtures (**Figures 4-7B and 4-7C**).

The concentrations of the fluorescent proteins determined with the FSI method are in complete agreement with the fluorescent protein concentrations measurements obtained via UV-Vis absorption measurements. Furthermore, we measure zero concentration dependence on the FRET efficiency, indicating a lack of interactions between the fluorescent proteins. This is expected for three-dimensional solutions of monomeric fluorescent proteins. Changing the excitation wavelength to 800 nm, and thus the amount of intrinsic acceptor excitation during the FRET scan (**Figure 4-8**), had no effect on the measured concentrations and FRET efficiencies. Thus, we see that the FSI equations are able to extract the proper fluorophore concentrations over a wide range of total concentrations and donor to acceptor ratios and offers great flexibility in the choice of excitation wavelengths.

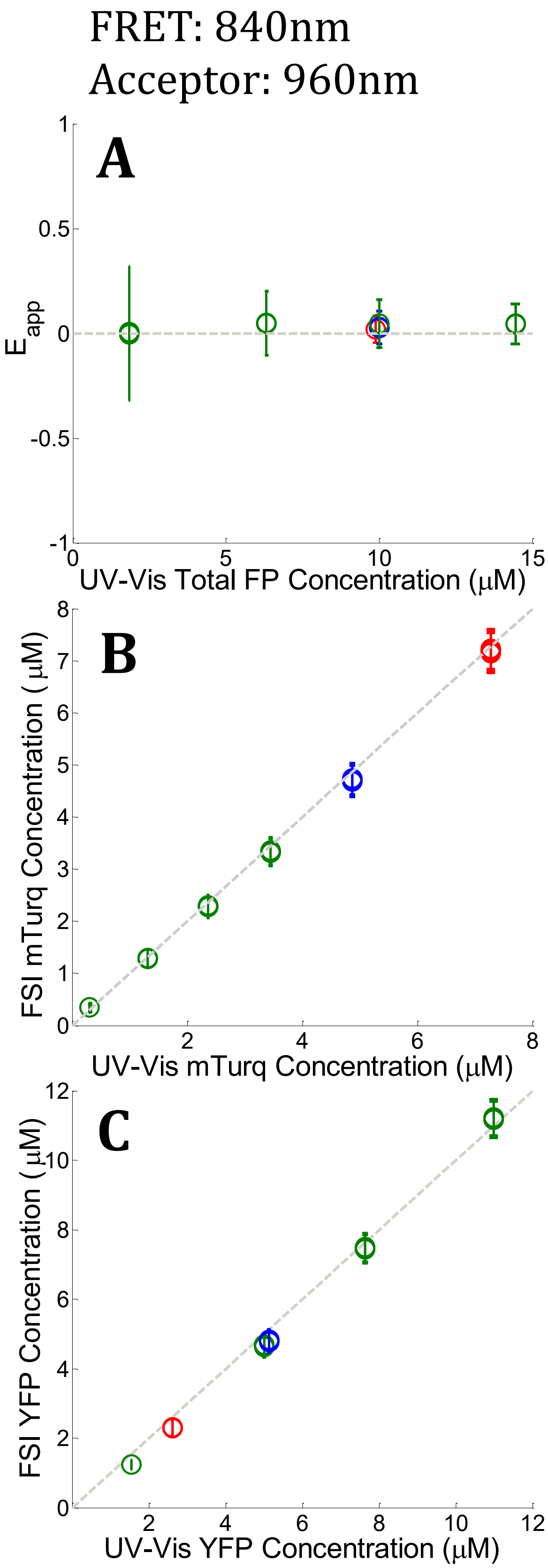

Figure 4-7. Verification of the FSI method with 840 nm excitation during the FRET scan and 960 nm excitation during the Acceptor scan. (A) FRET efficiencies measured for mixtures of soluble mTurq and YFP, as a function of total protein concentration. Dashed line: y = 0. (B) Comparison of mTurq concentrations, measured with FSI and Nanodrop. Dashed line: y = x. (C) Comparison of YFP concentrations, measured with FSI and Nanodrop. Dashed line: y = x. Red: 3:1 mTurqiouse:YFP; Yellow: 1:1 mTurqiouse:YFP; Green: 3:1 mTurqiouse:YFP. Dashed line: y = x.

Figure 4-8. Verification of the FSI method with 800 nm excitation during the FRET scan and 960 nm excitation during the Acceptor scan. (A) FRET efficiencies measured for mixtures of soluble mTurq and YFP, as a function of total protein concentration. Dashed line: y = 0. (B) Comparison of mTurq concentrations, measured with FSI and Nanodrop. Dashed line: y = x. (C) Comparison of YFP concentrations, measured with FSI and Nanodrop. Dashed line: y = x. Red: 3:1 mTurquoise:YFP; Yellow: 1:1 mTurquoise:YFP; Green: 3:1 mTurquoise:YFP. Dashed line: y = x.

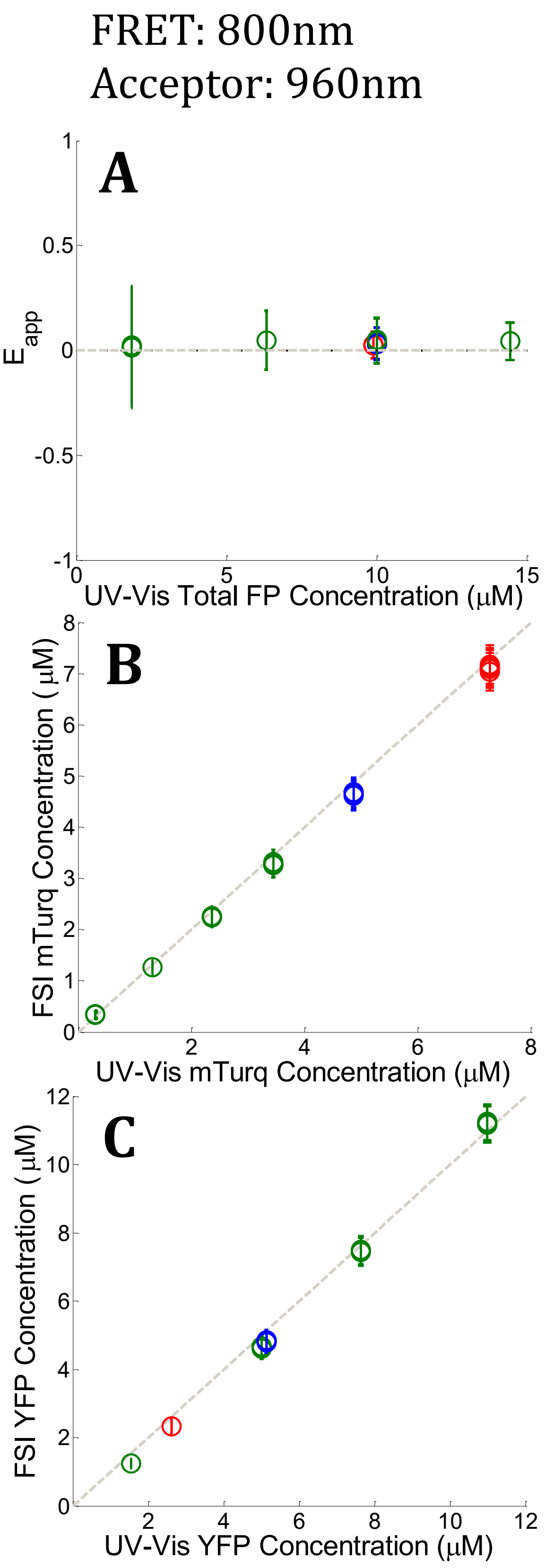

4-4. Technical Details Important for the Implementation of FSI

4-4.1. Image Acquisition

Spectral images with two-photon excitation are acquired with a Mai Tai laser (Spectra Physics) and the OptiMis True Line Spectral Imaging system (Aurora Spectral Technologies) utilizing a Zeiss Observer wide field microscope with a 63X NA 1.2 water immersion objective as described in detail in [80]. Two images of each cell are acquired: a "FRET scan" with primary donor excitation at 840 nm and an "Acceptor Scan" with primary acceptor excitation at 960nm. With a 35 ms line scan time of full-field of view (300x 440 pixels) , each spectral image requires approximately 15 seconds to acquire at full spectral resolution, with approximately 30 seconds required between scans for two photon laser emission wavelength tuning from 840 nm to 960 nm.

The FSI equations described in the theory section are implemented in a MATLAB graphical user interface designed by me with a MATLAB's GUI development tool, GUIDE. Linear least squares, or unmixing, is utilized to determine the best-fit $k^{DA}_{\lambda1,\lambda2}$ and $k^{AD}_{\lambda1,\lambda2}$ values for the donor and acceptor components of the measured spectrum in every pixel (see **Figure 4-5**). It took me hundreds of hours of my personal time and several thousand lines of code to write the GUI, and now the entire lab is able to use it for FSI measurements.

4-4.2. Noise Analysis

Straightforward spectral decomposition of every pixel of an image without considerations of noise, can lead to decreased accuracy in the calculated values of F^{DA} and F^{AD}, from which concentrations and thermodynamic parameters of interest are calculated. Specifically, the best-fit k-values can become negative when unmixing "dim" pixels. In this case, a large positive k-value for the other spectral component can provide a fit that basically adds up to a linear background contribution. This gives erroneous calculated pixel-level FRET efficiency and fluorescence information. Furthermore, negative k-values are not physically realizable (there is no such thing as negative fluorescence) and they need to be properly corrected.

With this goal in mind, approximately 500,000 pixels of PBS buffer-only scans at 840 nm and 960 nm laser excitation were analyzed in order to determine the typical k-values that occur in a signal comprised only of noise. The spectra were decomposed as a sum of donor and acceptor fluorescence and the k^{AD} and k^{DA} values were analyzed as shown in **Figure 4-9.**

As a result of this noise-only analysis, I found that the magnitude of the k-values from the unmixing of noise-only pixels was generally less than five. I decided on a minimum k value = 10, which is twice the value corresponding to noise. All pixels in which the k-values for both fluorophores are less than 10 are rejected as not having a useable signal and excluded from any further analysis. Regions of cells are allowed to be selected (they are rejected by the GUI) if they contain pixels with no measurable fluorescence.

In order to not bias the data in terms of erroneously rejecting pixels with no FRET (the FRET scan $k_{\lambda 1}{}^{AD}$could be low or zero), or very low donor excitation levels (Acceptor scans at 960 nm can give a $k_{\lambda 2}$ near zero), the minimum k value and negative k value corrections must be carefully applied as shown in **Table 4-1**, below. In the case of a correction, the negative k value is set to zero and the pixel is unmixed again, but with a composite signal lacking the negative fluorescence component. For example, if the k^{AD} value of a pixel in the FRET scan is less than zero, but the k^{DA} value is greater than 10, then the pixel will be decomposed as containing only the donor signal, with zero acceptor signal. This prevents the negative k-value from affecting the true value of the remaining component in the "best" fit. The results of applying these conditions to an image are shown in **Figure 4-10**. We see that these criteria are able to reject most pixels that do not exhibit any fluorescence.

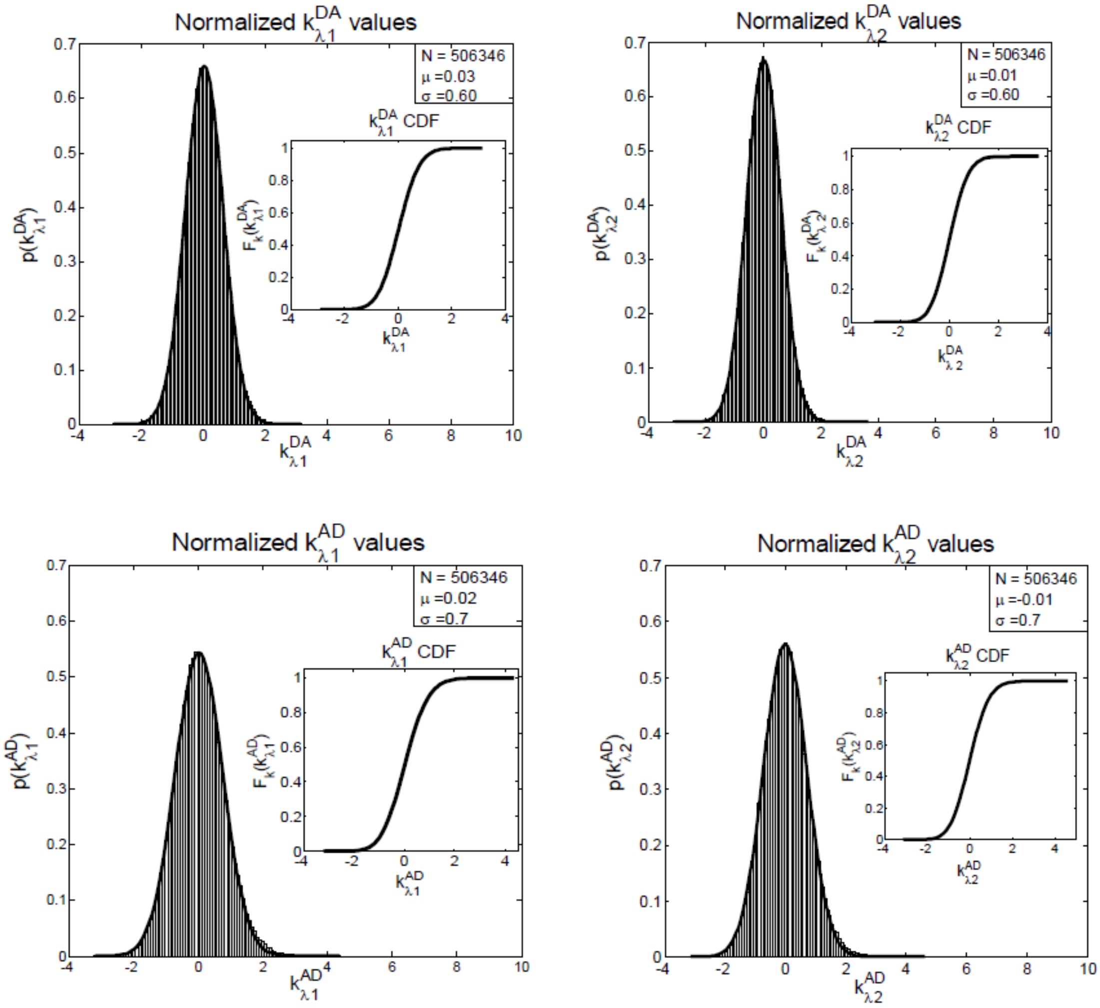

Figure 4-9. Noise analysis. Control buffer-only scans are unmixed in order to determine the typical signal contained within pixels that lack fluorescence. The normalized histograms of k-values were integrated to create cumulative distribution functions, which revealed that pixels lacking measurable fluorescence yield *k*-values < 5.

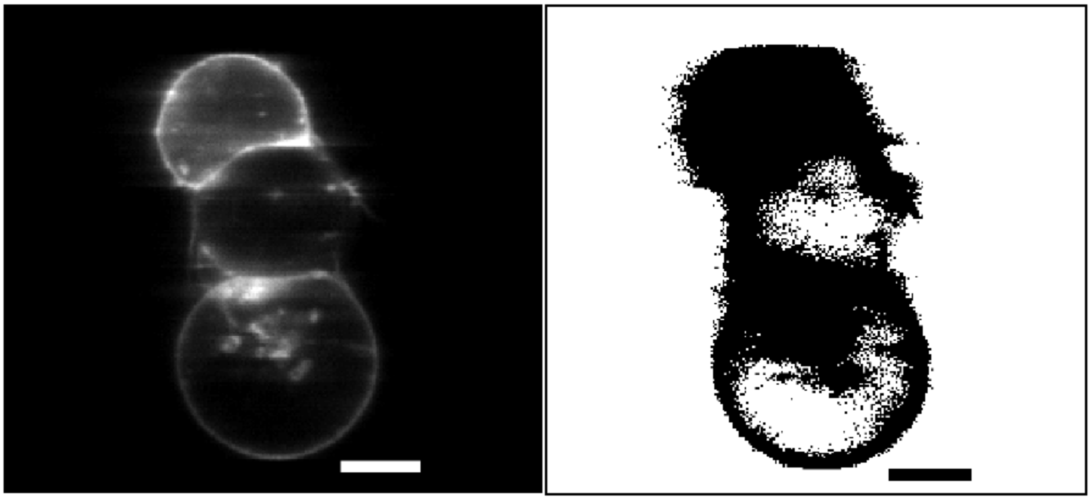

Figure 4-10. Pixel rejection based on noise analysis. Left: HEK293T cells co-expressing VEGFR2 EC+TM-mTurq and VEGFR2 EC+TM-YFP. Right: The spectra of every pixel in the image is unmixed and pixels that meet the criteria of Table 1 are shown in black, while pixels that failed to meet the unmixing criteria are shown in white. Pixels that do not meet the unmixing requirements are rejected from further analysis. Scale bars are 15 microns

FRET Scan	$k_{\lambda 1}^{DA} > 10$	$k_{\lambda 1}^{AD} > 10$	ACCEPT
	$k_{\lambda 1}^{DA} > 10$	$0 < k_{\lambda 1}^{AD} < 10$	ACCEPT
	$k_{\lambda 1}^{DA} > 10$	$k_{\lambda 1}^{AD} < 0$	CORRECTED
	$k_{\lambda 1}^{DA} < 10$	$k_{\lambda 1}^{AD} < 10$	REJECT
Acceptor Scan	$k_{\lambda 2}^{DA} > 10$	$k_{\lambda 2}^{AD} > 10$	ACCEPT
	$0 < k_{\lambda 2}^{DA} < 10$	$k_{\lambda 2}^{AD} > 10$	ACCEPT
	$k_{\lambda 2}^{DA} < 0$	$k_{\lambda 2}^{AD} > 10$	CORRECTED
	$k_{\lambda 2}^{DA} < 10$	$k_{\lambda 2}^{AD} < 10$	REJECT

Table 4-1. During unmixing, pixels are either accepted, corrected, or rejected based on the minimum k-value criteria shown here.

4-4.3. Image Registration

During the time required to tune the laser for the FRET and Acceptor Scans, a stage drift corresponding to one to two pixels is sometimes observed. To correctly align the cells in both images, a subsection of the full field image is selected for analysis and an image registration algorithm is applied to align the Acceptor Scan with the FRET scan (30). This ensures that the same regions are selected in both scans. Images with a correction greater than two pixels are excluded from analysis.

4-4.4. Donor- and Acceptor- Only Expressing Samples

Donor-only and acceptor-only samples are imaged in order to acquire the donor and acceptor emission spectra as a function of emission wavelength. A large region of a singly-transfected cell membrane is selected and the emission spectra for every pixel are averaged and smoothed over all emission wavelengths [84]. The donor and acceptor spectra are then normalized to their maximum value, so that the values range between 0 and 1, providing $F^D(\lambda)$ and $F^A(\lambda)$, which are used for spectral decomposition (unmixing) of pixels in the cotransfected samples, as discussed previously. The integrals of these normalized spectra over the emission wavelengths are denoted as w^D and w^A. The total integrated fluorescence is then calculated by multiplication of the best fit coefficients of the normalized donor and acceptor spectra with their respective w^D and w^A values.

It is observed that the fluorescence properties of the fluorescent proteins are the same in the cytosol and in PBS buffer. I measure the emission spectra for singly transfected cells in each experiment. The shape of the spectra and the peak emission positions are the same as in spectra measured in buffer with a fluorometer [85].

4-4.5. Membrane Region Selection

Cell images are inspected for membrane regions of uniform diffraction limited fluorescence. The fluorescence of the labeled proteins in the stretched membrane appears as a diffraction limited line that is approximately 600 nm wide (see **Figure 4-11)**. One or two regions of homogenous fluorescence, ~3 microns in length, are selected from each cell. Under 63X magnification of the microscope objective, the 16 μm pixels of the CCD are square, with a 254nm side length, as shown in **Figure 4-12**. The proper pixels are automatically selected in each region by selecting several points along the path length of the fluorescence. Connecting lines are drawn between these points, and the unit normal vectors to the vectors pointing from point i to point i + 1 are defined. A region half-width of 1.7 pixels is then used to draw a polygon that outlines the fluorescence of the selected region (see Supplementary Figure 5). With this, a region 3.4 pixels in width is outlined. The masking operation used to select pixels chooses the pixels such that their centers fall within the polygon of the region selected. Thus, the regions selected are 3 to 4 pixels wide, depending on the location and orientation of the line of fluorescence with respect to the CCD array.

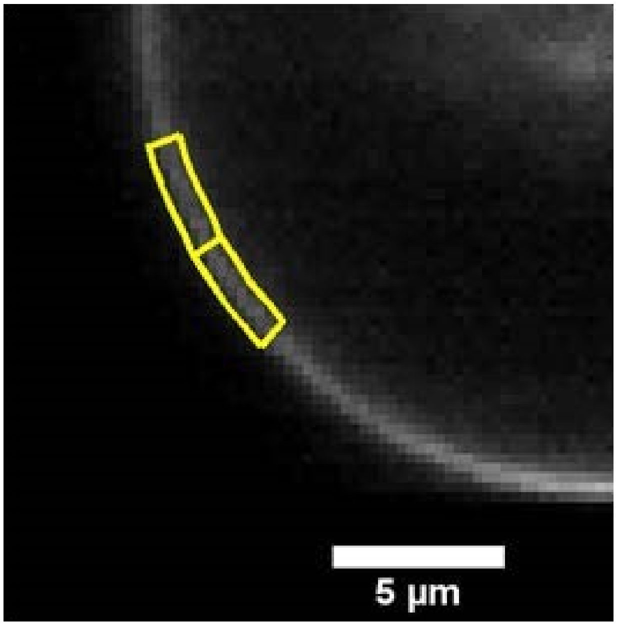

Figure 4-11. Selection of membrane regions: experiment. A cell under reversible osmotic stress is shown, with two ~3 µm regions selected. A 1.7 pixel half-width is used to outline the path of the membrane**.** Pixels with centers that fall within the outlined membrane region are selected and utilized for analysis.

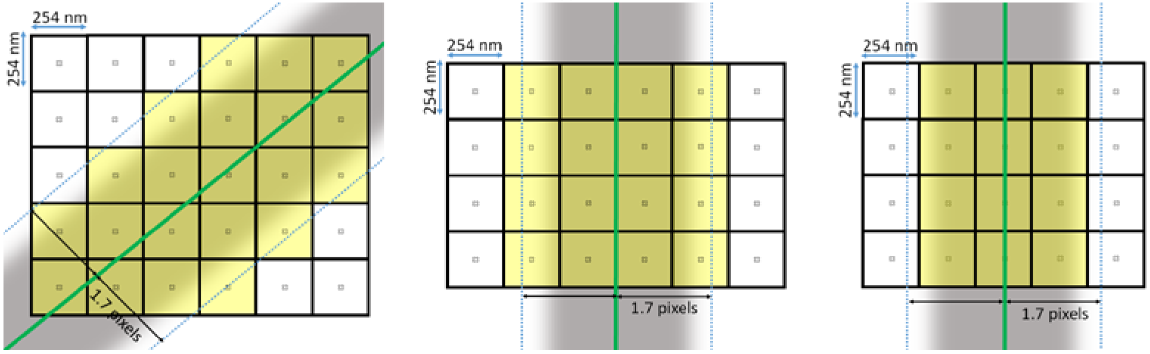

Figure 4-12. Selection of membrane regions. Shown here are three idealized representations of the orientation of the diffraction-limited line of membrane fluorescence that can be encountered in a cell image (light grey): diagonal to the pixels (left), in the center of a line of pixels (center) and between two lines of pixels (right). The line connecting points of fluorescence, chosen by the user, is shown in green. The region selection utilizing a 1.7 pixel region-half width will select regions three to four pixels across, depending on the orientation of the membrane with respect to the pixels of the CCD. Only pixels with centers that falls within the polygon outlining the fluorescence (blue dashed lines) are selected and used for further analysis (yellow).

4-4.6. Calculation of Region-level E_{app} and Receptor Surface Densities

The apparent pixel-level fluorophore (receptor) concentrations calculated during the image analysis must be integrated across the diffraction limited segment in order to properly determine the 2D surface density from the fluorescence and the calibration curves. To do so, F^D, F^A, and F^{AD} are integrated (summed) over every pixel selected in the region, $F_{\lambda i,Reg}^{D,A} = \int F_{region}^{D\ or\ A} dA = \sum F_{i,j}^{D\ or\ A}$. The apparent FRET efficiency of the region is then calculated as $E_{app} = 1 - {F_{\lambda 1,Reg}^{DA}}/{F_{\lambda 1,Reg}^{D}}$.

The total integrated fluorescence intensities for the region, $F_{\lambda 1,Reg}^{D}$, and $F_{\lambda 2,Reg}^{A}$, are then divided by the arc length, *s*, of the selected region to calculate the average integrated fluorescence per unit length of membrane (in units of pixel). We assume a perpendicular orientation of the membrane with respect to the focal plane. We also assume that the fluorescence originates from an infinitely thin sheet within the width of one pixel, or 254nm. To obtain the fluorescence that would be emitted by a full voxel of chromophores, the integrated fluorescence per unit pixel-length is multiplied by the pixel width, 254nm. By dividing the full voxel fluorescence by the average slope, $< i_{\lambda i}^{D,A} >$, and performing the appropriate unit conversion from micromolar concentrations to receptors per unit area (in units of rec/nm^2), the average receptor surface density for the region is calculated, as shown below in **Equation (4-34):**

$$[D\ or\ A]\left[\frac{rec}{nm^2}\right] = \frac{\sum F_{i,j}^{D\ or\ A}}{s \cdot < i_{\lambda i}^{D,A} >} \frac{[counts \cdot pixel^2]}{[pixel]} \left[\frac{counts}{\mu M}\right]^{-1} \cdot \frac{6.022 \cdot 10^{-7}}{[\mu M]} \left[\frac{rec}{nm^3}\right] \cdot 254 \left[\frac{nm}{pixel}\right] \tag{4-34}$$

4-4.7. The Need for Reversible Osmotic Stress

Measurements of dimer and oligomer stabilities (free energies of oligomerization) in membranes require knowledge of the 2D concentration of the proteins in the membrane and thus, detailed knowledge of membrane topologies and membrane areas [86]. The topology of the plasma membrane of cells, however, is very complex because cells possess 2 to 3 times the membrane needed to sustain their shape [87,88] (**Figure 4-13**). It has been shown, however, that the plasma membrane topology can be controlled in a completely reversible and non-lethal manner by subjecting cells to reversible osmotic stress [89]. As a result of the osmotic stress, cells disassemble their caveolae (60-80 nm cup-shaped invaginations) and "un-wrinkle" their membranes [89]. **Figures 4-13** and **4-14** compare the appearance of HEK293T cells, expressing VEGFR2 EC+TM, before and after the application of the reversible osmotic stress. The treatment results in a simple vesicle-like membrane topology[90], such that the 2D area of the membrane at the focal plane can be calculated precisely. Here I use such live cells under reversible osmotic stress to characterize VEGFR2 EC+TM interactions, in conjunction with the FSI method.

Correct two-dimensional concentrations in the membrane, and thus association curves and association free energies, cannot be determined if the cells are not subjected to reversible osmotic stress. This is consequence of the complex topology of the membrane within a voxel that is nearly a micron thick [87,88]. With the FSI methodology, in order to calculate the membrane-protein surface density, the topology of the 2-D surface must be known, and in this work, it is assumed that the proteins reside in a locally 2-D environment. **Figure 4-13** shows an image of a resting HEK293T cell, transiently transfected with VEGFR2 ECTM-GGS$_5$-Turq/YFP. **Figure 4-14** shows a hypotonically swollen HEK cell expressing the same fluorescent proteins. **Figure 4-15A**, top, shows a membrane patch from an intact cell, with diffraction limited features clearly visible, whereas **Figure 4-15A**, bottom, shows a membrane patch from a swollen cell. The membrane of the intact cell has a complex topology which is unknown, while the membrane of the swollen cell is perpendicular to the focal plane. The apparent pixel-level concentrations, and the apparent FRET efficiencies, calculated with the FSI method under the assumption that the membrane is perpendicular to the focal plane, are shown in **Figure 4-15B and C**.

For the intact cell, we see wide variations in fluorophore concentrations, but no such variations in FRET efficiencies. According to the thermodynamic formulation of the Kinetic Theory formalism, in a dimerizing system, the total fraction of dimers is dependent upon the total concentration of receptors, and thus a higher concentration must necessarily yield higher pixel-level FRET efficiency. The lack of correlation therefore demonstrates that the results for the intact cell have no physical meaning. To understand the consequence of working with intact cells, about 250 intact cells expressing EC+TM VEGFR2 were imaged and 513 regions of membrane were analyzed. The resultant FRET efficiency versus concentration data is shown in **Figure 4-16**, along with the complementary results for swollen cells. In addition to greatly increased scatter and the presence of negative FRET efficiencies, we see that the apparent concentrations appear much higher in intact cells despite the fact that the same protein is being expressed, a consequence of the membrane folds and wrinkles within the voxel thickness. Notably, the range of FRET efficiencies that are physically realistic are similar in the case of intact and swollen cells, suggesting that the interactions between membrane receptors are similar in both systems. Thus, swelling does not appear to have a significant effect on labeled membrane protein-protein interactions, but enables measurements of two-dimensional membrane protein concentrations. On the other hand, the use of intact, resting cells yields erroneous concentrations and thus precludes the calculations of association constants for membrane proteins.

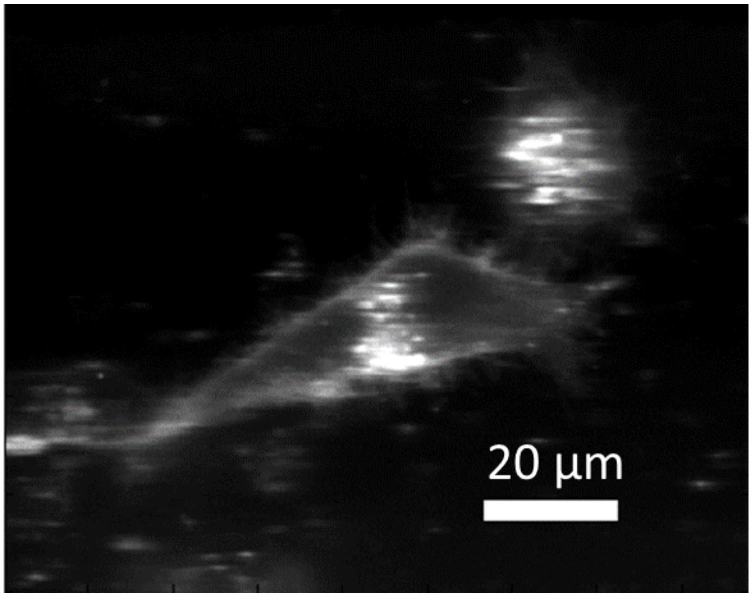

Figure 4-13. A resting HEK293T cell, transiently transfected with VEGFR2-ECTM-GGS$_5$-mTurquoise/YFP. VEGFR2 is localized to the cell membrane, and complex features are apparent in the membrane fluorescence.

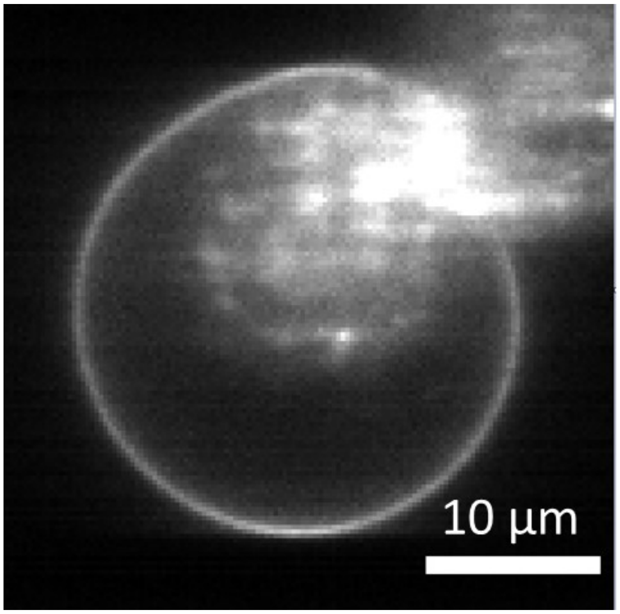

Figure 4-14. A hypotonically swollen HEK293T cell, transiently transfected with VEGFR2-ECTM-GGS$_5$-mTurquoise/YFP. VEGFR2 is localized to the cell membrane, and the diffraction-limited membrane fluorescence is smooth and homogenous.

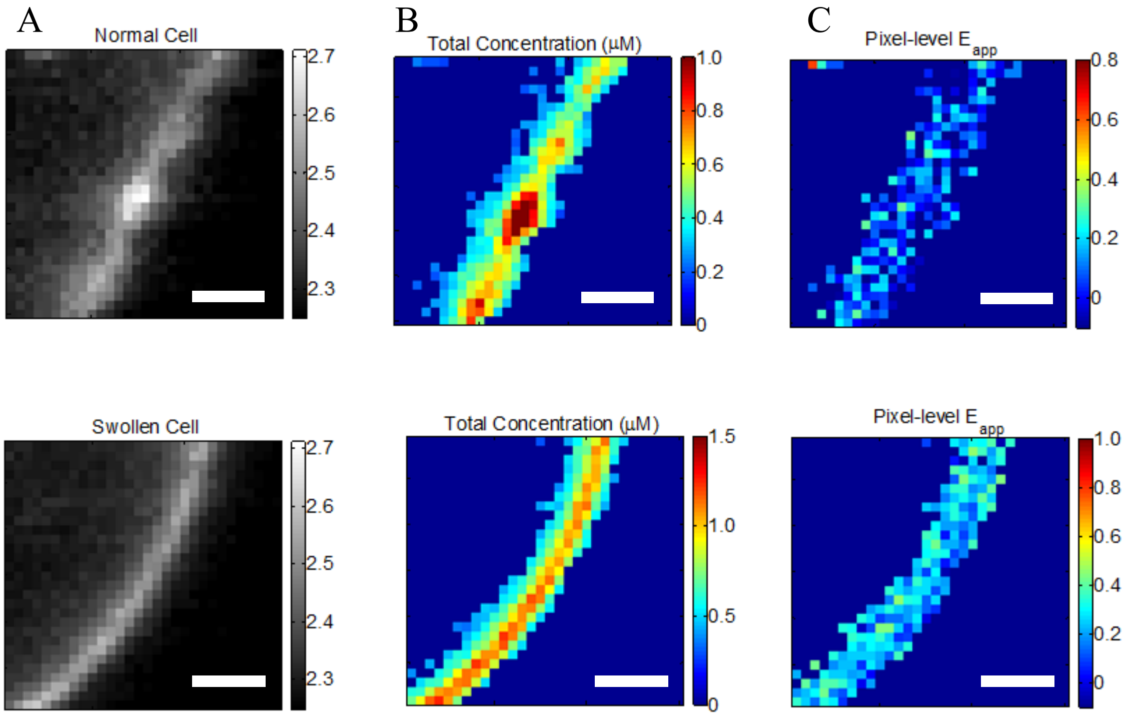

Figure 4-15. The effect of reversible cell swelling on membrane topology and FRET. Top: resting cell. Bottom: swollen cell. **A.** Selected membrane region. **B.** Map of pixel-level total concentrations. **C.** Map of pixel-level FRET efficiencies. In the intact cell, there is no correlation between the pixel-level apparent FRET efficiencies and the total concentration, in violation of the law of mass action. Scale bar: 2 microns.

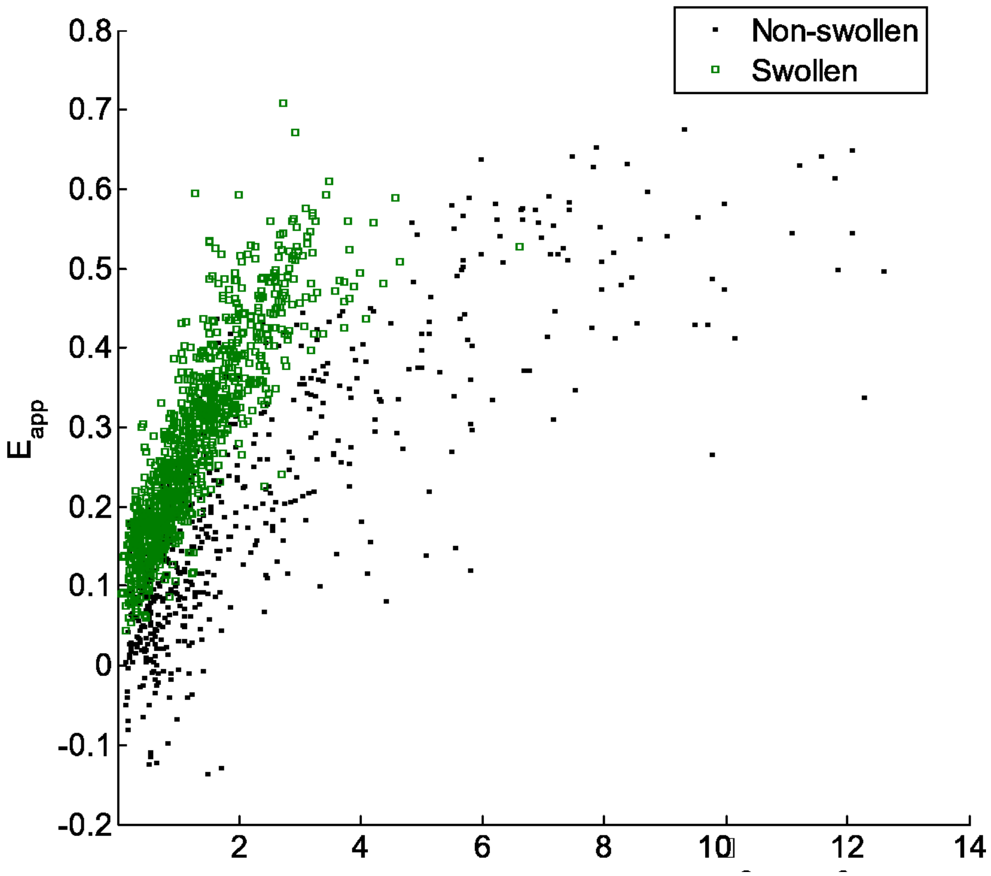

Figure 4-16. Measured FRET efficiencies versus total receptor concentrations, for cells under reversible osmotic stress (green) and intact cells (black). The calculated two dimensional concentrations for the intact cells are erroneous and thus association constants cannot be calculated. The range of measured FRET efficiencies is similar in both datasets indicating similar protein-protein interactions in the swollen cell membrane and the resting cell membrane.

4-5. Conclusions

In this chapter I have shown the theory and my implementation of the FSI method. In the next chapters, I will demonstrate the full utility of the FRET theory and the FSI methodology with a study into the heretofore unknown physical-chemical properties of VEGFR2 and its activating ligand VEGF, in the context of the living cell membrane. The methodology described up to this point will unlock the true mechanisms of many other receptors, ushering in a new paradigm for a thermodynamic understanding of *in vivo* receptor-receptor interactions and activation through direct measurement, instead of postulating based on a secondary reporter like phosphorylation in a Western Blot, or based on the behavior of isolated soluble domains in a crystal or a test tube.

Chapter 5. *Application of FRET Theory and FSI: VEGFR2 Mutagenesis and EC Domain Truncations Reveal Sequence-Specific Interactions in the Absence of VEGF*

5-1. Introduction

The model current model of VEGFR2 activation by VEGF says nothing about how the presence of VEGF causes the dimers of VEGFR2 to form. Since we (or at least I) believe that proteins and cells follow the laws of physics, this unphysical model of VEGFR2 interactions leaves much to be desired. Thus, to start, I worked to understand the behavior of the receptor in the absence of ligand, even if this state is not "biologically exciting." Therefore, I began by investigating the properties of a VEGFR2 construct composed of the EC and TM domains in the plasma membrane of live cells in the absence of VEGF, shown below in cartoon form in **Figure 5-1**.

I then investigated the specificity of the interactions between the EC domains in VEGFR2 dimers by first mutating a critical amino acid in the D7 subunit, D731, known to stabilize D7-D7 contacts in the isolated D7 crystals. Next, I created various rational truncations of the EC domain by removing sequential Ig-like domains from the VEGFR2 extracellular domain. A cartoon schematic of the truncated constructs, with fluorescent proteins attached to VEGFR2 TM domains via $(GGS)_5$ flexible linkers, is shown in **Figure 5-2**.

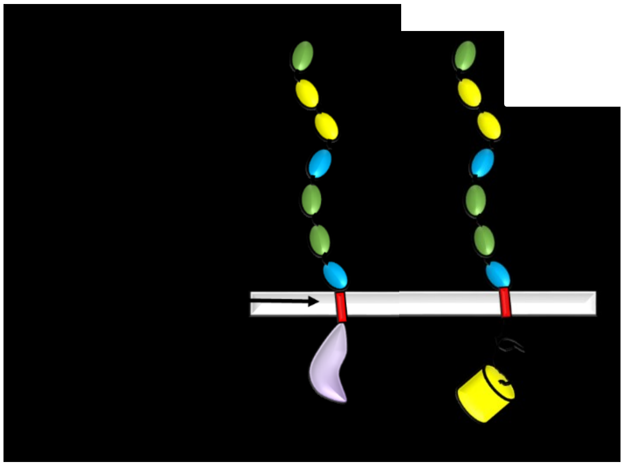

Figure 5-1. A cartoon of the VEGFR2 receptor and the construct with the intracellular domain replaced with a fluorescent protein used in my experiments. VEGFR2 has three primary domains: Extracellular (EC), Transmembrane (TM), and the intracellular kinase domain. The EC domain consists of seven Ig-like subunits known as subunits D1 through D7, with D1 at the N-terminus and D7 attached to the TM domain. The subunits D2 and D3, colored in yellow, are the ligand binding domains. D4 and D7, colored in blue, have been shown to be important in stabilizing the VEGFR2 ligand-bound dimer, but their role in the absence of ligand is unknown.

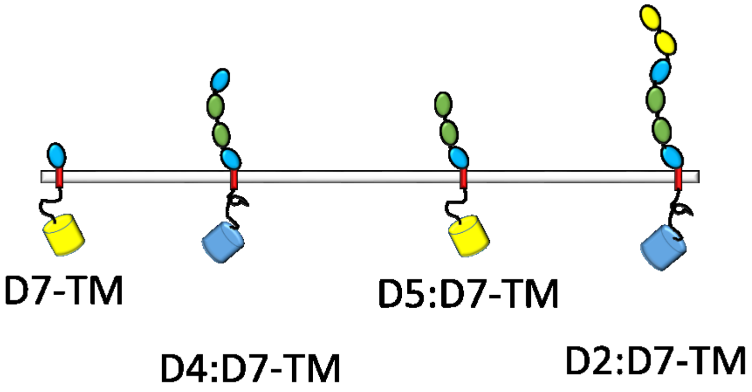

Figure 5-2. The different forms of VEGFR2 EC-TM with truncated EC domains. The D7-TM construct lacks domains D1-D6, and contains only the D7 subunit and the TM domain. The D4:D7-TM construct lacks the D1:D3 distal and VEGF-binding domains. The D5:D7-TM construct lacks the D1:D4 domains, and the D2:D7-TM construct lacks the VEGFR2 D1 domain.

The FSI method, developed in **Chapter 4** and used here to study VEGFR2, utilizes two excitation wavelengths, pixel-level full spectrum acquisition, and pixel-level fluorescence protein calibration curves. It yields approximation-free measurement of the apparent FRET efficiency, as well as the donor- and acceptor- labeled receptor surface densities of protein in the plasma membrane. As will be shown, FSI and the full Kinetic Theory formalism derived in **Chapter 2** allows the measurement of a complete binding (association) curve, and yields quantitative information about *in vivo* VEGFR2 interactions in the plasma membrane. The knowledge gained here through the use of the FSI methodology is new and challenges the current understanding of VEGFR2 signaling. Since VEGFR2 controls the development of blood vessels in a variety of solid tumors, the new knowledge could help guide the development of new VEGFR2 inhibitors as anti-cancer therapies.

5-2. Experimental Methods

5-2.1 Fluorescent Proteins

Soluble monomeric YFP and mTurquoise with an N-terminal 6x His tag were expressed and purified to near-milimolar concentrations as described previously. Fluorescent protein stocks were buffer exchanged into PBS buffer with a 20kDa MWCO concentrator (Pierce #87751) and filtered with a 0.2µm syringe filter. For each imaging session, the stocks were then diluted in buffer to micromolar concentrations to produce 100%, 75%, and 50% fluorescent protein solution standards. The mTurquoise and YFP solution standard concentrations were measured in a 1 cm path length quartz cuvette using NanoDrop 2000C (Thermo Scientific). Molar absorption coefficients of 83,400 Mol*cm^{-1} and 30,000 Mol*cm^{-1} were used to calculate the concentrations of the solution standards from the YFP and mTurquoise absorption maxima of 514 nm and 434 nm, respectively. Images of the 100%, 75%, 50% FP solution standards and a PBS buffer-only control were acquired at both excitation wavelengths and were used for the calculation of the pixel-level slope values, as described in the **Chapter 4**.

5-2.2 Plasmid Constructs

A pBE plasmid encoding for the VEGFR2 signal sequence, extracellular domain, transmembrane domain, a 15 amino acid GGS linker, and yellow fluorescent protein (YFP) was received from Dr. Kurt Ballmer-Hofer, Paul Scherrer Institute, and was the starting product for the mutagenesis required for this work. The A206K mutation was introduced into YFP using QuikChange to render it monomeric. The pcDNA 3.1+ VEGFR2-EC-TM-

$(GGS)_5$-mTurqoise construct was created by ligating a double-digested PCR insert of the mTurqoise gene between the AgeI and XbaI restriction sites that flank the fluorescent protein sequence, thus replacing YFP with mTurqoise. Ligations were performed with the Roche Rapid DNA Ligation Kit (#11635379001), according to the manufacturer's protocol. I am thankful to Sarvenaz Sarabipour for performing these subcloning steps, but I personally performed the subcloning for every other construct described here. VEGFR2 ECTM-GGS_5-FP constructs with a D731A mutation and a D731R mutation were created in the same manner as the YFP A206K mutagenesis using the QuikChange II XL Site-Directed Mutagenesis Kit (Catalog #200251) according to the manufacturer's protocol.

Ligation-dependent cloning utilizing restriction enzymes is difficult and tedious, and as such I searched for new, improved methods for cloning truncations of the VEGFR2 EC domain in to pcDNA. Ultimately, I decided that Gibson Cloning, developed in 2009, was the superior method for subcloning. Truncated ECTM constructs were designed based on the sequence locations of the VEGFR2 EC domain subunits, determined with UniProt. D2:D7-TM, D4:D7-TM, D5:D7-TM, D7-TM connected to GGS_5-mTurqoise or YFP were cloned using the NEBuilder® HiFi DNA Assembly Master Mix (E2621L) cloning kit, according to the manufacturer's protocol. Briefly, the pcDNA3.1+ was linearized with PCR. Primers for the truncated EC-TM-FP inserts were designed with 18 bp complementary overhangs to the pcDNA vector, which was produced via PCR using the pcDNA 3.1+ VEGFR2 ECTM-FP plasmid as a template. Two-piece assembly reactions were then performed with a 2:1 insert to vector ratio. All plasmids were completely sequenced and the proper sequence was verified with the NCBI BLAST tool.

5-2.3 Cell Culture and Transient Transfection

HEK293T cells used for the expression of the VEGFR2-EC-TM-FP plasmid constructs were a kind gift from Dr. D. Wirtz, Johns Hopkins University. The cells were cultured in DMEM supplemented with 10% FBS and 20mM glucose, at 37° C in a 5% CO_2 environment.

Twenty four hours prior to transfection, HEK293T cells were seeded in collagen-coated, glass bottom 35mm petri dishes (MatTek, P35GCOL-1.5-14-C) at a density of 2.5e5 cells per dish to achieve 60-70 percent confluency at the time of transfection, 24 hours later. Single transfections were performed with a total 3 μg of plasmid DNA and cotransfections were performed with a total 4-9 μg of plasmid DNA, using Lipofectamine 3000 (Invitrogen) according to the manufacturer's protocol. A 1:3 donor to acceptor plasmid ratio was used in many cotransfection experiments, but for the D7-TM constructs, D:A ratios were widely varied in an attempt to discern the oligomer order before I had developed the theory that shows the oligomer order is not discernable. Dang.

I found that the addition of 10 mM sodium butyrate greatly enhanced expression of the pcDNA 3.1+ VEGFR2 EC-TM-$(GGS)_3$–FP construct in HEK293T cells [91,92]. Thus, six hours after transfection, 10mM sodium butyrate was added to the cells. I learned about the effects of sodium butyrate on expression with plasmids containing the CMV promoter from a biologist at the FASEB conference on cell-membrane biophysics. Twelve hours after transfection, the cells were rinsed twice with phenol-red free, serum free DMEM (Sigma, D2902) to remove all traces of phenol red and the cells were serum starved for at least 12 hours in the presence of 10 mM sodium butyrate, prior to the application of osmotic stress and imaging.

5-2.4 Cells Under Reversible Osmotic Stress

Hypotonic swelling media was composed of serum-free media, diluted 1:9 with diH_2O, buffered with 25mM HEPES, and 0.2µm sterile filtered. Just prior to imaging, the starvation media was aspirated from the petri dishes and was gently replaced with 1mL of 37°C hypotonic swelling media[899878685848180807979797978787776757473706867]. The cells in each dish were allowed to stabilize for at least 10 minutes before imaging, and swollen cell images were acquired for up to two hours per dish post swelling.

5-3. VEGFR2 EC-TM

Results for the wild-type VEGFR2 EC+TM measurements are shown in **Figure 5-3**. 538 HEK293T cells, co-transfected with VEGFR2 EC+TM-mTurq and VEGFR2 EC+TM-YFP were imaged with the FSI method, yielding 1024 regions, ~3 μm in length, of homogenous membrane fluorescence for analysis. **Figure 5-3A** shows the measured total apparent FRET efficiency as a function of total VEGFR2 EC-TM expression in blue. There is a high variability in total receptor expression levels due to transient transfection of the HEK293T cells. In the FSI methodology, this variability is embraced and utilized to ultimately produce binding curves for the receptors. We see that the apparent FRET efficiency increases as a function of the total receptor concentration, suggesting a concentration dependent protein-protein association in the membrane. The mole-fraction of VEGFR2 EC+TM-YFP (the acceptor-tagged receptors), for each membrane region, is shown in **Figure 5-3B** (blue bars). The average values agree closely with those expected for the 1:3 donor-to-acceptor ratio used in transfection.

The wild-type VEGFR2 EC+TM data in blue in **Figure 5-3A** are used to determine the type of oligomer in the membrane (dimer, trimer, tetramer, etc) that best describes the data. The Kinetic Theory formalism developed in **Chapter 2** is used to compute the theoretical apparent FRET efficiency as a function of total concentration for different oligomeric models (e.g., monomer-only, monomer-dimer, monomer-trimer, monomer-tetramer, etc.). These models, which include a contribution for stochastic FRET [64,93] were fitted to the data. Theoretical binding curves for a particular oligomeric association model depend on two unknown parameters: the monomer-oligomer association constant K and the Intrinsic FRET, or the pairwise FRET efficiency. The Intrinsic FRET (the pairwise

FRET efficiency) is a structural parameter which depends on the average separation between the fluorescent proteins in the oligomer, but not on the association constant, K [86]. The least squared error is calculated for each oligomeric model, along with the optimal K and Intrinsic FRET values. The model which gives the lowest mean squared error (MSE) is considered the best overall model to represent the data.

For wild-type VEGFR2 EC+TM, the best-fit is achieved for the monomer-dimer equilibrium model**,** which yields the lowest overall MSE **(Figure 5-3C)**. **Figure 5A** compares the measured apparent FRET efficiency and the best-fit theoretical apparent FRET efficiency for VEGFR2 EC+TM, with the best-fit theoretical model for the total apparent FRET efficiency, shown in red. We see good agreement with the measured data and the theoretical model. The corresponding dimerization curve is shown in **Figure 5-3D**. With respect to $K_0 = 1\ (\text{rec/nm}^2)^{-1}$, the apparent Gibbs free energy, $-RT\ln(K/K_0)$, of VEGFR2 EC+TM dimerization is -3.5 ± 0.1 kcal/mol. The Intrinsic FRET for the donor-acceptor pair in the VEGFR2 EC+TM dimer is 0.85 ± 0.05, corresponding to a donor-to-acceptor distance of 4.1 nm (95% confidence interval: 3.8 to 4.3 nm).

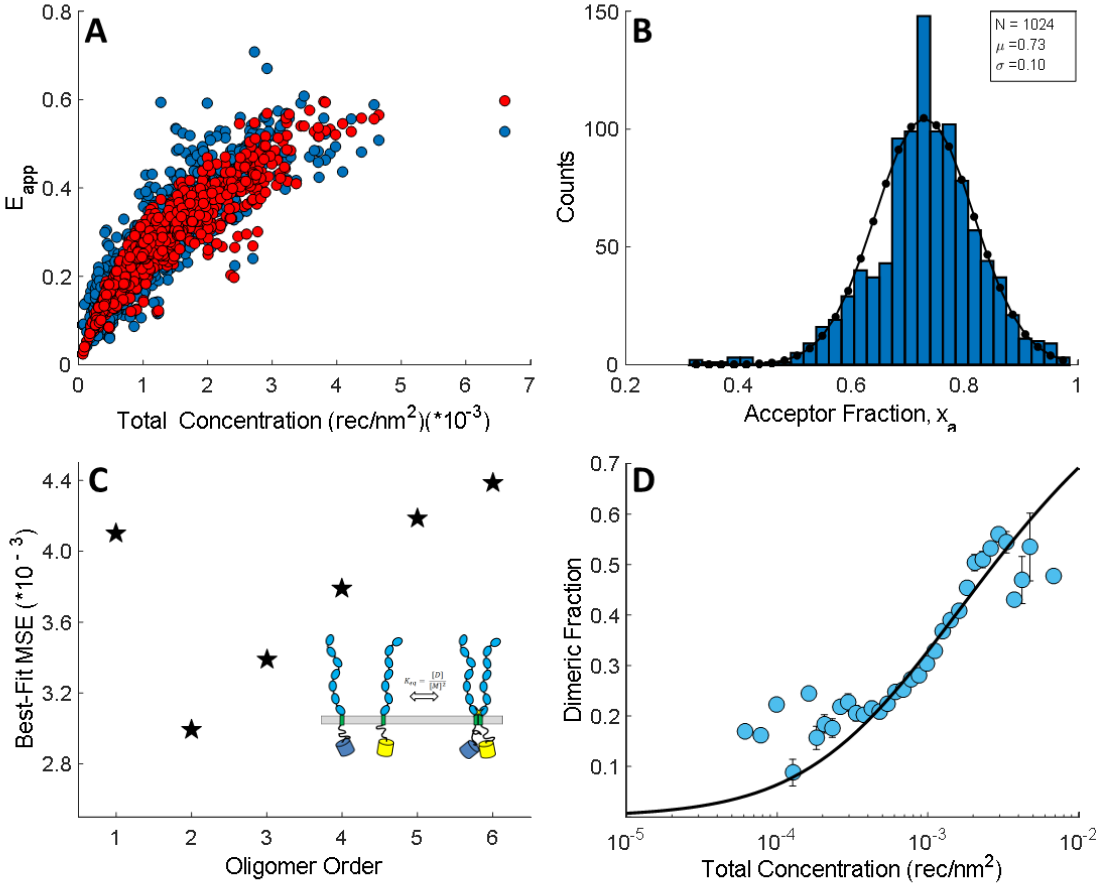

Figure 5-3. The results of the FSI measurements and the analysis with the full Kinetic Theory formalism for the VEGFR2 EC-TM construct. **A.** The measured total apparent FRET efficiency in the regions (blue) and the best-fit theoretical total apparent FRET efficiency (red) as a function of total VEGFR2 EC-TM expression. **B.** A histogram of measured acceptor fractions. **C.** The best-fit MSE as a function of oligomer order. The best-fit is a monomer-dimer equilibrium at $n = 2$. **D.** The measured total apparent FRET efficiency is transformed and binned to plot the dimeric fraction and the best-fit dimeric fraction as a function of total VEGFR2 EC-TM surface density.

5-4. *VEGFR2 EC-TM D731 Mutants*

The crystal structure of the isolated D7 VEGFR2 EC domains (PDB entry 3KQV) shows a very prominent salt bridge between residues D731 and R726, joining two adjacent molecules in the dimer [94]. It has been proposed that these contacts form in the ligand-bound dimer, and the occurrence and nature of sequence-specific EC domain contacts are not known. Previously published results show that mutant forms of VEGFR2 in which this salt-bridge is broken experience drastically reduced Tyrosine phosphorylation in the presence of VEGF. These results were interpreted to mean the VEGFR2 D731A mutant was predominantly monomeric.

5-4.1 VEGFR2 EC-TM D731A

To study if this salt bridge plays a role in VEGFR2 EC+TM dimer stabilization in the absence of ligand, I introduced a D731A mutation in VEGFR2 EC+TM and measured the self-association of this mutant in the plasma membrane with the FSI method. 278 swollen cells expressing the D731A mutant were imaged, and 523 ~3 μm membrane regions in these cells were analyzed to yield FRET efficiencies, donor concentrations, and acceptor concentrations. The results are shown in **Figure 5-4A** in green. While I expected that the D731A mutation would destabilize the VEGFR2 dimer and thus decrease the FRET efficiencies and dimerization propensity, I instead observed a very large increase in FRET over all receptor concentrations.

Next I sought to determine the type of oligomeric interaction in the membrane that best describes the mutant data. The MSE for tetramers, pentamers and hexamers are all very similar, with no apparent minimum in the MSE as the oligomer order was increased

(**Figure 5C**). Thus, no single oligomeric model greater than a dimer could be singled out as providing the best fit to the data. **Figure 5D** shows the best-fit oligomeric fraction as a function of total concentration. We see that the oligomeric fraction of the D731A construct is greatly enhanced over the dimeric fraction of VEGFR2 EC-TM. For example by comparing **Figure 5-3D** and **Figure 5-4D**, we see that at $1\text{x}10^{-3}$ receptors/nm^2, the oligomeric fraction of the D731A mutant is ~80%, while for VEGFR2 EC-TM, the dimeric fraction is ~40%. The MSEs for all these oligomers, however, were much smaller than the dimer MSE. Thus, the data analysis indicates that the D731A mutation induced higher-order oligomerization greater than dimerization of VEGFR2 EC+TM in the plasma membrane. This FRET signature is likely due to the formation of large aggregates, or due to heterogeneous populations of mutant VEGFR2 EC-TM D731A oligomers, undergoing non-specific associations. My simulations in **Chapter 3** predict this indeterminacy in analysis of the higher-oligomer order. Here we see that my previous work really does describe the FRET that will be measured for any possible situation and that in general, the order of higher-order oligomer formation will not be discernable with a bulk, two-color static quenching FRET experiment. **Figure 5-10** shows the oligomeric fractions for all of the constructs measured here for comparison.

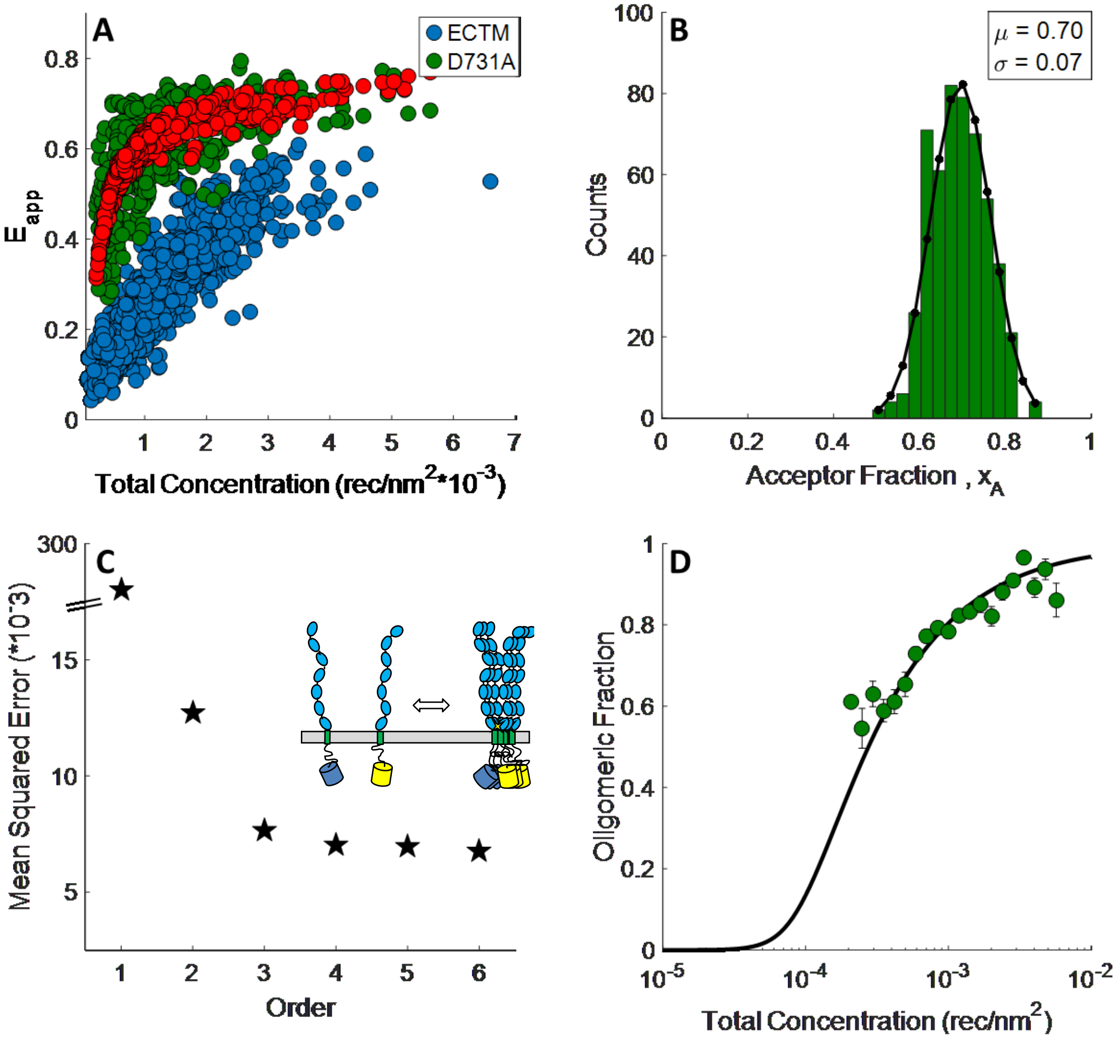

Figure 5-4. The results of the FSI measurements and the analysis with the full Kinetic Theory formalism for the VEGFR2 EC-TM D731A mutant construct. **A.** The measured total apparent FRET efficiency in the regions (green) and the best-fit theoretical total apparent FRET efficiency (red) as a function of total VEGFR2 EC-TM expression. The total apparent FRET efficiency of the VEGFR2 EC-TM construct is shown again in blue for comparison of FRET levels. **B.** A histogram of measured acceptor fractions. **C.** The best-fit MSE as a function of oligomer order. The best-fit is a monomer-oligomer equilibrium at $n > 2$. **D.** The best-fit oligomeric fraction is plotted as a function of total VEGFR2 EC-TM concentration.

5-4.2 VEGFR2 EC-TM D731R

In order to see if the D731A mutation underwent oligomerization due to the effect of the presence of the Alanine, I completely reversed the polarity of the aspartic acid side chain by replacing it with a positively charged Arginine. **Figure 5-5** shows the results of the FSI measurements with the VEGFR2 EC-TM D731R construct. In all, 118 cells were imaged, yielding 145 data points for analysis with the Kinetic Theory formalism. The measured total apparent FRET efficiency is plotted in **Figure 5-5A** as a function of total VEGFR2 EC-TM D731R surface density, in purple. **Figure 5-5B** shows the measured acceptor mole fractions in the experiment, and again they agree well with that expected for the ~1:3 D:A ratio of plasmid used for transient transfection.

Figure 5-5C shows the results of the analysis with the Kinetic Theory formalism derived in **Chapter 2**, where the best-fit MSE is plotted as a function of oligomer order. As with the D731A EC-TM mutant, the D731R EC-TM mutant undergoes strong oligomerization, and there is no minimum in the MSE versus oligomer order plot. In **Figure 5-5D**, the measured total apparent FRET efficiency data are transformed into the measured oligomeric fraction, and binned and plotted as a function of total concentration, along with the theoretical oligomeric fraction obtained through the analysis. This data along with the D731A mutant show that sequence specific interactions between unliganded VEGFR2 EC domains, at the very least, D7-D7 homotypic interactions involving the salt bridge, are required for proper dimerization of the receptor. Without these sequence-specific interactions, VEGFR2 has a robust propensity to oligomerize and is never monomeric. **Figure 5-10** shows the oligomeric fractions for all of the constructs measured here for comparison.

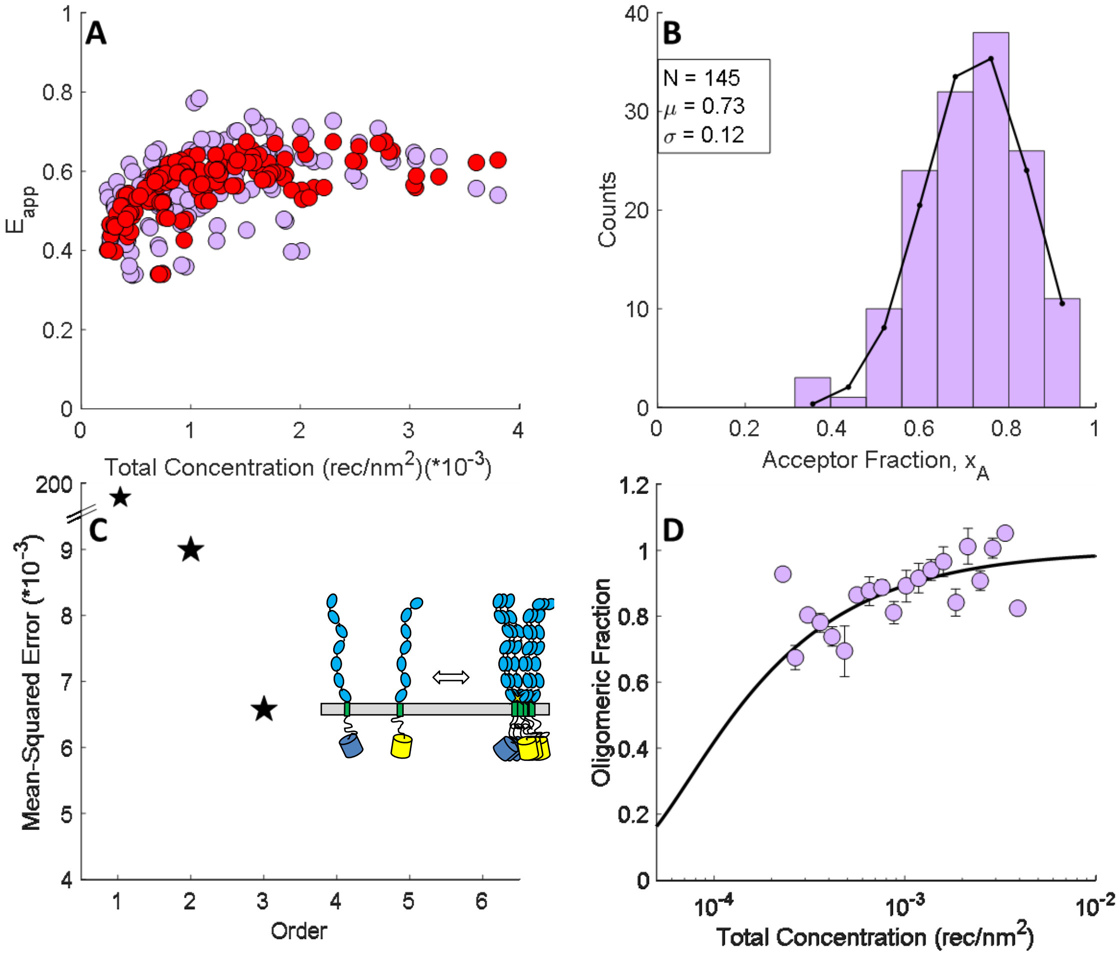

Figure 5-5. The results of the FSI measurements and the analysis with the full Kinetic Theory formalism for the VEGFR2 EC-TM D731A mutant construct. **A.** The measured total apparent FRET efficiency in the regions (purple) and the best-fit theoretical total apparent FRET efficiency (red) as a function of total VEGFR2 EC-TM expression. **B.** A histogram of measured acceptor fractions. **C.** The best-fit MSE as a function of oligomer order. The best-fit is a monomer-oligomer equilibrium at $n > 2$. **D.** The best-fit oligomeric fraction is plotted as a function of total VEGFR2 EC-TM concentration.

5-5. VEGFR2 D7-TM

A series of truncations of the VEGFR2 EC domain were created to determine which subunits are essential of dimerization of VEGFR2 EC-TM, shown in **Section 5-3.** To begin with, the entire EC domain was removed except for the juxtamembrane subunit D7. 666 cells expressing the VEGFR2 D7-TM truncated receptor were imaged yielding 1,170 regions for analysis with the Kinetic Theory formalism. **Figure 5-6** shows the results of the measurements and analysis of the VEGFR2 D7-TM construct. **Figure 5-6A** shows the measured total apparent FRET efficiency as a function of total concentration in yellow. The D:A (mTurquoise/YFP) transfection ratios were widely varied with this construct, as shown with the histogrammed acceptor fraction values in **Figure 5-6B**. As a result, we see a wide range of measured total apparent FRET efficiency values in **Figure 5-6A**.

I analyzed the data shown in **Figure 5-6A** with the Kinetic Theory formalism described in **Chapter 2**, and the results are shown in **Figure 5-6C.** I show the best-fit MSE as a function of oligomer order. There is no minimum in the MSE vs. oligomer order plot, and thus we see that the D7-TM constructs oligomerize in the cell membrane. The best-fit total apparent FRET efficiency is plotted in red in **Figure 5-6A** alongside the measured total apparent FRET efficiency. The best-fit total apparent FRET efficiency is in great agreement with the measured data. In **Figure 5-6D**, the measured total apparent FRET efficiency values are algebraically transformed into the measured oligomeric fraction, binned, and plotted alongside the best-fit oligomeric fraction. Comparing the oligomeric fraction of the D7-TM construct with that of the VEGFR2 EC-TM D731A and D731R oligomeric fractions shows that this D7-TM construct experiences a much stronger thermodynamic propensity for oligomerization. These experimental results are interpreted as showing that the presence of the D1:D6 subunits serves to reduce the dimerization/oligomerization propensity of VEGFR2 EC-TM domains. **Figure 5-10** shows the oligomeric fractions for all of the constructs measured here for comparison.

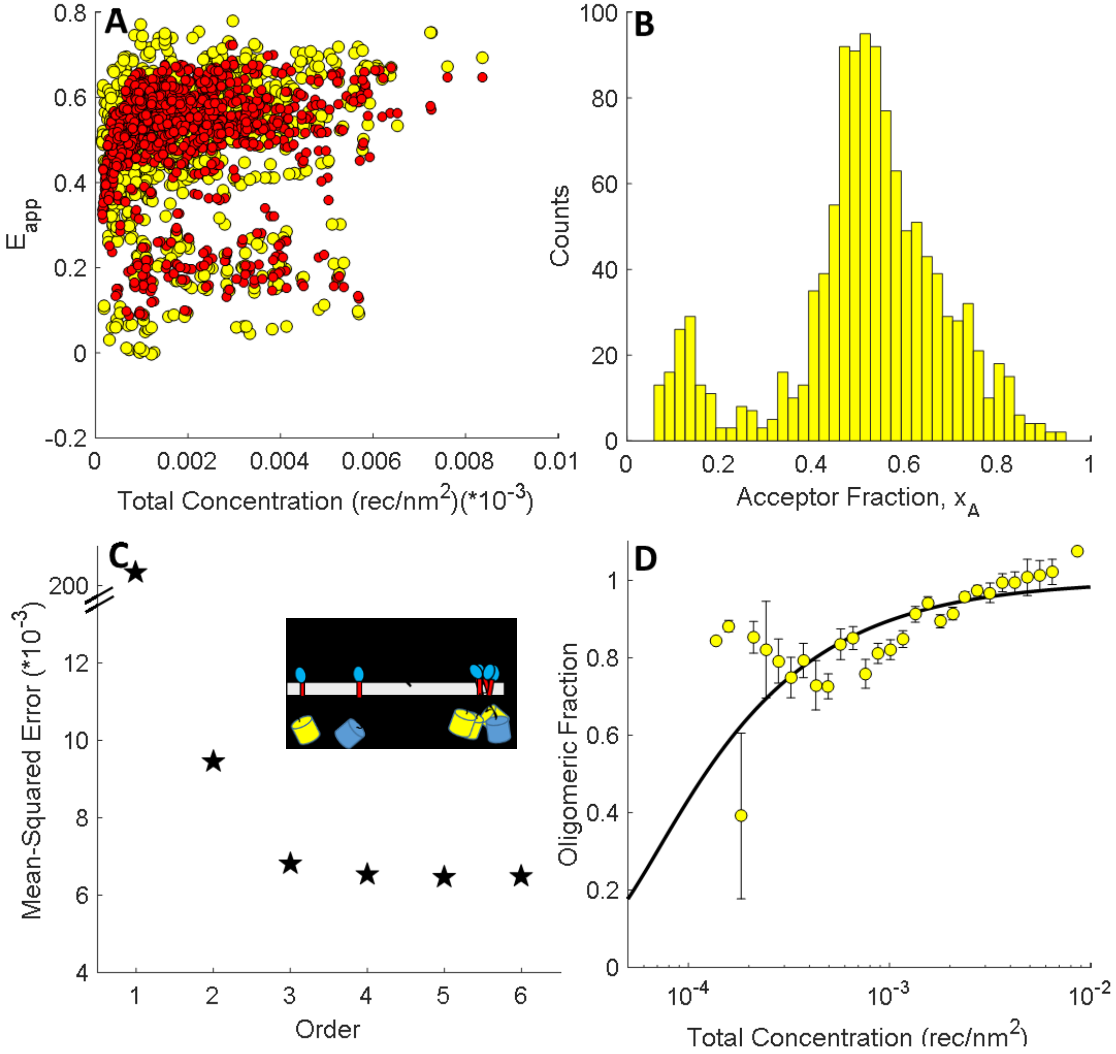

Figure 5-6. The results of the FSI measurements and the analysis with the full Kinetic Theory formalism for the VEGFR2 D7-TM truncated EC domain construct. **A.** The measured total apparent FRET efficiency in the regions (yellow) and the best-fit theoretical total apparent FRET efficiency (red) as a function of total VEGFR2 EC-TM expression. **B.** A histogram of measured acceptor fractions. **C.** The best-fit MSE as a function of oligomer order. The best-fit is a monomer-oligomer equilibrium at $n > 2$. **D.** The best-fit oligomeric fraction is plotted as a function of total VEGFR2 EC-TM concentration along with the measured oligomeric fraction of receptors.

5-6. VEGFR2 D5:D7-TM

In order to try to determine which subunits of the VEGFR2 extracellular domain are required for dimerization of VEGFR EC-TM constructs in the absence of ligand, the D5:D7-TM-GGS$_5$-mTurquoise and YFP constructs were cloned. The D5:D7-TM constructs are truncated VEGFR2 EC domains lacking distal domain D1, the ligand-binding domains D5 and D6, and a domain shown to participate in homotypic interactions in the ligand bound VEGFR2 dimer, D4. Images of 216 cells yielded 347 regions of homogenous, diffraction-limited membrane fluorescence for analysis. **Figure 5-7** shows the results of these measurements and the analysis of the data. In **Figure 5-7A** the total apparent FRET efficiency is plotted as a function of measured D5-D7:TM surface density in the transiently-transfected cell in purple. In **Figure 5-7B**, the measured acceptor-fractions are histogrammed and agree well with that expected for a ~1:3 D:A ratio of plasmids, as utilized for the transient transfections.

Figure 5-7C shows the best-fit mean-squared error as a function of theoretical oligomer order. The MSE versus order plot shows that the D5:D7-TM constructs also form oligomers, as the best-fit MSEs indicate that oligomer formation, $n > 2$, is occurring. The best-fit theoretical total apparent FRET efficiency for oligomer formation is plotted in red in Figure 5-7A. The best-fit agrees well with the measured data. The measured total apparent FRET efficiency is algebraically transformed into the measured oligomeric fraction, binned, and plotted as a function of total D5:D7-TM surface density, along with the best-fit oligomeric fraction in **Figure 5-7D**. Comparing the oligomeric fraction as a function of total concentration for the D5:D7-TM construct to that of the D7-TM construct in **Figure 5-6D** shows that the presence of D5 and D6 subunits greatly inhibits oligomerization of the VEGFR2 EC-TM construct. **Figure 5-10** shows the oligomeric fractions for all of the constructs measured here for comparison.

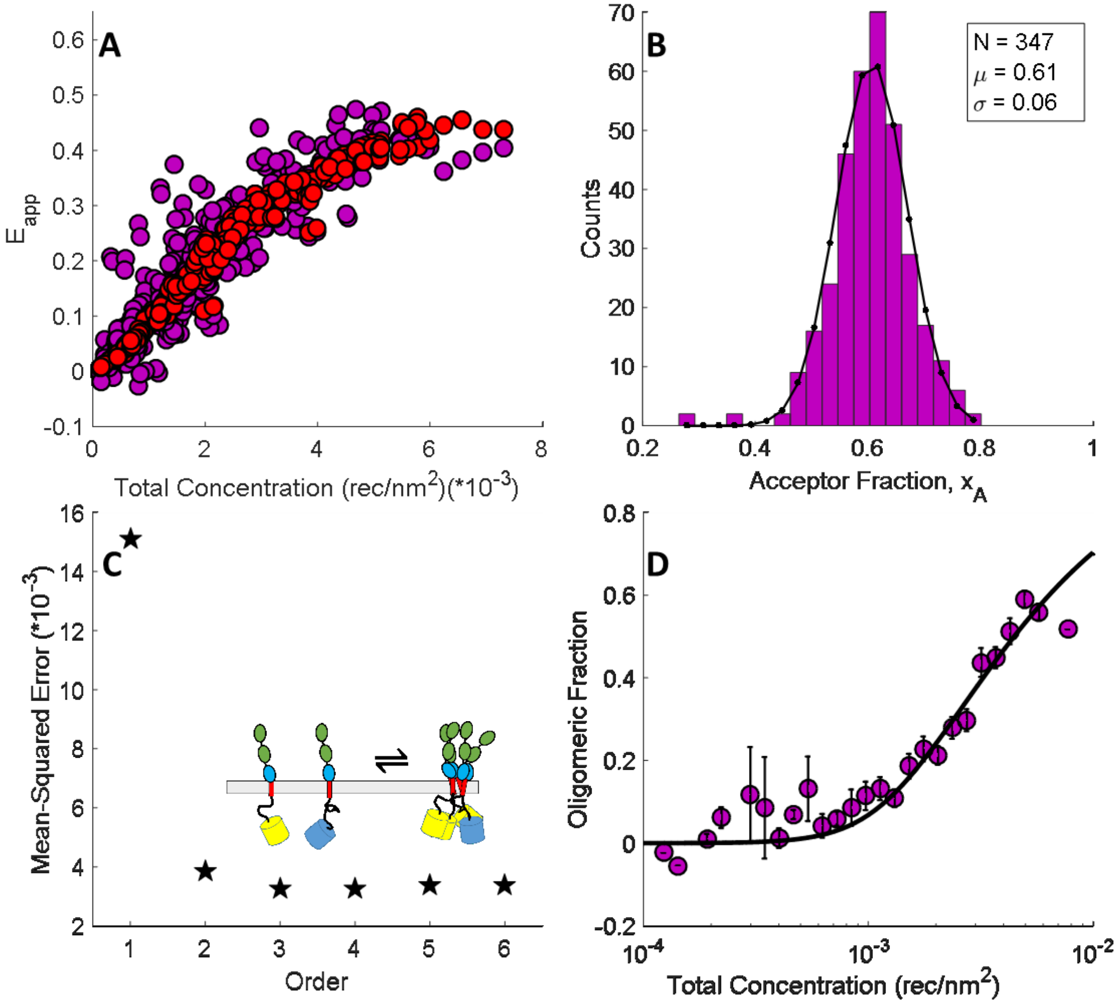

Figure 5-7. The results of the FSI measurements and the analysis with the full Kinetic Theory formalism for the VEGFR2 D5:D7-TM truncated EC domain construct. **A.** The measured total apparent FRET efficiency in the regions (purple) and the best-fit theoretical total apparent FRET efficiency (red) as a function of total VEGFR2 EC-TM expression. **B.** A histogram of measured acceptor fractions. **C.** The best-fit MSE as a function of oligomer order. The best-fit is a monomer-oligomer equilibrium at $n > 2$. **D.** The best-fit oligomeric fraction is plotted as a function of total VEGFR2 EC-TM concentration along with the measured oligomeric fraction of receptors.

5-7. VEGFR2 D4:D7-TM

The D4-D4 and D7-D7 homotypic interactions between VEGFR2 EC domain subunits in the ligand-bound dimer have been shown to be essential for proper signaling by the receptors. Thus, I created the D4:D7-TM-GGS$_5$-mTurquoise/YFP truncated VEGFR2 construct that lacks the distal domain, D1, and the ligand binding domains D2 and D3. 366 HEK293T cells co-transfected with the VEGFR2 D4:D7-TM construct were imaged, yielding 549 regions of diffraction-limited homogenous membrane fluorescence for analysis with the Kinetic Theory formalism. **Figure 5-8** shows the measured data and the analysis results. The measured total apparent FRET efficiency is plotted as a function of total VEGFR2 D4:D7-TM surface density in **Figure 5-8A**, in gray. In **Figure 5-B** the measured acceptor fractions are histogrammed, and agree well with that expected for a 1:3 donor-to-acceptor ratio of plasmids utilized in the transient transfection.

Figure 5-8C shows the results of the analysis of the measured data with the Kinetic Theory formalism, where the best-fit MSE is plotted as a function of theoretical oligomer order. The overall lowest MSE is found for the $n = 2$ model, indicating that dimerization is taking place between these truncated VEGFR2 constructs. The best-fit monomer-dimer model for the total apparent FRET efficiency is plotted in red in **Figure 5-8A**. The best-fit parameters for the monomer-dimer equilibrium model are an intrinsic FRET of $\tilde{E} = 0.74 \pm 0.03$ and a Gibbs free energy of association of $\Delta G° = -RTln\left({}^{K_A}/_{K_0}\right) = -3.0 \pm 0.1\ kcal/mol$, where $K_0 = 1\ {}^{rec}/_{nm^2}{}^{-1}$. Compared to the full-length VEGFR2 EC-TM construct, with an intrinsic FRET $\tilde{E} = 0.85 \pm 0.03$, the intrinsic FRET of the D4:D7-TM construct is significantly lower indicating that the fluorescent proteins are further apart, and that the C-termini of the TM domains is spaced further apart than the EC-TM construct's unliganded dimers. **Figure 5-8D** shows the measured dimeric fraction and the theoretical dimeric fraction.as a function of total concentration. The Gibbs free energy of association of the VEGFR2 EC-TM construct is 0.5 kcal/mol lower than that of the truncated D4:D7-TM construct, indicating slightly reduced dimerization of the truncated construct compared to that of the VEGFR2 EC-TM domains. **Figure 5-10** shows the oligomeric fractions for all of the constructs measured here for comparison.

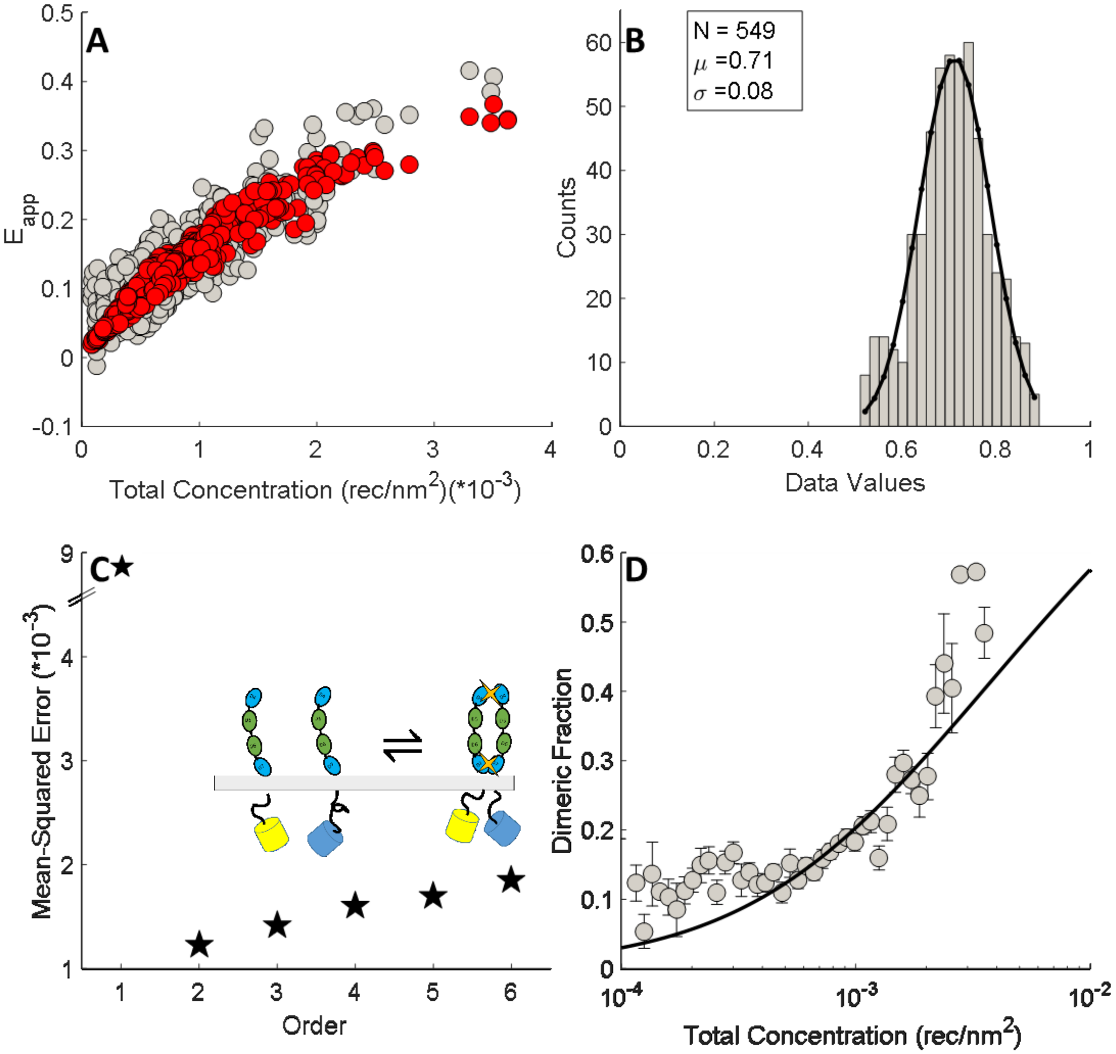

Figure 5-8. The results of the FSI measurements and the analysis with the full Kinetic Theory formalism for the VEGFR2 D4:D7-TM truncated EC domain construct. **A.** The measured total apparent FRET efficiency in the regions (gray) and the best-fit theoretical total apparent FRET efficiency (red) as a function of total VEGFR2 EC-TM expression. **B.** A histogram of measured acceptor fractions. **C.** The best-fit MSE as a function of oligomer order. The best-fit is a monomer-dimer equilibrium at $n = 2$. **D.** The best-fit dimeric fraction is plotted as a function of total VEGFR2 EC-TM concentration along with the measured, binned oligomeric fraction of receptors.

5-8. VEGFR2 D2:D7-TM

Since the D4:D7-TM construct had restored, but weaker dimerization of the VEGFR2 EC-TM construct, but with a structural shift in D:A distance and slightly reduced dimerization propensity, I reasoned that the presence of the distal domain, D1, or the ligand-binding domains, D2:D3, would be responsible restoring the dimerization of the VEGFR2 EC-TM constructs. Thus, I created the D2:D7-TM-GGS$_5$-mTurquoise/YFP truncated VEGFR2 construct that lacks the distal domain, D1 of the VEGFR2 extracellular domain. The cloning was performed and the plasmid constructs were sequence and verified to be correct with respect to the UniProt EC-domain sequence positions. Unfortunately, when HEK293T cells were transfected with this plasmid, the protein was retained the endoplasmic reticulum of the cells, and no cell-membrane fluorescence of properly localized proteins was observed. Thus, it appears that the properties of this truncated version of VEGFR2 will remain a mystery forever.

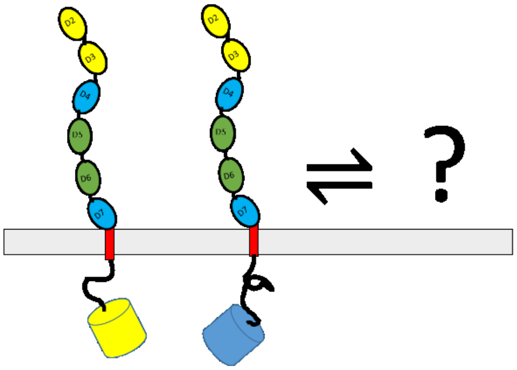

Figure 5-9. The thermodynamic properties of the VEGFR2 D2:D7-TM construct will remain unmeasured.

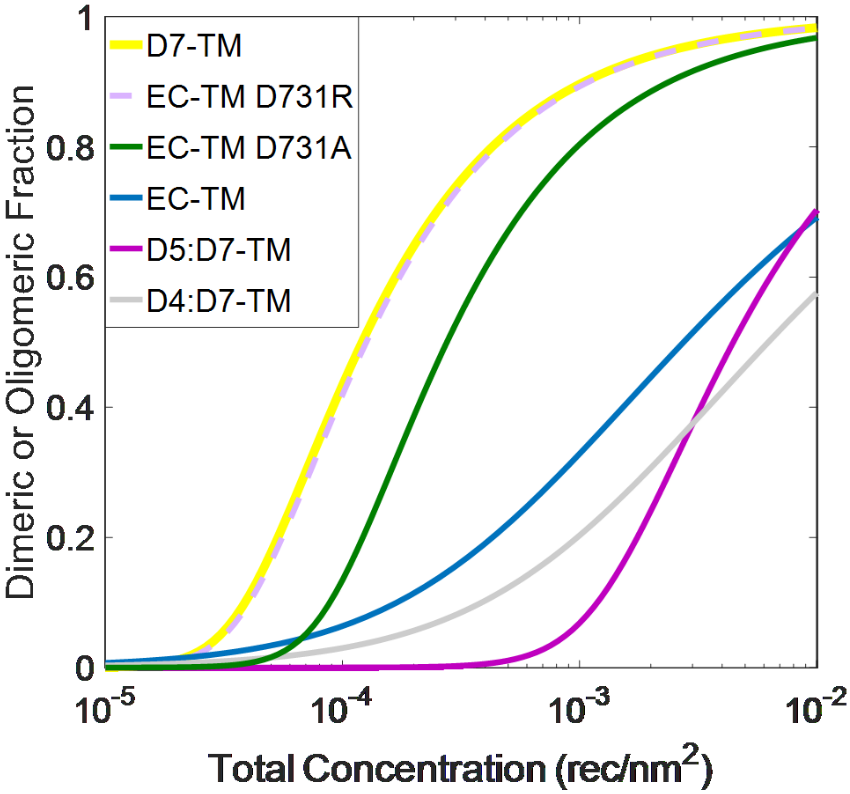

Figure 5-10. The best-fit dimeric fraction for the VEGFR2 EC-TM and the D4:D7-TM constructs, and the best-fit oligomeric fraction for the D7-TM, D5:D7-TM, EC-TM D731A , and EC-TM D731R as a function of total concentration.

5-9. Discussion and Conclusions

Here I sought to investigate the specificity of the 2D interactions between VEGFR2 EC domains in cellular membranes by destabilizing an inter-molecular salt bridge observed in crystal structures of isolated D7 dimers, and by creating versions of VEGFR2 with various truncations of the VEGFR2 extracellular domain. The mutagenesis of an aspartic acid involved in this interaction, D731, to alanine did not destabilize the VEGFR2 EC+ TM dimers, as we expected. Instead, the mutation introduced a very large, surprising perturbation in the receptor interactions, leading to receptor oligomerization. It is curious that engineered VEGFR2 TM domain mutations can also alter the oligomerization state of the isolated TM domain, inducing trimer formation [95]. It can be argued, therefore, that similar point mutations that are rationally designed by researchers to interrogate the function of VEGFR2, and RTKs in general, may have similar profound effects that complicate data interpretation if direct measurements of protein-protein interactions are not performed, such as with the FSI methodology and the Kinetic Theory formalism described earlier.

The large perturbation in interactions, observed here when D731 is mutated to Ala or Arg, suggests that the Asp731-Arg726 salt bridge between the D7 domains is important for VEGFR2 dimerization in the absence of ligand, as it ensures that VEGFR2 forms a dimer and not a higher-order oligomer. The mutagenesis therefore reveals that strong D7-D7 contacts occur in the VEGFR2 EC domain in the absence of ligand. This is fundamentally novel discovery, as D7-D7 interactions are currently believed to occur only upon ligand binding [16].

As shown in **Figure 5-10**, The strong oligomerization propensity of the D7-TM truncated construct shows that the primary function of the D7 subunit is to provide a robust thermodynamic base propensity for receptor-receptor interactions. We see that the D5:D7-TM truncated construct also oligomerizes, yet with drastically reduced oligomerization affinity. The oligomeric fraction is even much less than the dimeric fraction of the VEGFR2 EC-TM domains except at the lowest total concentrations of VEGFR2. Thus, it appears that the role of the D5 and D6 domains is to drastically reduce the strong propensity for oligomerization provided by the D7-TM construct.

The VEGFR2 D4:D7-TM construct showed restored dimerization, but with slightly weaker dimerization affinity than that of the VEGFR2 EC-TM construct, but with an enhanced dimeric fraction when compared to the D5:D7-TM construct. The D4:D7-TM constructs also had a larger donor-to-acceptor distance in the dimer, compared to that of the EC-TM protein. Thus, this data is interpreted to show that the same homotypic interactions that are required for functional VEGF-bound VEGFR2 dimers, D4-D4 and D7-D7 contacts, are also necessary for proper dimerization of the VEGFR2 EC-TM domains in the absence of ligand. Though I do not have direct experimental evidence, the lower dimeric binding affinity of the D4:D7-TM construct, compared to that of the VEGFR2 EC-TM, indicates that the D1 domain and/or the ligand binding domains D2 and D3 may participate in stabilizing the unliganded VEGFR2 dimer. **Figure 5-10**, below, gives the current model for VEGFR2 interactions in the absence of VEGF.

We see that essentially every subunit of the extracellular domain plays an important role in ensuring that VEGFR2 dimerizes at the “proper” affinity instead of oligomerizing with some different binding affinity. These sequence specific EC-domain interactions (and

TM domain contacts as well) are required for the structurally-proper form of the VEGFR2 dimer, even in the absence of ligand. I have shown that our previous understanding of the behavior of VEGFR2 in the plasma membrane of live cells in the absence of VEGF binding was incomplete. Despite many years of research, our understanding of VEGFR2 activation by VEGF, therefore, is likely incomplete as well, and deserves further investigation with the FSI methodology.

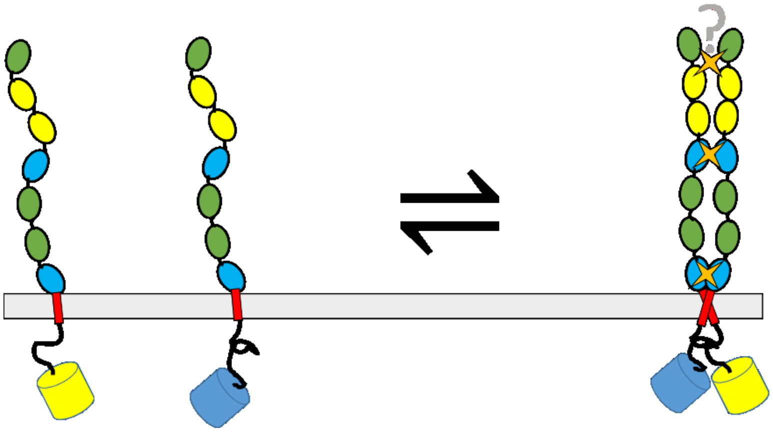

Figure 5-11. VEGFR2 dimerizes with sequence-specific interactions in the absence of VEGF. D7-D7 and D4-D4 homotypic contacts provide sequence specific interactions that ensure dimerization of VEGFR2, instead of oligomerization, as indicated by yellow stars. Additional interactions between D1, D2, or D3 are possibly indicated by the data, but the exact nature remains unknown.

Chapter 6. Advanced Application of FRET Theory and FSI: Measurement of VEGF Binding Affinity

6-1. Introduction

In this chapter, I utilize 2-photon excitation and the OptiMis spectral imaging system, in conjunction with the Fully Quantified Spectral Imaging (FSI) method, to measure the affinity of VEGF for monomeric and dimeric VEGFR2 on the surface of live cells. In addition to the ability to measure the three-dimensional concentration of freely diffusing fluorescently labeled moieties, FSI provides the unique ability to measure the surface density of fluorophore-labeled membrane proteins in 2-3 micron size patches of the cell membrane. I again utilize transiently transfected HEK293T cells expressing VEGFR2 ECTM, a truncated form of VEGFR2 that lacks the intracellular kinase domain, linked to YFP through a disordered $(GGS)_5$ linker. I then utilize a form of VEGF121 known as scVEGF (single chain VEGF) which is labeled with the organic dye Alexa Fluor 594. I measured the bound surface densities of VEGF as a function of expressed VEGFR2 surface density in many cells, each expressing a different total amount of VEGFR2. I also measured the free-ligand concentration directly in the buffer surrounding the cells. With this unique application of the FSI methodology, repeated for many different free-ligand concentrations, I am able to globally-fit 12 combined datasets and determine the separate values of the affinity of labeled VEGF for monomeric and dimeric forms of VEGFR2 EC domains. With these values in hand, there is full predictive power on the fraction of ligand bound dimers of full-length VEGFR2 for any local effective VEGFR2 surface density on the membrane of the cell and for any free-VEGF concentration.

6-2. *Theory: A Thermodynamic Cycle for VEGF Binding to VEGFR2*

Here I describe a thermodynamic cycle that accounts for all for all of the different forms of VEGFR2 that can exist in the presence of VEGF: monomeric (M), dimeric (D), ligand-bound monomers (LM), and ligand-bound dimers (LD) of VEGFR2 for measurement of VEGF binding affinities, as shown in **Figure 6-1**. This model assumes that one molecule of VEGF can bind per monomer or dimer of VEGFR2. With this thermodynamic cycle, all of the possible pathways for going from an unliganded-monomer of VEGFR2 to the active, VEGF-bound dimer of VEGFR2 are accounted for. We see along the top of the cycle, that VEGFR2 can undergo unliganded dimerization, with affinity K_R in units of receptors/nm^2.

$$K_R = \frac{[D]}{[M]^2} \tag{6-1}$$

VEGF can then bind to the pre-formed dimer of VEGFR2 with affinity K_{LD} having inverse molar units (M^{-1}):

$$K_{LD} = \frac{[LD]}{[L_{free}][D]} \tag{6-2}$$

Instead of dimerizing in the absence of ligand, if we move from the top left position in the thermodynamic cycle down in a counter-clockwise direction, VEGF ligand in solution can instead bind to a monomer of VEGFR2 with affinity $K_{LM}(M^{-1})$:

$$K_{LM} = \frac{[LM]}{[L_{free}][M]} \tag{6-3}$$

By moving right in the cycle, we see that a monomer of VEGFR with a bound VEGF, LM, binds to a monomer of VEGFR2 without bound ligand, M, and we again reach the ligand-bound, active dimeric form of VEGFR2. This association constant is defined in **Equation 4**, with units of $(rec/nm^2)^{-1}$:

$$K_{LMD} = \frac{[LD]}{[LM][M]} \tag{6-4}$$

Finally, if we continue counterclockwise down the cycle, we see that after a molecule of VEGF binds to both monomers with affinity K_{LM}, a molecule of VEGF can dissociate from a VEGFR2 receptor, providing the third pathway to a ligand-bound, active molecule of VEGFR2 with an association constant K_{LM-LD} with units of $\left({}^{M}/_{rec/nm^2}\right)$:

$$K_{LM-LD} = \frac{[LD][L_{free}]}{[M]^2} \tag{6-5}$$

In these experiments, I measure the total surface density of YFP-linked VEGFR2 EC-TM domains, [T] on the membrane of live cells:

$$[T] = [M] + 2[D] + [LM] + 2[LD] \tag{6-6}$$

The total bound VEGF surface density is also measured:

$$[L_{bound}] = [LM] + [LD] \tag{6-7}$$

Using the association constants defined above, **Equation (6-1) – Equation (6-3)**, we write the total concentration of VEGF2, $[T]$, in terms of the free-VEGF concentration, and the concentration of monomeric VEGFR2, as shown in **Equation (6-8):**

$$[T] = 2K_R\big(1 + [L]_{free}K_{LD}\big)[M]^2 + \big(1 + [L]_{free}K_{LM}\big)[M] \tag{6-8}$$

Next we write down the bound surface density of VEGF (**Equation (6-7)**) in terms of the monomeric VEGFR2 surface density, the free-VEGF concentration, and the association constants defined in **Equations (6-1) through (6-3)**:

$$[L]_{bound} = [L]_{free}[M](K_{LM} + [M]K_{LD}K_R) \tag{6-9}$$

By subtracting [T] from both sides of Equation 8, we then use the root of the second order polynomial to write the monomeric VEGFR2 surface density, [M], in terms of, K_R, $\left[L_{free}\right]$, $[T]$, the known and measured parameters, and our main parameters of interest: K_{LM} and K_{LD}. Substitution of $[M]$ into **Equation (6-9)**, provides a theoretical model for the bound surface density of VEGF as a function of the known parameters K_R, $\left[L_{free}\right]$, and $[T]$, and two unknown, adjustable parameters K_{LM} and K_{LD} . Due to linkage in the thermodynamic cycle, this model completely accounts for all of the different pathways for ligand binding to VEGFR2 EC domains, as depicted in **Figure 6-1**.

From the buffer fluorescence, I directly measure the three-dimensional equilibrium concentration of ligand in the dish surrounding the cells, $[L_{free}]$. Previous work has shown that the intrinsic binding affinity of VEGFR2 ECTM domains is equal to $K_R = \frac{[D]}{[M]^2} = 370\ ({}^{rec}/_{nm^2})^{-1}$. Thus, only two parameters remain undetermined in **Equation (6-8)** and **Equation (6-9)**: K_{LM} and K_{LD}. By measuring many cells with varying VEGFR2 surface densities and associated levels of bound VEGF, and repeating these measurements for many different levels of free-VEGF concentrations, global fitting can then be utilized on all of the combined datasets to determine the separate VEGF affinities for monomeric and dimeric forms of VEGFR2, K_{LM} and K_{LD}, with a non-linear least squares analysis implemented in MATLAB.

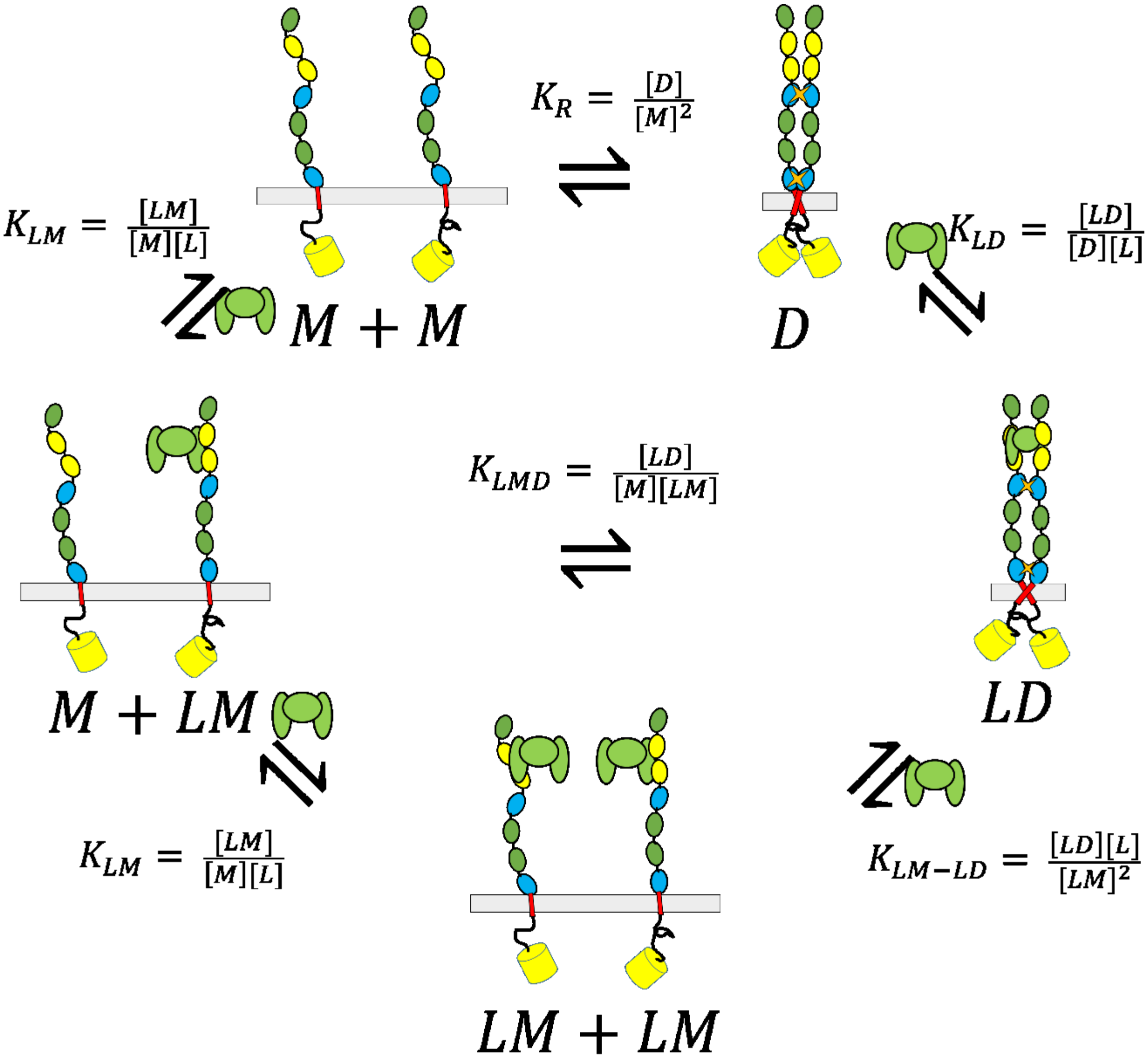

Figure 6-1. A thermodynamic cycle describing all of the ligand-free and ligand-bound forms of monomeric and dimeric VEGFR2, along with definitions of the association constants. As we move from top left to the right, we start with monomeric VEGFR2 (M). It can undergo unliganded dimerization (D) on the top path, with affinity K_R, whereby a free molecule of VEGF can then bind to the preformed VEGFR2 dimer (LD), which would represent the active form for the full-length receptors. On the other two paths to a liganded dimer of VEGFR2, if we move down from the M + M state, VEGF can bind to a monomer of VEGFR2 (LM). A liganded monomer can then bind to a monomeric receptor, or under saturating conditions, a molecule of VEGF will need to dissociate from a VEGFR2 monomer for dimerization to the active form of VEGFR2 with on molecule of VEGF bound. [L] has units of micromolar, while [M] and [D] have units of receptors/nm^2.

6-3. Methods

6-3.1. Plasmid Constructs

A pBE plasmid encoding for the VEGFR2 signal sequence, extracellular domain, transmembrane domain, a 15 amino acid GGS linker, and yellow fluorescent protein (YFP) was received from Dr. Kurt Ballmer-Hofer, Paul Scherrer Institute, and was the starting product for the mutagenesis required for this work. The A206K mutation was introduced into YFP using QuikChange to render it monomeric. The pcDNA 3.1+ VEGFR2-EC-TM-$(GGS)_5$-YFP construct was created by ligating a double-digested PCR insert of the ECTM-FP gene at restriction sites that flank the chimeric protein sequence, thus inserting the gene into the MCS of pcDNA 3.1+. Ligations were performed with the Roche Rapid DNA Ligation Kit (#11635379001), according to the manufacturer's protocol.

6-3.2. Alexa-Fluor 594 conjugated VEGF

In this work, I utilize scVEGF (single chain VEGF) conjugated to the organic dye Alexa Fluor 594, purchased commercially from Sibtech Inc (#SBT309) at >90% purity. The scVEGF conjugate utilized is a ~28 kDa moiety and consists of two fragments of human $VEGF_{121}$(AA 3-112) cloned head to tail and fused to an N-terminal Cys-Tag (SibTech #SBT301). The AF594-scVEGF (AF594-VEGF) conjugate is singly labeled in a site-specific manner at the C4 residue of the Cys-Tag, and retains 95-100% of VEGF activity. scVEGF was originally developed so that only one side of the cysteine-linked homodimer can be labeled at a time. I utilize it here to measure the binding affinity of VEGF to VEGFR2 EC domains.

6-3.3. Cell Culture and Transient Transfection

HEK293T cells are utilized with transient transfection in these experiments. The HEK293T cells used for the expression of the VEGFR2-EC-TM-YFP plasmid construct were a kind gift from Dr. D. Wirtz, Johns Hopkins University. The cells were cultured in DMEM supplemented with 10% FBS and 20mM glucose, at 37° C in a 5% CO_2 environment.

Twenty-four hours prior to transfection, HEK293T cells were seeded in collagen-coated, glass bottom 35mm petri dishes (MatTek, P35GCOL-1.5-14-C) at a density of 2.2e5 cells per dish to achieve ~65 percent confluency at the time of transfection, 24 hours later. Transfections were performed with a total 3 μg of plasmid DNA, using Lipofectamine 3000 (Invitrogen) transfection reagent, according to the manufacturer's protocol.

I found that the addition of 10 mM sodium butyrate greatly enhanced expression of the pcDNA 3.1+ VEGFR2 EC-TM-$(GGS)_3$ –YFP construct in HEK293T cells (37, 38). Thus, six hours after transfection, 10mM sodium butyrate was added to the cells. Twelve hours after transfection, the cells were rinsed twice with phenol red-free, serum-free DMEM (Sigma, D2902) to remove all traces of phenol red. The cells were serum starved for at least 12 hours in the presence of 10 mM sodium butyrate, prior to the application of osmotic stress and imaging. At the time of serum starvation, the dishes were blocked with 0.1% BSA to prevent non-specific binding of VEGF. A 0.1% BSA concentration is maintained throughout the rest of the experiment.

6-3.4. Reversible Osmotic Swelling and Addition of VEGF to Cells

Hypotonic swelling media was composed of serum-free media, diluted 1:9 with diH_2O, buffered with 25mM HEPES, supplemented with 0.1% BSA, and 0.2µm sterile filtered. AF594-scVEGF was re-suspended in PBS buffer at a concentration of 1mg/mL, and stored in aliquots of ~2.5 μg/aliquot at -20 C. These aliquots were then used at 1:1, 1:5, 1:10, 1:15, 1:20, 1:25, and 1:50 dilutions and mixed with swelling media. Just prior to imaging, the starvation media was aspirated from the petri dishes and was gently replaced with 1mL of 37°C hypotonic swelling media (39) containing AF594-labeled VEGF. The cells in each dish were allowed to stabilize for at least 15 minutes before imaging, and swollen cell images were acquired at room temperature for up to 2.5 hours per dish post swelling.

6-3.5. Image Acquisition

Spectral images in which we acquire the full fluorescence emission spectrum in every pixel of the image (see **Figure 6-3** for YFP and AF594-VEGF emission spectra obtained from cell membranes) are utilized in the FSI methodology. Two-photon fluorescence excitation is produced with a Mai Tai laser (Spectra Physics) and the OptiMis True Line Spectral Imaging system (Aurora Spectral Technologies), and provides excitation outside of the detectable range of the spectral imaging system. Images are acquired utilizing a Zeiss Observer wide field microscope, with a 63X NA 1.2 water immersion objective as described in detail in (30). Essentially, two different FSI experiments are performed per dish. Two images of each cell are acquired: a "FRET scan" to excite YFP with primary donor excitation at 960 nm and an “Acceptor Scan” to excite AF594-scVEGF with primary acceptor excitation at 800 nm or 840 nm. Additionally, images of buffer fluorescence, in a region of the dish where no cells were located, were acquired for determination of the free-VEGF concentrations, as shown in Figure 5. Different OptiMis image acquisition settings were used during these scans to either minimize (for cells) or maximize the buffer fluorescence signal (for free-ligand measurement). The settings for imaging of cell membrane fluorescence and buffer fluorescence are shown below in **Table 6-1**.

Table 6-1. The settings used for cell membrane fluorescence and buffer fluorescence measurements.

[L_{free}]	Cell Membrane Fluorescence				Buffer Fluorescence		
	Line Scan Δt	Spectral Resolution	FRET Scan λ_{ex}	Acceptor Scan λ_{ex}	Line Scan Δt	Spectral Resolution	Acceptor Scan λ_{ex}
42.3 nM	35 ms	1 nm	960 nm	840 nm	35 ms	2 nm	800 nm
38.5 nM	35 ms	1 nm	960 nm	840 nm	35 ms	2 nm	800 nm
6.81 nM	35 ms	2 nm	960 nm	840 nm	140 ms	2 nm	800 nm
5.88 nM	35 ms	2 nm	960 nm	840 nm	140 ms	2 nm	800 nm
2.00 nM	35 ms	2 nm	960 nm	840 nm	140 ms	2 nm	800 nm
3.00 nM	35 ms	1 nm	960 nm	800 nm	200 ms	2 nm	800 nm
1.09 nM	35 ms	1 nm	960 nm	800 nm	200 ms	2 nm	800 nm
1.54 nM	35 ms	1 nm	960 nm	800 nm	200 ms	2 nm	800 nm
1.23 nM	35 ms	1 nm	960 nm	800 nm	300 ms	2 nm	800 nm
0.98 nM	35 ms	1 nm	960 nm	800 nm	300 ms	2 nm	800 nm
0.45 nM	35 ms	1 nm	960 nm	800 nm	300 ms	2 nm	800 nm
0.21 nM	35 ms	1 nm	960 nm	800 nm	300 ms	2 nm	800 nm

6-3.6. VEGFR2, VEGF Surface Density and Free-VEGF Measurements

The Fully Quantified Spectral Imaging (FSI) method is utilized in this work to measure the bound AF594-VEGF surface densities, the expressed VEGFR2 ECTM-GGS$_5$-YFP surface density, and the three-dimensional concentration of free VEGF in the buffer surrounding the cells in the dish. **Figure 6-2** shows a cartoon of the imaging scheme utilized for these experiments:

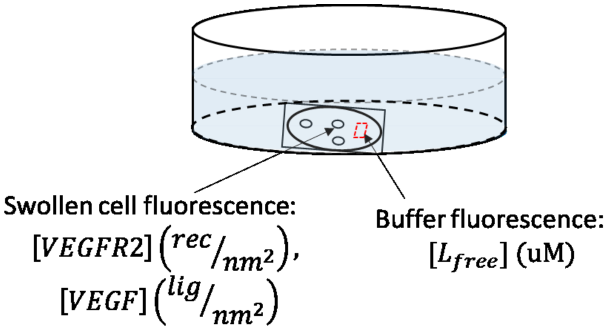

Figure 6-2. The scheme for the equilibrium binding experiments described in this chapter. Many swollen cells exhibiting homogenous diffraction-limited membrane fluorescence are imaged in a 35mm petri dish providing surface densities of expressed VEGFR2 ECTM-YFP and bound AF594-VEGF. A volume of buffer without cells is also imaged with settings optimized for measuring weak buffer fluorescence, providing a free-VEGF measurement in the buffer surrounding the cells.

Due to their spectral properties, YFP is regarded as the FRET donor, and AF594-scVEGF is considered the FRET acceptor (see **Figure 6-3** below). I measured the surface density of expressed VEGFR2 ECTM-YFP and the bound AF594-VEGF surface density in 2-3 micron size patches of membrane on hypo-osmotically swollen, adherent HEK293T cells. It has been previously shown that swelling the cells is required for proper extraction of the surface densities of labeled membrane proteins, and that the swelling does not perturb the protein-protein interactions in the swollen cell. 1-2 regions per swollen cell are measured, and 25-50 cells per dish are acquired. I also measure the free-VEGF concentration in the same dish by measuring buffer fluorescence in a region of the dish without adherent cells present.

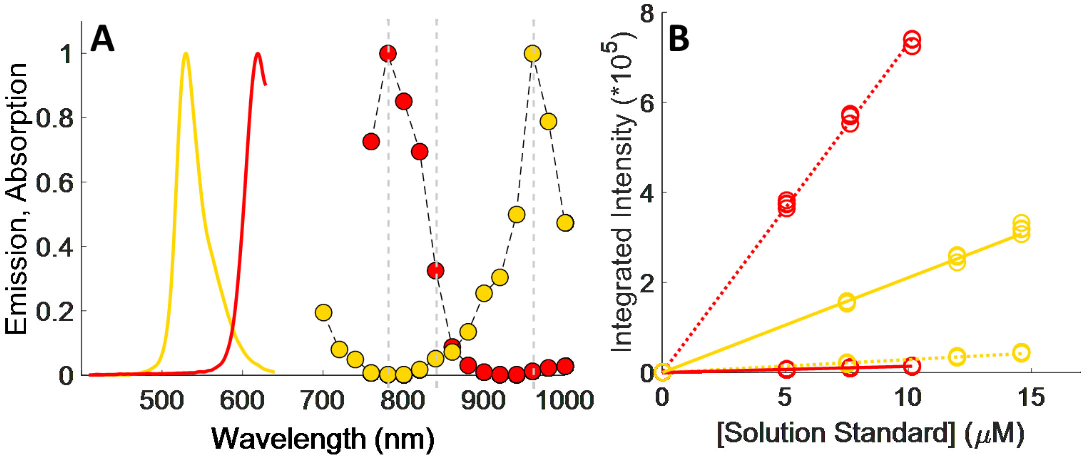

Figure 6-3. The spectral properties of the fluorophores utilized in this chapter. **A.** The emission spectra and absorption spectra (solid and dashed lines, repectively) are given for YFP in yellow and Alexa Fluor 594 in red. The grey dashed lines show the wavelengths utilized in the FRET scans to excite the YFP donor at 960nm and to excite the acceptor, AF594, at 800nm or 840nm **B.** The integrated intensity of the solution standards, YFP in yellow, and Alexa-Fluor 594 in red as a function of total concentration. A line is fit to the data for excitation during the FRET scan at 960nm (solid line) and for excitation during the Acceptor scan, shown here at 840 nm, for both fluorophores. YFP is primarily excited at 960nm, while Alexa Fluor 594 is primarily excited at 840nm. The fully-solved system of equations of the FSI method is able to account for intrinsic excitation of both fluorophores at both excitation wavelengths in an approximation-free manner by using the slopes of these lines of intensity versus fluorophore concentration.

Here, I only review the primary equations and ideas fundamental to performing the experiments. These equations are collected below:

$$E_{app} = F^{D}{}_{RET,\,\lambda 1}/F^{D}{}_{\lambda 1} = 1 - \; F^{DA}{}_{\lambda 1}/F^{D}{}_{\lambda 1} \quad \text{(6-10)}$$

$$[D] = \frac{F^{D}{}_{\lambda 1}}{i_{D,\,\lambda 1}} = \frac{1}{i_{D,\,\lambda 1}}\left(F^{DA}{}_{\lambda 1} + \frac{Q^{D}}{Q^{A}}\left(F^{AD}{}_{\lambda 1} - \frac{i_{A,\lambda 1}}{i_{A,\lambda 2}} F^{A}{}_{\lambda 2}\right)\right) \quad \text{(6-11)}$$

$$[A] = \frac{F^{A}{}_{\lambda 2}}{i_{A,\,\lambda 2}} = \frac{1}{i_{A,\,\lambda 2}}\left(F^{AD}{}_{\lambda 2} - \frac{i_{D,\lambda 2}}{i_{D,\lambda 1}} F^{AD}{}_{\lambda 1}\right) \cdot \left(1 - \frac{i_{A,\lambda 1}}{i_{A,\lambda 2}}\frac{i_{D,\lambda 2}}{i_{D,\lambda 1}}\right)^{-1} \quad \text{(6-12)}$$

In these equations, E_{app} is the measured total apparent FRET efficiency, $F^{D}{}_{RET,\,\lambda 1}$ is the theoretical fluorescence of the donor that is transferred to an acceptor instead of being emitted, for excitation in the FRET scan at λ_1. $F^{D,A}{}_{\lambda 1,2}$ is total fluorescence of the donor or acceptor in the absence of FRET for excitation at λ_1 or λ_2. $F^{DA}{}_{\lambda 1}$ is the measured fluorescence of the donor in the presence of acceptors, and $F^{AD}{}_{\lambda 2}$ is the measured fluorescence of the acceptor, enhanced due to FRET. $i_{D,\,\lambda 1}$ and $i_{A,\,\lambda 2}$ are the slopes of the solution standard intensity versus micromolar concentration curves determined by imaging solution standards of known concentration, described in the **YFP and Alexa-Fluor 594 Solution Standards** section below.

Equation (6-12) is directly applied to buffer fluorescence images and the measured pixel-level concentrations are histogrammed. A Gaussian curve is fit to the data to determine the values of the mean, μ, and the standard deviation, σ, the value and error in the free-ligand measurement.

For the surface density measurement, the apparent pixel-level fluorophore (receptor and bound ligand) concentrations calculated during the image analysis must be integrated across the diffraction limited segment in order to properly determine the 2D surface density from the fluorescence and the calibration curves. To do so, F^D, F^A, and F^{AD} are integrated (summed) over every pixel selected in the region, $F^{D,A}_{\lambda i,Reg} = \int F^{D\ or\ A}_{region} dA = \sum F^{D\ or\ A}_{i,j}$. The apparent FRET efficiency of the region is then calculated as $E_{app} = 1 - {F^{DA}_{\lambda 1,Reg}}\Big/{F^{D}_{\lambda 1,Reg}}$.

The total integrated fluorescence intensities for the region, $F^{D}_{\lambda 1,Reg}$, and $F^{A}_{\lambda 2,Reg}$, are then divided by the arc length, s, of the selected region to calculate the average integrated fluorescence per unit length of membrane (in units of pixel). By swelling the cells with osmotic stress, we are able to simplify the complex topology of the membrane and assume a perpendicular orientation of the membrane with respect to the focal plane. We also assume that the fluorescence originates from an infinitely thin sheet within the width of one pixel, or 254nm. To obtain the fluorescence that would be emitted by a full voxel of chromophores, the integrated fluorescence per unit pixel-length is multiplied by the pixel width, 254nm. By dividing the full voxel fluorescence by the average slope, $< i^{D,A}_{\lambda i} >$, and performing the appropriate unit conversion from micromolar concentrations to receptors per unit area (in units of rec/nm^2), the average receptor surface density for the region is calculated, as shown below:

$$[D\ or\ A]\left[\frac{rec}{nm^2}\right] = \frac{\sum F^{D\ or\ A}_{i,j}}{s \cdot < i^{D,A}_{\lambda i} >} \frac{[counts\ \cdot\ pixel^2]}{[pixel]} \left[\frac{counts}{\mu M}\right]^{-1} \cdot \frac{6.022 \cdot 10^{-7}}{[\mu M]} \left[\frac{rec}{nm^3}\right] \cdot 254 \left[\frac{nm}{pixel}\right] \tag{6-13}$$

6-3.7. YFP and Alexa-Fluor 594 Solution Standards

Soluble monomeric YFP with an N-terminal 6x His-tag was expressed and purified to near-milimolar concentrations as described (27). Fluorescent protein stocks were buffer exchanged into PBS buffer with a 20kDa MWCO concentrator (Pierce #87751) and filtered with a 0.2µm syringe filter. Unconjugated Alexa Fluor 594 (A37572) was purchased in lyophilized form from ThermoFisher Scientific and suspended in PBS buffer. For each imaging session, the stocks were then diluted in buffer to micromolar concentrations to produce 100%, 75%, and 50% fluorescent protein and AF594 solution standards. The solution standard concentrations were measured in a 1 cm path length quartz cuvette using NanoDrop 2000C (Thermo Scientific). Molar absorption coefficients of 83,400 Mol*cm^{-1} and 73,000 Mol*cm^{-1} were used to calculate the concentrations of the solution standards from the YFP and AF594 absorption maxima of 514 nm and 590 nm, respectively. Images of the 100%, 75%, 50% solution standards and a PBS buffer-only control were acquired at both excitation wavelengths (800nm or 840nm for AF594, and 960nm for YFP) and were used for the calculation of the pixel-level slope values as used with the FSI method described briefly in this work, but previously described in excruciating detail.

Figure 6-3A shows the shows the normalized YFP and AF594-VEGF fluorescence obtained from the membranes of live cells. I see no apparent change in the fluorescence emission properties in the AF594-VEGF or YFP fluorophores on the surface of the cells when compared to that of the solution standards, and the respective emission maxima of 618 nm and 527 nm remain unchanged. This is not surprising given the AF594 resides in buffer that is mostly water, and the fluorescent proteins exist in the cytosol, just on the intracellular side of the membrane. **Figure 6-3B** shows the measured fluorescence versus concentration curves of the solution standards for a single pixel. The slopes of these lines are measured for every pixel and utilized with the FSI method, as described in **Chapter 4**.

6-4. Results

Here, I used the FSI methodology to study the binding properties of AF594-VEGF with the EC domains of monomeric and dimeric VEGFR2. FSI allows one to measure the surface densities of fluorescently labeled membrane proteins, as well as FRET between the labeled moieties. Additionally, FSI allows measurement of three-dimensional concentrations of fluorophores in the buffer. These three features are utilized in conjunction to study VEGF affinities for VEGFR2.

As shown in **Figure 6-4A**, I utilized a truncated form of VEGFR2 where the kinase domain is replaced by a fluorescent protein, YFP, attached to the TM domain by a GGS_5 flexible linker (VEGFR2 ECTM-YFP) and a form of VEGF121, scVEGF, linked to the organic dye Alexa-Fluor 594. **Figures 6-4B,C** depict three transiently transfected HEK293T cells, swollen with hypo-osmotic stress, and expressing different amounts of VEGFR2 ECTM-YFP while in the presence of AF594-VEGF in the buffer. **Figure 6-4B** shows the cells under excitation at 960nm, which primarily excites VEGFR2-ECTM-YFP. We can see large stretches of homogenous membrane fluorescence and that the protein is primarily localized to the cell membrane, but the fluorescence of intracellular proteins being trafficked to the membrane is also visible. In **Figure 6-4C**, we see the same cells under excitation at 800 nm, which primarily excites AF594-VEGF. AF594-VEGF is highly concentrated on the surface of the cells, but no VEGF-fluorescence originates from the intracellular space, as the VEGFR2 ECTM domains do not contain the kinase domains, and thus activated receptors are not taken into the cell through endocytosis. In cells with no VEGFR2 ECTM-YFP fluorescence, I find no measurable AG594-VEGF fluorescence, indicating that non-specific binding plays a minimal contribution to these measurements.

Figure 6-4. A. A cartoon showing VEGF bound to a dimer of VEGFR2. The YFP is attached via a GGS_5 flexible linker to the ECTM domain of VEGFR2. VEGF, with an attached AF594 fluorophore, diffuses freely in the buffer and binds to subunits D2 and D3 of the VEGFR2 extracellular domain (colored in yellow). At 960 nm excitation, we elicit primarily YFP fluorescence. At 800nm or 840nm excitation, we elicit fluorescence primarily from AF594- VEGF. **B.** Three HEK293T cells transiently transfected with VEGFR2-ECTM-YFP and swollen with hypo-osmotic stress, in the presence of AF594-VEGF. The cells exhibit large stretches of homogenous membrane fluorescence when YFP is excited at 960nm. We see VEGFR2-ECTM-YFP being trafficked to the membrane in the intracellular space. **C.** The same cells as B., but under excitation at 800nm, which excites Alexa Fluor 594-VEGF. As with VEGFR2 ECTM-YFP, large stretches of homogenous membrane fluorescence are visible from bound AF594-VEGF, but we see no intracellular AF594 fluorescence. No ligand is taken up into the cell for the duration of the experiments. Scale bar is 30 μm. Images are colored to aid in excited-fluorophore identification.

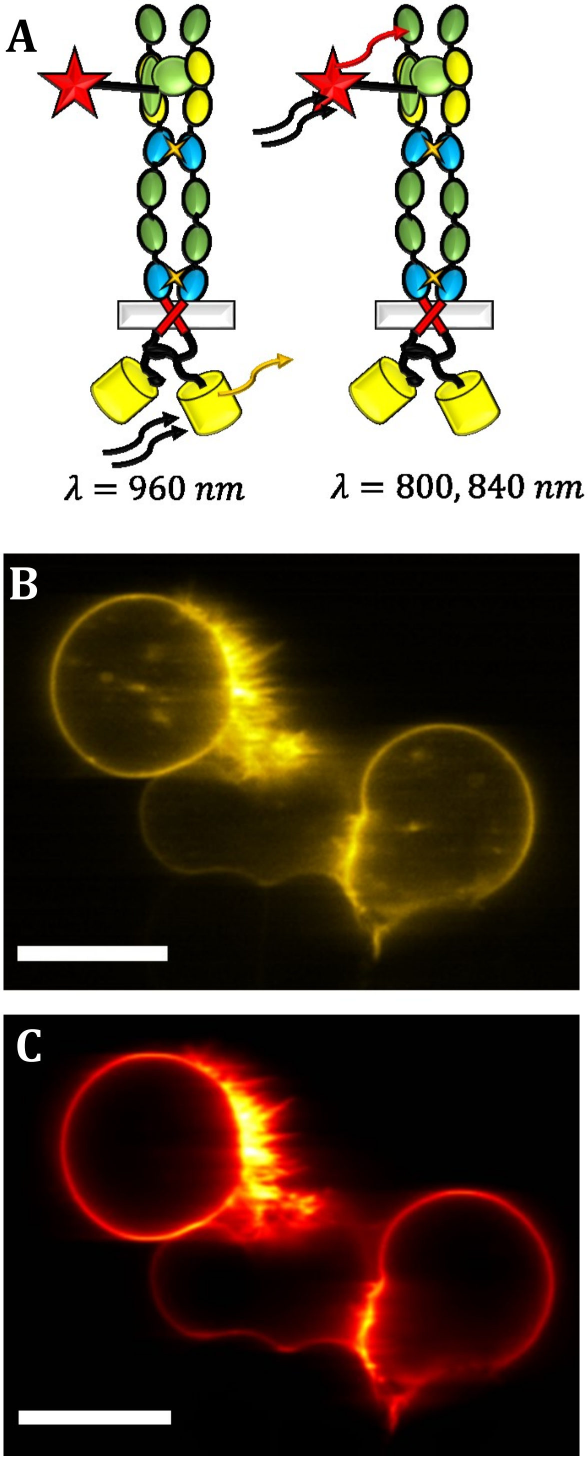

I measured VEGFR2 ECTM-YFP and bound AF594-VEGF surface densities in 12 independent experiments from a total of 387 cells. These images provided a total of 661 data points at twelve different free-VEGF concentrations. **Figure 6-5** shows the measured total apparent FRET efficiency between the intracellular YFP of VEGFR2 ECTM and the AF594-VEGF, bound to the distal region of the VEGFR2 EC domain. We see zero concentration dependence on the total apparent FRET efficiency, and the FRET is zero for all concentrations of VEGFR2. This data indicates that the YFP (FRET donor) and the AF594 (FRET acceptor) are greater than 10 nm apart when VEGF is bound to VEGFR2's EC domain. This lack of measured FRET is expected given that the cell membrane is ~5nm thick on its own, and YFP is a large beta barrel of considerable extent around the YFP chromophore, which is connected to VEGFR2 TM domains via a 15 amino acid GGS flexible linker.

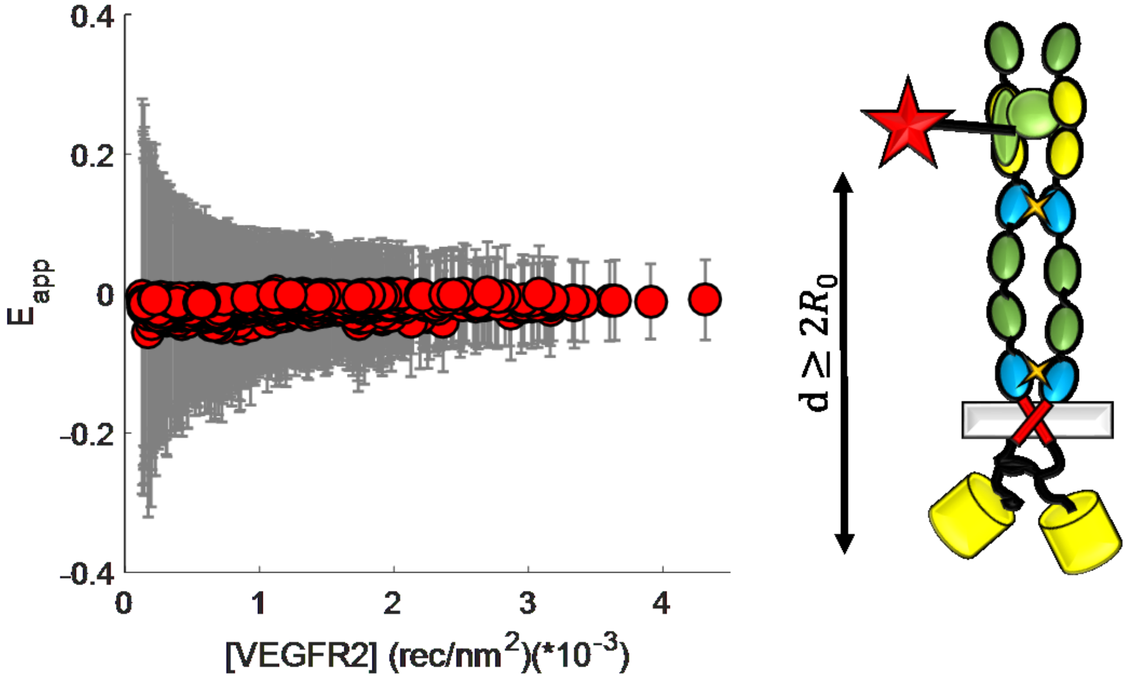

Figure 6-5. The measured total apparent FRET efficiency between VEGFR2-ECTM-YFP and bound AF594-VEGF is plotted as a function of total VEGFR2 surface density. The FRET is zero at all concentrations, indicating that the fluorophore of AF594-VEGF bound to the VEGFR2 EC domain is greater than 10nm from the intracellular YFP, linked to the VEGFR2 TM domain by a 15 amino acid GGS linker.

Figure 6-6 shows the bound AF594-VEGF surface density plotted as a function of the expressed VEGFR2 ECTM-YFP surface density for three values of free-VEGF concentrations: 42.3 nM, 1.54 nM, and 0.21 nM (green, orange, and blue circles, respectively). We a distinct dependence on the three-dimensional free-VEGF concentration on the bound VEGF vs expressed VEGFR2 surface densities. Since the number of data points at each free-VEGF concentration is not enough to determine K_{LM} and K_{LD} , I combined the data from the twelve datasets obtained at different free-VEGF concentrations and globally fit the data with **Equations (6-8) and (6- 9)** to find the best-fit values of the two adjustable parameters: the binding affinity of AF594-VEGF for monomeric VEGFR2 EC domains, K_{LM}, and the binding affinity of AF594-VEGF from dimeric VEGFR2 EC domains: K_{LD}. These are the best-fit values of K_{LM} and K_{LD} that globally minimize the error of the model, and as such the accuracy and precision of the fit is improved.

The best fit results are: $K_{lm} = 9.6e7 \pm 1.8e7\,M^{-1}$ and $K_{ld} = 4.3e9 \pm 0.6e9\,M^{-1}$ (95% confidence), indicating a ~40-fold enhancement of VEGF binding affinity dimeric VEGFR2 over the affinity of AF594-VEGF for monomeric VEGFR2 EC domains. Plotted in red solid lines in **Figure 6-6** are the predicted values of the bound VEGF as a function of expressed VEGFR2 ECTM surface density. The dashed red lines indicate the confidence limits on the fit, obtained through propagation of errors on K_{LM} and K_{LD} in **Equations (6- 8)** and **(6-9)**, with the 95% confidence limits on K_{LM} and K_{LD}. We see good agreement between the measured data and the best-fit predicted bound-VEGF surface densities as a function of free-VEGF and expressed VEGFR2 surface densities. **Figure 6-7** shows the measured bound-VEGF surface density as a function of the expressed

VEGFR2 ECTM surface density for each of the twelve individual datasets, as well as the best-fit theoretical bound VEGF surface density for that free-VEGF concentration. **Figure 6-8** shows the results of the free-AF594-VEGF buffer measurements.

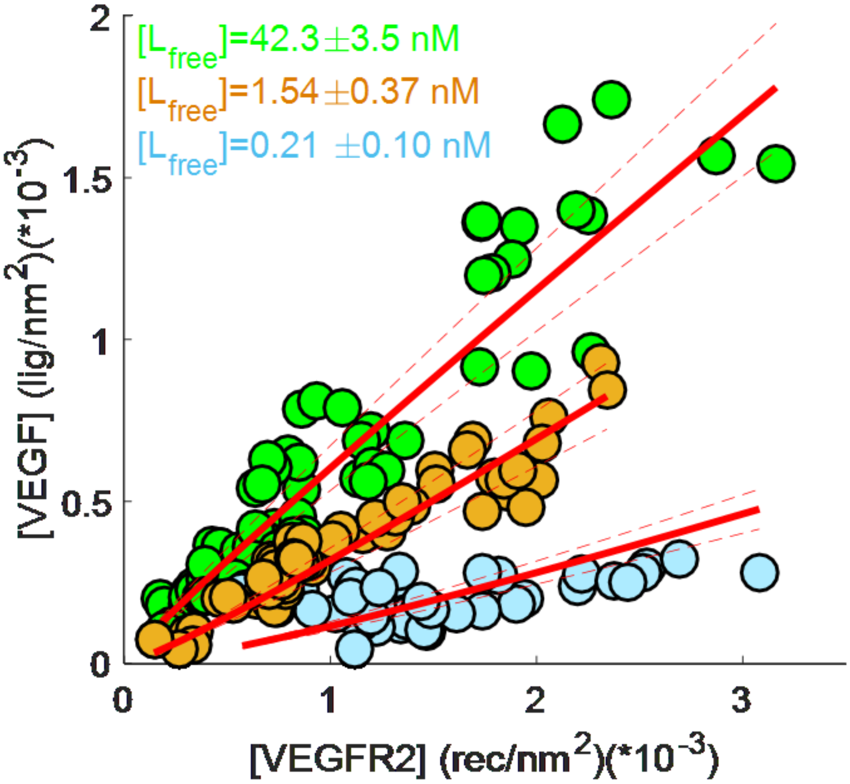

Figure 6-6. The bound AF594-VEGF surface density is plotted as a function of expressed VEGFR2 ECTM-YFP surface density for several values of free-VEGF in the buffer: 42.3 nM, 1.54 nM, and 0.21 nM (green, orange, and blue circles, respectively). We see that the bound VEGF is not only a function of VEGFR2 surface density, but also the three-dimensional free-VEGF concentration. Plotted in red is the best-fit result of the global fitting for the theoretical bound AF594-VEGF as a function of VEGFR2 surface density at each of the three free-VEGF values. The dashed lines indicate 95% confidence intervals on the fit. We see good agreement between the modeled and measured VEGF surface densities.

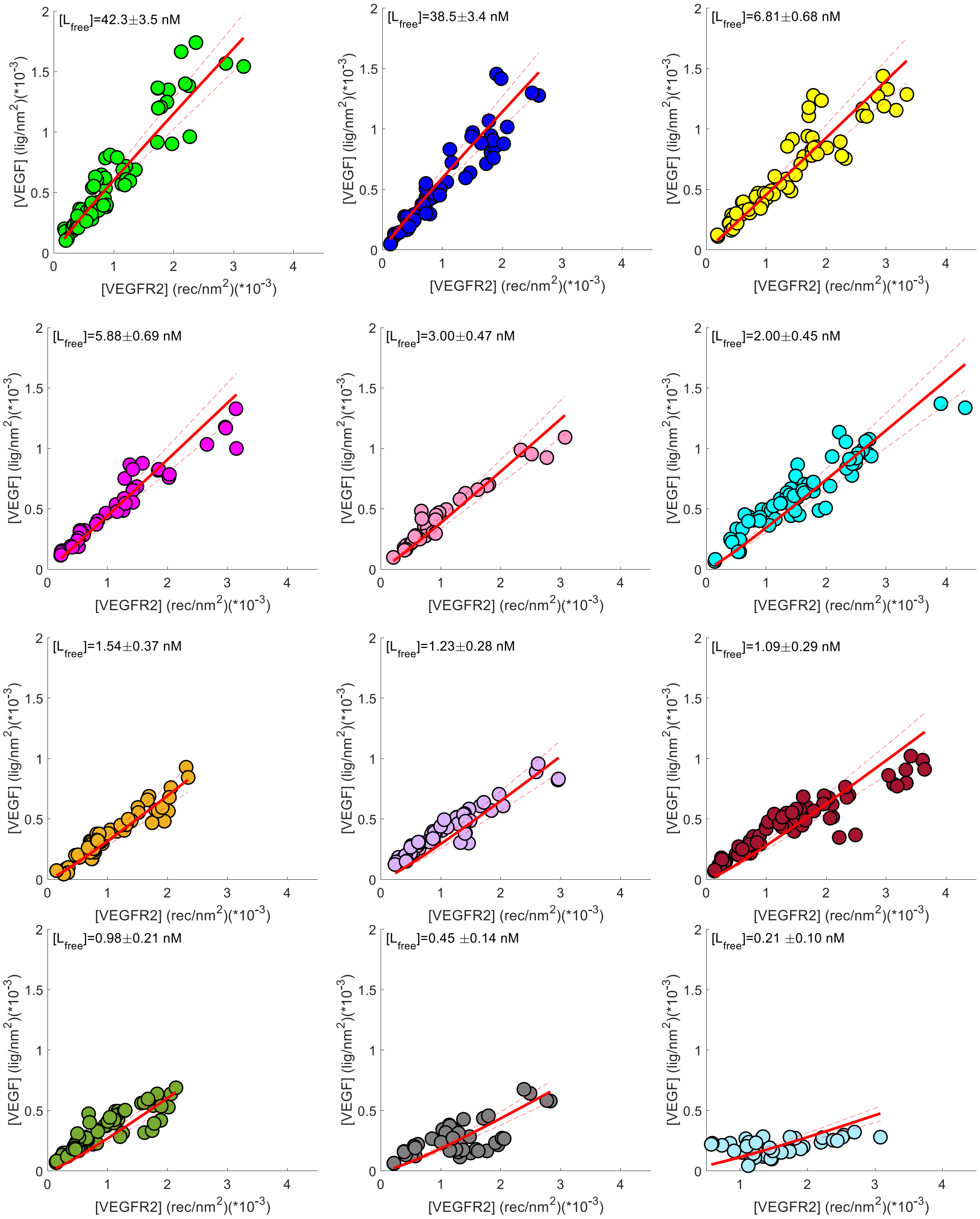

Figure 6-7. The measured AF594-VEGF surface density plotted as a function of the expressed VEGFR2 surface density (filled circles) for each of the 12 independent experiments performed at different values of the three-dimensional free-VEGF concentration. The data were combined and globally fit with the thermodynamic cycle described in the text, and the best-fit theoretical VEGF surface density for each experiment at a given free-VEGF value is plotted as a function of total VEGFR2 expression with a red line. The dashed lines indicate the error in the fit.

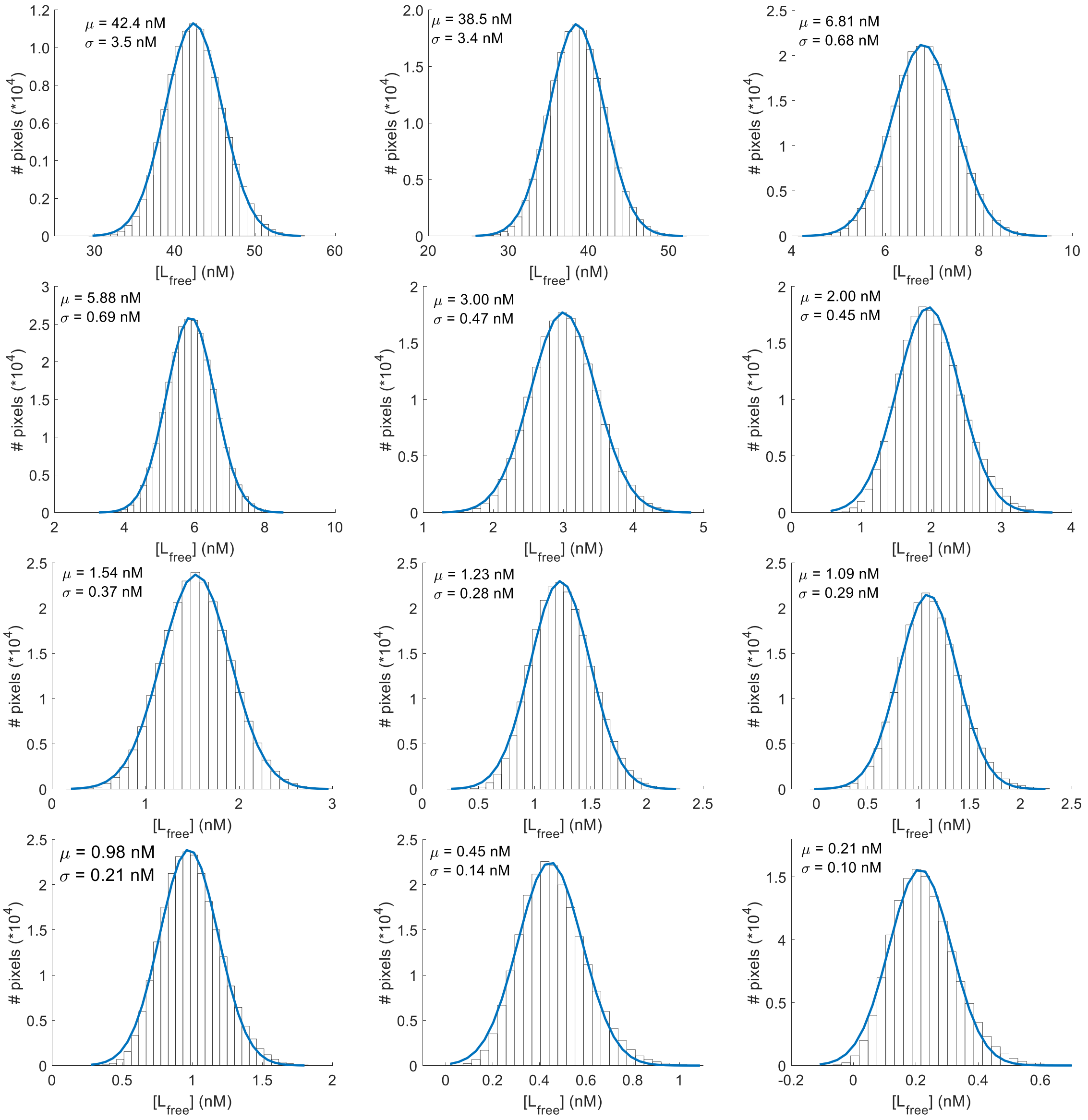

Figure 6-8. The free-VEGF measurement results for each of 12 experiments. The pixel-level buffer concentrations were obtained by imaging a region of buffer where no cells were located. A large region was chosen in each image, and the pixel-level AF594-VEGF concentrations were binned and histogrammed for each of the twelve experiments. Each histogram was fit to a Gaussian distribution, and thebest-fit values for mu and sigma are utilized as the free-VEGF value and its associated error, respectively.

6-5. Discussion and Conclusions

In this chapter, I utilized a thermodynamic cycle and global fitting of many combined datasets to measure the separate binding affinity of VEGF for monomeric and dimeric forms of VEGFR2 EC domains, in the context of the living cell membrane. Surprisingly, we find that the affinity of VEGF for dimeric VEGFR2 EC domains is substantially greater than the affinity of VEGF for monomeric VEGFR2 EC domains. The dimerization affinity of the full length VEGFR2 molecule known from previous measurements, $\Delta G°_{FL} = -6.1\ kcal/mol$ giving $K_R^{FL} = \frac{[D]}{[M]^2} = 2.97e4\ ({}^{rec}/_{nm^2})^{-1}$. Here I utilized the truncated form of VEGFR2 lacking the kinase domain, VEGFR2 ECTM-YFP, which dimerizes with a greatly reduced Gibbs free energy of $\Delta G°_{FL} = -3.5\ kcal/mol$ with $K_R = \frac{[D]}{[M]^2} = 370\ ({}^{rec}/_{nm^2})^{-1}$.

Figure 6-9 shows the dimeric fraction as a function of total VEGFR2 surface density for the full-length and the truncated ECTM VEGFR2 forms, in the absence of VEGF. We see that the dimeric fraction of the full-length VEGFR2 is significantly enhanced over that of the VEGFR2 ECTM construct. In these experiments, I overexpress membrane proteins to the range of 1e-5 to 4e-3 rec/nm^2, and in this range, full-length VEGFR is essentially a constitutive dimer in the absence of ligand. In addition to avoiding the complexities of receptor activation, endocytosis, and receptor trafficking that are involved when working with the full-length VEGFR2 construct and VEGF, by using the truncated ECTM construct I also expose a large population of monomeric VEGFR2 for AF594-VEGF binding, enabling a measurement of the VEGF affinity for monomeric VEGFR2 EC domains. Thus, the use of a form of VEGFR2 (ECTM) with significant fractions of monomeric and dimeric EC domains in the absence of VEGF was required to measure the separate affinities of VEGF for VEGFR2 monomeric and dimeric EC domains: K_{LM} and K_{LD}.

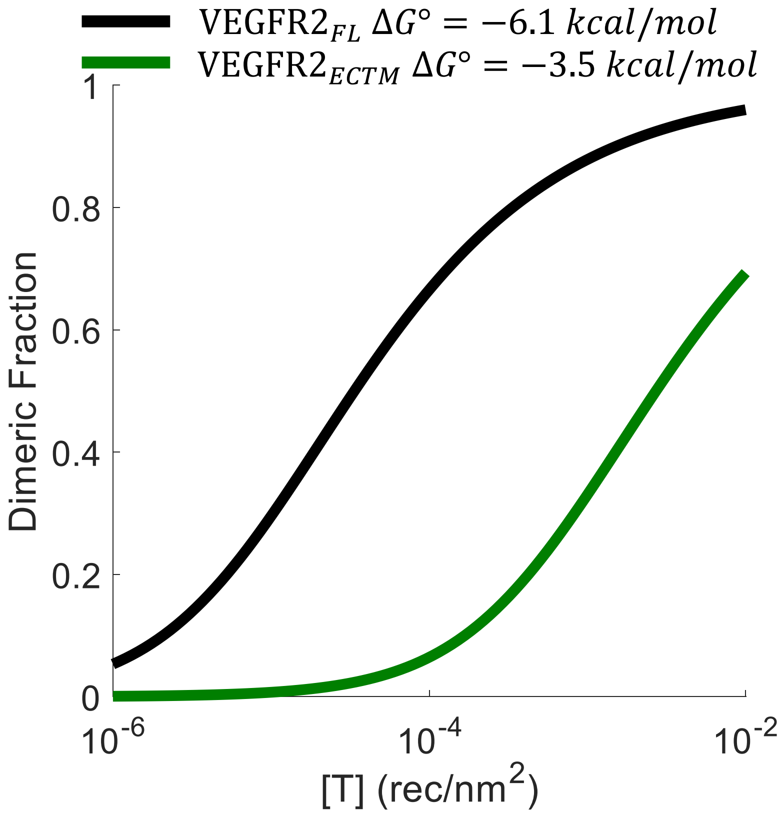

Figure 6-9. The dimeric fraction of full-length VEGFR2, which dimerizes with a Gibbs free energy of -6.1 kcal/mol is plotted as a function of total VEGFR2 surface density in black. The dimeric fraction of VEGFR2 ECTM domains, which dimerize with a Gibbs free energy of -3.5 kcal/mol, is also plotted as a function of total VEGFR2 surface density. The dimeric fraction of full-length VEGFR2 is significantly greater than the dimeric fraction of VEGFR2 ECTM membrane proteins for all concentrations of VEGFR2, due to the presence of the intracellular domain.

However, now that we know the binding affinities of VEGF for the monomeric and dimeric forms of VEGFR2 EC domains, we can utilize **Equations (6-8)** and **(6-9)** with the best fit values of K_{LM} and K_{LD} and the value of $K_R^{FL} = \frac{[D]}{[M]^2} = 2.97e4\ (^{rec}/_{nm^2})^{-1}$ to predict the saturation of VEGFR2 binding sites at any surface density of full-length VEGFR2 and any free-VEGF concentration. **Figure 6-10A** shows the fraction of occupied binding sites, $\bar{Y} = \frac{[LM]+[LD]}{[M]+[D]+[LM]+[LD]}$ as a function of total VEGFR2 surface density (left axis) and the free-VEGF concentration (bottom axis).

We can write $\bar{Y}$ as a sum of the saturations of monomeric and dimeric VEGFR2 binding sites:

$$\bar{Y} = \bar{M} + \bar{D} = \frac{[LM]}{[M]+[D]+[LM]+[LD]} + \frac{[LD]}{[M]+[D]+[LM]+[LD]} \tag{6-14}$$

In **Figures 6-10B, 6-10C** I have plotted $\bar{M}$ and $\bar{D}$ as a function of total VEGFR2 surface density and free-VEGF concentration. We see that dimeric VEGFR2 binding sites saturate at the lowest free-VEGF concentrations, 1e-9 M through 1e-7 M , while at higher VEGF concentrations, VEGF binding to dimers is reduced and binding of VEGF to monomeric VEGFR2 EC domains dominates. At surface densities of VEGFR2 > 1e-4 rec/nm^2, where unliganded VEGFR is > 70% dimeric, this condition of suppressed dimerization requires greater than micromolar concentrations of VEGF.

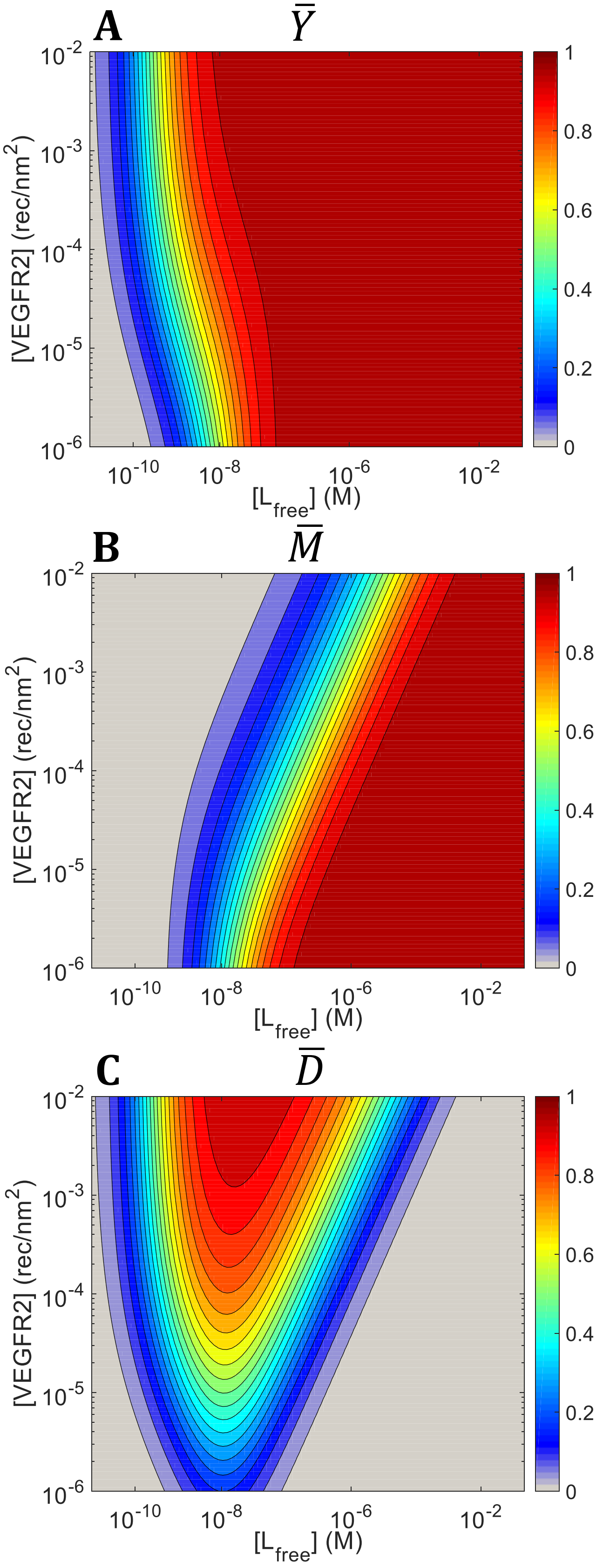

Figure 6-10. The predicted fractions of occupied VEGF binding sites for full-length VEGFR2 as a function of VEGFR2 surface density and free-VEGF concentration. **A.** The fractional saturation of all monomeric and dimeric VEGFR2 binding sites. **B.** The fractional saturation of monomeric VEGFR2 binding sites. **C.** The fractional saturation of dimeric VEGFR2 binding sites.

Figure 6-11 A-D shows the theoretical fractions of monomeric VEGFR2, [M], VEGF-bound monomeric VEGFR2, [LM], dimeric VEGFR2 [D], and VEGF-bound dimeric VEGFR2, [LD], as functions of total VEGFR2 surface density and the free-VEGF concentration. In **Figure 6-11A**, we see that the VEGFR2 full-length construct essentially never exists in the unliganded monomeric form. In **Figure 6-11B**, we see that free-VEGF concentrations greater than micromolar are required to force full-length VEGFR2 into the monomeric state. **Figure 6-11C** shows that unliganded dimers dominate at all concentrations of free-VEGF less than 100 pM. Finally, **Figure 6-11D** shows the active fraction of VEGFR2 as a function of free-VEGF and VEGFR2 surface density: at exceptionally high free-VEGF concentrations, the active fraction of VEGFR2 can be suppressed to near zero.

From these predictions, one can say much about how the cell must utilize the VEGFR2 receptor with its activating ligand, VEGF. We see that VEGF binds with higher affinity to dimers of VEGFR2 than to monomers of VEGFR2. With physiological surface densities of VEGFR2 ranging from 10-100 receptors/micron, or 1e-5- 1e-4 rec/nm^2, and due to the law of mass action, and the $\Delta G^{\circ}{}_{FL} = -6.1\ kcal/mol$ dimerization affinity, at these concentrations VEGFR2 will be 70-50 % monomeric and 30-50% dimeric. If there are only 10 receptors in a square micron, then there are only 1-2 preformed dimers of VEGFR2. Thus, it can be predicted from this data that the cells must be clustering the receptors in order to enhance the local effective concentration of VEGFR2 to ~10e-3 rec/nm^2, in effect pre-staging the VEGFR2 into unliganded dimers so that small amounts of VEGF can bind with high affinity specifically to VEGFR2 dimers.

Given that VEGFR2 can interact with a number of different membrane proteins, and that VEGF also binds to a number of different membrane proteins, this finding makes a lot of sense. The purpose of these co-receptors is probably to attract VEGFR2 molecules, and pre-stage dimers for efficient signal transduction. Binding of VEGF to a preformed dimer of VEGFR2 immediately and rapidly activates the receptor for signal transduction. Thus, even though full-length VEGFR2 has the ability to exist in its monomeric form, the pre-formed dimeric form of VEGFR2 is the “signaling-ready” complex, and relatively small amounts of VEGF can be released to specifically activate dimeric VEGFR2. An important question remains unanswered in that we still do not know exactly how many dimers of VEGFR2 must be activated for a cellular response to occur. Ultimately, this number of minimum required active VEGFR2 molecules per cell will decide the amount of VEGF required for signal transduction, and will determine the best course of treatment in order to control VEGFR2 signaling, especially in pathological cases like enhanced VEGF production observed in malignant tumors.

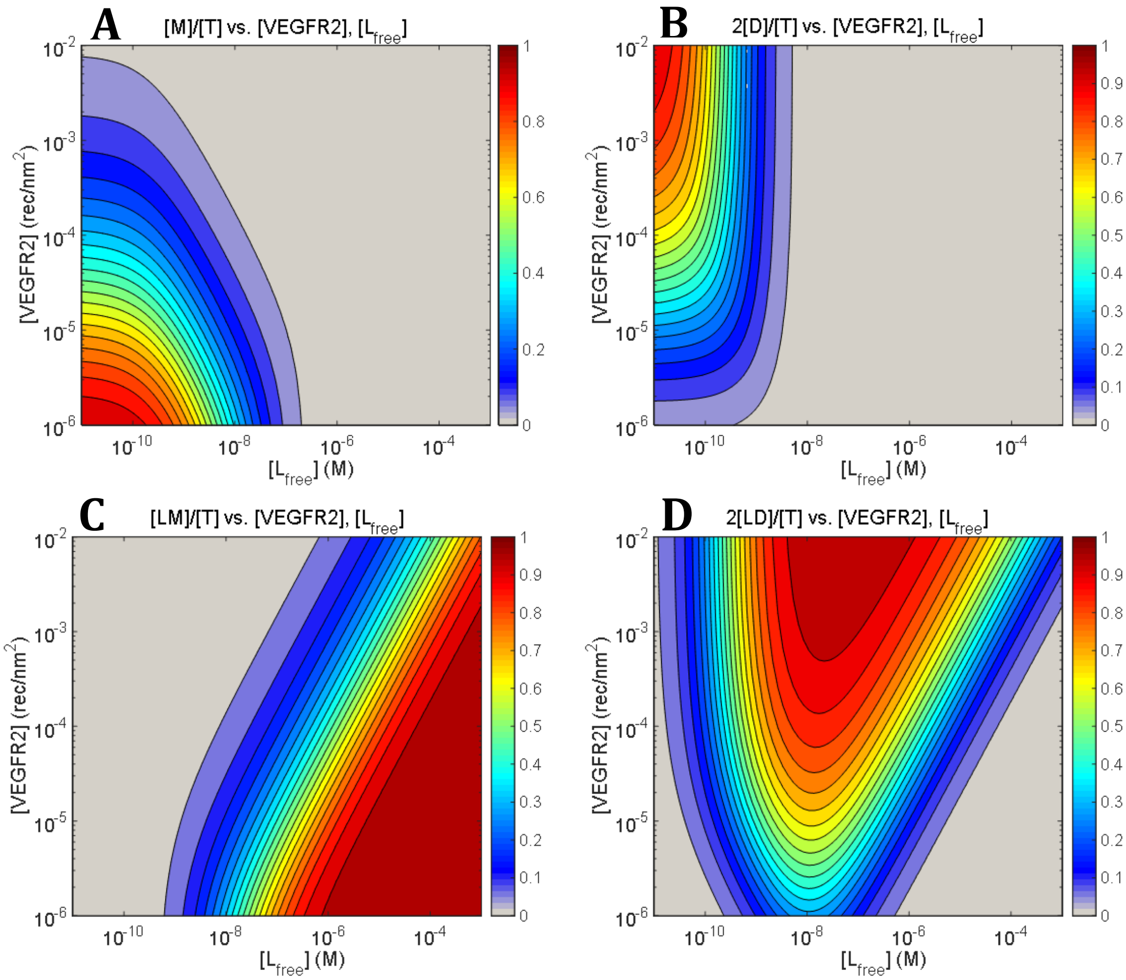

Figure 6-11: The predicted fractions of the various forms of VEGFR2 as a function of VEGFR2 surface density and free-VEGF concentration. **A.** The fraction of monomeric VEGFR2 without bound VEGF. **B.** The fraction of dimeric VEGFR2 without a bound VEGF. **C.** The fraction of monomeric VEGFR2 with VEGF bound. **D.** The fraction of dimeric VEGFR2 with bound VEGF. This Is the active form of the VEGFR2 receptor and thus can be interpreted as the active fraction of VEGFR2.

Chapter 7. Conclusion

In this body of work, I have taken quantitative FRET analysis to its edge and shown the limits of static quenching two-color FRET measurements utilizing fluorescent proteins linked to membrane proteins diffusing freely within a lipid bilayer. With a numerically estimated stochastic FRET contribution included in the model to the total apparent FRET efficiency, one is able to measure the thermodynamic properties of membrane proteins existing as monomers, dimers, or higher-order oligomers. Even though the oligomer order is not distinguishable in such an experiment involving oligomers greater than dimers, the oligomeric fraction is still accessible and can be compared to other proteins or conditions.

I also extended the limits of FRET measurements in cell membranes. The Fully Quantified Spectral Imaging method gives the researcher the unique ability to measure membrane protein surface densities in live cells, in addition to a FRET efficiency. Furthermore the FSI method allows for the measurement of the three-dimensional concentration of fluorophores freely diffusing in buffer. Here, I utilized all of these features of the FSI method to measure the previously unknown nature of the extracellular domain contacts of VEGFR2, in the absence of its activating ligand, VEGF. I then utilized the FSI methodology in an exceedingly tedious and difficult set of experiments that permitted a measurement the binding affinity of VEGF, labeled with a fluorescent dye, for the separate monomeric and dimeric VEGFR2 EC domains. VEGFR2 is a signal transducing membrane protein critical for angiogenesis, and thus a true understanding of this protein in the context of the live-cell membrane is critical to treating a variety of medical problems stemming from enhanced or suppressed angiogenic signaling.

I have shown that the theory and methodology developed during this thesis will revolutionize our understanding of membrane proteins by permitting their relatively unperturbed study in the context of the live-cell membrane. Many membrane proteins can be more completely understood by applying similar methodologies. This is especially true for the case of co-receptors, or scaffolding proteins with no direct function, like phosphorylation, to monitor as an observable in experiments. Thus, performing a direct measurement of protein-protein interactions is needed to truly understand the roles of these membrane proteins, which are primarily understood through secondary effects on binding partners. The theory and methodology that I have developed in this thesis is one set of powerful tools that can perform such highly needed measurements.

References

1. Lemmon, M. A. & Schlessinger, J. (2010). Cell Signaling by Receptor Tyrosine Kinases. *Cell* **141**, 1117-1134.

2. Schlessinger, J. (2000). Cell signaling by receptor tyrosine kinases. *Cell* **103**, 211-225.

3. Fantl, W. J., Johnson, D. E. & Williams, L. T. (1993). Signaling by Receptor Tyrosine Kinases. *Annu. Rev. Biochem.* **62**, 453-481.

4. Pasquale, E. B. (2010). Eph receptors and ephrins in cancer: bidirectional signalling and beyond. *Nature Reviews Cancer* **10**, 165-180.

5. L'Horte, C. G. M. & Knowles, M. A. (2005). Cell responses to FGFR3 signaling: growth, differentiation and apoptosis. *Experim. Cell Res.* **304**, 417-431.

6. He, L. & Hristova, K. (2012). Physical-chemical principles underlying RTK activation, and their implications for human disease. *Biochim. Biophys. Acta* **1818**, 995-1005.

7. Lin, C. C., Melo, F. A., Ghosh, R., Suen, K. M., Stagg, L. J., Kirkpatrick, J., Arold, S. T., Ahmed, Z. & Ladbury, J. E. (2012). Inhibition of Basal FGF Receptor Signaling by Dimeric Grb2. *Cell* **149**, 1514-1524.

8. Sarabipour, S. & Hristova, K. (2016). Mechanism of FGF receptor dimerization and activation. *Nat. Commun.* **7**, 10262.

9. Shibuya, M. & Claesson-Welsh, L. (2006). Signal transduction by VEGF receptors in regulation of angiogenesis and lymphangiogenesis. *Experim. Cell Res.* **312**, 549-560.

10. Ferrara, N., Gerber, H. P. & LeCouter, J. (2003). The biology of VEGF and its receptors. *Nature Medicine* **9**, 669-676.

11. Matsumoto, T. & Claesson-Welsh, L. (2001). VEGF receptor signal transduction. *Sci. STKE.* **2001**, re21.

12. Takahashi, H. & Shibuya, M. (2005). The vascular endothelial growth factor (VEGF)/VEGF receptor system and its role under physiological and pathological conditions. *Clinical Science* **109**, 227-241.

13. Koch, S., Tugues, S., Li, X., Gualandi, L. & Claesson-Welsh, L. (2011). Signal transduction by vascular endothelial growth factor receptors. *Biochem. J.* **437**, 169-183.

14. Olsson, A. K., Dimberg, A., Kreuger, J. & Claesson-Welsh, L. (2006). VEGF receptor signalling - in control of vascular function. *Nat. Rev. Mol. Cell. Biol.* **7**, 359-371.

15. Brozzo, M. S., Bjelic, S., Kisko, K., Schleier, T., Leppanen, V. M., Alitalo, K., Winkler, F. K. & Ballmer-Hofer, K. (2012). Thermodynamic and structural description of allosterically regulated VEGFR-2 dimerization. *Blood.* **119**, 1781-1788.

16. Hyde, C. A., Giese, A., Stuttfeld, E., Abram, S. J., Villemagne, D., Schleier, T., Binz, H. K. & Ballmer-Hofer, K. (2012). Targeting extracellular domains D4 and D7 of vascular endothelial growth factor receptor 2 reveals allosteric receptor regulatory sites. *Mol. Cell. Biol.* **32**, 3802-3813.

17. Kisko, K., Brozzo, M. S., Missimer, J., Schleier, T., Menzel, A., Leppanen, V. M., Alitalo, K., Walzthoeni, T., Aebersold, R. & Ballmer-Hofer, K. (2011). Structural analysis of vascular endothelial growth factor receptor-2/ligand complexes by small-angle X-ray solution scattering. *FASEB J.* **25**, 2980-2986.

18. Leppanen, V. M., Jeltsch, M., Anisimov, A., Tvorogov, D., Aho, K., Kalkkinen, N., Toivanen, P., Yla-Herttuala, S., Ballmer-Hofer, K. & Alitalo, K. (2011). Structural determinants of vascular endothelial growth factor-D receptor binding and specificity. *Blood.* **117**, 1507-1515.

19. Clegg, L. W. & Mac Gabhann, F. (2015). Site-Specific Phosphorylation of VEGFR2 Is Mediated by Receptor Trafficking: Insights from a Computational Model. *PLoS Comput. Biol.* **11**, e1004158.

20. Mac Gabhann, F., Qutub, A. A., Annex, B. H. & Popel, A. S. (2010). Systems biology of pro-angiogenic therapies targeting the VEGF system. *Wiley. Interdiscip. Rev. Syst. Biol. Med.* **2**, 694-707.

21. Qutub, A. A., Mac Gabhann, F., Karagiannis, E. D., Vempati, P. & Popel, A. S. (2009). Multiscale models of angiogenesis. *IEEE. Eng. Med. Biol. Mag.* **28**, 14-31.

22. Vempati, P., Popel, A. S. & Mac Gabhann, F. (2014). Extracellular regulation of VEGF: Isoforms, proteolysis, and vascular patterning. *Cytokine & Growth Factor Reviews* **25**, 1-19.

23. Gerhardt, H., Golding, M., Fruttiger, M., Ruhrberg, C., Lundkvist, A., Abramsson, A., Jeltsch, M., Mitchell, C., Alitalo, K., Shima, D. & Betsholtz, C. (2003). VEGF guides angiogenic sprouting utilizing endothelial tip cell filopodia. *J. Cell Biol.* **161**, 1163-1177.

24. Huang, K., Andersson, C., Roomans, G. M., Ito, N. & Claesson-Welsh, L. (2001). Signaling properties of VEGF receptor-1 and -2 homo- and heterodimers. *Int. J. Biochem. Cell. Biol.* **33**, 315-324.

25. Muller, Y. A., Christinger, H. W., Keyt, B. A. & de Vos, A. M. (1997). The crystal structure of vascular endothelial growth factor (VEGF) refined to 1.93 A resolution: multiple copy flexibility and receptor binding. *Structure* **5**, 1325-1338.

26. Ballmer-Hofer, K., Andersson, A. E., Ratcliffe, L. E. & Berger, P. (2011). Neuropilin-1 promotes VEGFR-2 trafficking through Rab11 vesicles thereby specifying signal output. *Blood* **118**, 816-826.

27. Scheidegger, P., Weiglhofer, W., Suarez, S., Kaser-Hotz, B., Steiner, R., Ballmer-Hofer, K. & Jaussi, R. (1999). Vascular endothelial growth factor (VEGF) and its receptors in tumor-bearing dogs. *Biol. Chem.* **380**, 1449-1454.

28. Cross, M. J. & Claesson-Welsh, L. (2001). FGF and VEGF function in angiogenesis: signalling pathways, biological responses and therapeutic inhibition. *Trends Pharmacol. Sci.* **22**, 201-207.

29. Sarabipour, S., Ballmer-Hofer, K. & Hristova, K. (2016). VEGFR-2 conformational switch in response to ligand binding. *Elife* **5**.

30. Chen, H., Puhl, H. L., Koushik, S. V., Vogel, S. S. & Ikeda, S. R. (2006). Measurement of FRET efficiency and ratio of donor to acceptor concentration in living cells. *Biophys. J.* **91**, L39-L41.

31. Clegg, R. M. (1996). Fluorescence resonance energy transfer (FRET). In *Fluorescence Imaging Spectroscopy and Microscopy* (Wang, X. F. & Herman, B., eds), pp. 179-252, John Wiley, New York.

32. Hoppe, A., Christensen, K. & Swanson, J. A. (2002). Fluorescence resonance energy transfer-based stoichiometry in living cells. *Biophys. J.* **83**, 3652-3664.

33. Merzlyakov, M., Chen, L. & Hristova, K. (2007). Studies of receptor tyrosine kinase transmembrane domain interactions: The EmEx-FRET method. *J. Membr. Biol.* **215**, 93-103.

34. Forster, T. (1948). Intermolecular energy migration and fluorescence. *Annalen der Physik* **2**, 55-75.

35. Jares-Erijman, E. A. & Jovin, T. M. (2003). FRET imaging. *Nature Biotechnology* **21**, 1387-1395.

36. Shaner, N. C., Steinbach, P. A. & Tsien, R. Y. (2005). A guide to choosing fluorescent proteins. *Nature Methods* **2**, 905-909.

37. Piston, D. W. & Kremers, G. J. (2007). Fluorescent protein FRET: the good, the bad and the ugly. *Trends Biochem. Sci.* **32**, 407-414.

38. Zimmermann, T., Rietdorf, J. & Pepperkok, R. (2003). Spectral imaging and its applications in live cell microscopy. *FEBS Lett.* **546**, 87-92.

39. Stryer, L. (1968). Fluorescence spectroscopy of proteins. Fluorescent probes provide insight into the structure, interactions, and dynamics of proteins. *Science* **162**, 526-533.

40. Wang, X. F. & Herman, B. (1996). *Fluorescence Imaging Spectroscopy and Microscopy* John Wiley & Sons.

41. Seddon, A. M., Curnow, P. & Booth, P. J. (2004). Membrane proteins, lipids and detergents: not just a soap opera. *Biochim. Biophys. Acta* **1666**, 105-117.

42. Li, E., Wimley, W. C. & Hristova, K. (2012). Transmembrane helix dimerization: Beyond the search for sequence motifs. *Biochimica et Biophysica Acta-Biomembranes* **1818**, 183-193.

43. Hong, H., Joh, N. H., Bowie, J. U. & Tamm, L. K. (2009). Methods for Measuring the Thermodynamic Stability of Membrane Proteins. *Methods in Enzymology: Biothermodynamics,Vol 455, Part A* **455**, 213-236.

44. MacKenzie, K. R. (2006). Folding and stability of alpha-helical integral membrane proteins. *Chem. Rev.* **106**, 1931-1977.

45. Finger, C., Volkmer, T., Prodohl, A., Otzen, D. E., Engelman, D. M. & Schneider, D. (2006). The stability of transmembrane helix interactions measured in a biological membrane. *J. Mol. Biol.* **358**, 1221-1228.

46. Schneider, D., Liu, Y., Gerstein, M. & Engelman, D. M. (2002). Thermostability of membrane protein helix-helix interaction elucidated by statistical analysis. *FEBS Lett.* **532**, 231-236.

47. Raicu, V. (2010). FRET-based determination of protein complex structure at nanometer length scale in living cells. In *Nanoscopy. Multidimensional Optical Fluorescence Microscopy.* (A.Diaspro, ed) CRC press.

48. Singh, D. R., Mohammad, M. M., Patowary, S., Stoneman, M. R., Oliver, J. A., Movileanu, L. & Raicu, V. (2013). Determination of the quaternary structure of a bacterial ATP-binding cassette (ABC) transporter in living cells. *Integrative Biology* **5**, 312-323.

49. Mathiasen, S., Christensen, S. M., Fung, J. J., Rasmussen, S. G. F., Fay, J. F., Jorgensen, S. K., Veshaguri, S., Farrens, D. L., Kiskowski, M., Kobilka, B. & Stamou, D. (2014). Nanoscale high-content analysis using compositional heterogeneities of single proteoliposomes. *Nature Methods* **11**, 931-934.

50. Kenworthy, A. K. & Edidin, M. (1998). Distribution of a glycosylphosphatidylinositol-anchored protein at the apical surface of MDCK cells examined at a resolution of <100 Å using imaging fluorescence resonance energy tranfer. *J. Cell Biol.* **142**, 69-84.

51. Kenworthy, A. K., Petranova, N. & Edidin, M. (2000). High-resolution FRET microscopy of cholera toxin B-subunit and GPI-anchored proteins in cell plasma membranes. *Mol. Biol. Cell* **11**, 1645-1655.

52. Abankwa, D. & Vogel, H. (2007). A FRET map of membrane anchors suggests distinct microdomains of heterotrimeric G proteins. *J. Cell Sci.* **120**, 2953-2962.

53. Chen, L. R., Novicky, L., Merzlyakov, M., Hristov, T. & Hristova, K. (2010). Measuring the Energetics of Membrane Protein Dimerization in Mammalian Membranes. *J. Am. Chem. Soc.* **132**, 3628-3635.

54. You, M., Li, E., Wimley, W. C. & Hristova, K. (2005). FRET in liposomes: measurements of TM helix dimerization in the native bilayer environment. *Analytical Biochemistry* **340**, 154-164.

55. King, C., Stoneman, M., Raicu, V. & Hristova, K. (2016). Fully quantified spectral imaging reveals in vivo membrane protein interactions. *Integr. Biol. (Camb.)* **8**, 216-229.

56. Raicu, V., Stoneman, M. R., Fung, R., Melnichuk, M., Jansma, D. B., Pisterzi, L. F., Rath, S., Fox, M., Wells, J. W. & Saldin, D. K. (2009). Determination of supramolecular structure and spatial distribution of protein complexes in living cells. *Nature Photonics* **3**, 107-113.

57. Chen, H. M., Puhl, H. L. & Ikeda, S. R. (2007). Estimating protein-protein interaction affinity in living cells using quantitative Forster resonance energy transfer measurements. *Journal of Biomedical Optics* **12**.

58. Placone, J. & Hristova, K. (2012). Direct Assessment of the Effect of the Gly380Arg Achondroplasia Mutation on FGFR3 Dimerization Using Quantitative Imaging FRET. *PLoS ONE* **7**, e46678.

59. Placone, J., He, L., Del Piccolo, N. & Hristova, K. (2014). Strong dimerization of wild-type ErbB2/Neu transmembrane domain and the oncogenic Val664Glu mutant in mammalian plasma membranes. *Biochim. Biophys. Acta* **1838**, 2326-2330.

60. Chen, L., Placone, J., Novicky, L. & Hristova, K. (2010). The extracellular domain of fibroblast growth factor receptor 3 inhibits ligand-independent dimerization. *Science Signaling* **3**, ra86.

61. Del Piccolo, N., Placone, J., He, L., Agudelo, S. C. & Hristova, K. (2012). Production of plasma membrane vesicles with chloride salts and their utility as a cell membrane mimetic for biophysical characterization of membrane protein interactions. *Anal. Chem.* **84**, 8650-8655.

62. Del Piccolo, N., Placone, J. & Hristova, K. (2015). Effect of Thanatophoric Dysplasia Type I Mutations on FGFR3 Dimerization. *Biophys. J.* **108**, 272-278.

63. Rizzo, M. A., Springer, G. H., Granada, B. & Piston, D. W. (2004). An improved cyan fluorescent protein variant useful for FRET. *Nature Biotechnology* **22**, 445-449.

64. Wolber, P. K. & Hudson, B. S. (1979). An analytic solution to the Förster energy transfer problem in two dimensions. *Biophys. J.* **28**, 197-210.

65. Snyder, B. & Freire, E. (1982). Fluorescence energy transfer in two dimensions. A numeric solution for random and nonrandom distributions. *Biophys. J.* **40**, 137-148.

66. Freire, E. & Snyder, B. (1982). Quantitative characterization of the lateral distribution of membrane proteins within the lipid bilayer. *Biophys. J.* **37**, 617-624.

67. Veatch, W. & Stryer, L. (1977). The dimeric nature of the gramicidin A transmembrane channel: conductance and fluorescence energy transfer studies of hybrid channels. *J. Mol. Biol.* **113**, 89-102.

68. Raicu, V. (2007). Efficiency of resonance energy transfer in homo-oligomeric complexes of proteins. *Journal of Biological Physics* **33**, 109-127.

69. Patowary, S., Pisterzi, L. F., Biener, G., Holz, J. D., Oliver, J. A., Wells, J. W. & Raicu, V. (2015). Experimental Verification of the Kinetic Theory of FRET Using Optical Microspectroscopy and Obligate Oligomers. *Biophys. J.* **108**, 1613-1622.

70. Raicu, V., Jansma, D. B., Miller, R. J. D. & Friesen, J. D. (2005). Protein interaction quantified in vivo by spectrally resolved fluorescence resonance energy transfer. *Biochem. J.* **385**, 265-277.

71. Murai, K. K. & Pasquale, E. B. (2003). 'Eph'ective signaling: forward, reverse and crosstalk. *J. Cell Sci.* **116**, 2823-2832.

72. Brieher, W. M., Yap, A. S. & Gumbiner, B. M. (1996). Lateral dimerization is required for the homophilic binding activity of C-cadherin. *J. Cell Biol.* **135**, 487-496.

73. Klingelhofer, J., Laur, O. Y., Troyanovsky, R. B. & Troyanovsky, S. M. (2002). Dynamic interplay between adhesive and lateral E-cadherin dimers. *Mol. Cell. Biol.* **22**, 7449-7458.

74. von Heijne, G. (1999). A day in the life of Dr. K. or How I learned to stop worrying and love lysozome: A tragedy in six acts. *J. Mol. Biol.* **293**, 367-379.

75. Hong, H., Blois, T. M., Cao, Z. & Bowie, J. U. (2010). Method to measure strong protein-protein interactions in lipid bilayers using a steric trap. *Proceedings of the National Academy of Sciences of the United States of America* **107**, 19802-19807.

76. Gerber, D., Sal-Man, N. & Shai, Y. (2004). Two motifs within a transmembrane domain, one for homodimerization and the other for heterodimerization. *J. Biol. Chem.* **279**, 21177-21182.

77. Sal-Man, N., Gerber, D. & Shai, Y. C. (2005). An all-D-aa transmembrane domain (TM) of the aspartate receptor tar recognizes the all-L aa TM and inhibits tar-mediated chemotaxis. *Biophys. J.* **88**, 78A.

78. Russ, W. P. & Engelman, D. M. (1999). TOXCAT: A measure of transmembrane helix association in a biological membrane. *Proc. Natl. Acad. Sci. USA* **96**, 863-868.

79. Schneider, D. & Engelman, D. M. (2003). GALLEX, a measurement of heterologous association of transmembrane helices in a biological membrane. *J. Biol. Chem.* **278**, 3105-3111.

80. Biener, G., Stoneman, M. R., Acbas, G., Holz, J. D., Orlova, M., Komarova, L., Kuchin, S. & Raicu, V. (2014). Development and Experimental Testing of an Optical Micro-Spectroscopic Technique Incorporating True Line-Scan Excitation. *International Journal of Molecular Sciences* **15**, 261-276.

81. Raicu, V., Jansma, D. B., Miller, R. J. D. & Friesen, J. D. (2005). Protein interaction quantified in vivo by spectrally resolved fluorescence resonance energy transfer. *Biochem. J.* **385**, 265-277.

82. Press, W. H., Flannery, B. P., Teukolsky, S. A. & Vetterling, W. T. (1989). *Numerical Recipes. The Art of Scientific Computing*, pp. 1-702, Cambridge University Press, Cambridge.

83. Lakowicz, J. R. (1999). *Principles of fluorescence spectroscopy* Kluwer Academic/Plenum.

84. Garcia, D. (2010). Robust smoothing of gridded data in one and higher dimensions with missing values. *Computational Statistics & Data Analysis* **54**, 1167-1178.

85. Sarabipour, S., King, C. & Hristova, K. (2014). Un-induced high-yield bacterial expression of fluorescent proteins. *Anal. Biochem.* **449**, 155-157.

86. Chen, L., Novicky, L., Merzlyakov, M., Hristov, T. & Hristova, K. (2010). Measuring the Energetics of Membrane Protein Dimerization in Mammalian Membranes. *J. Am. Chem. Soc.* **132**, 3628-3635.

87. Adler, J., Shevchuk, A. I., Novak, P., Korchev, Y. E. & Parmryd, I. (2010). Plasma membrane topography and interpretation of single-particle tracks. *Nat. Methods* **7**, 170-171.

88. Parmryd, I. & Onfelt, B. (2013). Consequences of membrane topography. *FEBS. J.* **280**, 2775-2784.

89. Sinha, B., Koster, D., Ruez, R., Gonnord, P., Bastiani, M., Abankwa, D., Stan, R. V., Butler-Browne, G., Vedie, B., Johannes, L., Morone, N., Parton, R. G., Raposo, G., Sens, P., Lamaze, C. & Nassoy, P. (2011). Cells respond to mechanical stress by rapid disassembly of caveolae. *Cell.* **144**, 402-413.

90. Sarabipour, S., Chan, R. B., Zhou, B., Di Paolo, G. & Hristova, K. (2015). Analytical characterization of plasma membrane-derived vesicles produced via osmotic and chemical vesiculation. *Biochim. Biophys. Acta* **1848**, 1591-1598.

91. Kruh, J. (1982). Effects of Sodium-Butyrate, A New Pharmacological Agent, on Cells in Culture. *Mol. Cell. Biochem.* **42**, 65-82.

92. Soneoka, Y., Cannon, P. M., Ramsdale, E. E., Griffiths, J. C., Romano, G., Kingsman, S. M. & Kingsman, A. J. (1995). A Transient 3-Plasmid Expression System for the Production of High-Titer Retroviral Vectors. *Nucleic Acids Res.* **23**, 628-633.

93. King, C., Sarabipour, S., Byrne, P., Leahy, D. J. & Hristova, K. (2014). The FRET signatures of non-interacting proteins in membranes: simulations and experiments. *Biophys. J.* **106**, 1309-1317.

94. Yang, Y., Xie, P., Opatowsky, Y. & Schlessinger, J. (2010). Direct contacts between extracellular membrane-proximal domains are required for VEGF receptor activation and cell signaling. *Proceedings of the National Academy of Sciences of the United States of America* **107**, 1906-1911.

95. Manni, S., Mineev, K. S., Usmanova, D., Lyukmanova, E. N., Shulepko, M. A., Kirpichnikov, M. P., Winter, J., Matkovic, M., Deupi, X., Arseniev, A. S. & Ballmer-Hofer, K. (2014). Structural and Functional Characterization of Alternative Transmembrane Domain Conformations in VEGF Receptor 2 Activation. *Structure* **22**, 1077-1089.

Christopher King

3606 Southern Avenue
Baltimore, MD 21214
Phone: (443) 633-8405
chris.king0313@gmail.com

Education

Bachelor of Science in Physics, May 2011
- Minor in Mathematics
- Graduation with Highest Distinction
- University of Iowa, Iowa City, Iowa, 52242

Doctor of Philosophy in Molecular Biophysics, expected Fall 2016
- The Johns Hopkins University, Baltimore, Maryland 21212

Affiliations

American Physical Society

Biophysical Society

National Science Foundation GRFP Fellow

Phi Beta Kappa

Current Research Interests

Biophysical properties of Receptor Tyrosine Kinases and other membrane proteins, live-cell microscopy, method development for new biophysical measurements, data analysis and modeling, molecular dynamics simulations

Publications

Christopher King, Michael Stoneman, Valerica Raicu, Kalina Hristova: *Fully quantified spectral imaging reveals in vivo membrane protein interactions †*. Integrative Biology 01/2016; DOI:10.1039/c5ib00202h

Deo R Singh, Fozia Ahmed, Christopher King, Nisha Gupta, Matt Salotto, Elena B Pasquale, Kalina Hristova: *EphA2 unliganded dimers suppress EphA2 pro-tumorigenic signaling*. Journal of Biological Chemistry 09/2015; 290(45). DOI:10.1074/jbc.M115.676866

Deo R Singh, QingQing Cao, Christopher King, Matt Salotto, Fozia Ahmed, Xiang Yang Zhou, Elena B Pasquale, Kalina Hristova: *Unliganded EphA3 dimerization promoted by the SAM domain*. Biochemical Journal 07/2015; 471(1). DOI:10.1042/BJ20150433

Christopher King*, Sarvenaz Sarabipour*, Patrick Byrne, Daniel J Leahy, Kalina Hristova: *The FRET Signatures of Noninteracting Proteins in Membranes: Simulations and Experiments*. Biophysical Journal 03/2014; 106(6):1309-17. DOI:10.1016/j.bpj.2014.01.039

Sarvenaz Sarabipour*, Christopher King*, Kalina Hristova: *Uninduced high-yield bacterial expression of fluorescent proteins*. Analytical Biochemistry 12/2013; 449(1). DOI:10.1016/j.ab.2013.12.027

Research Experience and Awards

Doctoral research as part of the Program in Molecular Biophysics at the Johns Hopkins University, Department of Biophysics, August 2011-November 2016

Fellow of the National Science Foundation Graduate Research Fellowship Program under the advising of Dr. Kalina Hristova of the Johns Hopkins University's Department of Material Science and Engineering, August 2013-November 2016

-Developed a new quantitative FRET method for measuring membrane protein concentrations in live cells

-Optimized a general method for the mass production of fluorescent proteins utilizing auto-induction in *E. coli*

-Performed PCR-based subcloning and mutagenesis for membrane proteins

-Performed tissue culture and transient transfection with HEK293T cells

-Developed image analysis and data analysis software utilizing MATLAB

-Developed formal FRET theory to account for inter-oligomeric FRET as well as intra-oligomeric FRET

-Utilized MATLAB to perform simulations of stochastic FRET in two-dimensional distributions of oligomers

-Performed all-atom molecular dynamics simulations with peptides and lipid bilayers utilizing GROMACS on the Maryland Advanced Research Computing Center's supercomputer

Invited Presenter at the St. Jude Children's Research Hospital's National Graduate Student Symposium; April 2015

-Poster and short oral presentation over quantitative FRET measurements of VEGFR2 interactions in cell membranes

Undergraduate Research Assistant under Dr. Craig Kletzing for the University of Iowa's Experimental Space Plasma Physics Group, Department of Physics and Astronomy; August 2009 – June 2011

-Developed software using LabVIEW for high-speed data acquisition, signal generation, and signal analysis for real-time simulation and testing of instrumentation installed on the Van Allen Space Probes, launched into orbit August 2012

Professional Experience

Electronic Warfare Systems Expert, Staff Sergeant (E-5), United States Air Force, October 2000 – October 2006

-Performed maintenance, inspection, and modification of offensive and defensive electronic systems for fixed-wing aircraft

-Promoted ahead of peers to first-level supervisor, performance evaluator, and training coordinator for new personnel

-Served on three deployments in support of Operation Iraqi Freedom